The Henryk Niewodniczański
Institute of Nuclear Physics
Polish Academy of Sciences
ul. Radzikowskiego 152, 31-342 Kraków
http://www.ifj.edu.pl/badania/publikacje

Kraków, 2022

Neutrino-Nucleus Cross-Section Measurements in the Near Detector of the T2K Experiment

Tomasz Wąchała

Habilitation dissertation

Wydano nakładem Instytutu Fizyki Jądrowej im. Henryka Niewodniczańskiego
Polskiej Akademii Nauk
Kraków 2022
Recenzenci: prof. Janusz Gluza, dr hab. Paweł Malecki
ISBN: 978-83-63542-25-2 (print)
ISBN: 978-83-63542-26-9 (pdf)
https://doi.org/10.48733/978-83-63542-26-9

Abstract

The studies of neutrino-nucleus cross sections play an important role in better understanding the mechanisms that rule the neutrino interactions and in more precise measurements of the neutrino oscillation parameters. This monograph is focused on the measurements of neutrino cross sections from the accelerator neutrino beam with the mean energy of 0.7 GeV using the near detector of the T2K experiment. The monograph describes in detail the models of neutrino-nucleus interactions in this energy regime that are currently on the market. It also gives an overview of the world experimental results and outlines the prospects for future cross-section measurements. An entire chapter of this monograph is dedicated to the analyses published by the T2K experiment.

The monograph contains a description of the T2K experiment, including the experimental setup, research program, and characterization of the Monte Carlo simulation and event reconstruction. A separate chapter is dedicated to the detailed explanation of the techniques and methods used in the cross-section measurements in T2K with a special emphasis on the maximum likelihood approach.

Two analyses describing the charged current single charged pion production (CC1π) on water and charged current with no pions on lead and carbon are reported. The measured CC1π total flux-integrated cross section is compatible with Monte Carlo predictions from the NEUT generator. GENIE predictions are within two standard deviations. Further extensions of these studies including the enlarged phase space of the measurement and using more data should allow analysers to compute a differential cross section and minimize the model dependence.

Streszczenie

Badania oddziaływań neutrin z jądrami atomowymi odgrywają istotną rolę zarówno w zrozumieniu mechanizmów, które rządzą oddziaływaniami neutrin, jak i w precyzyjnych pomiarach parametrów oscylacji neutrin. Niniejsza monografia koncentruje się na pomiarach przekrojów czynnych na oddziaływania neutrin z wiązki neutrin akceleratorowych o średniej energii równej 0.7 GeV z wykorzystaniem bliskiego detektora eksperymentu T2K. W pracy opisane są modele odziaływań neutrino-jądro atomowe w zakresie energii od kilkuset MeV do kilku GeV oraz przedstawiony został przegląd wyników eksperymentalnych. Jeden z rozdziałów poświęcony jest analizom przeprowadzonym w eksperymencie T2K, które zostały opublikowane. Krótka dyskusja na temat przyszłych eksperymentów i perspektyw w pomiarach przekrojów czynnych na oddziaływania neutrin również znajduje się w pracy.

Monografia zawiera opis eksperymentu T2K zarówno od strony techniczej (wiązka, detektory itd.), jak i charakterystykę programu badawczego oraz zarys wykorzystywanych metod symulacji i rekonstrukcji zdarzeń. Osobny rozdział poświęcony został szczegółowemu opisowi technik stosowanych w pomiarach przekrojów czynnych na oddziaływania neutrin w eksperymencie T2K, ze szczególnym uwzględnieniem dopasowania metodą największej wiarygodności.

Dwie analizy, które opisują oddziaływania z wymianą prądów naładowanych z produkcją pojedynczego pionu naładowanego (CC1π) na wodzie, jak i bez produkcji pionów na ołowiu i węglu zostały przedstawione w pracy. Zmierzona wartość całkowitego przekroju czynnego na oddziaływania CC1π jest zgodna z przewidywaniami Monte Carlo z generatora NEUT w granicach błędów pomiarowych. Wartość jest również zgodna z przewidywaniami generatora GENIE z dokładnością do dwóch odchyleń standardowych. Przeprowadzona została również dyskusja na temat przyszłych usprawnień wyżej wymienionych analiz, takich jak zwiększenie przestrzeni fazowej pomiaru poprzez wykorzystanie przypadków z mionem wychodzącym pod dużymi kątami i „do tyłu", czy wykorzystanie większej ilości danych. Wprowadzenie tych usprawnień powinno pozwolić w przyszłości na pomiar różniczkowego przekroju czynnego.

Contents

Chapter 1

Introduction

Although neutrinos are, after photons, the most abundant elementary particles in the entire universe, they remain the most elusive ones. This is because these half-spin particles are both charged and colorless, and therefore only interact effectively with charged fermions and massive gauge bosons through weak interactions. Nevertheless, the study of their properties, which required the use of (1) intense natural or artificial neutrino sources, (2) giant and expensive detectors operating preferably underground, and (3) long measurement time, has provided many exciting results. Suffice it to mention the discovery of the neutrino oscillation, which brought the 2015 Nobel Prize in Physics to Takaaki Kajita (Super-Kamiokande Collaboration) and Arthur B. McDonald (SNO Collaboration) for their leading role in *"the discovery of neutrino oscillations, which shows that neutrinos have mass"*. This discovery had far-reaching implications for all particle physics and the Standard Model in particular. It turned out that the Standard Model, which for many years successfully described the interactions of elementary particles, is not a complete theory because according to it neutrinos were devoid of mass. Since the discovery of neutrino oscillations, many experiments have studied the properties of neutrinos from artificial and natural sources, resulting in a very good description of the vast majority of neutrino data in the framework of mixing of three neutrino flavors. The only notable exception was the result from the Liquid Scintillator Neutrino Detector (LSND) experiment [1] at the Los Alamos 800 MeV proton accelerator, which reported an excess of $\bar{\nu_e}$ events in the $\bar{\nu_\mu}$ beam, which can not be attributed to the oscillation of the three (electron, muon, and tau) known neutrino flavours. The LSND signal was later confirmed by the MiniBooNE experiment [2] with neutrinos from the 8 GeV Booster Neutrino Beam at Fermilab interacting with a mineral oil Cherenkov detector, which traveled a different distance than those in LSND. Moreover, recently the LSND experiment has published a combined analysis of ν_e appearance data from 1.28 $\times 10^{21}$ protons on target in neutrino mode (approximately a factor of two increased statistics), and $\bar{\nu_e}$ appearance data from 1.13 $\times 10^{21}$ protons on target in antineutrino mode, which resulted in more than a 4σ excess of charged current quasi-elastic events in both modes. The most straightforward, two-neutrino oscillation interpretation of MiniBooNE data would require at least four neutrino types, thus pointing to physics beyond the Standard Model [3]. Further investigation of the event excess observed by the MiniBooNE experiment is one of the priorities of the Fermilab short-baseline neutrino (SBN) program [4]. On the other hand, the MiniBooNE excess was discovered for the low energy neutrino interactions where the understanding of the neutrino cross sections is poor. There are opinions within the neutrino community that this fact could also explain the disagreement observed by MiniBooNE.

Currently, both running long baseline neutrino experiments - T2K and NOvA have begun to be sensitive enough to determine the value of the parameter δ_{CP} describing CP symmetry breaking. They study a very subtle difference in ν_μ and $\bar{\nu}_\mu$ oscillations into ν_e and $\bar{\nu}_e$. In its Nature publication [5], the T2K Collaboration reported a preference for values of δ_{CP} close to the maximal CP violation, while both CP conserving points $\delta_{CP} = 0$ and $\delta_{CP} = \pi$ are ruled out at the 95% confidence level. There is no doubt that any reduction of systematic error, including that significant contribution from the neutrino-nucleus cross section, will allow the δ_{CP} to be measured in less time. This also applies to the two planned long baseline neutrino experiments - Hyper-K and DUNE, for which measurements of neutrino interactions on water and argon are particularly important, while most of the current measurements are performed on hydrocarbon or water targets.

This monograph is devoted to accelerator-based neutrino oscillation experiments, emphasizing the results obtained by the T2K collaboration related to measurements of the neutrino-nucleus interaction cross section. A substantial part of paper describes the analysis done to measure the charged current single-charged-pion production cross section on water for events occurring within the pi-zero detector of the T2K near detector. The result is provided in a single neutrino energy bin cross section integrated over the entire T2K muon neutrino flux (0 - 30 GeV) compared with predictions of two neutrino interaction generators NEUT and GENIE. A second analysis describes the selection procedure for CC0π interactions on lead and carbon targets. Although the CC0π cross section has not been obtained, the study constitutes a crucial ingredient for the future analyses of this interaction channel. Apart from the results mentioned above, the T2K experiment also published a number of analyses concerning neutrino-nucleus cross-section measurements. It is necessary to mention here the studies of transverse kinematic imbalance in CC1π interactions ([6]), the measurement of electron neutrino and antineutrino cross section ([7]), the simultaneous measurement of CC0π cross section on oxygen and carbon [8], nuclear effects in CC0π interactions ([9]), and many others.

The monograph's chapters provide all the information necessary to understand the importance of measurements of the neutrino-nucleus cross section. It also gives a complete description of the T2K experiment and methods used and developed to make the measurement. A short description of each chapter following the introductory one is provided here:

Chapter (2) presents models of neutrino-nucleus interactions with a short overview of neutrino cross-section experiments, emphasizing the results for the neutrino energy range $\sim$ 1 GeV, which is relevant for the T2K experiment.

Chapter (3) contains a brief introduction to neutrino oscillations and descriptions of the T2K research program and experimental setup.

Chapter (4) details the organization of data taking, reconstruction, and data analysis tools and simulation software used in the near detector of the T2K experiment. The new PØD-Tracker incremental matching algorithm, which improves the reconstruction of the particle tracks, developed by the author of this monograph, is also presented.

Chapter (5) describes the procedures and techniques used in the measurements of neutrino-nucleus cross sections in the T2K experiment, including the methods of determining systematic errors and details of the unfolding and likelihood fitting algorithms, which are well-established T2K methods of determining cross section.

Chapter (6) presents the most important total and differential cross-section results obtained with the off-axis near detector of the T2K experiment, with muon neutrino and muon antineutrino beams interacting with various targets.

Chapter (7) presents two analyses developed by the author of this monograph: ν_μ-induced charged current single charged pion production cross section on water and ν_μ induced charged current cross section without pions in the final state on lead.

Chapter (8) provides a summary and outlook.

Chapter 7 is dedicated to the results established by the author of this monograph and obtained with the use of the existing T2K analysis framework, Monte Carlo simulation and data. First, the author was fully responsible for establishing, testing and evaluating event selection, and the calculations of the systematic errors in the CC1π analysis presented in 7.1. This analysis is the first study of CC1π cross section on water in the T2K off-axis near detector. It has to be emphasized, that the analysis was very useful because it made it possible to test the tools for cross-section extraction and systematic errors evaluation. It is also needless to say that the CC1π analysis paved the way for the next generation of the cross-section measurements for this interaction channel.
Second, the study on the selection of CC0π interactions on lead reported in 7.2 was entirely performed by the creator of this monograph. The study constitutes a crucial ingredient for future analyses measuring cross sections on lead and carbon and their ratio. The study will be continued.
Finally, the author was also fully responsible for creating, implementing, and testing the PØD-tracker incremental matching algorithm detailed in 4.4. The algorithm concerns the track reconstruction of the particles traversing at least two sub-detectors (PØD and TPC) of the ND280 detector. This reconstruction method is used in the official software of the T2K off-axis near detector and helps in T2K cross-section measurements. It needs to be emphasized that the results presented in 7 should not be interpreted as the official result of the T2K collaboration. Results and figures from other works have been clearly attributed.

During the process of writing this monograph, the following technical notes of the T2K experiment were created with the major contribution of the author of this monograph: (1) T2K-TN-136 entitled *Measurement of neutrino induced charged current single pion production on water using the PØD detector* describing the analysis presented in 7.1, (2) T2K-TN-329 named *ND280 reconstruction for Production 7*, including a description of the PØD-tracker incremental matching algorithm detailed in 4.4.

Apart from the studies included in this work, the author has also a significant record of the activities in the T2K experiment. They are listed below:

- Leader of the Side Muon Range detector reconstruction group (2009-2011) and a person responsible for creating and testing the reconstruction package for this detector.
- Convener of the T2K Near Detector reconstruction group (2013-2018) - responsible for coordinating the reconstruction in the PØD detector. During this period, the PØD-tracker incremental matching algorithm was implemented and included in the official software of the T2K near detector.
- Convener of the T2K Near Detector software group (2018-2020).
- Reviewer of the T2K technical notes dedicated to neutrino cross-section measurements (2015-now).

The author of this monograph delivered the following talks on behalf of the T2K collaboration:

1. T2K Experiment Neutrino Oscillation Results, Matter to the Deepest conference, Katowice, 2019, [10]
2. The latest results from the long-baseline neutrino experiment T2K, New Trends in High Energy Physics conference, Budva, 2018, [11]
3. Recent Results on the CP Violation Search in the Accelerator Neutrino Oscillations, 2nd Jagiellonian Symposium of Fundamental and Applied Subatomic Physics, Krakow, 2017, [12]
4. Recent results from the T2K experiment, 29th Rencontres de Physique de La Vallée d'Aoste, La Thuile, 2015, [13]
5. Recent Results on Neutrino Cross Sections in the Intermediate Energy Range, 39th International Conference of Theoretical Physics: Matter to the Deepest, Ustron, 2015, [14]

Chapter 2

Neutrino-nucleus cross sections

This monograph is devoted to accelerator-based neutrino oscillation experiments, emphasizing the results obtained by the T2K collaboration. Nowadays, such experiments measure the ν_μ and ν_e interaction rate R both in the near and far detectors and benefit from the near/far detector reduction of systematic errors. The near detector, usually located close to the neutrino source, measures R before possible neutrino oscillations occur, whereas the far detector measures R after neutrino travels the distance L between the near and far detector, i.e., after possible development of neutrino oscillations. Three factors, namely neutrino flux $\Phi(E_\nu)$, neutrino interaction cross section $\sigma(k, k')$ and the detector efficiency ϵ influences R. They depend on neutrino energy E_ν, initial and final lepton kinematic variables k, k', whereas ϵ is a function of any measured particle kinematics. Currently, systematic uncertainties for the neutrino-nucleus cross sections are at the level of 5-10%, being a significant limitation of precision in neutrino oscillation experiments, besides the uncertainties for accelerator neutrino flux. In this chapter, after presenting multiple motivations for measuring neutrino-nucleus cross-sections, models of neutrino interactions are discussed. Finally, the results obtained in cross-sectional experiments (excluding T2K, whose results are presented in detail in Chapter 6 are briefly summarized.

2.1 Importance of the neutrino cross-section measurements

In an excellent NuSTEC [1] study, the importance and challenges of neutrino-nucleus scattering have been discussed in detail [15]. Those that are and can be addressed by the T2K experiment are presented in this chapter.

Currently running long baseline neutrino experiments - T2K and NOvA, have begun to be sensitive enough to determine the value of the parameter δ_{CP}, which describes CP symmetry breaking. They study a very subtle difference in ν_μ and $\bar{\nu}_\mu$ oscillations into ν_e and $\bar{\nu}_e$. Any reduction of systematic error, including that significant contribution from the neutrino-nucleus cross section, will allow the δ_{CP} to be measured in less time. This also applies to the two planned long baseline

---

[1] Neutrino Scattering Theory Experiment Collaboration http://nustec.fnal.gov

neutrino experiments - Hyper-K and DUNE, for which measurements of neutrino interactions on water and argon are particularly important.

Monte Carlo (MC) methods are widely used in accelerator-based oscillation and neutrino scattering experiments. As a result of MC simulation, one obtains (1) kinematic information (energy, momentum) about the produced particles, taking into account their possible re-interactions within the target nuclei, and (2) the inclusive cross section divided into contributions from individual types of neutrino interactions. The following three generators are most commonly used in beam neutrino experiments: NEUT [16], GENIE [17] and NuWro [18].

The scattering of neutrinos on atomic nuclei can provide complementary information to that obtained from nucleus-nucleus, photon-nucleus, or a charged lepton-nucleus collisions. Therefore, neutrino-nucleus cross section measurements are interesting, apart from their usefulness in e.g., neutrino oscillation experiments.

2.2 Models of neutrino interactions

Neutrinos are devoid of both electric and color charge, and therefore, in the Standard Model, they interact only through weak forces. Charged Current (CC) mediated by $W^{\pm}$ bosons, and Neutral Current (NC) mediated by Z^0 boson are two types of neutrino interactions with nuclei in the Standard Model. A CC neutrino interaction on quark leads to the production of a lepton of the same flavor as the neutrino flavor. The charged lepton can be relatively easily detected. Moreover, its identification allows the flavor of the incoming neutrino to be found. In the NC interaction, an incoming neutrino only transfers energy and momentum to a quark and is present in the final state. Therefore, the neutrino NC interaction can be determined by detecting reaction products or recoil nucleus, and as a result the flavor of the incoming neutrino cannot be identified. Of course, neutrino interactions do not occur on free quarks but on quarks bound in nucleons, which in turn are bound in atomic nuclei. Nuclear targets are used to increase the number of detected neutrino interactions. Therefore, nuclear effects comprising: the binding energy of the nucleons, Fermi motion of the initial nucleons, Pauli blocking of final nucleons, short- and long-range correlations between nucleons, and final-state interactions (FSI) of the outgoing nucleon with the residual nucleus must be taken into account in the neutrino-nucleus interaction models. They are included in the description of CCQE interactions, whose uncertainties will largely limit the precision of oscillation analyzes in the current (T2K and NOvA) and future (Hyper-Kamiokande and DUNE) long baseline neutrino experiments. They will be shortly described in this section, together with such models used in neutrino generators as Relativistic Fermi Gas (RFG) [19], Local Fermi Gas [20], Spectral Function [21], and nucleon-nucleon correlation models, such as exchange current approach (Meson Exchange Currents MEC, 2p2h [22], [25] or Random Phase Approximation (RPA).

2.2.1 Initial state effects

Since nucleons are localized inside the atomic nucleus with a radius of several femtometers, they must have a momentum of 100-200 MeV/c. This is due to the Heisenberg uncertainty principle. The Fermi motion is the motion of nucleons bound in a nucleus before any interaction with momentum distribution assumed to be isotropic. For heavier nuclei, the precise distribution of nucleons momenta cannot be given because their movement takes place in the complicated environment of other nucleons, i.e., the initial momentum spectra of nucleons can vary significantly, even between nuclei with similar mass. Therefore, each nucleon has an unknown Lorentz boost in the laboratory frame for each neutrino interaction [26]. Approaches that try to give a recipe for the nucleons momentum distribution before the interaction are known as spectral function models. In neutrino interaction generators, the most commonly used models are (1) Fermi gas (relativistic or local), and (2) the spectral function (same misleading name as for models) by Benhar et al. [21]. They predict different nucleon momentum distributions, as shown in Fig. 2.1.

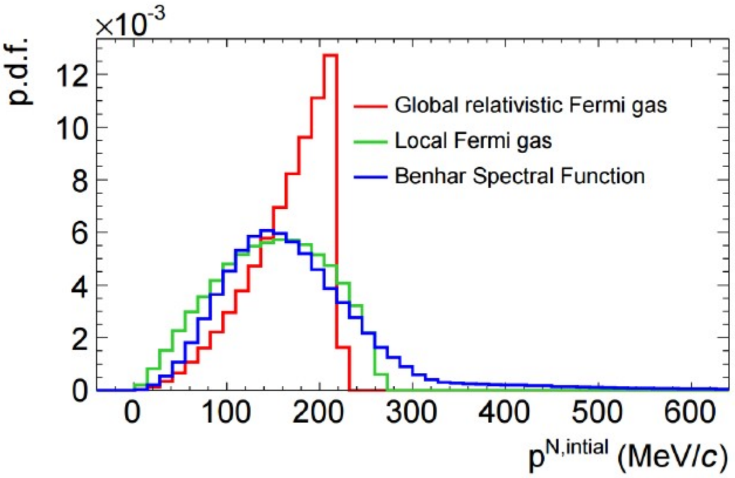

Figure 2.1: The NuWro simulated initial nucleon momentum distributions obtained with RFG, LFG and Benhar spectral function. Figure from [26].

Relativistic Fermi Gas (RFG) is the simplest spectral function model. The nucleons inside the nucleus are treated as a gas of non-interacting fermions in a constant nuclear potential, different for protons and neutrons. The proton potential well is shallower than the one for neutrons because protons are subject to Coulomb interaction. The states are filled successively, starting from the ground state. The highest of them has the momentum p_F called the Fermi momentum, whereas the corresponding Fermi energy E_F is the energy of the highest occupied state. So, the p_F depends on the number of nucleons and is the same for both protons and neutrons. Otherwise, for stable nuclei, a β decay to an energy-preferred state would occur. Adopting a constant, distance-independent potential well depth results in a sharp cut-off in the nucleons momentum distribution at p_F, as can bee seen in Figure 2.1 ($p_F \sim 230$ MeV/c for ^{12}C). As it is a fermion system, it meets Fermi-Dirac statistics, the consequence of which is Pauli's exclusion principle. The simplest description is often called the global Fermi gas model because the nuclear ground state is a Fermi gas of non-interacting nucleons characterized by a global Fermi momentum.

The results of elastic electron scattering show radial dependence of nuclear density [27], i.e., nuclear potential has to be a function of the nucleus radius r through the local nuclear density $\rho(r)$, known as local density approximation. This is the basis for the construction of the **local Fermi gas (LFG)** spectral function. The dependence of the potential on the radius removes the non-physical sharp cut-off in the initial nucleon momentum distribution (Figure 2.1). However, it should be noted that, similarly as in the RFG approach, it is still assumed that nucleons do not interact.

To date, **spectral function (SF)** models give the most realistic momentum distributions of nucleons, taking into account nucleon-nucleon interactions within the nucleus. Those nucleon-nucleon interactions modify the distribution of nucleon momenta, the fact was already been noticed in 1987 in the analysis of high resolution $(e, e'p)$ data [28]. Two and three body nucleon interaction potentials are incorporated into the nuclear shell model in the Benhar et al. SF [21], resulting in a modification to the orbitals. Moreover, short range correlations of strongly repulsive nucleon pairs are also included. They give rise to the high momentum part of the initial state nucleon momenta (see Figure 2.1).

The neutrino-nucleus cross section in these three models, i.e., RFG, LFG, and SF, is calculated assuming the **impulse approximation (IA)**, in which the incoming neutrino interacts with only one nucleon, while the other nucleons are spectators. Therefore, the neutrino-nucleus cross section can be calculated as an incoherent sum of cross sections for individual processes taking place on free nucleons with some initial energy and momentum distribution.

2.2.2 Correlations inside nucleus

The incoming neutrino may interact not only with a single nucleon but also with n nucleons simultaneously. They are commonly referred to as n-particle - n-hole (np-nh or npnh) interactions due to short range correlations between the nucleons. Two models built by Nieves [22] and Martini [23] have been proposed to account for multi-nucleon correlations exploiting a multi-body expansion. The first term of the expansion 1p1h describes CCQE interaction, whereas the second 2p2h is dominated by the meson exchange current (MEC) process. The 2p2h interaction involves more than one nucleon, therefore it is different from CCQE. Two nucleons in its final state will most likely be absorbed and will not leave the nucleus, contributing to the irreducible background to CCQE. As a consequence of this fact, the CCQE neutrino energy calculation can be no longer based only on the outgoing lepton momentum.

It should be noted that the development of np-nh models was triggered by the surprisingly high value, compared to the global one, of best-fit axial-mass $M_A = 1.35 \pm 0.02(stat) \pm 0.06(syst)$ GeV/c^2 obtained in [24] from the fit to MiniBooNE CCQE double differential cross section on carbon [49]. Fitting the MiniBooNE data with the M_A value consistent with the global one was only possible by including the multi-nucleon-neutrino effects. This clearly shows the importance of high quality neutrino scattering data in developing neutrino interaction models.

In addition to short range correlations between nucleons, also long range ones should be taken into account. The **Random Phase Approximation (RPA)**, a method taken from solid state physics is commonly used to estimate the nuclear effect of long range correlations on neutrino-nucleus scattering. The RPA, contrary to the mean-field (MF) approach, in which a nucleon experiences the presence of the remaining nucleons only through the MF generated by their mutual interactions, allows for nucleon interactions through the residual two-body force. The correlations present in a nucleus are described as the coherent superposition of individual particle-hole states. Summing up - in neutrino-nucleus scattering, the RPA is a nuclear screening effect, which can be considered as a correction to the non-interacting nucleons in RFG to account for their long-range correlations. The RPA influences the neutrino-nucleus cross section in the following way: at high Q^2 values the RPA effect vanishes and the IA applies, while at medium (low) Q^2 the RPA enhances (suppresses) the cross section.

The role of different mechanisms can be seen in Figure 2.2. Only by taking into account both the RPA and 2p-2h corrections, the RFG gives the correct data description. One can notice that for low muon energies, the contribution from RPA decreases, while the contribution of the multinucleon correlations 2p-2h is of greater importance.

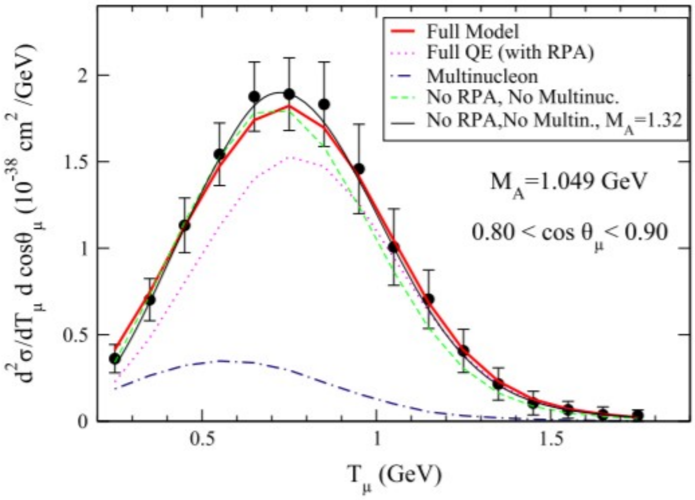

Figure 2.2: ν_μ–^{12}C double differential cross section as a function of muon kinetic energy T_μ for $0.80 < \cos\theta_\mu < 0.90$. The thick solid line stands for the full model (RFG + RPA + 2p2h), whereas dashed lines represent partial contributions. All these curves are obtained with $M_A = 1.049$ GeV. For reference, results from RFG only with $M_A = 1.320$ GeV are also presented. Figure from [51].

2.2.3 Final State Interactions

In the neutrino-nucleus scattering, in addition to the primary neutrino-nucleus interaction vertex, secondary vertices may occur owing to interactions of hadrons produced in the primary vertex. Such hadrons, e.g., a proton from a CCQE or a pion from a CC1π, undergo the strong force interactions within the target nucleus before escaping it and possibly being detected. Such hadron re-interactions are called Final State Interactions (FSI) and comprise hadron scattering, absorption and particle production. Therefore, the FSI affects the values of measured observables, being particularly important at $E_\nu \sim 1$ GeV when low energy nucleons and pions are produced. The FSI in neutrino interactions are widely described by the Intranuclear Cascade (INC) model, which is used in most neutrino generators. The incoming neutrino initiates a cascade inside the nucleus, and subsequent interactions take place with individual nucleons in the nucleus. The basic steps of the INC model are as follows: (1) uniform distribution of the spatial point at which the incident neutrino enters the nucleus, (2) the path length of a projectile particle is calculated upon corresponding hadron-hadron cross section and region-dependent nucleon densities, whereas particle angles after the collision are sampled from experimental differential cross sections, and (3) determination of the reaction type and four momenta of reaction products. It should be noted that the same hadron-hadron cross sections that are applicable in free space are used; however, Pauli's exclusion principle is preserved inside the nucleus. The INC develops until all the hadrons are absorbed or leave the nucleus. FSI uncertainties are one of the sources of systematic errors used to calculate the cross section. They fall into cross section modeling uncertainties, being related to the detector systematic errors.

Pions are most often produced at the primary interaction vertex at low neutrino energies. Their most common FSI are as follows: the elastic scattering, absorption, and charge exchange processes, which mask the primary vertex interaction making it difficult to separate CCQE, CC resonant, etc., cross sections (a selected CCQE event can be CC resonant one, in which pion has been absorbed). As leptons do not interact strongly, their FSI are neglected.

There is no doubt that the description of neutrino-nucleus interactions is complex. Nuclear effects, detector acceptance and efficiency limit the reconstruction of the true neutrino interaction type. Defining the experimental observables in the terms of final states with inclusive topologies allows to minimize the model dependence of the measurements. The examples of such definitions are: CC-0π (CC0π) - charged current interactions without pions, CC-1π (CC1π) - CC interactions with one pion in the final state, and CC-Other (CCOther) - other CC interactions. The division of neutrino-nucleus interactions into many categories enables more complete description of them. To account for the complexity of interactions occurring during the neutrino-nucleus interaction, many different models have been proposed. Those most commonly used, in neutrino generators, for modeling nuclear effects for the CCQE, resonant production, and coherent neutrino scattering are briefly described below, together with a review of experimental data.

2.3 Overview of the current and future neutrino cross-section experiments and main results

In the last few decades, many experiments have collected results on neutrino interactions with various targets. Most of them are charged current reactions. Various detection techniques have been exploited. The use of intense neutrino beams, and more precise knowledge of neutrino flux, have recently resulted in a number of accelerator-based neutrino cross section measurements. They are shortly summarized in this section, whereas the T2K results are presented in detail in Chapter 6. We focus on the cross-section measurements for ν_μ and $\bar{\nu}_\mu$ scattering because the

T2K experiment uses neutrino beams of that flavor. A complete summary of the results of measurements of neutrino cross sections can be found in [29].

CC inclusive cross section

The CC inclusive cross section represents the basic measurement performed by many experiments in a very wide range of neutrino energies from $\sim$ 300 MeV to $\sim$ 300 GeV. Its importance is due to the simplicity of the definition - registration of only one charged lepton, which is usually relatively straightforward and much less dependent on the background than exclusive channels. Fig. 2.3 shows the results of many measurements of ν_μ and $\bar{\nu}_\mu$ CC inclusive cross section σ_{CC} as a function of neutrino energy E_ν. For higher neutrino energies, the linear behaviour of $\sigma_{CC}(E_\nu)$ exhibits neutrino scattering on point-like objects (quarks), therefore neglecting nuclear effects. At lower E_ν values, neutrino scattering is affected by nuclear effects, which is reflected in the deviation of linear $\sigma_{CC}(E_\nu)$ dependence. One can notice that the antineutrino cross section is approximately half of the neutrino cross section.

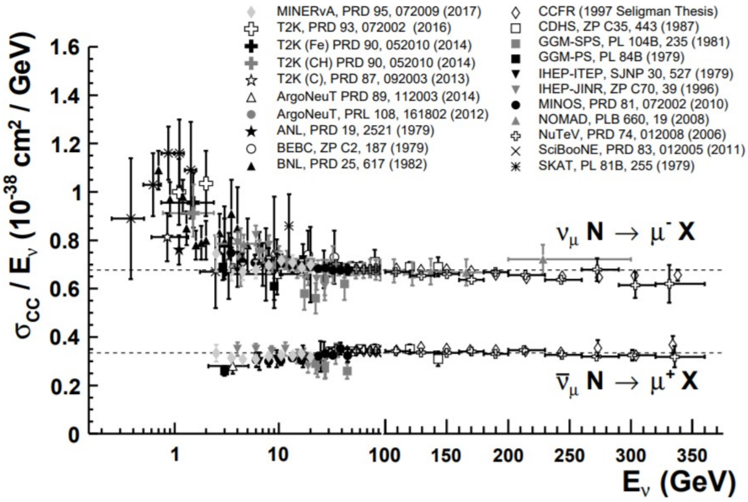

Figure 2.3: ν_μ and $\bar{\nu}_\mu$ CC inclusive cross section per nucleon divided by neutrino energy as a function of E_ν (E_ν scale is partly logarithmic). Figure from [29].

Increasing the intensity of neutrino beams allowed physicists to measure CC inclusive single and double differential cross sections. Such data was provided for ν_μ and $\bar{\nu}_\mu$ scattering on various nuclear targets. And so the ArgoNeuT experiment published ν_μ and $\bar{\nu}_\mu$ single differential CC cross sections on argon in terms of outgoing muon angle and momentum in the range $0° < \theta_\mu < 36°$ and $0 < p_\mu < 25$ GeV/c, at a mean ν_μ ($\bar{\nu}_\mu$) energy equal to 9.6 GeV (3.6 GeV) [30]. The results, consistent with the GENIE [17] predictions, have also served for tuning neutrino event generators. The MINERvA collaboration performed a number of ν_μ and $\bar{\nu}_\mu$ inclusive CC cross section measurements on a variety of targets using the Fermilab NUMI (Neutrinos at the Main Injector) neutrino beam [31], whose production begins when 120-GeV protons interact with a graphite target. A broad energy range of ν_μ and $\bar{\nu}_\mu$ beam make it possible to study both nuclear effects in neutrino interactions and neutrino scattering on point-like quark constituents of the nucleus. The MINERvA measurements of ν_μ CC cross section ratios on C, F, and Pb relative to CH scintillator, in the neutrino-energy range 2-20 GeV [32], showed (1) a depletion at low values of the Bjorken scaling variable x and enhancement at large x, and (2) discrepancy with predictions of neutrino interaction generators. The analysis of the data in a wider neutrino energy range (5-50 GeV) [33] confirmed the deficit in the DIS cross section ratio at large neutrino energy ($E_\nu > 20$ GeV and low Bjorken variable ($x < 0.1$).

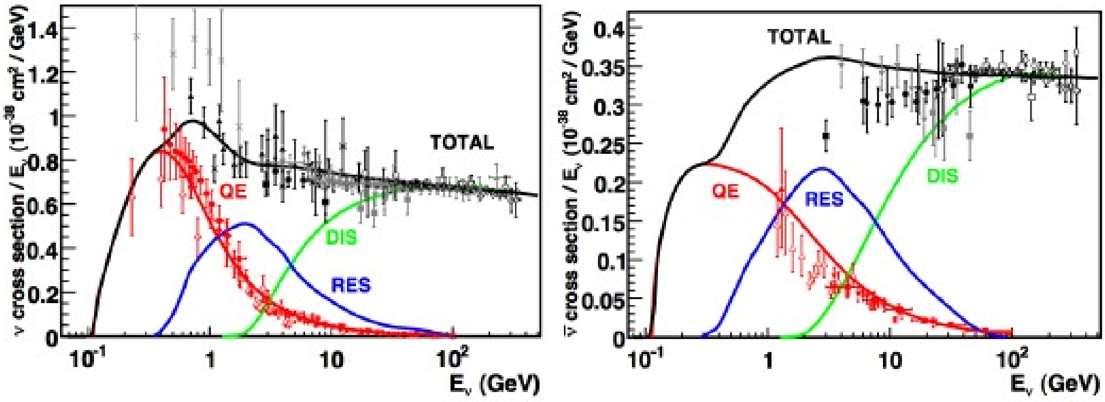

.

Figure 2.4: ν_μ and $\bar{\nu}_\mu$ CC inclusive cross section measurements and predictions as a function of neutrino energy. per nucleon divided by neutrino energy as a function of E_ν (E_ν scale is partly logarithmic). Three contributing processes: quasi-elastic (QE) scattering, resonance production (RES), and deep inelastic scattering (DIS) are shown. Figure from [47]

The measured squared mass difference between the second and third neutrino mass eigenstates $\Delta m^2_{23} \simeq 2.4 \times 10^{-3} eV^2$ dictates $\sim GeV$ energy of the accelerator ν_μ ($\bar{\nu}_\mu$) beam to obtain the oscillation length ($L(km) \simeq 2.48 E(GeV)/\Delta m^2_{23}(eV^2)$) in the order of several hundred to several thousand km. In this energy range, three types of neutrino interactions, namely quasi-elastic (QE) scattering, resonance production (RES), and deep inelastic scattering (DIS) provides contributions to the cross section (see Fig. 2.4). These processes are described below, together with coherent pion production, which represents a different pion production mechanism in the energy range of RES. However, it should be noted that the neutrino flux distributions for current (T2K and Nova) and future (DUNE and Hyper-Kamiokande) accelerator-based experiments cover the energy range in which, in addition to those already mentioned, there are other neutrino interaction processes, such as 2p2h (two particles, two holes - two-nucleon knockout, when the momentum transferred to the target is shared among correlated nucleons) that may occur (Fig. 2.5).

Charged current quasi-elastic neutrino scattering

Neutrino ν (antineutrino $\bar{\nu}$) charge current quasi-elastic (CCQE) scattering refers to the processes $\nu + n \to l^- + p$ ($\bar{\nu} + p \to l^+ + n$), where $l^\pm$ denotes charged lepton and p (n) stands for proton (neutron). The interaction proceeds via W-boson exchange between incoming neutrino and a nucleon. From the point of view of the experiment CCQE cross section corresponds to a process in which only the charged lepton is detected in the final state, and no mesons (pions). In bubble chambers experiments,

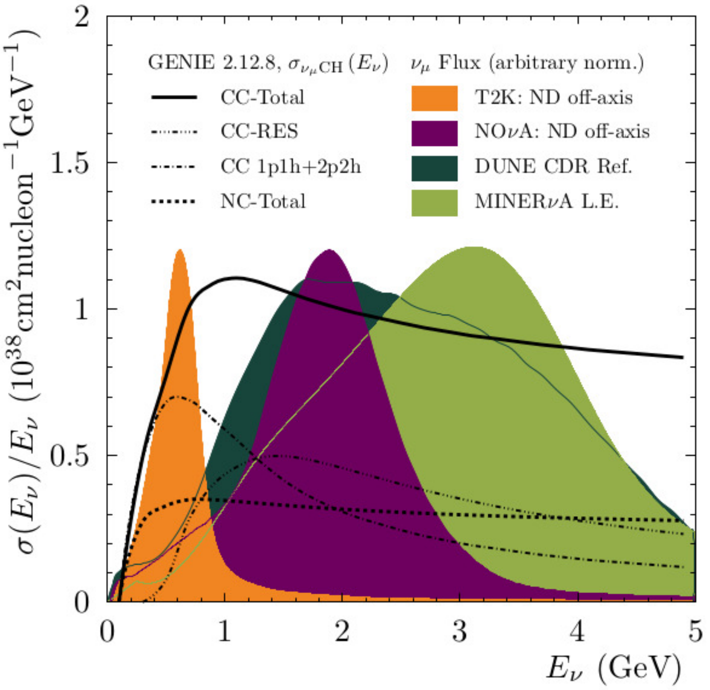

.

Figure 2.5: Neutrino fluxes of T2K off-axis near detector ND, NOvA ND, MINERvA - low energy configuration and DUNE (CDR - Conceptual Design Report). Hyper-Kamiokande flux is very similar to T2K ND off-axis. GENIE v2.12.8 predictions of CC-total, CC cross section contributions (RES - nucleon resonances, 1p1h - single nucleon knockout also known as CCQE, and 2p2h - two-nucleon knockout) and NC-total are also shown. Figure from [48]

investigating neutrino scattering on very light targets (hydrogen or deuterium) even a nucleon was detected. However, for heavier nuclei, it may happen that a pion produced in the neutrino interaction is absorbed again in the nucleus and therefore is not detected. Currently, experimental data for neutrino scattering without pions in the final state are often called CC0π or CCQE-like. This refers to accelerator-based neutrino experiments using C, CH, H_2O, Ar, Fe, or Pb as target for neutrino interactions. Double differential CCQE cross sections, as a function of lepton energy and opening angle, provided recently by several experiments, are not so dependent on the models, and therefore they help to develop theoretical approaches. For ν_μ ($\bar{\nu}_\mu$) with energy below 1 GeV, the CCQE interaction is dominant and extremely important for neutrino oscillation experiments. It is two-body scattering, that is why the energy of the interacting neutrino can be determined from the momentum and angle (with respect to the direction of the incoming neutrino) of the outgoing muon. However, it should be noted that this relatively simple description gets complicated when the nucleon is bounded in an atomic nucleus, which is the case with the scattering of neutrinos on heavy targets. In this chapter, we limit ourselves to presenting the latest results from neutrino-nucleus double differential cross-sections, because the use of kinematic variables leads to a better understanding of nuclear processes occurring during neutrino-nucleus interaction. A more comprehensive list of CCQE-like neutrino-nucleus measurements can be found in [29]. The first, high statistics measurements of the double differential cross section for CCQE scattering on carbon were published by the MiniBooNE collaboration in [49] and [50], for ν_μ ($\langle E_\nu \rangle \simeq 0.79$ GeV) and $\bar{\nu}_\mu$ ($\langle E_{\bar{\nu}} \rangle \simeq 0.67$ GeV), respectively. The double differential cross sections were expressed as a function of two fundamental kinematic variables, namely the muon kinetic energy T_μ and muon scattering angle $cos\theta_\mu$, which were extracted from the track reconstruction assuming a muon hypothesis. Recently, the MINERvA experiment ([52], [53], and [54]) presented the results of ν_μ and $\bar{\nu}_\mu$ CCQE scattering on hydrocarbon (CH) tracking target, obtained with the peak neutrino beam energy of $\sim 3GeV$ (Fermilab's NUMI low-energy beam configuration). The double differential cross section was reported using the muon transverse and longitudinal momentum, whereas a quasi-elastic hypothesis was applied to calculate the differential cross sections as a function of the square of the four-momentum transferred and the neutrino energy. Moreover, it was found that reconstructed energy near the interaction vertex can be used for testing 2p2h models because interactions on multinucleon pairs involve more low-energy nucleons than standard CCQE implies. Therefore the authors added 2p2h processes to the default GENIE 2.8.4 scattering model for the random phase approximation (RPA). In [53] the correction for hadron re-interactions in the target nucleus was investigated in measurements of the CCπ^+ (1μ+$1\pi^+$ in the signal) and CCQE (1μ+$no\pi$ in the signal) cross sections. With both π^0 and μ^- reconstructed in the final state, the authors concluded that $\nu_\mu CC\pi^0$ occurs mainly through the $\Delta_{33}(1232)$ resonance for $E_\nu < 2GeV$ [54]. The MINERvA results clearly confirm the need for high quality neutrino cross section data, measured as a function of various kinematic variables to improve models of neutrino-nucleus interactions. The T2K contribution in extending ν_μ and $\bar{\nu_\mu}$ CCQE scattering data, including their impact on the development of neutrino-nucleus interaction models, is described in Chapter 6.

Resonance production

As shown in Fig. 2.4, in the neutrino energy range from about 1.5 GeV to about 4 GeV, the resonance production is the dominant mode of a neutrino interaction. First of all, the lowest baryon resonant state $\Delta_{33}(1232)$ decaying (still inside the nucleus) into a nucleon, and a pion is produced. The resonant single pion production represents, after CCQE, the second most important interaction for the energy range of neutrinos in the T2K beam. In neutrino scattering, there are three CC channels of resonant pion production:

$$\begin{aligned} \nu_l + p \rightarrow l^- + p + \pi^+, \qquad & \bar{\nu_l} + p \rightarrow l^+ + p + \pi^-, \\ \nu_l + n \rightarrow l^- + p + \pi^0, \qquad & \bar{\nu_l} + p \rightarrow l^+ + n + \pi^0, \\ \nu_l + n \rightarrow l^- + n + \pi^+, \qquad & \bar{\nu_l} + n \rightarrow l^+ + n + \pi^-, \end{aligned} \tag{2.1}$$

and four NC:

$$\begin{aligned} \nu_l + p &\to \nu_l + p + \pi^0, & \bar{\nu}_l + p &\to \bar{\nu}_l + p + \pi^0, \\ \nu_l + p &\to \nu_l + n + \pi^+, & \bar{\nu}_l + p &\to \bar{\nu}_l + n + \pi^+, \\ \nu_l + n &\to \nu_l + n + \pi^0, & \bar{\nu}_l + n &\to \bar{\nu}_l + n + \pi^0, \\ \nu_l + n &\to \nu_l + p + \pi^-. & \bar{\nu}_l + n &\to \bar{\nu}_l + p + \pi^-. \end{aligned} \tag{2.2}$$

At higher neutrino energies, higher mass resonances decaying into heavier mesons can also be produced, but a resonance decay into a single pion remains the most important. Here, we discuss briefly only the results of recent (except for T2K, which is discussed in Chapter 6) CC neutrino scattering cross section measurements with a pion in the final state. The references to NC data can be found in [29]. In a series of publications [55], [56], [57], the MiniBooNE experiment presented measurements of the ν_μ-induced CCπ^+ and ν_μCCπ^0 absolute total cross section as a function of neutrino energy, and flux-averaged differential cross sections obtained in terms of muon and pion kinematics on mineral oil (CH_2) in the GeV energy range as a function of incoming neutrino energy. It was concluded that most CCπ^+ events come from decays of the delta(1232) resonance.

The Rein-Sehgal model [58] is used to simulate resonance production for both CC and NC neutrino interactions in almost all Monte Carlo neutrino generators, and therefore, it is shortly presented. 18 resonances, below the invariant mass of the final hadronic system $W = 2$ GeV and an interference between them are included in the Rein-Sehgal model for single pion production[2]. A simple, purely empirical, noninterfering, nonresonant background of isospin 1/2, is incorporated in the model. The cross-section for an individual channel is calculated in the following way: the amplitude for the production of each resonance is obtained and multiplied by the probability of the resonance decaying into that individual channel. The corresponding background cross section is added incoherently to the resonant cross section. The Rein-Sehgal model uses the relativistic quark model proposed by Feynman, Kislinger, and Ravndal [59] for the calculation of three-quark excited states wavefunctions in a harmonic oscillator potential. Summing up, the Rein-Sehgal model describes the energy levels of the three-quark system, the transitions between them, and finally, the hadronic widths of the resonances.

Coherent neutrino scattering and coherent pion production

When a four-momentum transfer to a nucleus is small during the neutrino-nucleus collision, the nucleus A can recoil as a whole, i.e., its quantum state remains unchanged. This neutrino interaction mode is known as *coherent* scattering. At higher neutrino energies, coherent neutrino scattering leading to the production of a meson, primarily a pion, can occur. This process is called coherent meson (pion) production (Cohπ):

---

[2] Production of heavier mesons (e.g., kaons) at T2K neutrino beam energies is very rare.

$$\begin{aligned} \nu_l + A &\to l^- + \pi^+ + A, \\ \bar{\nu_l} + A &\to l^+ + \pi^- + A, \\ \nu_l + A &\to \nu_l + \pi^0 + A, \\ \bar{\nu_l} + A &\to \bar{\nu_l} + \pi^0 + A. \end{aligned} \tag{2.3}$$

If it proceeds via CC, a pion, and a lepton of opposite charge are produced, whereas NC leads to the production of a neutral pion being the only registered particle. The last two constitute a significant background for neutrino oscillation experiments searching for ν_e or $\bar{\nu_e}$. Namely, a π^0 decays almost exclusively into two photons, which can be detected as a single electromagnetic shower, since in the laboratory frame, they are either almost collinear or one of them carries most of the energy. Therefore, a π^0 can be incorrectly identified as an electron. The requirement of the small four-momentum transfer to the nucleus, causes that produced particles (lepton and pion in CC coherent pion production) are emitted at small angles with respect to the direction of incoming neutrino. This limits the available phase space resulting in a relatively small value of the coherent scattering cross section. The first evidence for coherent pion production originates from the Aachen-Padova experiment performed in 1983 [36] with CERN PS ν_μ and $\bar{\nu}_\mu$ beams. By comparing two data samples, one with only a π^0 produced and the other with π^0 produced along with a proton, the physicists noticed a clear excess of events in the forward-going direction in the first sample [46]. This excess was attributed to the coherent pion production. It should be noted that resonance production is by far the largest part of the total ν_{mu} and $\bar{\nu_\mu}$ pion production cross section. Therefore, identifying the CC Cohπ process is not simple and requires the use of kinematic variables, which will demonstrate the coherent nature of the reaction. The ongoing and future accelerator-based neutrino experiments use neutrino beams in the energy range up to several GeV. Therefore, we only discuss the results of recent Cohπ measurements for $E_\nu <$ few GeV. NC Cohπ cross section on carbon was measured by SCiBooNE [37], MiniBooNE [38] and NOvA [39] experiments, at $\langle E_\nu \rangle \simeq 0.8$ GeV, 2.0 GeV and 2.7 GeV, respectively. CC Cohπ searches in the K2K [40] and SciBooNE [41] experiments only yielded the determination of the upper limit on the CC Cohπ cross section on carbon at $\langle E_\nu \rangle \simeq 1.3$ GeV and 1.1 (2.2) GeV, respectively. The evidence for CC Cohπ production was found later by three experiments, namely MINERvA and T2K for muon neutrino (muon antineutrino) scattering on carbon and ArgoNEUT for ν_μ and $\bar{\nu_\mu}$ scattering on argon. MINERvA published data on ν_μ and $\bar{\nu_\mu}$ for 9 energy bins, from 1.5-2.0 GeV to 15.0-20.0 GeV, obtained with the Fermi Lab NuMI wide-band neutrino beam [42], [43]. The T2K measurement is the first measurement of the flux-averaged cross section for CC coherent π^+ production on carbon for neutrino energies lower than 1.5 GeV [44]. This measurement is discussed in detail in Chapter 6. The only measurements of CC ν_μ and $\bar{\nu_\mu}$ Cohπ production on argon performed so far come from the ArgoNEUT experiment [45]. It should be noted that although Cohπ production cross section is small when compared to the resonant one, it can be very helpful in oscillatory analyses. Namely, owing to its relative simplicity, Cohπ production can constrain neutrino fluxes and neutrino-energy reconstruction, as stated in [15].

Deep Inelastic neutrino scattering

If the neutrino energy is large enough to distinguish between individual quarks in a nucleon a process called Deep Inelastic Scattering (DIS) takes place. This happens when the neutrino momentum transfer is sufficient to resolve the nucleon structure and the neutrino scatters directly off a quark. It should be noted that DIS of neutrinos, which interact only through a weak interaction, were used to determine nucleon structure functions, providing data complementary to DIS of charged-leptons. In the second half of the 1990s, three experiments, namely NuTeV [60], CHORUS [61] and NOMAD [62], measured both ν_μ and $\bar{\nu}_\mu$ CC DIS on heavy targets Fe, Pb, and C, respectively, using wide-band neutrino beams: $E_\nu = 30 - 360$ GeV ($\langle E_\nu \rangle = 120$ GeV) for NuTeV and $E_\nu = 10 - 200$ GeV ($\langle E_\nu \rangle = 27$ GeV) for CHORUS and NOMAD. Each of these three experiments collected more than 10^5 events in the CC DIS sample, with a well-reconstructed high energy muon track and energy of the hadronic system above the threshold of 10 GeV (NuTeV), 4 GeV (CHORUS) and 2.5 GeV (NOMAD). The NuTeV and NOMAD results are shown in Fig. 2.3.
FermiLab NUMI (Neutrinos at the Main Injector) ν_μ and $\bar{\nu}_\mu$ beams [31] of variable energy (2-20 GeV) were used by several neutrino experiments, including MINOS, which collected data in 2005-2012 and measured $\nu_\mu - Fe$ ($\bar{\nu}_\mu - Fe$) cross section in the energy range 3-50 GeV (5-50 GeV). These energies covered both the well-described 'pure' DIS region and the less understood few GeV energy range.
The fine-grained MINERvA detector, with a segmented CH scintillator target, surrounded by electron and hadron shower calorimeters, is also exposed to the NuMI beam. It was designed to study the A-dependence of neutrino interactions with C, Fe, and Pb targets. Most of the MINERvA cross section results refer to $E_\nu \sim 4$ GeV; however, there are some at neutrino energies 2 - 20 GeV, e.g. measurements of ratios of inclusive CC ν_μ total cross sections [63].
Finally, it is necessary to mention the future experiments that are planned or under construction and should play a significant role in the neutrino-nucleus cross section measurements. Among the most meaningful projects are the experiments from the US liquid argon program. They use or will be using a neutrino beam produced in Fermilab and have detectors mostly built using Liquid Argon TPC (LAr TPC) technology. This tech nology should allow the detection thresholds (e.g., for protons) to be significantly lowered and should provide a unique opportunity to measure neutrino cross sections for exclusive final states such as CC0π1p, CC0π2p, CC0πNp, etc. An important role in improving our understanding of neutrino interactions will be played by the US short baseline projects such as MicroBooNE [64], SBND [66], and Icarus [65] as well as the near detector of the US long baseline experiment DUNE [67].
On the other side of the globe, the Hyper-Kamiokande (Hyper-K) [68] experiment will study neutrino oscillations from the accelerator neutrino beam in J-PARC.

Hyper-K is a continuation of the T2K experiment and will use the upgraded T2K near detector (ND280) (more details in 6.3). The upgraded ND280 should be able to measure the neutrino cross sections in the kinematic phase space extended to full solid angle thanks to the additional Horizontal TPCs that will be installed there. The proton detection threshold will be lowered as well with the Super Fine Grained Detector in place. A more extensive description of the upgraded ND280 physics program can be found in 6.3.

Chapter 3

T2K experiment

The T2K (Tokai to Kamioka) long-baseline experiment in Japan is mainly designed to measure neutrino oscillations. A high-intensity beam of muon neutrinos/antineutrinos is produced using the Japan Proton Accelerator Research Complex (J-PARC) and sent towards the near detector station (280 meters away from the neutrino source) and the far detector Super-Kamiokande with a baseline (the distance from the production point to the far detector) of 295 km. The change in the measured intensity and composition of the beam is used to provide information on the neutrino oscillation parameters.

A schematic view of the T2K setup is shown in Fig. 3.1.

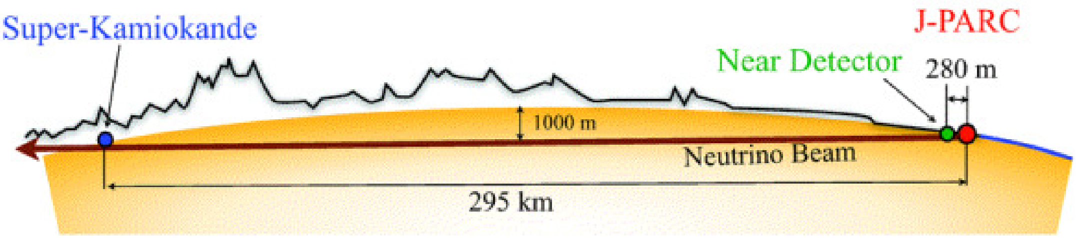

Figure 3.1: Schematic view of the T2K experiment: the locations of the Near Detector complex at J-PARC and far the Super-Kamiokande detector are shown. Figure from [69].

This chapter begins with an introduction to neutrino oscillations and is followed by a brief description of the research program and the experimental setup of the T2K experiment.

3.1 Introduction to neutrino oscillations

Neutrino oscillations are a quantum-mechanical effect where the observed neutrino flavor states from the Standard Model ν_e, ν_μ, and ν_τ (electron neutrino, muon neutrino and taon neutrino) propagate in space as linear combinations of the mass eigenstates ν_1, ν_2, and ν_3. The relation between the neutrino flavor states and the mass eigenstates is described by the Pontecorvo-Maki-Nakagawa-Sakata (PMNS) matrix [70], which can be parametrized using three mixing angles θ_{13}, θ_{23}, θ_{12}, and one complex phase δ_{CP}. The description of the oscillation probabilities uses three additional parameters - the differences of mass squared of the neutrinos (also called mass splittings): Δm^2_{21}, Δm^2_{32}, Δm^2_{23} out of which two are independent. There are two possible scenarios of neutrino mass ordering (hierarchy): Normal Ordering (NO) or Normal Hierarchy (NH), where $m_3 > m_2 > m_1$ and $\Delta m^2_{32} > 0$ and Inverted Ordering (IO) or Inverted Hierarchy (IH), where $m_2 > m_1 > m_3$ and $\Delta m^2_{32} < 0$.

Historically, θ_{12} and Δm^2_{21} are called 'solar parameters' or parameters from the solar sector because they were first measured by the experiments studying neutrinos from the Sun. Similarly, θ_{23} and Δm^2_{32} are called 'atmospheric parameters' from the experiments studying the neutrinos produced in the Earth's atmosphere.

In the case of the beam of neutrinos of the flavor α one can measure the following probabilities:

1. The probability of appearance of the neutrinos of the flavor β in the beam of ν_α: $P(\nu_\alpha \to \nu_\beta)$
2. The probability of disappearance of the neutrinos ν_α from the beam: $P(\nu_\alpha \to \nu_\alpha) = 1 - P(\nu_\alpha \to \nu_\beta)$ also called survival probability.

The formulas for the main channels of neutrino oscillations that are of interest to the T2K experiment can be written as follows [71]:

$$P(\nu_\mu \to \nu_\mu) \approx 1 - \sin^2 2\theta_{\mu\mu} \sin^2 \frac{\Delta m^2_{\mu\mu} L}{4E_\nu} \approx 1 - \cos^2\theta_{13} \sin^2(2\theta_{23}) \sin^2 \frac{\Delta m^2_{32} L}{4E_\nu} + \mathcal{O}(\alpha, \sin^2_{13}), \tag{3.1}$$

where:

$$\sin^2\theta_{\mu\mu} = \cos^2\theta_{13}\sin^2\theta_{23},$$

$$\Delta m^2_{\mu\mu} = \sin^2\theta_{12}\Delta m^2_{31} + \cos^2\theta_{12}\Delta m^2_{32} + \cos\delta_{CP}\sin\theta_{13}\sin 2\theta_{12}\tan\theta_{23}\Delta m^2_{21},$$

and

$$\begin{aligned} P(\overset{(-)}{\nu}_\mu \to \overset{(-)}{\nu}_e) \approx 4\sin^2\theta_{13}\sin^2\theta_{23}\frac{\sin^2\Delta}{(1-A)^2} + \alpha^2\sin^2 2\theta_{12}\cos^2\theta_{23}\frac{\sin^2 A\Delta}{A^2} \\ + 8\alpha J^{max}_{CP}\cos(\Delta \pm \delta_{CP})\frac{\sin\Delta A}{A}\frac{\sin\Delta(1-A)}{1-A}, \end{aligned} \tag{3.2}$$

where:

$$J^{max}_{CP} = \cos\theta_{12}\sin\theta_{12}\cos\theta_{23}\sin\theta_{23}\cos^2\theta_{13}\sin\theta_{13},$$

$$\Delta \equiv \frac{\Delta m^2_{31} L}{4E_\nu}, \ A \equiv \frac{2E_\nu V}{\Delta m^2_{31}}.$$

In the formulas above, L is the distance between the target station and the detector, E_ν is the energy of neutrinos, V is the effective matter potential in the Earth crust and $\alpha \equiv \Delta m^2_{21}/\Delta m^2_{31}$.

As one can observe in Eq. (3.1), the ν_μ disappearance formula is sensitive to atmospheric parameters: θ_{23} and Δm^2_{32}. On the other hand, the probability of ν_e appearance (Eq. 3.2) provides dominant information about θ_{13} angle and δ_{CP} phase. The plus (minus) sign applies to neutrinos (antineutrinos) and for antineutrinos $V \rightarrow -V$ and $A \rightarrow -A$. Additionally, the ν_e appearance formula is sensitive to the sign of Δm^2_{32} and matter effects (Mikheyev–Smirnov–Wolfenstein (MSW)). MSW effect modifies the neutrino oscillation probabilities in matter due to charged current coherent forward scattering of the electron neutrinos on electrons.

The fact that neutrinos oscillate was first revealed by the Super-Kamiokande experiment in 1998 [72]. Numerous experiments confirmed and supplemented Super-Kamiokande results and provided information about all mixing angles and mass splittings with good precision [71]. Although most of the oscillation parameters have been measured, there are still open questions related to neutrino oscillation physics. Two of the most important ones are: (1) is there a CP violation in the neutrino sector (is the δ_{CP} phase different from 0 or π)?, (2) what is the neutrino mass ordering related to the sign of Δm^2_{32}: normal ordering or inverted ordering?

At present, the two world-leading long-baseline neutrino experiments which are trying to answer these questions are T2K and NuMI Off-axis ν_e Appearance (NOvA) experiment. The parameter δ_{CP} can be measured because it modifies the probabilities of oscillation differently for neutrinos and antineutrinos. Similarly, the mass ordering can be determined because the neutrinos pass through the Earth and are affected by the MSW effect, which modifies the probabilities of oscillation differently for neutrinos and antineutrinos. The formula (3.2) shows that the electron appearance probability depends on both CP and matter terms; therefore, it is challenging to disentangle both effects. The relationship of the matter term on the baseline is linear: therefore, T2K, owing to its relatively short baseline (295 km) is sensitive to the CP phase while being very little sensitive to the neutrino mass ordering. On the other hand, the NOvA experiment in the USA has a longer baseline (810 km) and can observe subtle effects related to mass ordering. Cooperation between both experiments is crucial to disentangle CP violation effects from matter effects. There is an ongoing effort to combine NOvA and T2K results and improve the CP violation and mass ordering sensitivity.

3.2 T2K research program

The main goals of the T2K experiment are to constrain the PMNS oscillation parameters and the neutrino mass splittings by searching for the $\nu_e/\bar{\nu}_e$ appearance in the $\nu_\mu/\bar{\nu}_\mu$ beam (sensitive to $sin^2 2\theta_{13}$ and δ_{CP}), and the disappearance of $\nu_\mu/\bar{\nu}_\mu$ from the beam (sensitive to $sin^2 2\theta_{23}$ and Δm^2_{32}). Additionally, T2K aims at measuring neutrino-nucleus cross-sections on various targets.

The most important results from the T2K experiment can be summarized as follows:

1. The first single experimental indication that θ_{13} is non-zero with 2.5σ significance, based on an observation of electron neutrino appearance (six events passed all selection criteria at the far detector) in the muon neutrino beam cor-

responding to the analysis of 1.43×10^{20} Protons On Target (POT) [73]. The analysis of ~ 4 times bigger data sample, with 28 observed ν_e events, gave the best-fit value $sin^2 2\theta_{13} = 0.14^{+0.038}_{-0.032}$ ($sin^2 2\theta_{13} = 0.17^{+0.045}_{-0.037}$) for NO (IO), with a 68% confidence level. [74]. The calculated significance for a non-zero value of θ_{13} was 7.3σ.

2. The world's-best measurement of the θ_{23} parameter [75]. A joint fit of the ν_μ and $\bar{\nu}_\mu$ disappearance channels and ν_e and $\bar{\nu}_e$ appearance channels resulted in central values and 68% confidence intervals for $sin^2\theta_{23} = 0.55^{+0.05}_{-0.09}$ ($sin^2\theta_{23} = 0.55^{+0.05}_{-0.08}$) NO (IO), compatible with maximal mixing. For Δm^2_{32} the value of 2.54 ± 0.08 (2.51 ± 0.08) was obtained for NO (IO).

3. First confidence intervals for δ_{CP} with a 3 σ significance [5]. The analysis of 1.49×10^{21} (1.63×10^{21}) POT for neutrino (antineutrino) beam mode, using neutrino reactor experiments constraint of θ_{13} [77] resulted in the best fit value of $\delta_{CP} = -1.89$ radians ($\delta_{CP} = -1.38$ radians) for NO (IO), and rule out both CP conserving values $\delta_{CP} = 0, \pi$ at the 95% confidence level.

4. A series of world-leading cross-section measurements which are described in detail in Chapter 6. As already pointed out, they are essential for oscillation analyses and development of neutrino-nucleus interaction models.

5. Constraints on the sterile neutrino mass and Lorentz Invariance Violation and the measurement of neutrino time of flight [78].

Additionally, Dr. Koichiro Nishikawa and the members of the T2K collaboration have been awarded the prestigious Breakthrough Prize for Fundamental Physics, "for the fundamental discovery of neutrino oscillations, revealing a new frontier beyond, and possibly far beyond, the standard model of particle physics". More details can be found at the Breakthrough Prize Laureates webpage [76].

3.3 Experimental setup

The T2K experimental setup is composed of: (1) the neutrino beamline at J-PARC, (2) the ND280 near detector complex at J-PARC, and (3) the far Super-Kamiokande detector in Kamioka. The first two components are described in detail, as they are essential for the material contained in this monograph devoted to the cross section measurements with the use of the ND280 detector. The far detector Super-Kamiokande, critical for neutrino oscillation measurements, is shortly presented.

A charged pion two-body decay is the primary process of neutrino production in the accelerator neutrino beams. Kinematic considerations indicate that the outgoing neutrino energy is less dependent on the parent pion energy as the outgoing neutrino angle increases. Taking advantage of this fact, T2K uses the off-axis beam idea to produce a narrow-band neutrino beam directed to one of the near detectors (ND280) and the far detector, located 2.5° away from the proton beam axis. This setup allows T2K to produce a neutrino beam with a narrow energy spectrum peaked at 0.6 GeV, tuned to maximize the neutrino oscillation probability at 295 km (Fig. 3.3). Such a

Figure 3.2: View of the J-PARC complex. The high-intensity neutrino beam is produced as follows: (1) linear accelerator (Linac, in red) accelerates hydrogen ions to 181 MeV of kinetic energy, (2) protons are collected into Rapid-Cycling-Synchrotron (RCS, in red) and accelerated to 3 GeV, (3) protons are injected into 50 GeV (currently operated at 30 GeV) Main Ring (MR) Synchrotron (in yellow), (4) MR sends 30 MeV protons to the graphite neutrino production target (teal arrow). Figure from [79].

configuration also minimizes the background to the $\nu_e/\bar{\nu}_e$ appearance measurement. In T2K, it is the first time for the off-axis technique to be used in a search for neutrino oscillations.

3.3.1 J-PARC neutrino beamline

The T2K neutrino beamline consists of two consecutive parts: a primary and secondary beamline. The primary beamline guides the 30 GeV proton beam from the J-PARC's 'Main Ring' (MR) accelerator to the target station. The Main Ring accelerates protons every 2 to 3 seconds. For each acceleration cycle, the beam is extracted to the T2K beamline as a *spill*. Each spill contains eight proton bunches separated by 5 μs. In the secondary beamline, the protons extracted from MR interact with the a target. The target is 1.9 interaction length (91.4 cm long) and 2.6 cm in diameter graphite rod cooled by the helium gas. In the proton-target interactions, secondary pions and other hadrons are produced. Next, they are focused by three magnetic horns. The polarity of the horns can be changed to focus either positively or negatively charged pions and produce either muon neutrinos (*neutrino mode* running) or antineutrinos (*antineutrino mode* running). The neutrino mode and antineutrino mode are often called Forward-Horn Current (FHC) running and Reversed-Horn Current (RHC) running, respectively. The pions enter a 96 m-long decay volume where they decay and produce neutrinos which travel further away to the near and far detectors and muons. The muons with momenta below 5 GeV/c are stopped on the beam dump, whereas those with momenta above 5 GeV/c penetrate the muon monitor MUMON. MUMON serves to measure the beam position

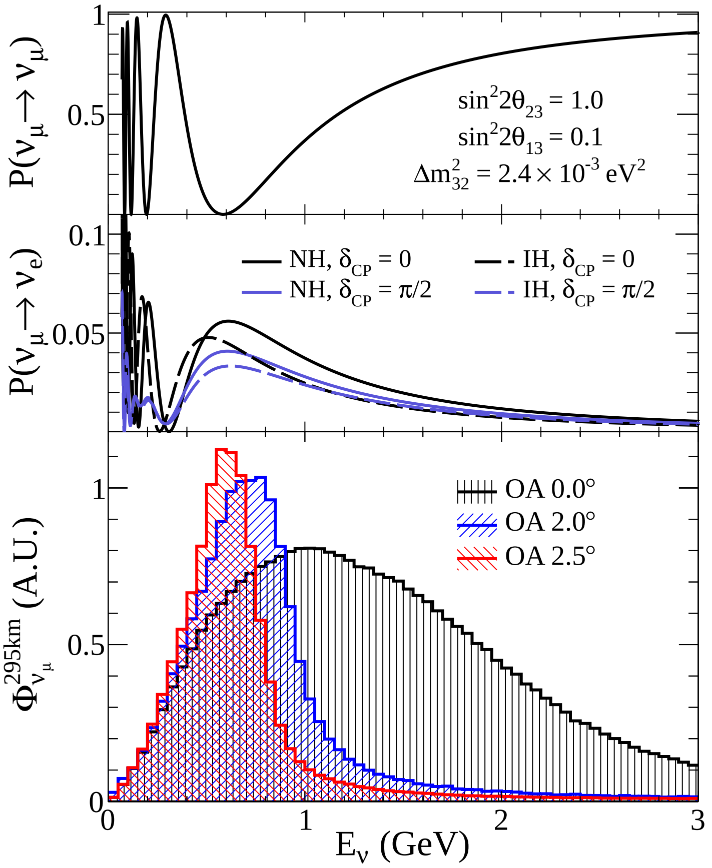

Figure 3.3: Muon neutrino disappearance probability (top), electron neutrino appearance probability (middle), and muon neutrino fluxes for various off-axis angles (bottom) in the far detector of the T2K experiment. The angle 2.5° is used in T2K for the far detector and near detector ND280. Figure from [80].

and intensity. Neutrinos or antineutrinos travel further away to the near and far detectors.

It is necessary to mention that the neutrino beam produced has a spatial spread increasing with the distance from the target station. Therefore the number of neutrino interactions in the near detectors is much larger than in the far detector. The near detector sees an almost entire initial beam of neutrinos while the far detector only a small fraction of it.

The neutrino flux at the near detector is shown in Fig. 3.4. The beam in the neutrino mode consists mainly of muon neutrinos ($\sim$ 97% in the peak of the neutrino energy distribution) with a small addition of muon antineutrinos, electron neutrinos (at the order of 1-2% in the peak), and a negligible portion of electron antineutrinos. The beam in antineutrino mode is less pure ($\sim$ 95% in the peak) with the main contamination from muon neutrinos ($\sim$ 5%).

3.3.2 Near detector complex of the T2K experiment

The near detector complex, located 280 m away from the production target, consists of four near detectors: INGRID, WAGASCI, Baby MIND and ND280 (Fig. 3.5).

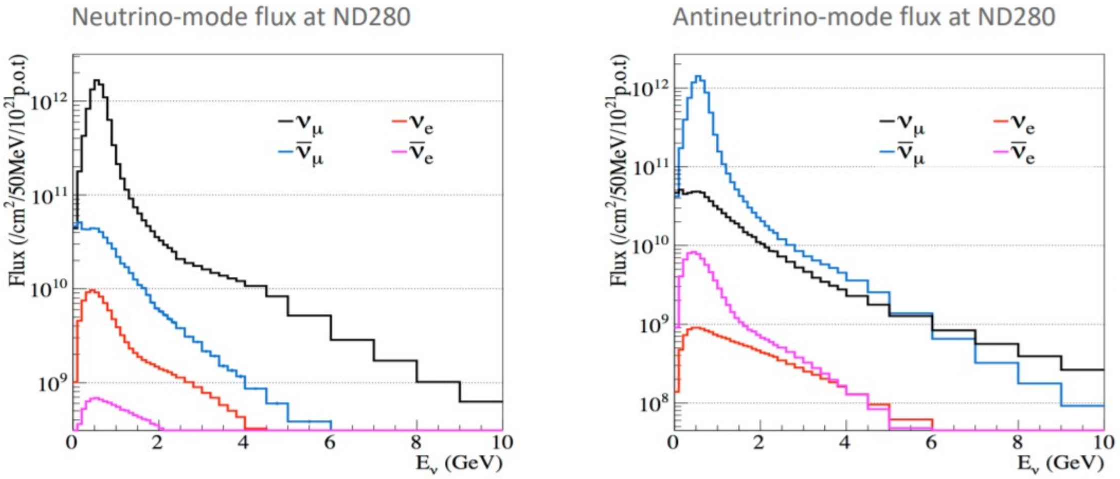

Figure 3.4: Neutrino flux for neutrino mode (left) and antineutrino mode (right) at the ND280 detector. Figure from [83].

As shown in Fig. 3.5, they occupy a pit with a diameter of 17.5 m. The INGRID is placed at the center of the neutrino beam (on-axis). At the depth of 37 meters, the lowest floor houses the bottom module of INGRID, whereas the horizontal modules of INGRID are located 33 m underground at the Service Stage. The INGRID detector is used to monitor the direction, position, and stability of the beam. The WAGASCI detector is exposed to the J-PARC neutrino beam at an off-axis angle 1.5 degrees. It is used to study neutrino-nucleus interactions on water, which is its main target material. Two main parts compose the WAGASCI detector: (1) the central module, which serves as a target, contains four alternating water and 3D grid structured plastic scintillator modules, and (2) two muon range detectors that identify muons and measure their momenta. The charge current neutrino cross section ratio between water and scintillator targets will be measured with the WAGASCI detector [81]. The Baby MIND detector is placed behind the central module of the WAGASCI detector. The momenta and charge of muons and other particles, resulting from neutrino interactions in the WAGASCI central module and escaping it will be measured with the Baby MIND detector. For this purpose, it consists of 33 magnetised metal plates and 18 scintillators modules [82]. The ND280 detector is located 2.5 degrees off-axis and, about 24 m below the surface. It consists of five sub-detectors placed inside a magnet: a π^0 detector, two fine grained detectors, three time projection chambers, an electromagnetic calorimeter, and a muon range detector. The ND280 detector is used to measure the neutrino-nucleus cross-sections.

INGRID and most of the components of the ND280 are built of active plastic scintillator slabs with the immersed WaveLength-Shifting (WLS) fiber which transmits the light produced by the charged particle traversing the slab into Multi-Pixel Photon Counter (MPPC). Moreover, detectors such as INGRID, PØD, and FGD (FGD2) also contain sectors which are filled with water used as a target for neutrino interactions. This approach allows neutrino interactions to be studied on the same target material as in the far detector and reduce the systematic uncertainties. In addition, the off-axis detector contains gaseous time projection chambers. Both

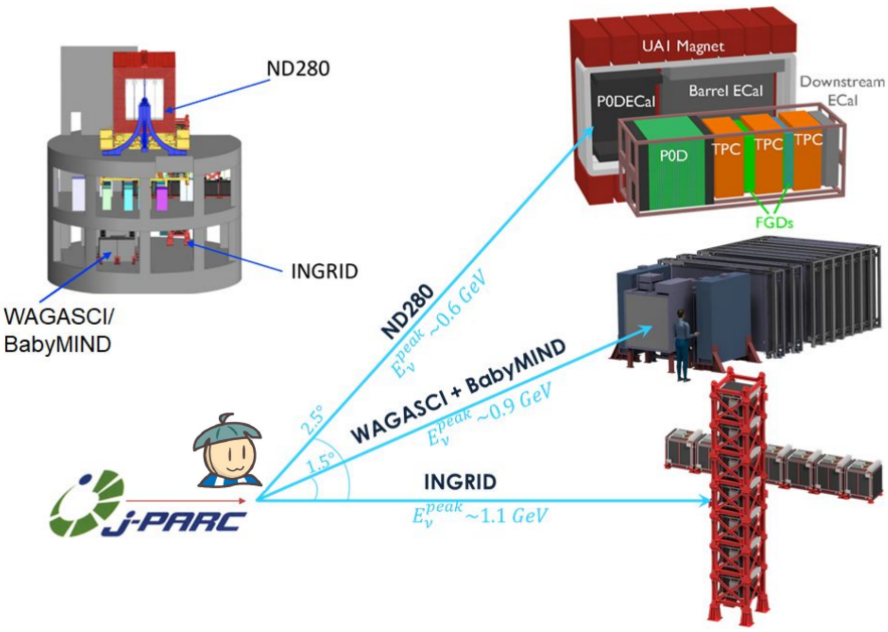

Figure 3.5: The near detector complex of the T2K experiment. The picture on the left shows the pit with the ND280 detector located at the top, INGRID and WAGASCI/BabyMIND at the bottom. Picture on the right shows the schematic view of all detectors along with the mean energies and angles with respect to the neutrino beam.

on-axis and off-axis detectors are described in detail in the following sections.

On-axis detector: INGRID

The INGRID (Interactive Neutrino GRID) is a neutrino detector positioned on-axis, 280 m downstream from the graphite target. It is a tracking scintillator detector that monitors the neutrino beam profile and intensity. It is also used for the measurements of neutrino cross sections.

The INGRID detector, shown in Fig. 3.6 is comprises 16 identical, standard modules and two extra modules, namely the Proton Module and the Water Module. The standard modules form a cross with 7 (7) modules in the horizontal (vertical) axis, whereas 2 extra modules are placed outside the main cross. Two standard modules are in the cross center, which corresponds to the neutrino beam center. Each INGRID standard module has a sandwich structure of 11 plastic scintillator plates and 9 iron plates, with no iron plate between the 10th and 11th scintillator planes, because of weight restrictions. To veto cosmic muon events and neutrino interaction events occurring outside the INGRID modules, scintillator planes surrounding the modules are used. The dimensions of iron plates are 1240 mm × 1240 mm, perpendicularly to the beam direction. The thickness is equal to 65 mm. The total iron mass of 7.1 tons per module is sufficient to acquire a number of neutrino interactions to monitor the beam profile on a day-by-day basis. Each tracking scintillator plane consists of 48 bars of dimensions of 10 mm × 50 mm and × 1203 mm, arranged in two 24 bars layers, the first (second) being the horizontal (vertical) one. A wavelength shifting fiber for light collection is inserted in 3 mm diameter hole along the length of each bar. The light is then detected by MPPC and converted to an electrical signal.

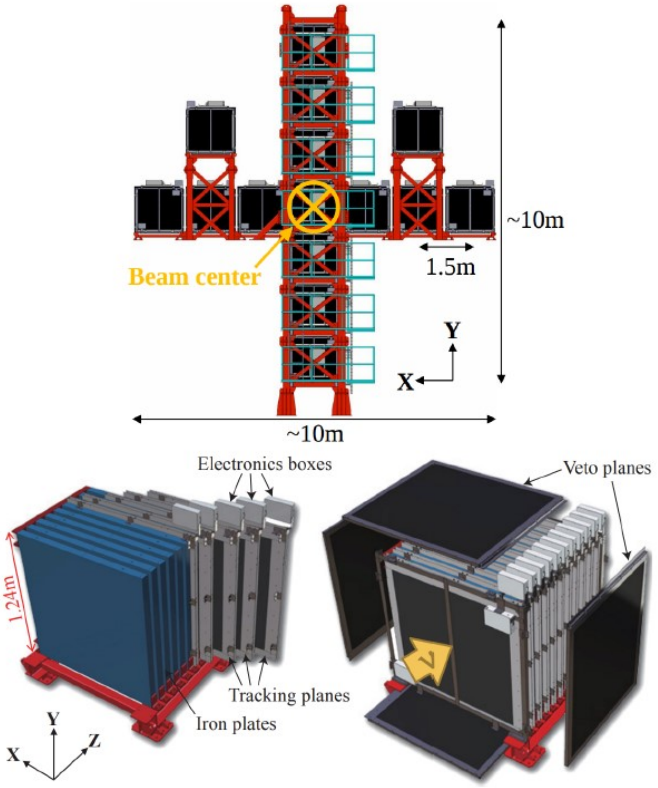

Figure 3.6: The INGRID on-axis detector. Horizontal and vertical arms of the cross configuration are shown (top), with some details of the INGRID standard module (bottom). Figure from [69].

Both INGRID special modules are located between the two central standard modules at the on-axis direction. The Proton Module contains 34 finer grained (compared with standard modules) scintillator bars and no iron plates, so it is a fully active tracking device. It is used to measure of neutrino cross sections on scintillator material. The Water Module consists of a grid structure of scintillator bars submerged in a 1200 mm × 1200 mm × 500 mm stainless steel water tank. The main purpose of the INGRID Water Module is a high-precision measurement of neutrino cross section on water.

The INGRID detector monitors the beam center position with an accuracy better than 100 mm, corresponding to the beam direction shift of 0.023°. This value is obtained by comparing the ν_μ CC interactions rate in each module with about 4% uncertainty for 1-day measurement [84]. The excellent stability of the neutrino beam, in terms of both direction and intensity, during many T2K run periods is shown in Fig. 3.7.

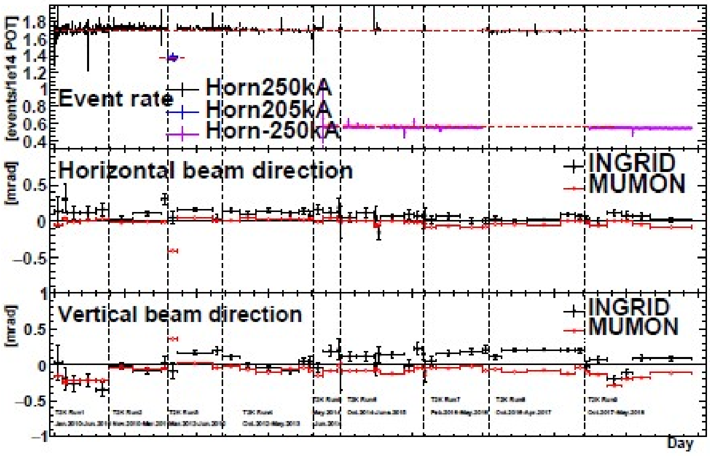

Figure 3.7: Neutrino beam vertical and horizontal position measured by the INGRID and MUMON detectors as a function of T2K data taking periods. The neutrino interaction rate obtained with INGRID is also shown.

Off-axis detector (ND280)

The ND280 detector is located 2.5° away from the main axis [1] and is built of several sub-detectors encapsulated in the UA1/NOMAD magnet constituting the source of a 0.2 T magnetic field (Fig. 3.8). The official ND280 coordinate system is defined in such a way that the the z-axis lies approximately on the beam axis while the x and y axes are perpendicular to the beam axis. The main ND280 components

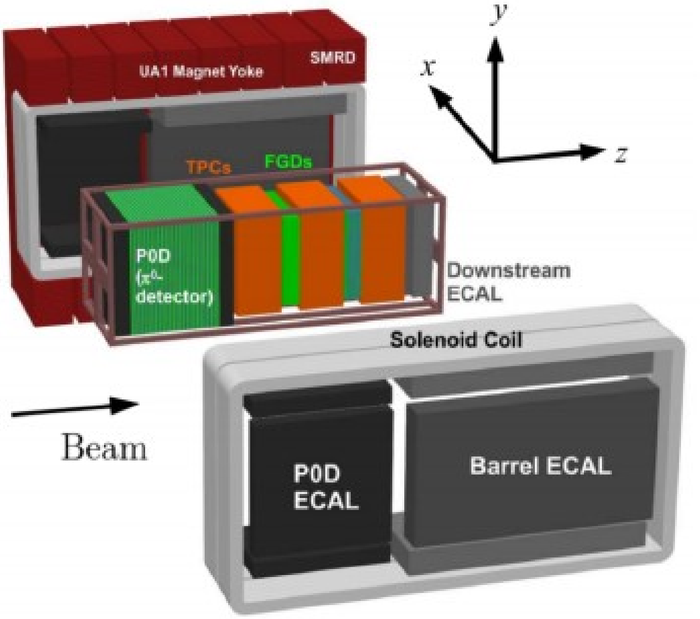

Figure 3.8: An exploded view of the ND280 off-axis detector with sub-detectors. An official ND280 coordinate system is shown in the top-right corner. Figure from [69].

---

[1] main axis - proton beam axis

are: Pizero detector (PØD), Tracker - containing three Time Projection Chambers (TPCs) and two Fine-Grained Detectors (FGDs), Electromagnetic Calorimeter (ECAL), and Side Muon Range Detector (SMRD). The detectors that are the components of ND280 are also called the *sub-detectors*. A more detailed description of the ND280 sub-detectors is below.

Pi-zero detector PØD

The π^0 detector (PØD) consists of 40 sub-modules referred to as PØDules (Fig. 3.9). There are three regions in the PØD, also called Super-PØDules: Water Target (WT), Upstream Electromagnetic Calorimeter (Upstream ECal or USECal) and Central Electromagnetic Calorimeter (Central ECal or CECal) with two types of PØDules. The water target PØDules contain a brass sheet, a plastic bag that can be filled with water, and two scintillator planes. The ECal PØDules are constructed with a lead sheet and two scintillator planes. The central water target region of the PØD is made of 25 water target PØDules. The Upstream ECal and Central ECal regions contain 7 PØDules each. Data can be collected in the PØD with the water bags in the central water target filled with water or being empty. Reference [85] gives more details of the PØD detector.

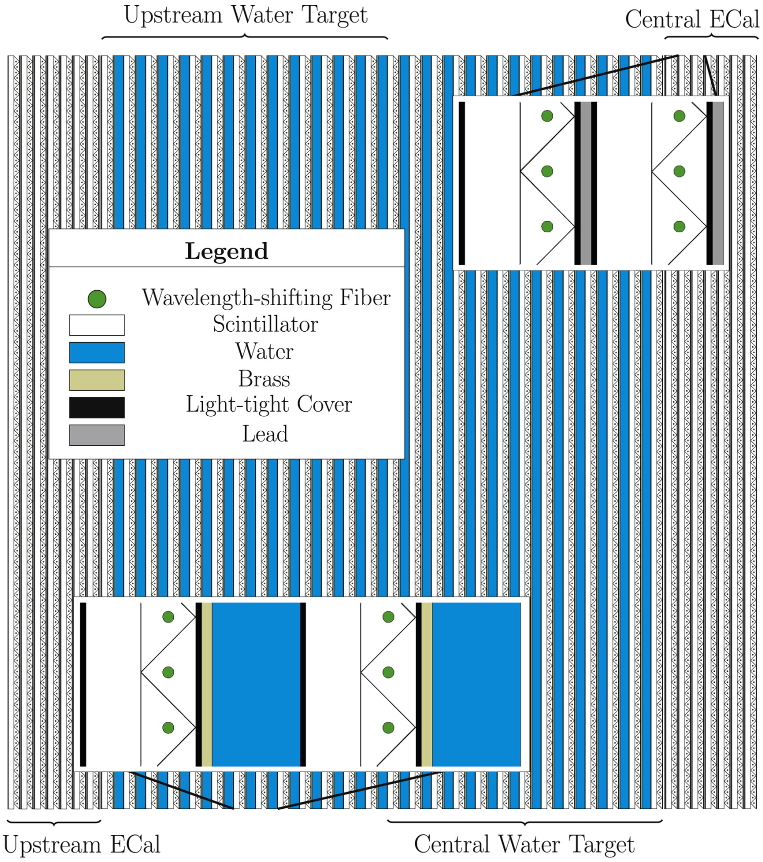

Figure 3.9: Schematic picture of the P0D detector. Figure from [85].

Time Projection Chamber (TPC)

The three-dimensional reconstruction of charged particle tracks is performed basically with the use of three identical TPCs, which are parts of the ND280 tracker region. As they are located in a magnetic field of ND280 magnet, the charged particles momenta can be measured. Moreover, particle identification can be performed by combining the charged particle momentum with the energy loss over travelled distance dE/dx.

The outer volume of a single TPC (Fig. 3.10) is: 2302 mm (width) × 2400 mm (height) × 974 mm depth. The inner volume is filled with 3000 liters of argon-based drift gas: Ar:CF_4:iC_4H_{10} in the ratio 95:3:2. Insulating CO_2 gas fills the space between the inner copper and outer aluminum walls. A uniform electric drift field, aligned with the magnetic field, is generated between the central cathode panel and strip pattern machined into the copper walls.

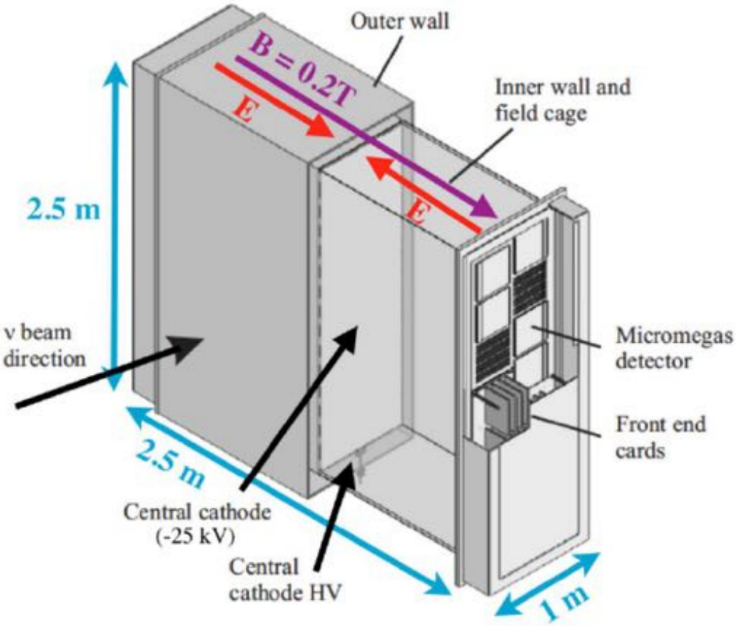

Figure 3.10: Simplified cut-away drawing with main TPC components. Figure from [86].

The ionization electrons produced along charged particle tracks during their passage through TPC are drifted away from the cathode to the readout planes, where they are multiplied by the segmented micromega (MM) modules. Each MM 342 mm × 359 mm module has 1728 anode pads (7.0 mm (width) × 9.8 mm (height)) used for signal amplification and 3D reconstruction of a track. Each readout plane contains 12 MM modules arranged in two slightly offset vertical columns. The horizontal and vertical coordinates are determined by the pattern of signals in the pad plane, whereas the third coordinate is obtained by combining the hit time and known electron drift velocity.

The ND280 TPC performance can be summarized as follows:

- the spatial resolution depending on the drift length is better than 1 mm,
- the resolution of the deposited energy is $\sim 8\%$ for minimum ionising particles, which is sufficient to distinguish muons from electrons,
- the relative momentum resolution is $\sim 0.1 \times p_T/GeV/c^2$. p_T is the transverse momentum of the particle.

A detailed description of the construction, calibration, and performance of the ND280 TPC can be found in [87].

Fine Grained Detector (FGD)

The FGDs serve as targets for neutrino interactions. Their high granularity, combined with precise time information, enables reconstructing both the interaction vertex and charged particles tracks. The most upstream FGD, called FGD1, is made solely of scintillator bars, while the downstream FGD2 consists of a plastic scintillator and water layers in between. The material of each FGD corresponds to about 0.85 interaction length X_0. Each FGD has a weight of 1.1 t, and external dimensions of 2300 mm × 2400 mm × 365 mm (width × height × depth in the beam direction). They are sandwiched between three TPCs of the ND280 detector. The scintillator bars are 1864.3 mm long and have 9.61 mm × 9.61 mm square cross section. The FGD1 consists of 30 layers of 192 bars each (5760 bars in total). They are oriented alternately in horizontal X and vertical Y directions, perpendicular to the beam direction, forming 15 XY modules. Fig. 3.11 shows the picture of the FGD detector.

The FGD2 consists of 14 layers (7 XY modules) of 192 bars each (2688 bars in total) oriented in the same way as for FGD1. In the FGD2, 7 XY scintillator modules are interleaved with 6, 2.5 cm thick water panels. The cross section measurements on the FGD2 water target, the same as for the Super-Kamiokande far detector play an important role in reducing the neutrino oscillation parameters estimation errors. Moreover, separate measurements of neutrino cross sections on carbon and water can be performed by comparing event rates in FGD1 and FGD2. A more detailed description of FGDs can be found in [88].

Electromagnetic Calorimeter (ECAL)

The reconstruction of neutral particles, including π^0 decay photons, is performed vitally with the use of ECAL surrounding the inner detectors: PØD, TPCs, and FGDs. The ECAL also helps in full event reconstruction measuring photon energies and directions, along with the identification/separation of charged particles from interactions in the inner detectors. There are three sections of the ECAL: the Downstream ECal (DsECal) placed behind the most downstream TPC, the Barrel ECal (BrECal) residing between the FGDs and TPCs detectors and magnet coils, and the PØD ECal located between the PØD and magnet coils. The arrangement of the ECAL sections is shown in Fig. 3.8, whereas a single module is depicted in Fig. 3.12. The ECAL modules are consecutive layers of scintillator bars and a

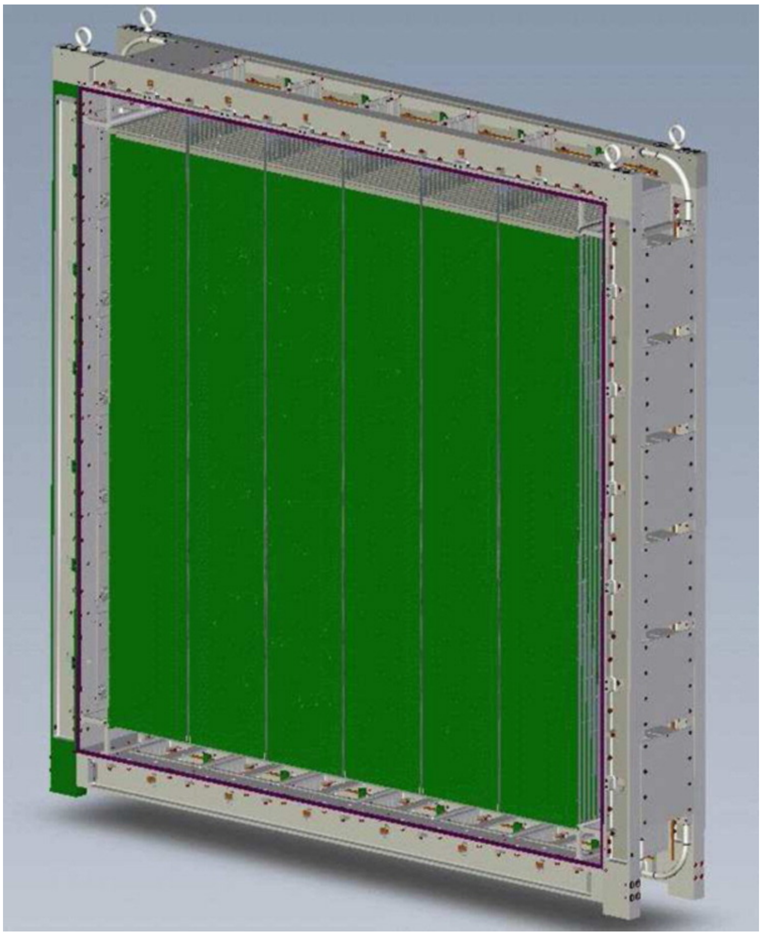

Figure 3.11: A view of FGD with scintillator bars shown in green. Figure from [69].

lead converter. The DsECal consists of a single scintillator module, whereas the BrECal and PØD ECAL have six modules each. Each ECAL scintillator bar has a rectangular cross section (40 mm × 10 mm) whereas the length depends on its location (side, bottom, or top) and direction with respect to the beam direction and is in the range from 1520 mm to 3840 mm. The WLS fibers are inserted in elliptical holes along the full length of scintillator bars. There are 34 layers in the DsEcal module, separated by a 1.75 mm thick lead plane, with bar orientation alternating at 90° for three-dimensional reconstruction of electromagnetic cascades and tracks of charged particles. The BrECal module consists of 31 layers as in the DsECal. The scintillator bars of BrECal and DsECal placed along the beam direction are read by the MPPCs at both ends, whereas the BrECal bars running in directions perpendicular to the beam direction are read by MPPCs only at one end. The PØD ECAL module consists of 6 scintillator layers (with bars along the beam direction read by MPPCs only at one end) separated by 4 mm thick lead slabs. The ECAL energy resolution depends on the momentum of the particles and varies from about 10% to about 20%. The ECAL is described in detail in [89].

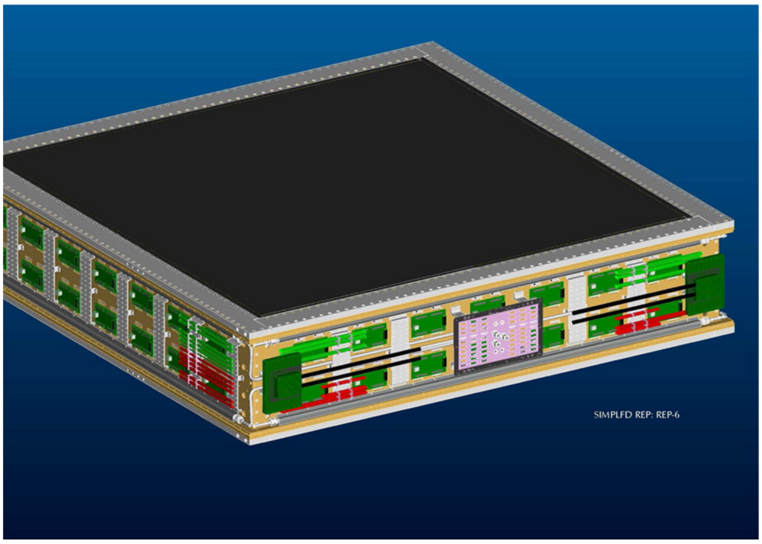

Figure 3.12: A view of one ECAL module. Figure from [69].

Side Muon Range Detector (SMRD)

The threefold functions of the SMRD are (1) measurement of momenta of muon tracks escaping inner ND280 parts at large angles with respect to the beam direction, (2) identification of beam related neutrino interactions in the cavity walls and magnet yoke, and (3) triggering on cosmic ray muons used for the detector calibration. The SMRD consists of 440 scintillator modules of paddle shape, placed in the 1.7 cm air gaps between 4.8 cm thick steel yoke plates. Each paddle is 875 mm long, 7 mm deep, whereas their width varies from 167 to 175 mm, which is due to the different horizontal and vertical gaps in the magnet yoke. This maximizes the active volume in each magnet yoke gap. Each SMRD scintillator counter (paddle) consists of extruded polystyrene, wavelength WLS fiber which snakes through and exits at both sides, as shown in Fig. 3.13. A total of 4016 MPPCs are connected to the WLS ends for readout.

A minimum ionizing particle average light yield is about 50 photoelectrons for the summed signal from both ends of a single SMRD scintillator counter. In the neutrino beam direction, the position resolution is about 7 cm, using time signals from both ends of the counter. A detailed description of the SMRD can be found in [90].

3.3.3 Far detector

The Super-Kamiokande water Cherenkov detector [91] is the far detector for the T2K experiment. It is the world's largest 'land-based' [2] water Cherenkov detector, which has been operating since 1996. Therefore both the technology and operation are well understood. The detector is placed 295 km west of the ND280, in the Mozumi mine, under Mt. Ikenoyama, with 1000 m of rock overburden. It is a cylindrical tank (39

---

[2] Land-based means located on land

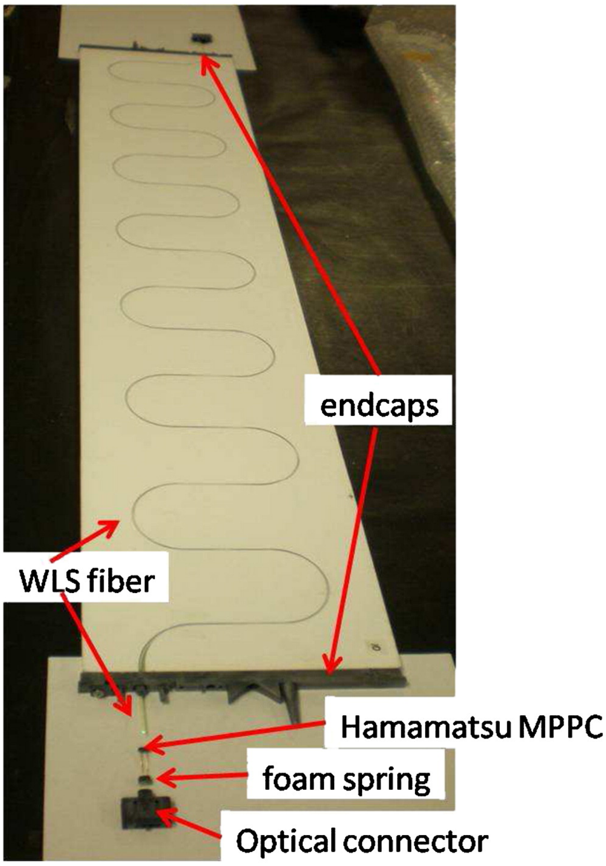

.

Figure 3.13: An SMRD paddle with a serpentine-routed WLS fiber in the scintillator counter. Figure from [69]

m in diameter and 42 m in height) filled with 50 ktons of ultra-pure water. Super-Kamiokande is composed of inner (ID) and outer (OD) detectors that are optically separated. The Cherenkov radiation is emitted at a characteristic polar angle that depends on the charged particle velocity when it moves through a dielectric medium (e.g., water) faster than the phase velocity of light in that medium. The ID registers Cherenkov radiation emitted by charged particles running in water. The OD is used to veto interactions caused by cosmic muons and radioactivity from the rock surrounding the tank. The Cherenkov light rings, different in shape for electrons and muons produced in neutrino interactions, are registered by 11,129 photomultipliers of the Super-Kamiokande detector. The electron-muon discrimination technique, which is very important for distinguishing between ν_e and ν_μ interactions, is well developed by the Super-Kamiokande Collaboration. The muon ring has sharp edges, while the electron ring is fuzzier because of the showering (see Fig. 3.14). The mis-identification for a muon as an electron and vice versa is less than 1%.

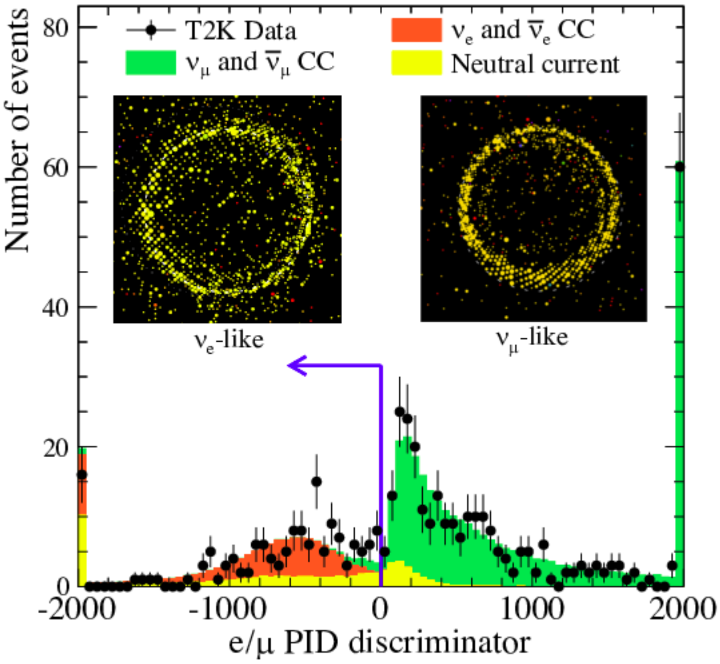

Figure 3.14: Example of T2K events in Super-Kamiokande detector shown unrolled onto a plane: an electron-like ring (top-left) and an muon-like ring (top-right). The bottom plot shows the output of the electron/muon discriminating tool. Monte Carlo predictions for various interaction channels are shown in colored histograms. Black dots with errors represent the data from the far detector. Figure from [83].

Chapter 4

Data and software in ND280

This chapter contains a short description of the data and software tools used in the near detector of the T2K experiment. The first section briefly describes the procedures and organization of data taking and data distribution in ND280. Event reconstruction and data analysis software are described in the second section. The third section contains an overview of the simulation software with a particular emphasis on event generator packages used in the T2K experiment. The last section describes the new algorithm implemented in the ND280 software by the author of this monograph to improve the reconstruction of the tracks of the particles that traverse TPC and PØD sub-detectors.

4.1 Data taking and organization

By the time of writing this monograph, 3.6×10^{21} protons on target (POT) of data has been analysed in the near detector of the T2K experiment with neutrino mode antineutrino mode ratio approximately equal to 6/5. A detailed history of the accumulated number of POTs and the beam power can be found in Fig. 4.1.

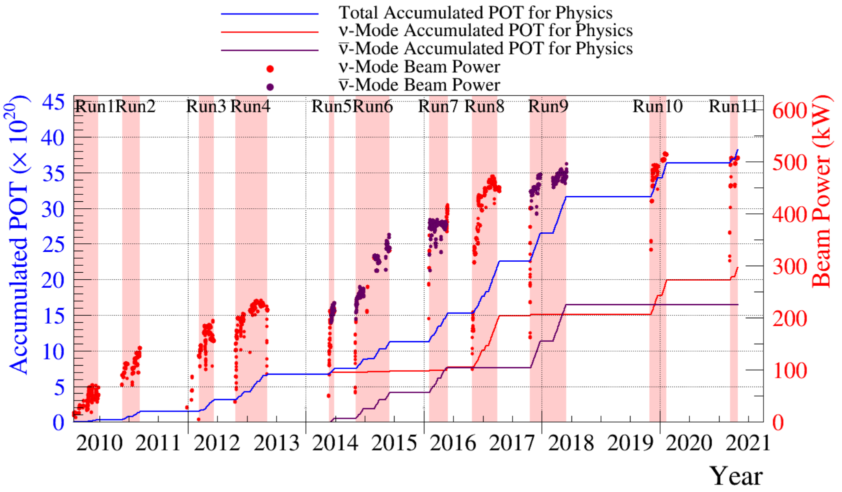

Figure 4.1: Accumulated data in proton on target units by the T2K experiment for the entire period of data-taking for neutrino mode (solid red line) and antineutrino mode (solid black line). The beam power is also overlaid on the plot [83].

The beam runs recorded by the ND280 detector and used in the latest T2K oscillation analysis are shown in Table 4.1.

Run	Data (POT 10^{19})	MC (POT 10^{19})	MC/data
2 (air) ν_μ	3.59457	167.99	46.73
2 (water) w ν_μ	4.33765	120.375	27.75
3 ν_μ	15.8103	307.766	19.47
4 (air) ν_μ	17.8338	361.225	20.26
4 (water) ν_μ	16.4302	361.215	21.98
5 $\bar{\nu}_\mu$	4.3468	221.103	50.87
6 $\bar{\nu}_\mu$	34.0928	346.986	10.18
7 $\bar{\nu}_\mu$	24.3782	332.995	13.66
8 (air) ν_μ	41.5013	361.098	8.70
8 (water) ν_μ	15.8053	254.225	16.08
9 $\bar{\nu}_\mu$	20.5391	245.61	11.96
Total	198.67	3080.58	15.51
Total ν_μ	115.31	1933.89	16.77
Total $\bar{\nu}_\mu$	83.36	1146.69	13.76

Table 4.1: ND280 data used for the latest T2K oscillation analysis from runs 2-9 for ν_μ and $\bar{\nu}_\mu$ beam modes, the POT for data and Monte Carlo, and their ratio. The data is divided into periods with the POD filled with water (water) or without water (air).

Productions

The campaign of processing the data and Monte Carlo with a specific version of the software is called 'production X', where X numbers the subsequent campaigns. The ND280 software is frozen every time the more significant improvements are implemented into the major packages. Before the freeze, the improvements have to be approved by the entire collaboration. The software which is being frozen in this way is called the 'production X' software. The calibration constants have to be calculated and ready before the production starts. Next, the data is processed, and Monte Carlo samples corresponding to each data run are produced using as input the *vector* files generated by the neutrino event generators. *Vector* files are the neutrino event generator output files that contain four vectors of the particles in the final state of the neutrino-nucleus interaction.

4.2 Simulation program

The simulation chain begins with the process of generating vector files by neutrino event generators. NEUT [16] is the T2K's primary event generator and, along with GENIE [17], is used in the official Monte Carlo production process in the T2K experiment. NuWro [18] is adopted as an auxiliary generator.

4.2.1 Neutrino event generators

The following subsection details the neutrino interaction models used in the T2K neutrino event generators with a particular emphasis on NEUT. The models used for particular interaction channels are listed below. The CC0π models:

- NEUT (version 5.4.1): Local Fermi Gas (LFG) assuming an axial mass $M_A^{QE} = 1.03 GeV/c^2$ [1] and corrections from the Random Phase Approximation (RPA) approach with 2p2h. A 1p1h and 2p2h model is used in this case from Ref. [142];
- GENIE (version 3.00.04, configuration G18 10b 000 00) LFG assuming an axial mass $M_A^{QE} = 0.99 GeV/c^2$ with 2p2h and RPA corrections from Ref. [142];
- NuWro (version 18.02.1) with LFG [143] assuming an axial mass $M_A^{QE} = 1.03 GeV/c^2$ with 2p2h and ARPA corrections also from Ref. [142];
- NuWro Spectral Function (SF), as developed in Ref. [144], using the same 2p2h model as NEUT.

Rein and Sehgal's model is used to simulate the neutrino induced single pion production in the NEUT generator, where the interaction is split into:

$$\nu + N \rightarrow l + N*$$
$$N* \rightarrow \pi + N',$$

where N and N' are the nucleons and N* is the baryon resonance. The cross sections are calculated by multiplying the amplitude of each resonance production by the decay probability of the resonance into one pion and one nucleon. The interference terms between the resonances are also taken into account. In total, 18 resonances below 2 GeV are considered, and the axial mass $M_A^{RES} = 1.21 GeV/c^2$. M_A^{RES} is, analogically to CCQE, the parameter in axial form factor parametrisation in the formula for calculating the cross section.

A Neutral Current (NC) and Charged Current (CC) coherent pion production is simulated using the Rein-Sehgal model [149]. The CC coherent pion production includes the PCAC (Partially Conserved Axial Vector Current) and lepton mass corrections [150].

DIS (Deep Inelastic Scattering) processes are simulated using the GRV98 [151] parton distribution with low-Q2 corrections by the Bodek and Yang model [152].

4.2.2 Simulating electronics and detector response

After the neutrino event simulation performed by NEUT or GENIE is completed, a response of the electronics is simulated by the custom software, and the particles are propagated through the detector using the GEANT4 package [153]. GEANT4 simulates the passage of the particles through the matter. Once the simulation

---

[1] M_A^{QE} is the parameter in the dipole ansatz for the nucleon axial form factor present in the formula for CCQE cross section.

process is finalized the event reconstruction algorithms attempt to reconstruct the trajectories and the physical properties of the particles produced both in the neutrino interaction vertex and in the secondary interactions.

4.3 Event reconstruction and data analysis

This section describes the event reconstruction and data analysis routines that are used in the T2K experiment.

The main objects common for the entire reconstruction in ND280 are as follows:

- Hit (`TReconHit`) - energy deposited in the active element that is read out by the MPPC [2];
- Cluster (`TReconCluster`) - a group of neighboring hits;
- Track (`TReconTrack`) - a cluster which has a length significantly larger than its width;
- Shower (`TReconShower`) - a cluster that has the characteristic cone shape;
- Particle (`TReconPID`) - a track or a shower which has a particle hypothesis assigned by the particle identification algorithm.

Although the reconstruction in TPC uses algorithms that are specific for Time-Projection Chambers (except cellular automaton), FGD, ECAL, PØD, and SMRD are built based on plastic scintillator bars and adopt the same pattern recognition and short track reconstruction methods such as cellular automaton, Hough Transform and Principal Component Analysis (PCA).

The common pattern recognition routines are the custom libraries or the libraries provided by the ROOT package. A critical piece of the software also extensively used by the sub-detector reconstruction packages and the global reconstruction is RecPack [154]. RecPack provides a fitting, matching, and filtering algorithms with the most critical tool Kalman Filter [155]. A more detailed description of the reconstruction packages is written below.

TPC reconstruction

The first step of the TPC reconstruction is to apply the calibration constants and to dispose of dead and noisy channels. The output of this action is the *waveform* that represents the charge acquired in a single anode pad along the readout time. Next, a search for clusters of waveforms in the same row is executed. The clusters are then merged into tracks using a pattern recognition algorithm.

The drift distance is reconstructed by determining the T_0, which is the time when the track was created. This is achieved by matching the TPC track with objects in the fast detectors: FGD and ECAL. The reconstruction of the track kinematics is done using likelihood fit or Kalman Filter. The final step of the TPC reconstruction

---

[2] MPPC - Multi Pixel Photon Counter

is to calculate the ionization energy released in the gas as a function of the track length. It is used later for particle identification.

FGD reconstruction

The FGD reconstruction is run after the TPC reconstruction and can be summarized in the following steps:

1. Time binning - FGD hits are separated into separate groups of hits (bins), based on their times. The bins correspond to beam bunches.
2. FGD-TPC matching, where TPC tracks are matched with FGD hits using Kalman Filter.
3. An 'isolated' FGD reconstruction - a reconstruction of FGD hits from tracks that start and stop in the FGD (or do not enter the TPC). Two pattern recognition methods are implemented: one based on a cellular automaton, the other based on the Radon transform [156].
4. FGD Particle Identification - uses a method based on particle's deposited energy vs. track length relation. It is useful only for the particles stopping in FGD.
5. FGD Track Time calculations. Track time is calculated using the timing of the hits.

ECAL reconstruction

The reconstruction in the ECAL begins with the calibrated data. In the first step, a hit preparation is applied, and the hits are grouped in the bins corresponding to beam bunches after the removal of the noise hits. The hits from both ends of the scintillator bar are combined, resulting in the computation of the coordinate along the bar. Next, the clustering of the hits is performed in two projections using several methods mainly based on the neighboring criteria. The clusters are then matched to form three-dimensional objects. Michel electron reconstruction algorithm is applied to find the hits delayed in time originating from the electrons from the muon decay. Next, the electromagnetic energy of the clusters is estimated using the likelihood fit. The showers are fitted using the PCA method, whereas the tracks are fitted using a simple linear fit. Finally, the particle identification (PID) method is run. The PID algorithm in ECAL uses a neural network classifier with the input parameters related to the shape and charge distribution of the reconstructed clusters. A neural network is used to discriminate between the tracks and showers. An additional step is the ECAL-TPC matching using RecPack's Kalman Filter.

SMRD reconstruction

The reconstruction in SMRD is based mainly on the results of the reconstruction in other ND280 sub-detectors. The main algorithm matches SMRD hits with the reconstructed objects in inner detectors (TPC, FGD, ECAL, PØD) using Kalman Filter.

If the SMRD-inner detectors matching algorithm fails and there are enough SMRD hits, then a stand-alone SMRD algorithm is run. The algorithm uses a common pattern recognition approach such as Hough transform, PCA, and nearest neighbors algorithm to find the clusters in two projections XZ and YZ. Next, the XZ and YZ tracks are matched to form a three-dimensional track. Finally, tracks are fitted with a simple parametric, linear fit.

PØD reconstruction

The principle of the PØD reconstruction is presented in more detail in the next section, in which the author of this monograph presents the achievements in matching the PØD objects with the TPC.

In the first step of the PØD reconstruction, the track segments are constructed from the cleaned (noise) detector hits using the Hough Transform in the XZ and YZ projections. The track segments are then joined together using a road following algorithm forming two dimensional (2D) track candidates. Two-dimensional tracks from different projections are matched together into three-dimensional (3D) objects. If the matching of the 2D tracks into a 3D object fails, then the object is treated as two-dimensional. In the next step, the reconstructed tracks are fitted using the Kalman Filter algorithm. When Kalman Filter algorithm fails (when the track is very short or steep) the parametric fitting algorithm is used. The minimum number of readout planes that the track needs to cross to be fitted with Kalman Filter is six, which is equivalent to three PØDules [3]. The result of the first two steps of the reconstruction is called `TP0DTrackRecon`.

The common primary vertex for the tracks is found by `TP0DPairwiseVertex` algorithm. `TP0DPairwiseVertex` uses a simple closest approach strategy to find vertices. The vertex is the point of the closest approach of a pair of tracks and is defined as the point where the distance between the extrapolated back tracks reaches its minimum. Our analysis uses both `TP0DTrackRecon` and `TP0DPairwiseVertex` algorithm results.

Next, each track is passed through a particle identification algorithm. The algorithm is based on the energy deposit of the tracks within the PØDule layers. After the last step of the tracking stage, the reconstructed objects can be passed to the shower reconstruction stage when the particle identification algorithm identifies them as a shower or a track. A dedicated reconstruction algorithm is applied for showers, which utilizes the knowledge that all hits from a shower will fall in a cone when viewed from the interaction vertex. When all standard reconstruction steps are completed, the Michel electron tagging algorithm is run. There are two Michel tagging algorithms in the PØD reconstruction chain, and they both use time and position clustering to associate reconstructed objects with Michel electron candidates. We use one of these algorithms called `TP0DTagMuonDecay`. For a complete description of the PØD reconstruction package (p0dRecon), please check [134].

---

[3] Definition of the PØDule can be found in 3.3.2

Global reconstruction

The global reconstruction aims to match the reconstructed objects from all combinations of the sub-detectors, re-fit them using the information from the entire ND280 detector and reconstruct the interaction vertices. The main tool used to perform fitting and matching is RECPACK, [154] which contains routines based on Kalman Filter [155]. The package which is responsible for global reconstruction is called *oaRecon*.

4.4 Improving event reconstruction in the ND280 detector with PØD-Tracker incremental matching

This Section presents an improved track-reconstruction algorithm for reconstructing the tracks of charged particles in the PØD and TPC detectors. The improvements were prepared, developed and implemented by the author of this monograph.

In the T2K production 6 ND280 software reconstruction of the particles in the tracker and PØD sub-detectors operates independently. In the first step the tracks are created by the stand-alone tracker and PØD algorithms, with no information exchange. Next, the objects from both the tracker and PØD reconstructions are matched together using the RECPACK's Kalman Filter algorithm used by the global reconstruction package. This approach fails in the case of the particles produced at the downstream end of the PØD that often trigger fewer than three hits in the Pizero sub-detector and the stand-alone PØD reconstruction is not able to find their trajectories. In the case described above the starting position of the reconstructed track is shifted downstream if the particle travelled further to the TPC1. The situation is illustrated in Fig. (4.2). In order to deal with the particles that are produced at the downstream end of the PØD, it is necessary to exchange the information between the PØD and the tracker during the reconstruction process. The algorithm described in this section addresses the problem characterized above by matching incrementally TPC1 tracks with the PØD hits ('hit-by-hit') using Kalman Filter.

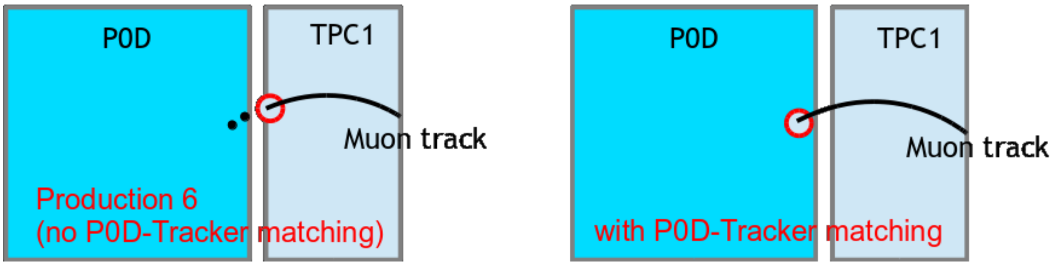

Figure 4.2: The problem of mis-reconstruction of the tracks of particles produced in the interactions at the downstream end of the PØD sub-detector in production 6 (left). The situation after introducing PØD-Tracker incremental matching algorithm (right). The neutrino beam direction is from left to right.

4.4.1 Algorithm description

The inputs for the algorithm are the tracks that have a part (segment) in the TPC1 detector and PØD hits. Such tracks are called *seeds*. The following steps are performed for every tracker track with the TPC1 segment:

1. Pre-selection and preparation of the PØD hits:
    - PØD-tracker timing difference cut. The time difference between the tracker track and the hit must be smaller than the TimeCutWindow parameter value (300 ns). This cut prevents matching PØD hits in different bunches than the TPC1 track.
    - Sorting in the reversed-Z coordinate order. The hits are sorted in the decreasing Z position order (starting from the most downstream to the most upstream one).
    - Grouping the hits into groups called 'layers'. A 'Layer' is a group of hits in the same scintillator layer. 'Layers' are ordered (and assigned a number) starting from the most upstream (#1) to the most downstream one (#14).
2. Looping over 'layers' of hits:
    - Calculate how many layers are between the current hit and the last hit matched to the seed track. If this number is larger than the fMaxModulesToSkip parameter, then the matching procedure is stopped. The fMaxModulesToSkip parameter is currently equal to zero. Consequently, no gaps between the layers are allowed as the hit reconstruction efficiency in the PØD is as high as 99%.
    - Sort the hits in each 'layer' in an ascending order using the calculated matching χ^2 of the hit to the seed track. An additional 'safety cut' on the X coordinate residual [4] is applied. The hits with the X residual larger than fResidualCut parameter (equal to 100) are rejected.
    - Loop over hits in each 'layer' (previously sorted according to their χ^2).
    - Compute the matching χ^2 between the hit and the current state. The state is a seed track with PØD hits matched to it in the previous steps.
    - Add the current hit to the matched object if the χ^2 is smaller than the cut value fChi2Cut (equal to 5.0) and update the current state.
    - Add the matching χ^2 of the current hit to the total χ^2 of the track.
    - Compute how many 'layers' have been searched by the algorithm to find the PØD hits matching the seed track. If this number is larger than fMaxPenetrated layers parameter (equal to 12), then the algorithm is stopped. This cut saves the computing time since the objects with the hits deeper in the PØD are being reconstructed well by the stand-alone PØD reconstruction.

---

[4] Residual is the difference between the measured and fitted value divided by the uncertainty

The algorithm is fully configurable and its parameters can be changed by modifying the parameters file. It is implemented as a `TP0DTrackerMatcherIncremental` class in the p0dRecon reconstruction package. The flow of the procedure is shown in Fig. 4.3. PØD hits that are the input for the algorithm are prepared in a standard way by the `TP0DClean` algorithm, which removes the noise hits by examining their charge. The reconstruction in the PØD sub-detector operates within each integration cycle of the Trip-T Frontend Board (TFB) electronics which corresponds to the beam bunch window. `TP0DTrackerMatcherIncremental` is run in `TP0DCycleRecon` class which is responsible for the reconstruction in the TFB integration cycle. The PØD-tracker matching algorithm loops over the tracks reconstructed by the trackerRecon package (tracker objects) and tries to match them with PØD hits. The object which is the output of the matching is the re-fitted track with additional PØD hits. If the output track has more than two PØD hits, it is used as a seed for standard PØD tracking routines. In the opposite case, the reconstructed track is saved directly in the global reconstruction (oaRecon) output.

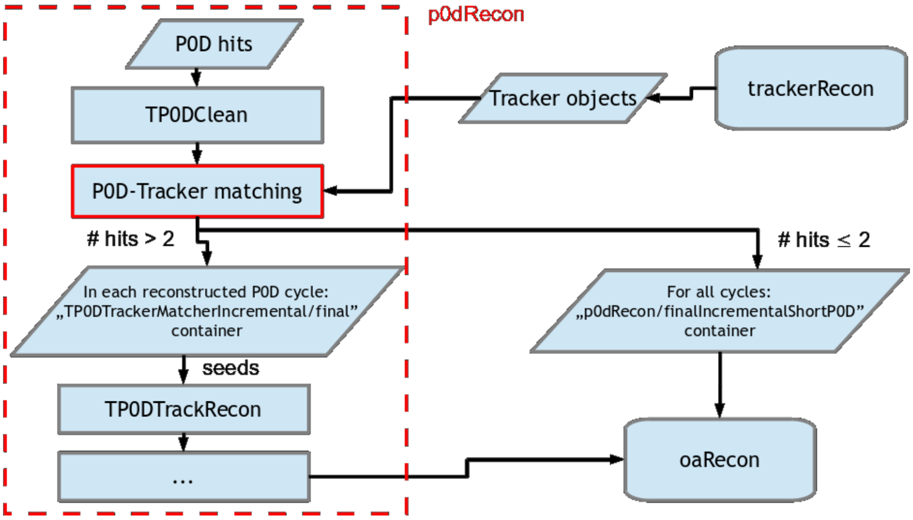

Figure 4.3: PØD-Tracker incremental matching steps within the p0dRecon package and its interplay with the tracker and global reconstruction.

4.4.2 Tuning of the χ^2 cut

In order to estimate the optimal value of the χ^2 cut parameter (fChi2Cut), which can be interpreted as the maximal width of the matched PØD-tracker track, the tuning procedure was performed. The Monte Carlo sample of neutrino interactions in the Central ECAL was used as the input for the study. The events were reconstructed with several pre-defined values of the χ^2 cut, and the matching quality was examined using parameters such as track completeness, cleanliness, and reconstruction efficiency. Track completeness is defined as the ratio of the number of hits in the reconstructed track that truly belong to the particle's trajectory $Nhits^{rec}_{true}$ and the number of all hits belonging to that trajectory $Nhits_{true}$:

$$Completeness = \frac{Nhits^{rec}_{true}}{Nhits_{true}}. \tag{4.1}$$

Track cleanliness is a fraction of reconstructed hits truly belonging to the particle's trajectory $Nhits^{rec}_{true}$ and all hits in the reconstructed track $Nhits_{rec}$:

$$Cleanliness = \frac{Nhits^{rec}_{true}}{Nhits_{rec}}. \tag{4.2}$$

Efficiency is defined as the number of reconstructed tracks $Ntracks^{matched}$ divided by the number of all tracker tracks with at least one hit in the PØD $Ntracks$:

$$Efficiency = \frac{Ntracks^{matched}}{Ntracks}. \tag{4.3}$$

To find the optimal value of the χ^2 cut the Figure Of Merit (FOM) was defined. FOM is the product of cleanliness, completeness and efficiency. The optimal value of χ^2 cut was chosen to maximize the FOM function. The results of the study are shown in Fig. 4.4. The study showed that the optimal value of χ^2 cut is 5. One can also observe that the maximum of FOM is mainly driven by the maximum of the achieved track completeness, which reaches its maximum at χ^2 equal to 5.

4.4.3 Validation and tests

Validation tests constitute an essential part of the implementation procedure. The aim of the validation is to verify whether the algorithm works properly, gives the expected improvement, and does not harm other pieces of the reconstruction procedure. This subsection presents the details of the validation studies that preceded the final inclusion of the PØD-tracker matching algorithm into the official ND280 software.

Particle-gun muon tests:

The first study was performed using the Monte Carlo 'particle gun' sample of 25 000 single muon events. The muons with kinetic energy $E_k = 2GeV$ were injected into Central ECAL with the uniform distribution in X, Y, Z and direction along the Z axis. Events were reconstructed with PØD-tracker incremental matching algorithm switched on and off. The output of the global reconstruction was analyzed using the reconstruction efficiency per PØDule defined as:

$$Efficiency(P0Dule) = \frac{N_{Reco}(P0Dule)}{N_{True}(P0Dule)}, \tag{4.4}$$

where: $N_{Reco}(P0Dule)$ is the number of events that have a true interaction vertex in this PØDule and a reconstructed track with PØD and TPC segments was found, $N_{True}(P0Dule)$ is the number of events that have a true vertex in this PØDule. The efficiency per PØDule illustrates how often there is a reconstructed global track with PØD and TPC segments when the true vertex is in the specific PØDule. The results of the study are shown in Fig. 4.5. A significant improvement was observed in the four most downstream PØDules (True Z > -1100 mm).

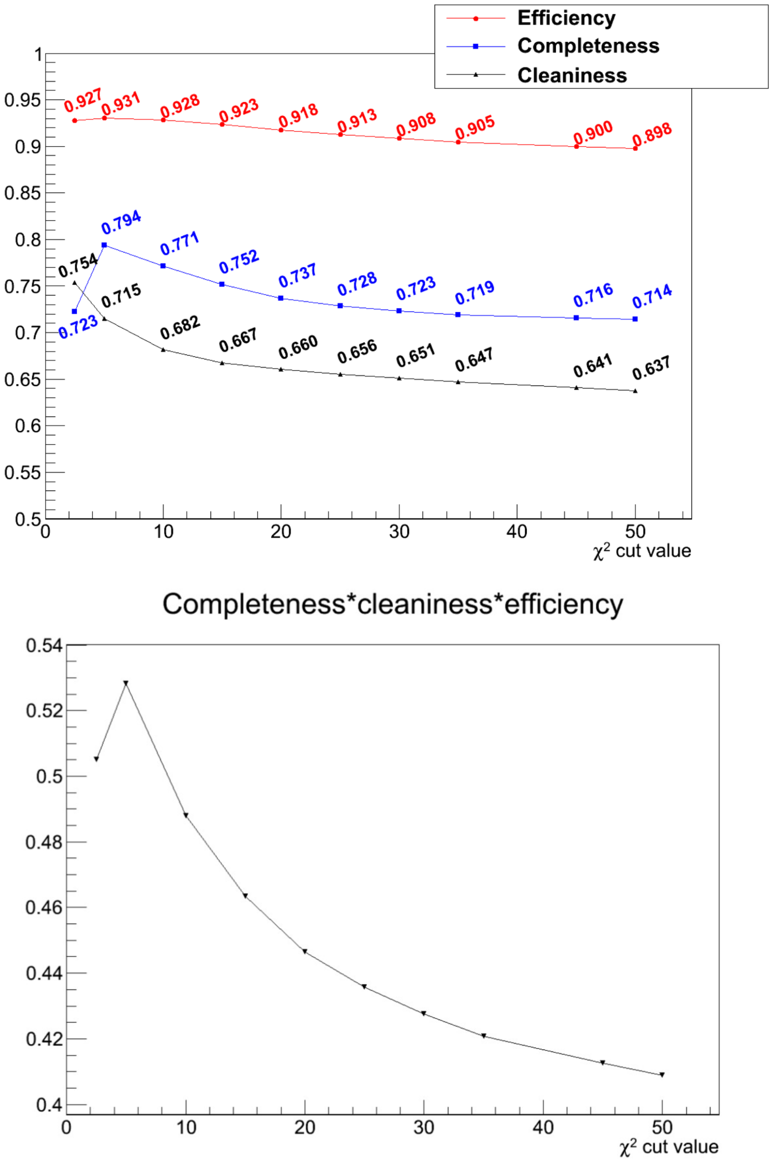

Figure 4.4: Results of the tuning of χ^2 cut in PØD-tracker incremental matching. The top plot shows the completeness, cleanliness of the reconstructed tracks, and efficiency of matching as a function of the χ^2 cut value, while the bottom plot illustrates the behavior of their product (Figure of Merit). The maximum of the product defines the optimal value of the cut (equal to 5).

Neutral pion reconstruction efficiency in the PØD:

Another validation test aimed at verifying whether the presence of the additional PØD-tracker matching algorithm did not decrease the efficiency of reconstructing π^0s. This efficiency is essential for the measurements of π^0 production rate and cross section. The input for the analysis was a set of 50 000 Monte Carlo events with 'particle gun' π^0's. Neutral pions were injected into PØD fiducial with the kinetic energy between 10 MeV - 1 GeV and the downstream direction with the angle with respect to the Z-axis between 30 and -30 degrees. Spatial, energetic and angular distributions were uniform. The output of the p0dRecon package, with

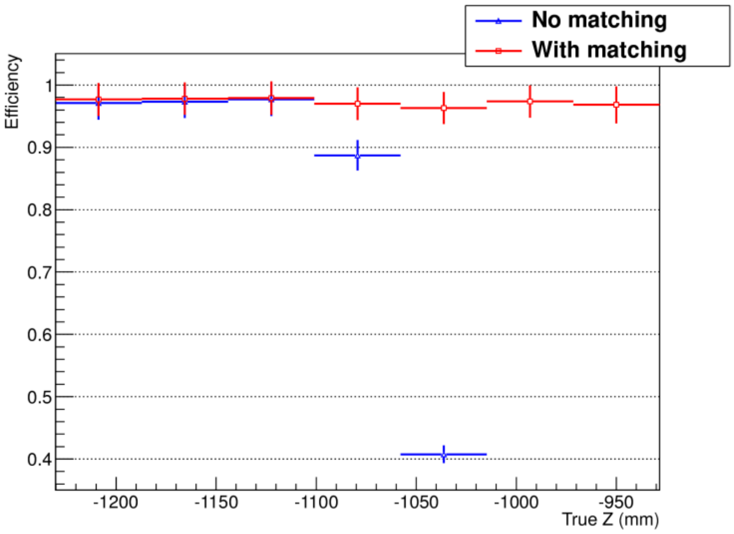

Figure 4.5: Efficiency of track reconstruction per PØDule for particle gun muon study with PØD-tracker matching switched on (red) and off (blue).

PØD-Tracker incremental matching turned on and off was examined.

The efficiency of selecting events with the presence of the two most energetic electromagnetic showers with the invariant mass between 350 MeV and 1150 MeV was calculated. The results are shown in Fig. 4.6 The conclusion agrees with the expectations: PØD-Tracker incremental matching turned on does not affect on the PØD π^0 selection efficiency.

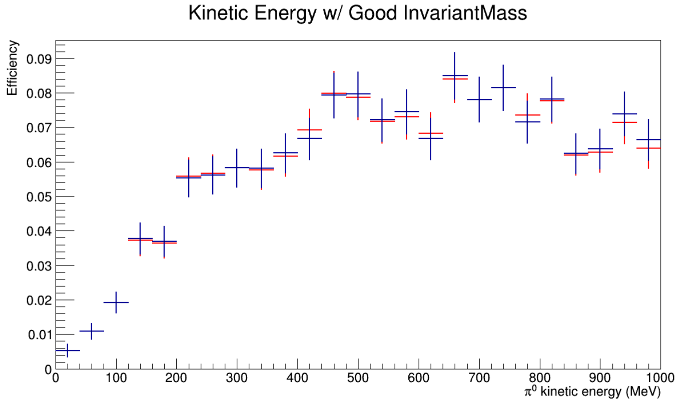

Figure 4.6: Efficiency of selecting the two highest energy electromagnetic showers with an invariant mass between 350 MeV and 1150 MeV in PØD reconstruction.

Muon neutrino charged current selection efficiency

The following analysis refers to the efficiency of selecting muon neutrino charged current interactions with the vertex in Central ECAL and activity in PØD and tracker. This selection is an important part of the CC0π analysis on lead.
The output of global reconstruction with PØD-tracker incremental matching switched on and off was evaluated, and the efficiency of selecting charge current events was

calculated using Monte Carlo. The following cuts that mimic the cuts used in PØD CC0π analysis on water [124] were applied in this selection:

1. Select highest momentum negative (HMNT) PØD-TPC1 track,
2. Require the initial position of HMNT to be in CentralECal (CECal),
3. Muon likelihood of HMNT has to be higher than 0.05 (rejecting electrons).

The ultimate goal of the PØD-tracker incremental matching is to improve the efficiency of selecting events in Central ECal. The efficiency per PØDule was defined in a similar way as in Eq. 4.4. The result of the study is shown in Fig. 4.7. As can be seen in Fig. 4.7, the goal was achieved since the PØD-Tracker incremental matching gives a significant improvement of the CC selection efficiency at the most downstream CentralECal PØDules.

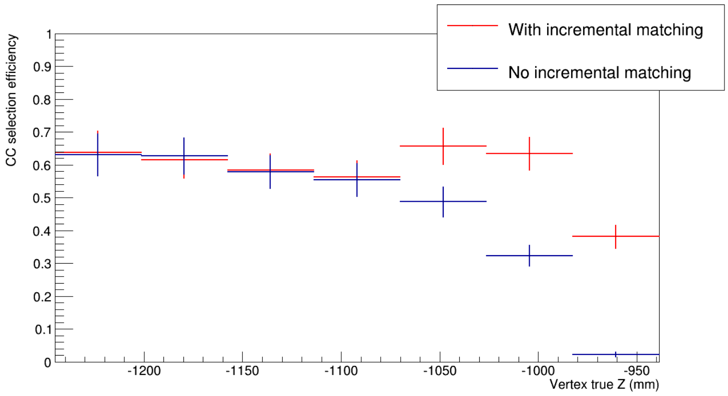

Figure 4.7: Efficiency of selecting neutrino interactions per PØDule for the charged current selection in Central ECal.

Tests with backward-going muons

Another validation study was done using Monte Carlo with muons injected into the middle plane of FGD1 and backward-going (from FGD1 towards PØD). The kinetic energy of the muons ranged between 50 and 200 MeV. As in the previous validation studies described in this subsection, the reconstruction was tested with PØD-tracker incremental matching turned on and off. The overall PØD-TPC1 matching efficiency was computed and defined as:

$$Efficiency = \frac{NTrackerTracks^{Matched}}{NTrackerTracks}, \tag{4.5}$$

where $NTrackerTracks^{Matched}$ was the number of tracker tracks matched to PØD hits and $NTrackerTracks$ was the number of all tracker tracks with minimal energy to reach the PØD. The efficiency as a function of the muon momentum measured in TPC1 is shown in Fig. 4.8. One can observe a significant improvement in the PØD-TPC1 matching efficiency for low momentum muons which stop in the most downstream PØDules. The completeness of the matched tracks was also studied

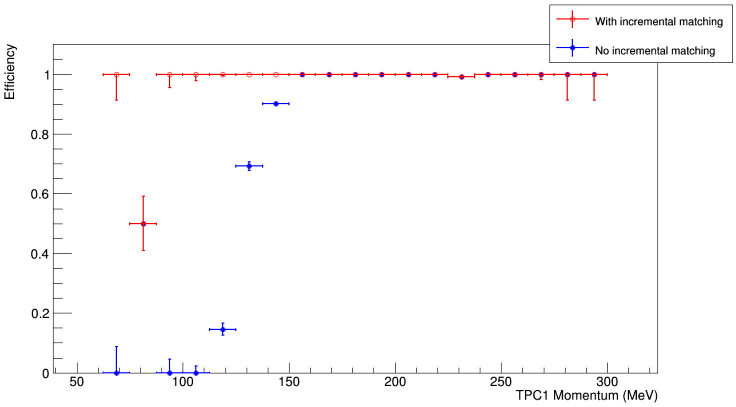

Figure 4.8: PØD-TPC1 matching efficiency for FGD1 backward-going muons.

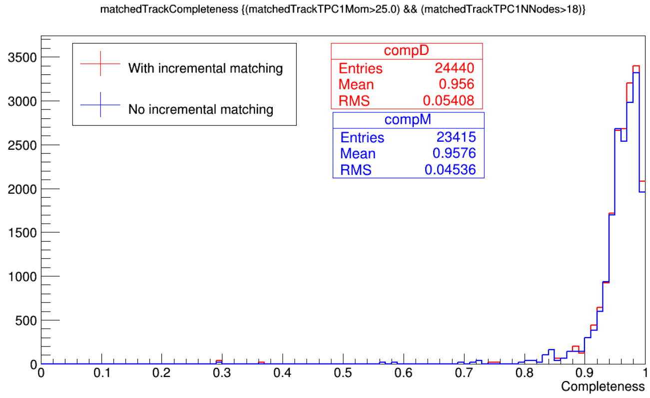

Figure 4.9: Reconstructed track completeness for FGD1 backward-going muons. No decrease is observed with the incremental matching turned on.

and the results are depicted in Fig. 4.9. No decrease in the track completeness with PØD-tracker incremental matching turned on was observed. The χ^2/NDF of the matched tracks, which is related to the reconstruction quality, was calculated for data and Monte Carlo samples of FGD1 backward-going muons and compared, as seen in Fig. 4.10. No significant differences in hit matching χ^2/NDF between the

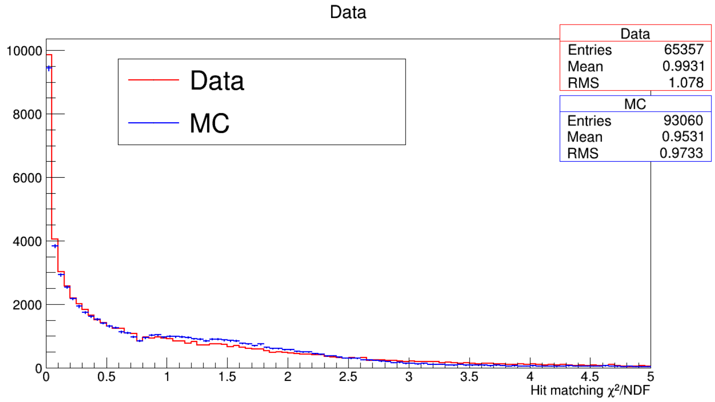

Figure 4.10: PØD-TPC1 hit matching χ^2 for data and Monte Carlo. No significant discrepancies were observed.

data and Monte Carlo were observed. It confirms that the simulation worked well and that all physics effects present in the data were correctly implemented in Monte Carlo.

Matching residuals (differences between fitted and true position) also agreed between the data and Monte Carlo (Fig. 4.11). A small shift of approximately 2 mm is due to the misalignment between PØD and TPC1. This value is expected and confirmed by other independent measurements.

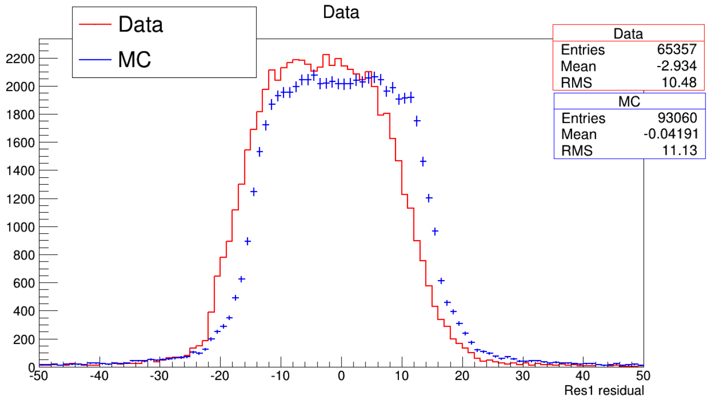

Figure 4.11: PØD-TPC1 hit matching residuals. There is a good agreement between the data and Monte Carlo result. A small shift (2 mm) is due to the misalignment of the PØD and TPC1.

Layer-by-layer matching efficiency with through-going sand muons

The last study uses official samples of through-going *sand* muons in data and Monte Carlo. Sand muons are the muons produced outside the ND280 detector, usually in neutrino interactions in the sand that surrounds the detector pit. Through-going sand muons which traverse the entire ND280 detector are very useful and are used extensively for validation and calibration studies in T2K.

The testing procedure consists of the following steps:

1. Mask out (make invisible for the reconstruction) the hits in every but the most downstream layer of the PØD;
2. Re-run PØD-tracker incremental matching algorithm;
3. Calculate matching efficiency for this layer defined as in Eq. 4.5;
4. Proceed layer-by-layer and repeat steps 1-3.

The procedure is illustrated in Fig. 4.12.

The results of the layer-by-layer efficiency comparison between the data and simulation are shown in Fig. 4.13. No significant difference between the two samples was observed which once again confirms that the physics processes are simulated well in Monte Carlo, and the algorithm takes into account all the effects for particles traversing the PØD and tracker.

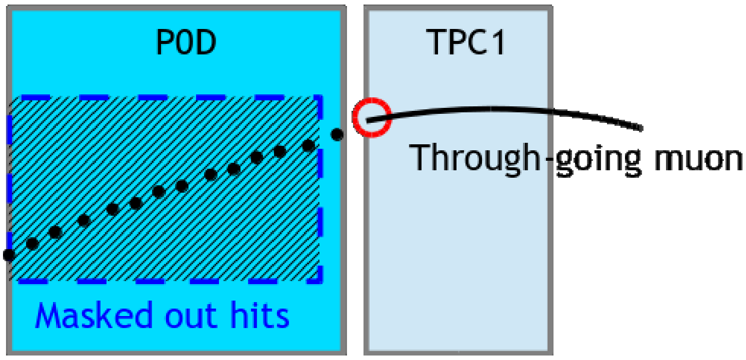

Figure 4.12: Single step of the PØD-TPC1 layer-by-layer matching efficiency study idea. Sand muons traversing PØD and TPC1 in data and Monte Carlo are used in the analysis. PØD hits in the dashed rectangle are masked out and are not visible to the reconstruction.

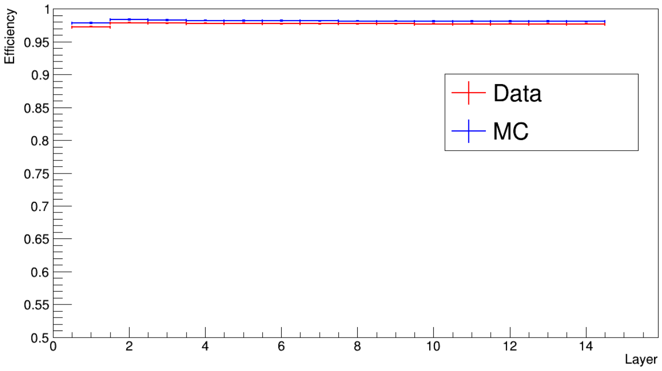

Figure 4.13: PØD-TPC1 layer-by-layer matching efficiency. No significant differences between data and Monte Carlo are present.

4.4.4 Summary

It is clearly visible that introducing the PØD-tracker incremental matching algorithm significantly improves the efficiency of reconstructing particle trajectories and neutrino interactions in the most downstream part of the PØD. The implementation of the method increases the efficiency of reconstructing muons produced in the most downstream layers of the PØD and entering TPC1 from zero up to 98%. A significant boost in the efficiency of reconstructing backward-going FGD1 muons stopping in the PØD is also observed.
Studies show that there is a 30-40% gain in efficiency of selecting neutrino interactions on lead in Central ECAL while no decrease in π^0 selection efficiency is observed. There is also good agreement between the results of the method for data and Monte Carlo. The algorithm was implemented in the test mode, tuned, and validated on production 6 data and Monte Carlo. Finally, it successfully passed all the validation tests and has been approved by the T2K collaboration, and included in the official reconstruction chain for production 7.

This chapter described the procedures and methods used to process and analyze the data and generate Monte Carlo samples. The last section of the chapter illustrated the improvements to the event reconstruction implemented by the author of this monograph. The next chapter is devoted to the characterization of the techniques that are used in the cross-section measurements in T2K.

Chapter 5

Overview of the strategy of the cross-section measurements in T2K

This chapter describes the procedures and techniques used in the neutrino-nucleus cross-section measurements in the T2K experiment.

The first section describes the basics of the cross-section measurement. The second and third sections explain the true and reconstructed kinematic phase space concept and describe how the transformations between these phase spaces are performed. Next, the formalism of binned likelihood fitting in the cross-section measurement is characterized. Finally, the last section details the methods of calculating systematic uncertainties in the likelihood fitting approach.

5.1 Calculating neutrino cross section

The basic quantity describing the probability of scattering a neutrino on a target is the *total flux-integrated cross section.* This quantity is also called *single-bin* cross section as the outcome is a single number - a cross section integrated over the entire available phase space. The total flux-integrated cross section can be written as:

$$\sigma = \frac{N_{sel,data} - B}{\epsilon \Phi N_T}, \tag{5.1}$$

where the selection efficiency ϵ is given as:

$$\epsilon = \frac{N_{sel,MC} - B}{N_{Gen}}. \tag{5.2}$$

The selection efficiency describes the fraction of all neutrino interactions of the specific type we can measure (select) with our detector.

The parameters used in the equations 5.1 and 5.2 are as follows: $N_{sel,data/MC}$ - number of selected events in data / Monte Carlo, B - number of selected background events in Monte Carlo (selected events that are not signal), Φ - integrated flux of neutrinos, N_T - number of targets, N_{Gen} - number of all signal events generated by Monte Carlo.

The scheme of selecting $N_{sel,data/MC}$ (most often it is a sequence of cuts) is called *signal selection* and the events selected with this selection are called *signal events* while the entire set of signal events - a *signal sample.* The region of the phase space of kinematic parameters of outgoing particles occupied by the events from the signal sample is called a *signal region.*

Additionally, the term $N_{sel,data} - B$ in Eq. 5.1 corresponds to the expected number of signal events selected in the data. The method of estimating the number of background events using Monte Carlo and subtracting it from the selected number of events in data to get the expected number of signal events in data is called the *background subtraction* method. Apart from the background subtraction, other approaches were applied in the past, among which one should mention *purity correction.* These methods were abandoned since they are considered as more model dependent than the background subtraction procedure.

The expected number of signal events in data $N_{sel,data} - B$ needs to be corrected because we do not have a perfect detector that is able to measure all events. These detector effects are incorporated into efficiency ϵ. The operation of dividing $N_{sel,data} - B$ over ϵ is called *efficiency correction.* If there are no restrictions imposed on in the kinematic properties of the outgoing particles (e.g., momentum, scattering angle), we say that the cross section is measured in the *full phase space.* In practice, detectors have limited *acceptance* which means that they have detection thresholds, e.g., particles with a momentum below 200 MeV, or those scattered at an angle larger than 60 degrees are not detected.

Because of limited detector acceptance, the efficiency of selecting particular events can be low, or it can change rapidly with a change in kinematic parameters. Poor efficiency or its rapid variations lead to the escalation of the systematic error of the efficiency correction and, ultimately of the cross-section measurement. The increment of the systematic uncertainty is mainly related to the fact that the extrapolation of the event rates for the regions of phase space with low efficiency has to be done. To avoid this problem, the measurement is performed in the so-called *limited phase space (restricted phase space)*, where the cuts on the kinematic properties of the outgoing particles are imposed, and the cross section is measured only in a specific region of the phase space.

The uncertainty on the number of background interactions B can be significantly reduced by using additional data and Monte Carlo samples called *control samples.* The procedure of selecting events for the control sample focuses on getting the highest purity for the desired type of background in the sample e.g., CC0π, CC1π, CCOther. Most often, events in the control sample are selected by inverting one or more of the cuts of the signal selection. Apart from that method, there are also other recipes depending on the type of background that we want to select. With the control samples, one can estimate the number of background interactions in the region of the phase space, which is in the direct vicinity of the region occupied by the signal sample (*signal region*). The next step of the method is the extrapolation of the number of background interactions to the signal region. The primary requirement for that procedure is that the background characteristics in the control sample, in terms of the measured variables should be similar to the characteristics of this type of background in the signal sample.

It needs to be emphasised that at the time of writing this monograph, there is much larger interest in the neutrino cross-section community in measuring differential cross sections than total cross sections. The main reason behind this fact is that differential cross sections are less dependent on the Monte Carlo model and the uncertainties can be reduced to much smaller values. The formula for total cross section 5.1 can be extended and used for calculating the single differential cross section as a function of the observable X for scattering neutrinos on the target:

$$\frac{d\sigma}{dX} = \frac{1}{\Phi}\frac{N-B}{\epsilon \Delta X}, \tag{5.3}$$

where ΔX is the width of the bin of the distribution of parameter X in which the measurement is done.

An important aspect in the differential cross section measurement is the choice of the binning. The decision in which observables the cross-section measurement is done and the choice of the binning depends on the interest of the community on the dependence of a cross section on a particular observable, the efficiency of the reconstruction, and the detector acceptance. In practice, the bins are usually chosen by balancing the following criteria:

1. The statistical uncertainty of the expected number of signal events in data in each analysis bin should be reasonable (below a given value).

2. The selection efficiency in each analysis bin should be relatively high and not vary too much across each bin. This requirement attempts to ensure that the uncertainty on the efficiency correction is reasonable (below a given value). If some of the bins have very low selection efficiency, the efficiency correction for a cross-section measurement is model dependent because an extrapolation from Monte Carlo simulation has to be done. For this reason, the bins with very low efficiency are not included in the final cross section measurement. Bins that are included in the measurement are called *in-phase-space (IPS) bins*. Bins that are outside of the phase space where the cross section is to be measured are referred to as *out-of-phase-space (OOPS)*.

3. The bins should have an appropriate size depending on the detector resolution. They should be fine enough so that local detector resolution effects are reasonably represented and coarse enough so that the detector resolution does not cause too large uncertainty on the results. This requirement keeps the balance between the bias to the detector response (too coarse bins) and bin-to-bin migrations within the detector resolution (too fine bins). Bin-to-bin migration is a transfer of events from one bin to another due to the smearing of kinematic properties of the particle(s) induced by the detector apparatus.

5.2 True and reconstructed kinematic phase space

This section explains the concept of the true and reconstructed kinematic phase space. The idea arises from the fact that our detectors are not perfect and measure physics quantities with a certain accuracy. As a result, the reconstructed kinematic properties of the particles are smeared with respect to the true quantities and we need a transformation to acquire true values. It is necessary to stress that both the quality of the data and the precision of the Monte Carlo simulation is fundamental in measuring neutrino cross sections.

It is essential to understand how well the detector can measure the quantities in which the differential cross section will be expressed. Let us assume that for specific selection, we are interested in measuring differential cross section by a set of observables related to the kinematics of the outgoing particles. A *kinematic phase space* or simply *phase space* is a space formed by all kinematic observables of interest. For example, one can point to the phase space formed by the momentum and angle with respect to the incoming neutrino direction of the outgoing particle in the final state. It is often called p-θ space. A point in the p-θ space represents the outgoing particle with momentum p and angle θ. Because of the detector effects (calibration, event reconstruction etc.), the particle with specific p and θ might have different values of these parameters measured by the detector. *True kinematic phase space* or simply *true space* refers to the true kinematics of a set of events. The *reconstructed phase space* or *reconstructed space* means the phase space related to the kinematics measured in the detector.

In the case of the binning for the specific differential cross-section measurement, the existence of the true and reconstructed kinematic phase space means that the binning has to be chosen for both spaces, although usually, it is identical. *True analysis binning* refers to the binning for the true kinematic phase space and *reconstructed binning* to the binning for the reconstructed phase space.

5.3 Unfolding

The analysis technique that was created to solve a problem of the transition between the true and reconstructed phase space in the cross-section measurement is called *unfolding*. Almost every analysis aims at calculating the cross section as a function of true quantities, but we only have access to the reconstructed variables. This is true for the data and the place where Monte Carlo simulation enters and helps to transform the reconstructed parameters into true parameters.

Let us assume that we would like to measure a differential cross section by some kinematic phase space, but the various ingredients make the measurement not entirely defined in either of the two (true, reconstructed) kinematic phase spaces. We want to establish a mapping between the two spaces. Using that mapping we can convert all the quantities into either the true kinematic space or the reconstructed one and then perform the differential cross section extraction. The process of creating a mapping from the reconstructed space to the true space is referred as *unfolding*. For the selected Monte Carlo events, we have access to both the true kinematics and the reconstructed ones. Using Monte Carlo the mapping from the true space to the reconstructed can be easily defined and studied. Both spaces can be divided into discrete bins; each bin corresponds to a range of values for each kinematic quantity. These bins are labeled with an integer $1, ..., Nb$. Now, the mapping can be defined as a matrix problem. Let the vector $\vec{t}$ be the vector, whose elements t_i are the number of Monte Carlo selected events with true kinematics corresponding to bin i. Similarly, let $\vec{r}$ be the vector whose elements r_j are the number of Monte Carlo selected events with reconstructed kinematics corresponding to bin j. Smearing matrix $\hat{S}$ is formulated as:

$$S_{ij} = \frac{N^{true\_in\_i}_{reco\_in\_j}}{N^{true\_in\_i}}, \tag{5.4}$$

where $N^{true\_in\_in\_i}_{reco\_in\_j}$ is the number of selected Monte Carlo events that had true kinematics corresponding to bin i and reconstructed kinematics corresponding to bin j. $N^{true\_in\_i}$ is the number of selected Monte Carlo events that had true kinematics corresponding to bin i. The elements of the smearing matrix are interpreted as the probabilities that an event that had true kinematics corresponding to bin i and was reconstructed in bin j. The smearing matrix $\hat{S}$ transforms true vector $\vec{t}$ into the reconstructed vector $\vec{r}$ in the following way:

$$\vec{r} = \hat{S}\vec{t}. \tag{5.5}$$

The smearing matrix is constructed using Monte Carlo predictions that give information about the migrations of the number of events between the bins. For the cross-section measurement, it is necessary to inverse the mapping in so that the cross section extraction can be calculated in the true space. In practice, this can be performed by trying to invert the smearing matrix and then unfold the data to the true space before extracting the cross section. The procedure of constructing the *unsmearing matrix* enabling a transfer from the reconstructed to the true space is called *unfolding*. The most straightforward method for solving this problem is a matrix inversion, where the unsmearing matrix is simply the inverted smearing matrix. The main issues in this approach are that the smearing matrix is easy to define, but small variations in the reconstructed space can lead to large variations in the true phase space, when one attempts to invert it. In experimental physics, there are always uncertainties on the data (reconstructed space). These uncertainties lead to large variations in the true space or even degeneracies, and the problem becomes less well defined (or undefined). There are also other methods of finding the unsmearing matrix like Singular Value Decomposition (SVD) [158] or TUnfold [159], but they are not discussed here.

One of the recipes for unfolding, which is also used in the T2K experiment, is the iterative Bayesian/D'Agostini unfolding [94]. This technique uses the Bayes theorem to construct an unsmearing matrix iteratively from the smearing matrix. In the first iteration, the unsmearing matrix is defined as:

$$U_{ij} = \frac{P_{eff}(r_j|t_i)P_0(t_i)}{\sum_{i=1}^{i=Nb} P(r_j|t_i)P_0(t_i)}, \tag{5.6}$$

where $P(r_j|t_i)$ is a probability of true events in bin i to be measured in bin j and can be formulated as:

$$P(r_j|t_i) = \frac{N_{ji}}{t_i}. \tag{5.7}$$

N_{ji} is the number true events in bin i measured in bin j. $P_{eff}(r_j|t_i)$ is normalized as:

$$P_{eff}(r_j|t_i) = \frac{\frac{N_{ji}}{t_i}}{\sum_{j=1}^{j=Nb} \frac{N_{ji}}{t_i}}, \tag{5.8}$$

$P_0(t_i)$ is a prior, which is defined as the predicted number of events in bin i:

$$P_0(t_i) = \frac{t_i}{\sum_{i=1}^{i=Nb} t_i} \tag{5.9}$$

The unfolded spectrum $\vec{t'}$ can be written as:

$$t_i^{'} = \sum_{j=1}^{j=Nb} U_{ij} r_j^{data}. \tag{5.10}$$

where r_j^{data} is the number of events measured in bin j in data and U_{ij} is given by Eq 5.6. After each iteration $P_0(t_i)$ is updated with the posterior of the previous iteration.

Finally, the likelihood fitting method might be used to address the problem of unfolding. The likelihood fitting is explained in detail in 5.4. Here, only general ideas are presented for the purpose of unfolding. The main concept behind the likelihood fitting is that various parameters from Monte Carlo are allowed to vary within defined constraints. The Monte Carlo, which is varied, is then compared to the signal in data until a set of parameters that allows the Monte Carlo to agree maximally with the data is found. This set of parameters is often called *best-fit* or *best-fit parameters*. In the next step, best-fit parameters are used to extract a cross section. To address the unfolding in the likelihood fitting approach, the parameters to fit are defined as the number of signal events in each true bin (e.g., true momentum bin) along with the neutrino interactions model parameters. The MC is then varied in the true kinematic space and *smeared* to the reconstructed space. Next, the smeared, varied MC could be compared to the signal in data and the set of parameters that has a maximal agreement with the data could be used. In this way, the data has been effectively unfolded, and background has been subtracted so an estimate of the number of signal events in true momentum bins in the data has been obtained. This is equivalent to the $N - B$ term from 5.3. This operation was performed with the minimal assumption of the signal model and without attempting to invert or find a pseudo-inverse of the smearing matrix. Only the smearing matrix itself, which is well defined, was used. It is a general scheme showing how a likelihood fitter might be used to unfold simultaneously and subtract the backgrounds for a particular measurement.

5.4 Likelihood fitting

In this section the likelihood fitting approach to the cross-section measurement is discussed. This is currently the most common method of extracting cross section and is considered to give the most model independent results. The section presents the general ideas of how a binned likelihood fitting machinery is usually used in a cross-section extraction and provides some of the mathematical formalism of the framework.

The goal of the fitter is to extract the best estimate of the number of signal interactions (also called *event rates*) in each true analysis bin by re-weighting the input Monte Carlo (MC) event rates in each true analysis bin. The event rates estimated by the fitter are used later to calculate the cross section using the formula from Eq. 5.3. Re-weighting refers to the operation of multiplying by weight, which is a number that can change in each iteration of the procedure.

$$N_j^{sig} = c_j N_j^{sig,MC}. \tag{5.11}$$

In the equation above, N_j^{sig} is the estimate of the number of signal events in data in true analysis signal, MC bin j. The c_j factors that are the main free parameters of the fit and are treated as the weights. $N_j^{sig,MC}$ is the number of signal events in the true analysis bin j in Monte Carlo. In the data, we select both signal and background and the number of signal and background events N_j in true bin j is:

$$N_j = c_j N_j^{sig,MC} + \sum_k^{bgtypes} N_j^{bgk,MC}. \tag{5.12}$$

In the term on the right, the summation is done for all background types k and $N_j^{bgk,MC}$ refers to the number of background interactions of the type k in the true analysis bin j in Monte Carlo.

It was explained in 5.3 that, in order to get from the true kinematic space to the reconstructed kinematic space, we use the smearing matrix previously defined as S_{ij} in Eq. (5.4). To acquire the number of signal and background events in the reconstructed bin i, we use Eq. (5.12) and perform a sum over all true bins j:

$$N_i = \sum_j^{bins} N_j = \sum_j^{bins} (c_j N_j^{sig,MC} + \sum_k^{bgtypes} N_j^{bgk,MC}) S_{ij} \tag{5.13}$$

The c_j parameters are acquired using the data by minimizing the following likelihood function:

$$\chi^2_{stat} = \sum_i^{bins} 2(N_i - N_i^{obs} + N_i^{obs} ln \frac{N_i^{obs}}{N_i}) \tag{5.14}$$

Where N_i^{obs} is the observed number of events in data in the reconstructed bin i. In order to include the systematic uncertainties in the fit, the additional term is added to the χ^2_{stat} and overall likelihood looks as follows:

$$\chi^2 = \chi^2_{stat} + \chi^2_{sys}, \tag{5.15}$$

where χ^2_{sys} is the sum of contributions from all sources of systematic errors. More details about the treatment of the systematic uncertainties can be found in 5.5.

5.4.1 Inputs

The objects that have to be provided to the likelihood fitter, often called *fitter inputs*, are as follows:

1. The set of Monte Carlo parameters to be fitted (e.g., event rates in each true bin, model parameters, etc.).

2. For each sub-set of the Monte Carlo parameters, which is relevant to a source of systematic uncertainty, a covariance matrix needs to be provided.
3. The data and Monte Carlo samples selected using a signal selection procedure.
4. Any number of control samples that are meant to constrain the sources of background in the signal selection (data and Monte Carlo samples). The idea of control samples is explained in more detail in the next subsection (5.4.2).

5.4.2 Control samples

As previously written in Sec. 5.1, the number of background interactions can be constrained using additional data and Monte Carlo samples called *control samples*, *sideband samples*, or simply *sidebands*. In the likelihood fitting approach, if the control samples are provided in addition to the signal selection, the fitting mechanism can be applied to all samples simultaneously. This procedure is often called *simultaneous fit*. It means that the fitter minimizes the sum of the χ^2 for each sample. In the best situation, one would use a selection for each N_j term in equation 5.12 and utilize the control samples for all significant backgrounds making the measurement dependent on the Monte Carlo model in a minimal way. For example, in the measurement of CC-0π cross section on lead, there would be a sample sensitive to CC-0π interactions on lead, and control samples for the significant backgrounds, such as CC-0π interactions on carbon, CC-1π, CC-Other, etc. In practice, this condition might be difficult to fulfill and in the case of more complicated backgrounds, one has to rely on the Monte Carlo model.

Another important aspect, when using control samples are the correlations. Different samples usually have correlations between them with respect to the detector systematics, as they are selected with similar sets of cuts. This is taken into account in the measurement by enlarging the covariance matrix for the detector systematic parameters to include one dimension per parameter per sample. In this way, the correlation across the samples is taken into account and covariances between each parameter in each sample are calculated.

5.4.3 Output

The most important output of the likelihood fitter is the set of best-fit parameters. With this set, we estimate the number of signal events (event rates) in each true kinematic bin defined by the fitter inputs. The estimates are then used to calculate the cross section. The output also contains the covariance matrix that has the information about the uncertainty on the number of signal events in each true bin due to each source of uncertainty that was considered. Additionally, the output covariance matrix has the information on how the event rate in each true kinematic bin is correlated to the others.

The covariance matrix can then be decomposed using Cholesky decomposition [157] to generate properly correlated variations on the number of signal events in each true kinematic bin. Using many variations (*toy experiments*), a distribution of the derived quantities from the unfolded event rate can be calculated. The mean and spread in the resulting distribution of the derived quantity (cross section, etc.) can be taken to be the central value and error for that quantity.

5.5 Systematic errors in likelihood fitting approach

The following section specifies how the systematic uncertainties are accounted for in the likelihood fitting method. This is currently the most common procedure of calculating cross section in the T2K experiment. First, it characterizes the concepts of covariance matrices and toy experiments that are vital in the calculations. Next, it describes the mechanism of modeling various contributions to the systematic uncertainties.

5.5.1 Covariance matrices and toy experiments

If $\vec{z}$ is a random vector with elements distributed with Gaussian distribution and each of the variables is simultaneously sampled N times then z_i^j is the jth measurement of the variable z_i. The sample covariance between each variable can then be calculated using the measured values:

$$\sigma_{ij}^2 = \frac{1}{N}\sum_{k=1}^{N}(z_i^k - \bar{z}_i)(z_j^k - \bar{z}_j). \tag{5.16}$$

In the above, $\bar{z}_i$ is the mean of the measurements of the variable z_i. Using the formalism of the matrices, the covariance matrix can be written as:

$$\sigma = \hat{\boldsymbol{E}}(\vec{z}(\vec{z})^T) \tag{5.17}$$

where $\hat{\boldsymbol{E}}$ is the expectation operator.

In the cross-section measurements, the procedure is usually as follows: given a covariance matrix for a set of random variables, generate properly correlated variations of those parameters N times. This is executed by calculating the Cholesky decomposition of the covariance matrix and by multiplying it by a vector of randomly distributed Gaussian numbers many times, each time with a new vector of random numbers, and each time taking the output vector as one sampling of the distributions being built. An informal way of describing the above procedure is 'throw against the covariance matrix over many toys.' A 'throw' is a multiplication of the decomposed matrix by a new vector of random numbers to get a correctly (including correlations) varied set of the x_i variables. Each varied set of the x_i variables would constitute a 'toy variation.' The Cholesky decomposition exists for any semi-positive definite matrix and can be calculated numerically.

In the simulation, many things can affect the number of events calculated using Eq. 5.13. The dominant effects can be grouped into three categories:

- Background model effects,
- Incident neutrino flux effects,
- Detector response simulation effects.

The above effects are all simulated in the Monte Carlo, but one needs to remember that the simulation is not perfect. Eq. 5.13 depends on the simulation, and the uncertainties on how these effects are simulated need to be propagated. Subsections 5.5.2-5.5.4 present how each of these sources of uncertainty is dealt with in the likelihood fit. The general approach is that the source of uncertainty is parameterized and then the propagation describing the way in which the variations of the parameters affect the relevant event rates, is performed. The minimizer (fitter) is then told how much of the variation in the parameters is allowed and how the parameters are correlated using the the covariance matrix. Next, at each iteration of the minimizing procedure, the χ^2 is calculated with varied c_i and varied systematic parameters. In consequence, in addition to the main fit parameters c_i, the systematic parameters are also fit.

5.5.2 Background model

The first source of systematic uncertainty is the background model. The cross-section measurements depend on the simulation for the background event rates. Therefore it is important to propagate the uncertainties on the background simulation to the result. This is introduced by taking a parametrization of the background physics models and varying the background distributions to study the variations on the extracted cross section due to the background model variations. The parametrization is conducted using re-weighting functions (*response functions*) that are introduced into Eq. 5.13. They allow the number of events in each bin to vary when the background parameters are varied. In consequence, Eq. 5.14 is modified by adding the so-called *penalty term*. The penalty term increases the total χ^2 when the background parameters are varied. The number of events in the reconstructed bin i is now described by the following formula:

$$N_i = \sum_j^{bins} (c_j N_j^{sig,MC} + \sum_k^{bgtypes} N_j^{bgk,MC} \prod_a^{model} w(a)_j^k) S_{ij}, \tag{5.18}$$

where $w(a)_j^k$ are the response functions that vary the event rate k in the true bin j for a background parameter a, and S_{ij} is the smearing matrix defined in Eq. 5.4. A penalty term added to the χ^2 can be written as:

$$\chi^2_{bgmodel} = (\vec{a} - \vec{a}_{prior})(V_{cov}^{model})^{-1}(\vec{a} - \vec{a}_{prior}), \tag{5.19}$$

with V_{cov}^{model} being a covariance matrix that contains the information on the uncertainties of the background parameters and their correlations. The $\vec{a}_{prior}$ is a prior value of the background parameters $\vec{a}$. The prior value here means the value provided by the nominal Monte Carlo (Monte Carlo with nominal parameters used in the experiment).

5.5.3 Flux model

Another source of systematic uncertainty is the flux model. In order to take into account this uncertainty, the following modification was introduced to the Eq. (5.18):

$$N_i = \sum_j^{bins}(c_j N_j^{sig,MC} + \sum_k^{bgtypes} N_j^{bgk,MC} \prod_a^{model} w(a)_j^k) S_{ij} \sum_n^{E_\nu} f_n^i. \tag{5.20}$$

The term $\sum_n^{E_\nu} f_n^i$ is a normalized sum over fractional variations of the incident neutrino flux binned by neutrino energy. In the case of the T2K experiment, the flux is provided in 11 neutrino energy bins. The parameters f_n^i are distributed around 1, which represents the nominal flux tuning.

Similarly to the background model, the penalty term related to the flux is added to the overall χ^2 and can be written as:

$$\chi^2_{fluxmodel} = (\vec{f} - \vec{f}_{prior})(V_{cov}^{flux})^{-1}(\vec{f} - \vec{f}_{prior}), \tag{5.21}$$

where V_{cov}^{flux} is the covariance matrix of the flux parameters, and $\vec{f}_{prior}$ is the prior value of the flux parameters $\vec{f}$. In T2K, flux covariance matrices are provided by the beam group.

5.5.4 Detector model

The last source of the systematic errors discussed in this chapter is a detector model. The detector response is modeled in the fit by introducing additional parameters that allow the event rates to vary, as shown below:

$$N_i = \sum_j^{bins}(c_j N_j^{sig,MC} + \sum_k^{bgtypes} N_j^{bgk,MC} \prod_a^{model} w(a)_j^k) S_{ij} r_i \sum_n^{E_\nu} f_n^i \tag{5.22}$$

The r_i parameters vary the events fractionally in each reconstructed bin due to the variation of each detector systematic source. The following penalty term is introduced to overall χ^2 taking into account these effects:

$$\chi^2_{detmodel} = (\vec{r} - \vec{r}_{prior})(V_{cov}^{det})^{-1}(\vec{r} - \vec{r}_{prior}), \tag{5.23}$$

where V_{cov}^{det} is the covariance matrix that incorporates the uncertainties and correlations of the detector parameters, and $\vec{r}_{prior}$ is the prior value of the detector parameters $\vec{r}$.

Chapter 6

Neutrino cross-section measurements in T2K

This chapter describes the most important cross-section results from the off-axis near detector of the T2K experiment. The results are presented on a historical and subject-oriented basis. Selected measurements are also presented in [93] and compared with the results from other experiments.

The first section describes the measurements using the initial set of the T2K neutrino mode data where the cross sections are calculated in the limited phase space of the outgoing particles. A series of total and differential cross-section measurements for neutrinos and antineutrinos as well as for various nuclear targets is presented.

The second section describes the most advanced analyses where, both the integration between the sub-detectors is at the highest level and the amount of data collected is large. These measurements are performed in the extended phase space and use more advanced techniques of cross-section extraction such as simultaneous fits for neutrinos and antineutrinos, various targets, etc.

The last section presents the impact of the T2K cross-section measurements on the progress in neutrino-nucleus interactions modelling.

6.1 Total and differential neutrino cross-section measurements

After the first period of T2K data-taking a series of papers with neutrino-nucleus cross sections in the ND280 detector has been published [97, 100, 101, 113]. First results were statistically limited and, due to not entirely completed integration of the sub-detectors, were done in the restricted phase space. Because of the limited amount of available data, the analyses most often were focused around a single number, which represented the total cross section integrated over the entire available phase space. These kinds of studies are usually called flux-averaged, total/absolute cross-section measurements.

It is necessary to mention the limitations of such an approach. The ND280 detector at its initial stage was not able to reconstruct particles in all regions of solid angle, suffering from poor reconstruction efficiency for high-angle and backward-going particles. Therefore the extrapolations to these regions, based on Monte Carlo expectations, had to be made. This approach introduces a model-dependence, which should be avoided in the cross-section measurements. The easiest way to minimize the model-dependence, in this case, is to calculate and present the cross section(s) in the region(s) of the phase space where the efficiency of selecting events does not change rapidly as a function of the measured quantities (e.g. muon momentum, muon $\cos\theta$). It is often called a measurement in the *restricted phase space* or *restricted kinematic region*.

6.1.1 Initial measurements

During the first stage of the neutrino experiment the common approach is to measure inclusive charged current (CC) cross section. It is often used as a 'standard candle' in neutrino interaction physics. Event selection for the inclusive CC analysis is usually simple because it only requires the charged lepton (muon, electron) in the final state of the interaction. Therefore the measurement is robust and can provide a precise prediction of the shape and normalization of the cross section. The momentum of the outgoing muon (electron) $p_{\mu(e)}$, as well as the cosine of the angle between the muon (electron) direction and the neutrino direction ($\cos\theta$ or $\cos\theta_{\mu(e)}$) is a common choice of the variables in which the charged current cross section is expressed.

CC inclusive measurements

The first cross section in T2K was measured for ν_μ inclusive CC interactions on carbon [97]. It was reported as a flux-averaged double-differential cross section in muon momentum and angle, and the total cross section. The procedure of selecting events that had been developed for this analysis (aka ν_μ *CC-inclusive selection*) became the standard method of selecting CC interactions for the analyses using the first portion of the T2K data and FGD1 detector (mainly hydrocarbon) as a target. The procedure is described below for reference. The events are required to have a negatively charged track starting in FGD1 fiducial volume which has the ionization energy loss per unit length (dE/dx) in TPC compatible with the muon hypothesis. The events with any activity in the upstream part of the detector are rejected (upstream veto cut). The upstream veto cut lowers the background from the interactions outside of the fiducial volume significantly but also reduces the available phase space of the measurement by cutting out the events with backward-going muons. Therefore, there is almost no efficiency for selecting interactions with high-angle and backward-going muons in the analysis as shown in Fig. 6.1. To deal with this problem, the true $cos\theta$ bins are split into a backward bin $[-1, 0]$ and more forward bins with $\cos\theta > 0$. Next, the double differential cross section is determined in the forward direction only, while the total cross-section is extrapolated into the backward direction using the Monte Carlo and Bayesian Unfolding [94].

The data used for the ν_μ CC inclusive measurement were taken in 2010 and 2011, with a total of 10.8×10^{19} POT. After the event selection, 4485 inclusive charged current interaction candidates were used in the analysis. The flux-averaged total cross section for mean neutrino energy of 0.85 GeV is shown in Fig. 6.2).

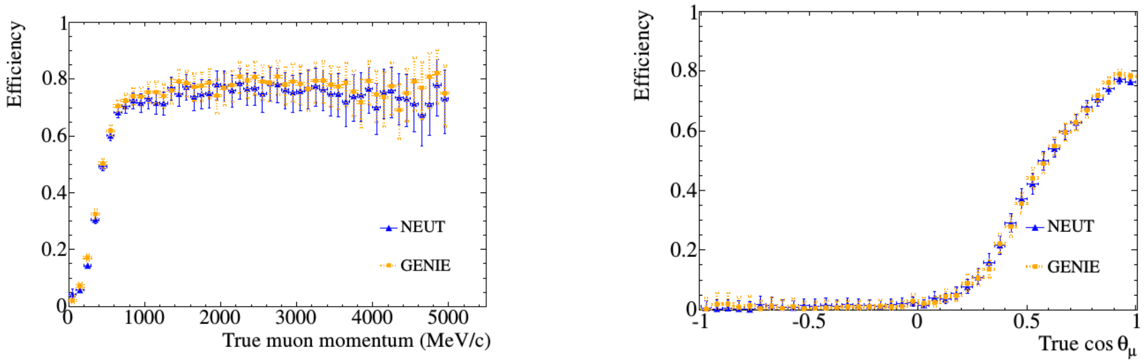

Figure 6.1: Efficiency of selecting ν_μ CC inclusive interactions in FGD1 as a function of true muon momentum (left) and true muon $\cos\theta$ (right) with statistical errors. Figure from [97].

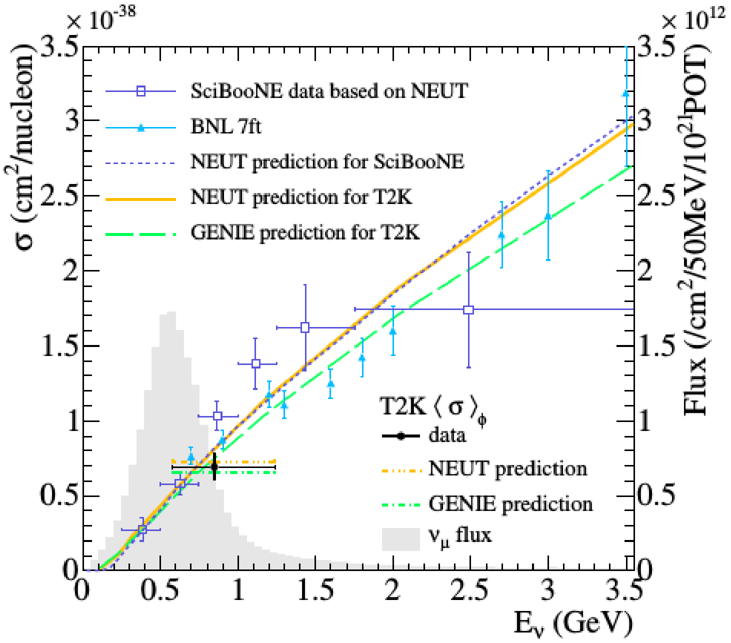

Figure 6.2: First total flux-averaged ν_μ CC inclusive cross section on carbon measured by T2K. NEUT and the GENIE predictions for the T2K and SciBooNE experiments are also shown. The T2K data point is placed at the mean energy of the T2K flux. The vertical error is the total (statistical and systematic) uncertainty, and the horizontal bar represents 68% of the flux at each side of the mean energy. The T2K flux distribution is shown in grey. The predictions for SciBooNE for a C^8H^8 target [95] are also shown and they can be compared with the mixed T2K target. The data from the BNL experiment (deuterium target) [96] is presented. Figure from [97].

Although this result agrees with the predictions of the NEUT and GENIE neutrino event generators, it has to be interpreted with care. The model dependence is introduced in the analysis by the extrapolation of the result to the regions of the phase space where the selection efficiency is low. A more model-independent way of presenting results - differential cross section as a function of the muon momentum and angle is also reported but is dominated by the statistical errors and large systematic errors for bins with high angle muons. The analysis reported in [130] and presented later in Subsec. 6.1.2 is a natural extension of the ν_μ CC inclusive measurement presented above and fixes most of the mentioned problems.

In the analysis described above, the ν_μ CC inclusive cross section on carbon at the mean energy of 0.85 GeV was measured with the ND280 detector. The on-axis near detector (INGRID) complements this study with the measurement of cross section on hydrocarbon and iron at the mean neutrino energy equal to 1.51 GeV [101]. The analysis uses runs 2-4 of the T2K data with 6.04×10^{20} POT recorded by INGRID. The measured inclusive charged current cross sections on iron and hydrocarbon averaged over the T2K on-axis flux are:

$$< \sigma_{CC}^{Fe} >_\Phi = (1.44 \pm 0.002(stat)^{+0.189}_{-0.157}(syst)) \times 10^{-38} cm^2/nucleon \tag{6.1}$$

and

$$< \sigma_{CC}^{CH} >_\Phi = (1.379 \pm 0.009(stat)^{+0.178}_{-0.147}(syst)) \times 10^{-38} cm^2/nucleon \tag{6.2}$$

respectively, and their cross-section ratio is $1.047 \pm 0.007(stat) \pm 0.035(syst)$. These results agree well with the predictions of the neutrino interaction model in NEUT and GENIE but, similarly to the previous analyses, incorporate model dependence related to the extrapolating cross section to the regions of phase space with no detector acceptance. Cross section on hydrocarbon also agrees with the results from the SciBooNE experiment within the total uncertainties as shown in Fig. 6.3.

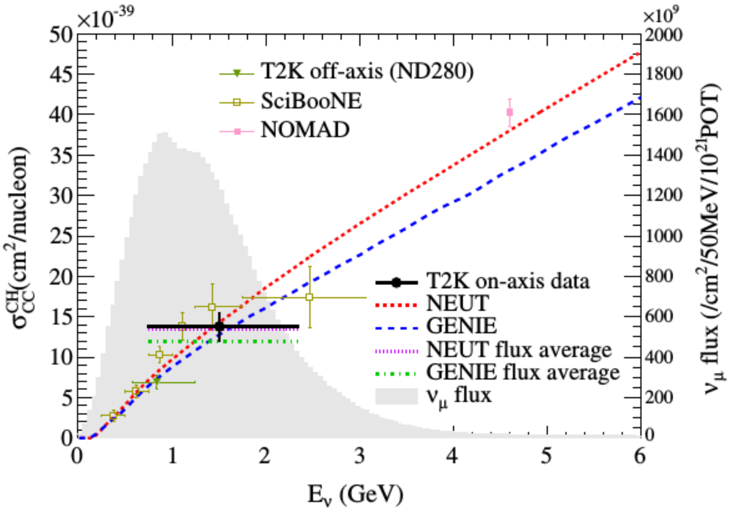

Figure 6.3: INGRID ν_μ CC inclusive cross section on hydrocarbon. T2K on-axis data point is placed at the on-axis flux mean energy. The vertical error bar represents the total (statistical and systematic) uncertainty and the horizontal bar represents 68% of the on-axis flux at each side of the mean energy. T2K off-axis, NOMAD, and SciBooNE results are also plotted [97, 102, 103]. Figure from [101].

Measuring the charged current electron neutrino cross section is very important from the point of view of accelerator neutrino experiments. To precisely determine the oscillation parameters for ν_e appearance, one has to quantify the differences between electron and muon neutrino cross sections. A first attempt to measure charged current ν_e cross section at the energies 1 GeV was made in the off-axis detector of the T2K experiment [100].

The data for this analysis corresponds to 5.90×10^{20} protons on target. The ν_e CC inclusive cross-section measurement in ND280 uses very similar event selection as in the ν_μ CC-inclusive analysis. Electron neutrino interactions are selected by applying electron particle identification criteria (TPC dE/dx) to the highest momentum negative track starting inside the fiducial volume of FGD1. Additionally, the information about the shape and the energy of the shower in ECAL is used to identify electrons. Although these cuts remove 99.9% of muon tracks and a pure sample of electrons is selected, 62.4% of events that are selected originate from photons which convert into electron-positron (e^+e^-) pairs in FGD1. Additional cuts are applied to reduce this type of background (γ background). CC inclusive ν_e interaction candidates are selected by searching for a positron and applying an invariant mass cut, vetoing on activity upstream of FGD1 (TPC1, the P0D, and ECAL). A number of 315 ν_e CC interaction candidates are selected, with the purity of 65%, predicted by Monte Carlo. Additionally, a control sample of photons from outside of FGD1 and converting into e^+e^- pairs is used to constrain γ background. As in ν_μ CC-inclusive analysis described above, the Bayesian Unfolding method is used to calculate the total flux-averaged ν_e charged current cross-section on carbon, which is shown in Fig. 6.4. The total cross-section measurement agrees with the predictions of the NEUT and GENIE generators and the data from the Gargamelle experiment. This result, similarly to the ν_μ CC inclusive cross section presented above fully relies on the Monte Carlo model in the regions of backward-going and high angle electrons. The differential cross sections as a function of electron momentum, electron scattering angle and four-momentum transfer of the interaction are also provided, despite

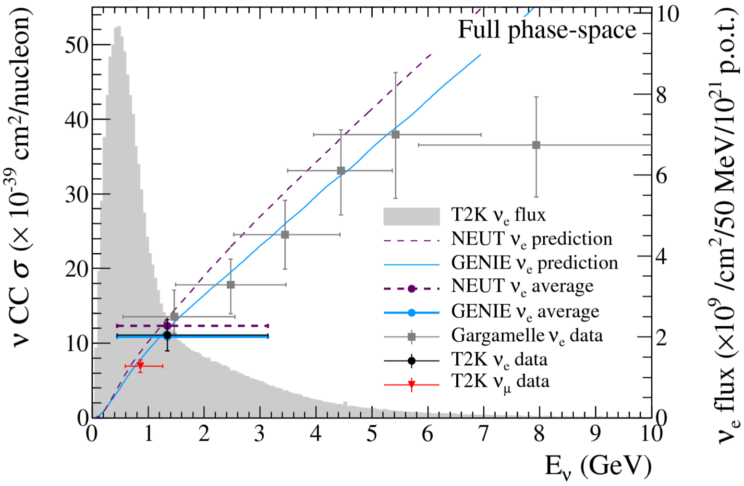

Figure 6.4: Total ν_e CC inclusive flux-averaged cross section. The T2K data point is placed at the ν_e flux mean energy. The vertical error is the total uncertainty, and the horizontal bar represents 68% of the flux on each side of the mean. The T2K flux distribution is shown in grey. The NEUT and GENIE predictions are the total ν_e CC inclusive predictions as a function of neutrino energy. The NEUT and GENIE flux-averaged predictions are also shown. The result is also compared with the T2K ν_μ CC inclusive result on carbon [97] and Gargamelle experiment data [99]. Figure from [100].

large statistical errors related to the limited amount of experimental data.

ν_μ CC coherent pion production

One of the important exclusive channels for the study of neutrino-nucleus interactions is neutrino-induced charged current coherent pion production. It is a background for the neutrino oscillation experiments and a critical component of precise understanding of pion production in neutrino interactions. A search for ν_μ charged current coherent pion production on ^{12}C was performed at the T2K experiment's ND280 detector in the restricted kinematic region of 0.18 GeV $< p_\mu$, 0.18 GeV $< p_\pi <$ 1.6 GeV, $\theta_{\mu,\pi} < 70°$ [113]. The data used in this analysis corresponds to 5.54×10^{20} protons on target. The analysis uses ν_μ CC-inclusive selection defined above with some additional cuts to select coherent pion events. Additional requirements are imposed on track multiplicity (exactly two tracks per event), vertex activity, pion identification using TPC dE/dx, and vertex reconstruction (common vertex for muon and pion).

It is necessary to stress that this analysis, as the first one in T2K, uses the vertex activity variable. Vertex activity is an energy deposited in a pre-defined volume around the vertex. This variable helps to get the information about the low energy particles that are produced in the neutrino-nucleus interaction and cannot be tracked because of their short range in the detector. In the CC coherent pion analysis of the events with vertex activity above 300 Pixel Equivalent Units (PEU) are rejected.

In many models, coherent interactions are characterised by the low transfer of four-momentum to the nucleus. This quantity is defined as [113]:

$$|t| = |(q - p_\pi)^2| = \left(\sum_{i=\mu,\pi} (E_i - p_i^L)\right)^2 + \left(\sum_{i=\mu,\pi} p_i^T\right)^2 \tag{6.3}$$

with the approximation that the energy transfer to the nucleus is negligible and p^T, p^L are the transverse and longitudinal components of the particle's momentum with respect to the neutrino beam direction. The microscopic models of coherent interactions predict clustering of events at low values of $|t|$. It is an observable that is well defined regardless of the model which is considered. As a result of the analysis an excess of CC coherent pion interactions with a significance of 2.3σ was found above the background prediction (Fig. 6.5). This fact constitutes the first experimental evidence of CC coherent pion production below 1.5 GeV. It is necessary to point out that the model of CC Coherent interactions available in NEUT at the time of preparing this analysis was very old, and the predictions were unreasonable. Therefore they are omitted in the presented plot. Shortly after the analysis was completed the NEUT model was updated.

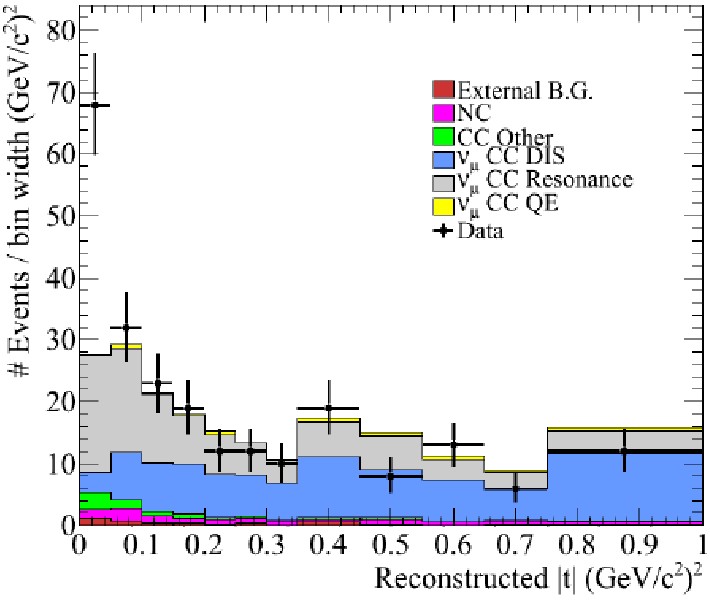

Figure 6.5: The distribution of the reconstructed four-momentum transfer to the nucleus for the ν_μ CC coherent analysis. The errors on the data are statistical. An excess at the low $|t|$ can be observed. Figure from [113].

6.1.2 Measurements on various targets

As the T2K experiment was collecting more and more data, the near detector station entered the mature stage and the second portion of the analyses was published [9, 101, 104, 106, 111, 114, 119, 120, 124, 126, 130]. These analyses are described in the following section and benefit from the larger dataset and from more accurate calibration and event reconstruction in most of the sub-detectors. Therefore more precise differential measurements on various nuclear targets could be performed.

ν_μ CC inclusive measurements

Previously described in Subsec. 6.1.1 ν_μ CC inclusive analysis on carbon in ND280 was improved and extended in [130] with 5.7×10^{20} protons on target. The standard ν_μ CC inclusive selection focused on interactions with forward-going muons; the high-angle and backward-going selections were added to the analysis. Events with high-angle muons were selected using the FGD and ECAL detectors, while backward-going muons were selected using the time of flight. The improvement in the total selection efficiency is clearly seen in Fig. 6.6. The largest number of events has been recovered for $\cos\theta_\mu < 0$, but a general improvement is also visible.

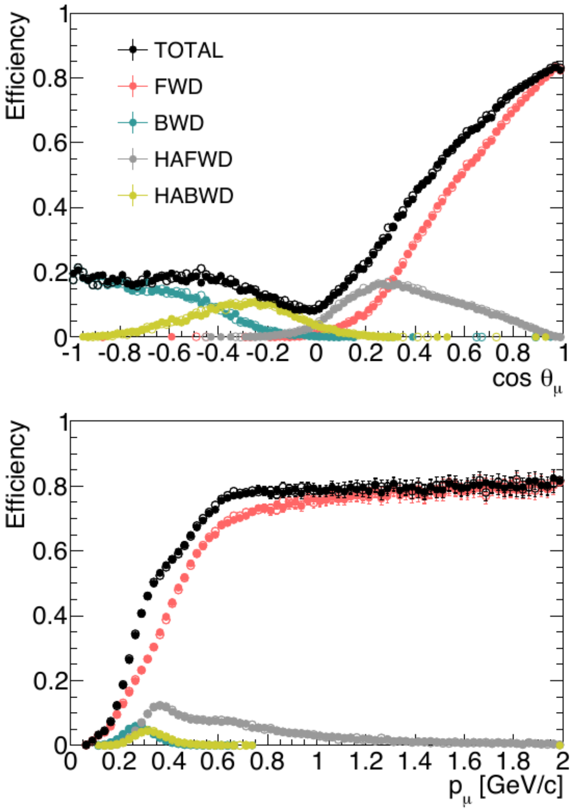

Figure 6.6: Improved (total) ν_μ CC inclusive selection efficiency used in [130] (black color) as a function of outgoing muon momentum (bottom) and $\cos\theta_\mu$. All events used in the analysis (TOTAL) are selected using: forward selection (FWD), backward selection (BWD), high-angle forward selection (HAFWD), and high-angle backward selection (HABWD). Empty dots represent efficiency estimated using NEUT and full dots efficiency estimated using GENIE. Figure from [130].

The total cross section result is compatible with predictions from the two event generators: NEUT and GENIE. It agrees well with the one reported in [97]. It has been mentioned that the ND280 detector performance varies substantially as a function of the momentum and angle of the outgoing muon. Therefore, the reported value of the total cross section must be interpreted cautiously.

The flux-integrated, double-differential cross section is computed in this analysis as a function of the outgoing muon kinematics. Two different Monte Carlo generators were used to calculate the efficiency correction and perform unfolding. Fig. 6.7 shows the results of the analysis and a comparison with the NEUT and GENIE predictions. In the low momentum and very forward regions, a small disagreement between the result and the predictions is observed for the fits with both event generators used as priors. It was demonstrated that this difference was due to the efficiency corrections being different in that region of the phase space for NEUT and GENIE.

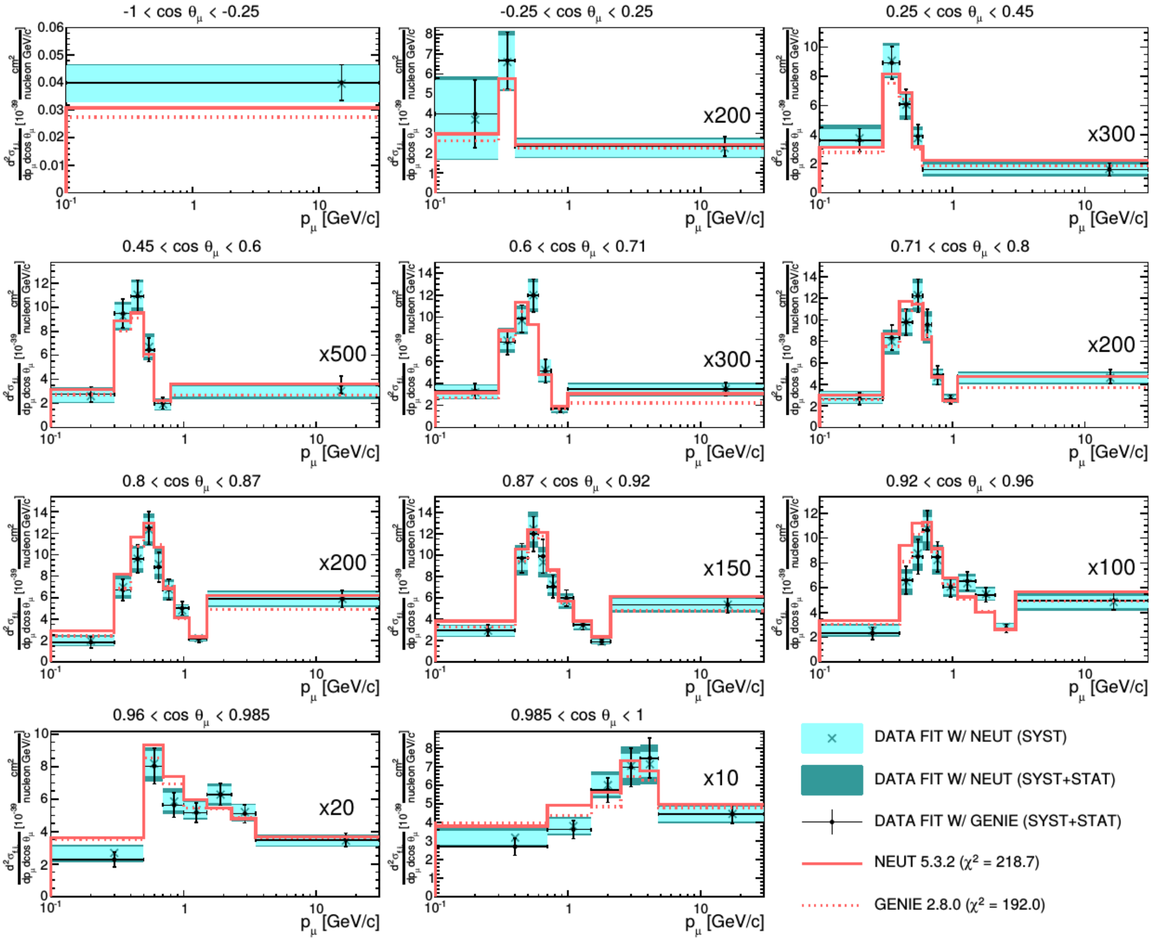

Figure 6.7: Flux-integrated double-differential ν_μ CC inclusive cross section per nucleon predicted by NEUT (solid red line) and GENIE (dashed red line). Results of the fit for data with prior from NEUT and GENIE are also shown. Figure from [130].

It is encouraging to see the results of the cross section analysis in the new regions of phase space (high angle and backward-going muons), but uncertainties are still large. In the case of forward-going muons, the binning is finer, and some structures can be identified.

The INGRID ν_μ CC inclusive measurement [101] presented in Subsec. 6.1.1 was also supplemented with the upgraded analysis based on the fact that the on-axis detector consists of 14 modules, which are spread over a range of off-axis angles from 0° to 1.1° [104]. The variation in the neutrino energy spectrum, which is a consequence of the change in off-axis angle, is used to calculate the charged current cross section on iron as a function of neutrino energy. This analysis uses data corresponding to 6.27×10^{20} protons on target. The measured cross sections at energies of 1.1, 2.0, and 3.3 GeV are shown in Fig. 6.8. The results are also consistent with the predictions from the NEUT and GENIE event generators.

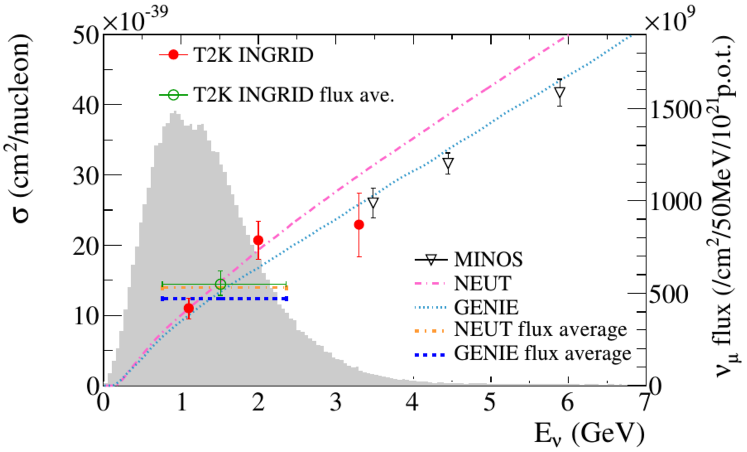

Figure 6.8: INGRID ν_μ CC inclusive cross section on iron. The measurement is done at the energies of 1.1, 2.0, and 3.3 GeV compared to the NEUT and GENIE predictions. The T2K on-axis neutrino flux is shown in grey. The result from the near detector of the MINOS experiment is also shown for comparisons [105]. Figure from [104].

Finally, the flux-integrated ν_μ charged current cross sections on water, hydrocarbon, and iron in the T2K on-axis neutrino beam with mean neutrino energy of 1.5 GeV are reported in [111]. This analysis uses data samples with the total number of protons on target equal to 5.89×10^{20}. The measured cross sections on water, hydrocarbon, and iron are:

$$\sigma_{CC}^{H_2O} = (0.840 \pm 0.010(stat)^{+0.10}_{-0.08}(syst)) \times 10^{-38} cm^2/nucleon \tag{6.4}$$

$$\sigma_{CC}^{CH} = (0.817 \pm 0.007(stat)^{+0.11}_{-0.08}(syst)) \times 10^{-38} cm^2/nucleon \tag{6.5}$$

$$\sigma_{CC}^{Fe} = (0.859 \pm 0.003(stat)^{+0.12}_{-0.10}(syst)) \times 10^{-38} cm^2/nucleon \tag{6.6}$$

respectively, for a restricted phase space of induced muons: $\theta_\mu < 45°$ and $p_\mu > 0.4 GeV/c$ in the laboratory frame. The measured cross-section ratios are shown in Fig. 6.9. These results show good agreement with the current neutrino interaction models used in the T2K oscillation analyses and have an unprecedented precision for the measurements of neutrino cross sections on water in the studied energy region.

ν_μ charged current quasi-elastic(-like) / without pions in the final state

The charged current quasi-elastic scattering channel is crucial for neutrino oscillation studies. A measurement of the ν_μ charged current quasi-elastic cross-sections on

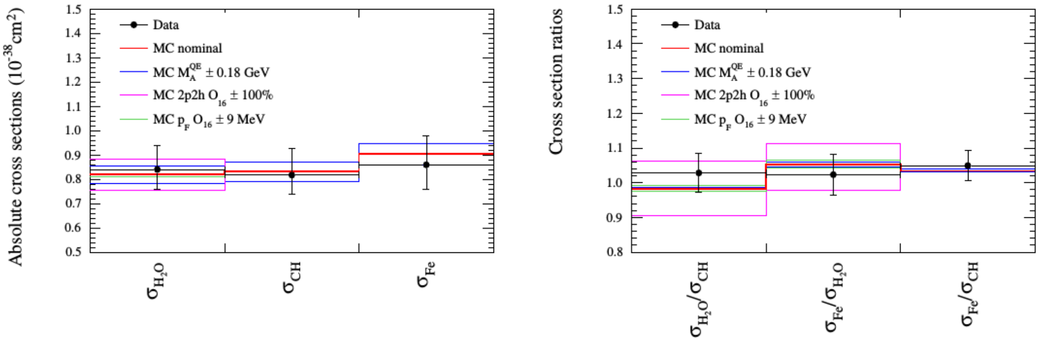

Figure 6.9: Absolute ν_μ CC inclusive cross sections and cross-section ratios with total uncertainties for water, hydrocarbon, and iron measured by the T2K on-axis detector INGRID. Theoretical predictions are shown for the NEUT generator with nominal setup and modifications applied to various model parameters. Figure from [111].

carbon in the T2K on-axis neutrino beam is reported in [106]. The total dataset for this analysis corresponds to 6.04×10^{20} POT. The signal reaction is defined as the event with one muon-like track or two tracks: muon-like and proton-like. The cross section on carbon is measured at two mean neutrino energies of 1.94 GeV and 0.93 GeV: $(11.95 \pm 0.19(stat)^{+1.82}_{-1.47}(syst)) \times 10^{-39} cm^2/neutron$, and $(10.64 \pm 0.37(stat)^{+2.03}_{-1.65}(syst) \times 10^{-38} cm^2/neutron$, respectively. The results agree well with the predictions of neutrino interaction models.

In addition, in this analysis the CCQE cross-section in each energy bin is estimated for a one-track sample, two-track sample, and combined sample, separately (Fig. 6.10). The one-track sample has an enhanced content of low energy protons from CCQE interactions while the two-track sample contains the events with reconstructed protons with kinetic energies above 100 MeV. This approach allows two different regions of the phase space to be probed. The measurement of the total

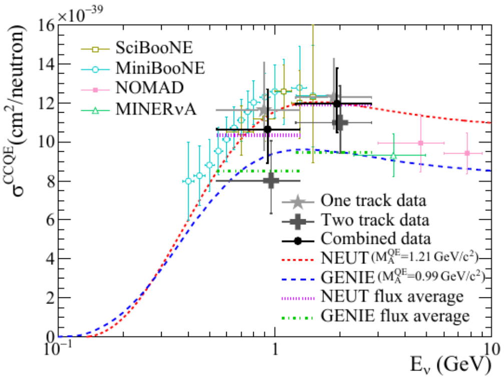

Figure 6.10: INGRID ν_μ CCQE cross section with efficiency correction predicted by the Relativistic Fermi Gas model without multi-nucleon interactions. The T2K data point is placed at the flux mean energy. The vertical error bar represents the total (statistical and systematic) uncertainty, and the horizontal bar represents 68% of the flux at each side of the mean energy. Results from SciBooNE [108], MiniBooNE [107], NOMAD [109] and MINERνA [110] are also shown. Figure from [106].

CCQE cross sections for the one- and two-track sample separately gives a taste of the significance of understanding the hadronic system in neutrino-nucleus interactions. The disagreements between the one-track and two-track results may be a key to understanding this system.

A further, important and extensive investigation of nuclear effects in neutrino scattering is done in two T2K analyses reported in [9]. The analyses use 6×10^{20} POT and probe nuclear effects by using variables related to both muon and proton kinematics in CC0π interactions. A signal reaction is defined as a charged current interaction with no final state pions and any number (analysis 1) or at least one (analysis 2) final state proton. The FGD1 detector is used as a hydrocarbon target for the measurements.

One of the analyses uses a novel approach with Single Transverse Variables (STV). For this analysis, the presence of at least one reconstructed proton is required (CC0π + Np). In the case of events with multiple protons, the properties of the most energetic one are taken into account. STV are defined by projecting lepton and proton momentum on the plane perpendicular to the neutrino direction, as shown in Fig. 6.11. When there are no nuclear effects, the proton and muon momenta are equal and opposite in this plane. The measured difference between their projections is a direct probe of nuclear effects in quasi-elastic interactions and is defined as follows:

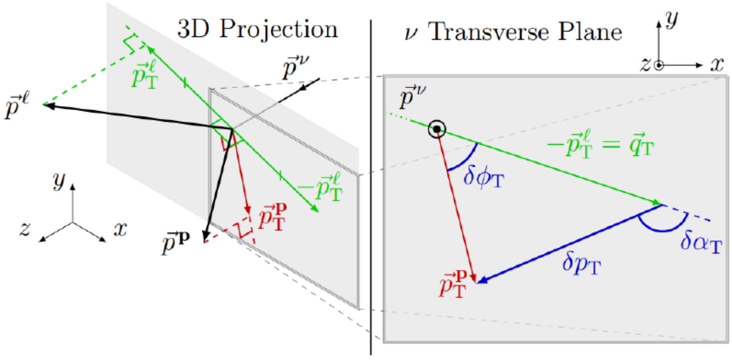

Figure 6.11: Definition of the Single Transverse Variables (STV): δp_T, $\delta\alpha_T$ and $\delta\phi_T$. The left side shows an incoming neutrino interacting and producing a lepton and a proton, whose momenta are projected onto the plane transverse to the neutrino. The right side then shows the momenta in this transverse plane and how the STV are formed from considering its imbalance. Figure from [9].

$$\delta\overrightarrow{\mathrm{p}}_T = \overrightarrow{\mathrm{p}}_T^N - \Delta\overrightarrow{\mathrm{p}}_T, \tag{6.7}$$

where $\overrightarrow{\mathrm{p}}_T^N$ is the transverse momentum of the initial state nucleon and $\Delta\overrightarrow{\mathrm{p}}_T$ is the modification due to the final state effects. The modification can be written in terms of the vector magnitude and two angles in the following way:

$$\delta p_T = |\overrightarrow{\mathrm{p}}_T^l + \overrightarrow{\mathrm{p}}_T^p| \tag{6.8}$$

$$\delta\alpha_T = \arccos\frac{-\overrightarrow{\mathrm{p}}_T^l \cdot \delta\overrightarrow{\mathrm{p}}_T}{p_T^l \delta p_T} \tag{6.9}$$

$$\delta\Phi_T = \arccos\frac{-\overrightarrow{\mathrm{p}}_T^l \cdot \overrightarrow{\mathrm{p}}_T^p}{p_T^l p_T^p} \tag{6.10}$$

where: p_T^l and p_T^p are projections of the momentum of outgoing lepton and proton in the transverse plane, respectively. In the absence of nuclear effects, δp_T and $\delta\phi_T$ vanish, while $\delta\alpha_T$ is undefined. Monte Carlo truth study shows that STV behave differently when changes are applied to quasi-elastic axial mass M_A^{QE} and different nuclear effects. Therefore these variables allow us to probe the nuclear effects that are primarily independent of the CCQE cross-section. Furthermore, different aspects of the STV spectra are associated with specific nuclear effects and allow some separation between the effects of Fermi motion and FSI. The cross-section extraction method for this study is a regularized likelihood template fit.

The second analysis reported in [9] utilizes the variables based on differences between the measured proton kinematics, and the proton kinematics inferred from the muon kinematics using the quasi-elastic hypothesis. Therefore, the variables can indicate the existence of the nuclear effects, making the impulse approximation not valid. These effects are called 'inferred kinematic imbalance' and are potentially powerful tools to test nuclear effects. The cross-section extraction method used in the second analysis is an iterative unfolding technique based on D'Agostini's method [94]. The selection for this analysis separates events without protons, with 1 proton, or with more than 1 proton in the final state above a 500 MeV momentum threshold. This allows the proton multiplicity to be measured. The minimisation of the model dependence of the measurement in efficiency corrections, background subtraction, and cross-section evaluation was a priority in both analyses. Therefore a large set of model comparisons with the results is provided. Since the prediction of proton kinematics in neutrino-interaction simulations is still poor, it is challenging to draw quantitative conclusions from the results of the two analyses. An extensive comparison with Monte Carlo predictions should enable drawing some qualitative conclusions. One of the comparisons of the Single Transverse Variable distributions and Monte Carlo predictions is described below.

The nucleon dynamics for $\delta p_T < 400MeV$, seems to be better described by Spectral Function than Fermi gas models. The agreement between data and SF predictions at $\delta p_T \sim 300MeV$ suggests that the correlations between nucleons included in SF are required. In the future, the measurements with higher statistics should reveal the nature of these correlations.
Above $\sim 400MeV$, the δp_T distribution shows that Fermi gas and SF model predictions become similar. An important note is that the implementation of the SF model in this region is not fully consistent because it uses two particles - two holes contribution calculated for a Local Fermi Gas model. The comparison of the result with the SF model without a 2p2h clearly shows that an additional contribution is needed for the large values of δp_T and $\delta\phi_T$. The size of this contribution is consistent with the one predicted by the 2p2h model. The RFG and LFG models agree in the aspect of the total cross section and the $\delta\alpha_T$ distribution, which can be interpreted as the direction of the initial nucleon momentum p_N. There is a significant difference in the shape of predictions of the Fermi gas and SF models for $\delta\alpha_T$ distribution. The discrepancy at low $\delta\alpha_T$ in NuWro predictions between Fermi gas models and the data result is caused by including Random Phase Approximation (Fig. 6.12). It appears that without RPA, the shapes would be consistent. Again, the requirement for a 2p2h contribution is visible in the hard tail of δp_T, $\delta\phi_T$, and $|\Delta\overrightarrow{\mathrm{p}}_p|$ distribu-

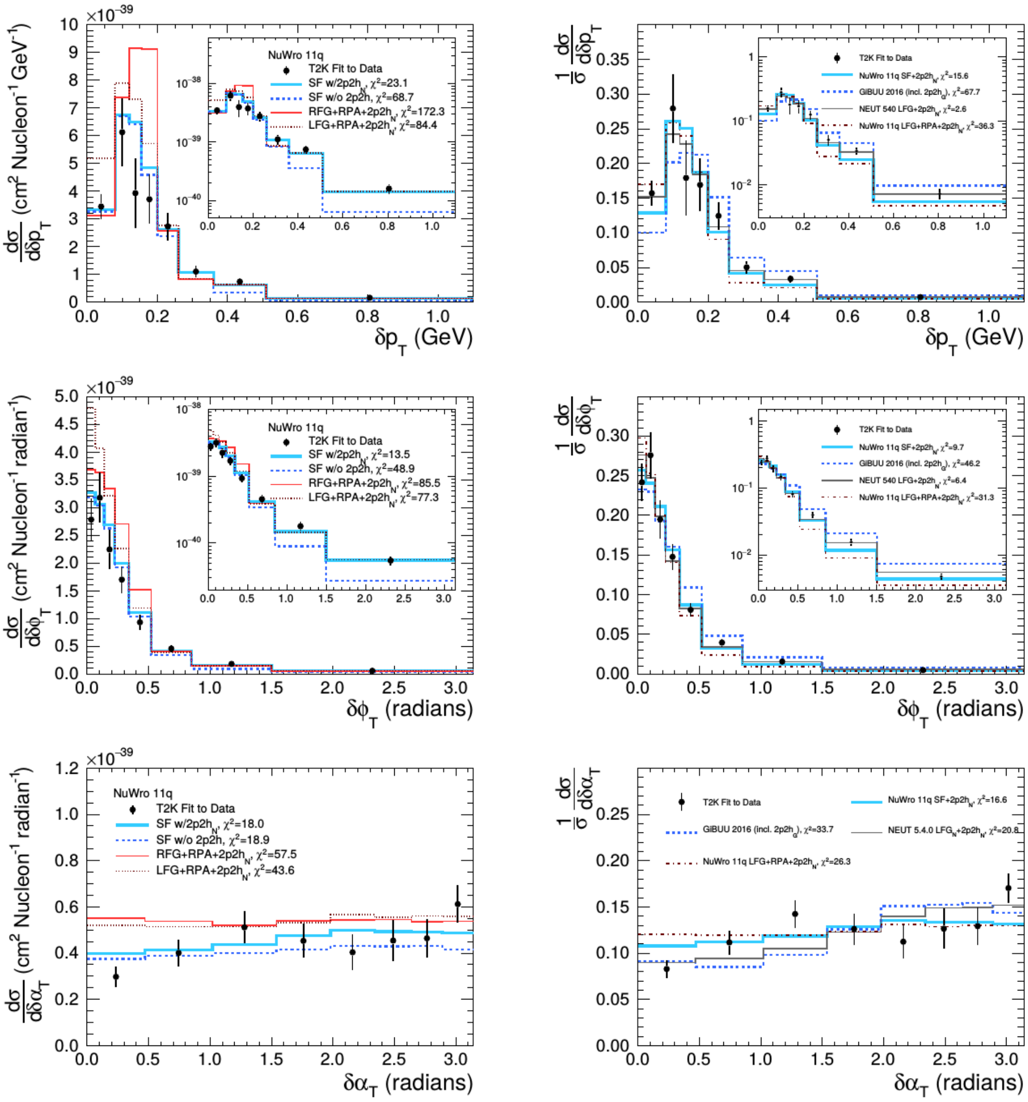

Figure 6.12: ν_μ CC0pi cross section as a function of single transverse variables compared to different initial state models in the NuWro 11q simulation (left); shape-only predictions from NuWro 11q and GiBUU 2016 (right). Although it is not shown, the NEUT 5.3.2.2 SF prediction has an almost identical shape to the NuWro 11q SF prediction. The NuWro 11q RFG+RPA prediction shown is similar to the NEUT model used as a starting point for T2K's oscillation analyses. $2p2h_N$ indicates the Nieves et al. model of Ref. [121] as implemented in NEUT or NuWro, while $2p2h_G$ indicates an extrapolation from electron-scattering data implemented in the GiBUU 2016 simulation [122]. More details of these models can be found in [9]. The inlays show the same comparisons on a logarithmic scale. Figure from [9].

tions. Two particles-two holes contribution is required for most of the FSI models available in the simulations.

The CC0π interactions with no pions were also investigated in [124]. This time an important aspect of comparing the cross sections on water and carbon (hydrocarbon) has been raised. The ν_μ $CC0\pi$ cross section on water is measured using the interactions in the Pi-Zero (PØD) sub-detector of ND280 with the data of 5.52×10^{20} protons on the target. A selection of charged current events occurring within the PØD with the charged tracks entering and identified by the TPC was used. The dataset is separated into two sets: first - the time period when the PØD is filled with water and the second - when it is empty. A water-subtraction method provides a way to select the ν_μ interactions only on water. The resulting ν_μ CC0π cross section as a function of muon momentum for various slices of the cosine of the muon angle is shown in Fig. 6.13. The result complements the previous T2K CC0π cross-

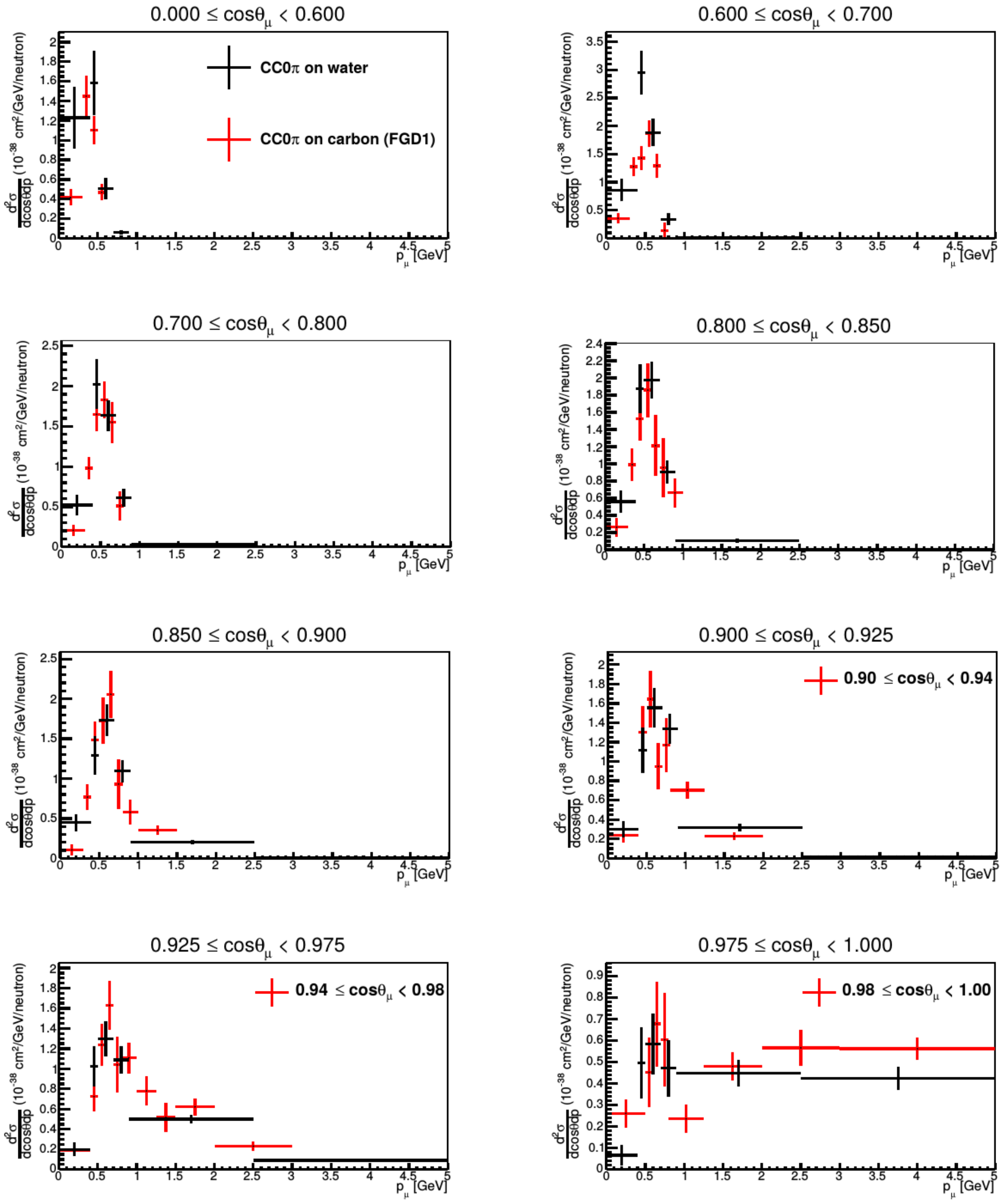

Figure 6.13: ν_μ CC0π cross section on water vs. carbon. Results for carbon are taken from [120]. The error bars shown include all sources of uncertainty except for the flux. In the regions where $\cos\theta_\mu$ slices are different between the water and hydrocarbon results, the bin edges are noted in the legend. Figure from [124].

section measurements and shows good agreement with a T2K's double-differential cross-section result on hydrocarbon reported in [120] except for a few low momentum bins in the high-angle region. In these bins, the CC0π cross section on water is larger than the hydrocarbon cross section. It also appears that the NEUT prediction is favored over GENIE, except for the angular regions with $0.7 < \cos\theta_\mu < 0.85$.

ν_μ charged current single pion production

Another channel of neutrino-nucleus interactions essential for current and upcoming neutrino oscillation experiments is single charged pion production induced by charged current interactions of muon neutrinos (CC1π^+). In the regime of neutrinos with an energy lower than a few GeV, it has the largest cross section after the CC quasi-elastic process and constitutes a background for the ν_μ disappearance measurement when the charged pion is not observed. Observable (defined using the particles in the final state) single pion production is sensitive mainly to resonant processes but also to non-resonant contributions as well as coherent pion production. Moreover, in the case of nuclear targets, there are contributions from multi-nucleon and final-state interactions. The correct modeling of these effects is crucial in reducing the systematic uncertainties in neutrino oscillation experiments.

First, the measurement of the ν_μ $CC1\pi^+$ cross section on hydrocarbon is described [114]. This analysis uses the dataset of 5.56×10^{20} POT and employs an advanced approach to the measured cross section. The $CC1\pi^+$ signal is defined by requiring a negative muon, a positive pion and any number of nucleons in the final state. The cross section is measured using the Bayesian unfolding method. The results are presented in single or double differential cross section for a set of various kinematic variables of interest for single pion production studies. A series of model-independent measurements, as well as model-dependent ones, are presented in the framework of this analysis. A total cross-section value, obtained without any phase-space restrictions, is measured to be: $(11.76 \pm 0.44(stat) \pm 2.39(syst)) \times 10^{-40} \frac{cm^2}{nucleon}$. To be consistent with the previous statements, the total cross section needs to be interpreted with care and is only reported here for reference.

Fig. 6.14 shows the flux-integrated cross section as a function of pion momentum $d\sigma/dp_\pi$, measured in the restricted phase space of muon and pion kinematics: $\cos\theta_\mu > 0.2, p_\mu > 0.2$ GeV/c and $\cos\theta_\pi > 0.2$. One can observe that both generators over-predict the data in the entire momentum range. NEUT shows a good agreement above 0.7 GeV/c. A similar model excess at low momentum pions was observed in MiniBooNE [115] and MINERνA [116–118].

The flux-integrated cross section as a function of pion angle $d\sigma/d\theta_\pi$ is also shown in Fig. 6.14. The cross section is measured in the restricted phase space $\cos\theta_\mu > 0.2$, $p_\mu > 0.2GeV/c$ for the muon and $\cos\theta_\pi > 0$, $p_\pi > 0.2GeV$ for the pion. Consistently with the $d\sigma/dp_\pi$ cross section above, the measured differential cross section as a function of the pion angle also shows a disagreement with the predictions.

The shape of the distribution of the $d\sigma/dQ^2$ cross section as predicted by Monte Carlo generators shows large discrepancies with data all over the available Q^2 space, as shown in Fig. 6.14. The discrepancies are more pronounced for $Q^2 \leq 0.3GeV^2/c^2$, and the model excess might indicate deficiencies in the nuclear model. In addition, the following conclusions from the differential cross-section measurements can be drawn:

1. A good description of the data for the muon kinematics observables. All pions, including the low energy ones identified by Michel electron tagging, are used in these distributions.

2. In general, the models predict larger cross sections for the angular pion ob-

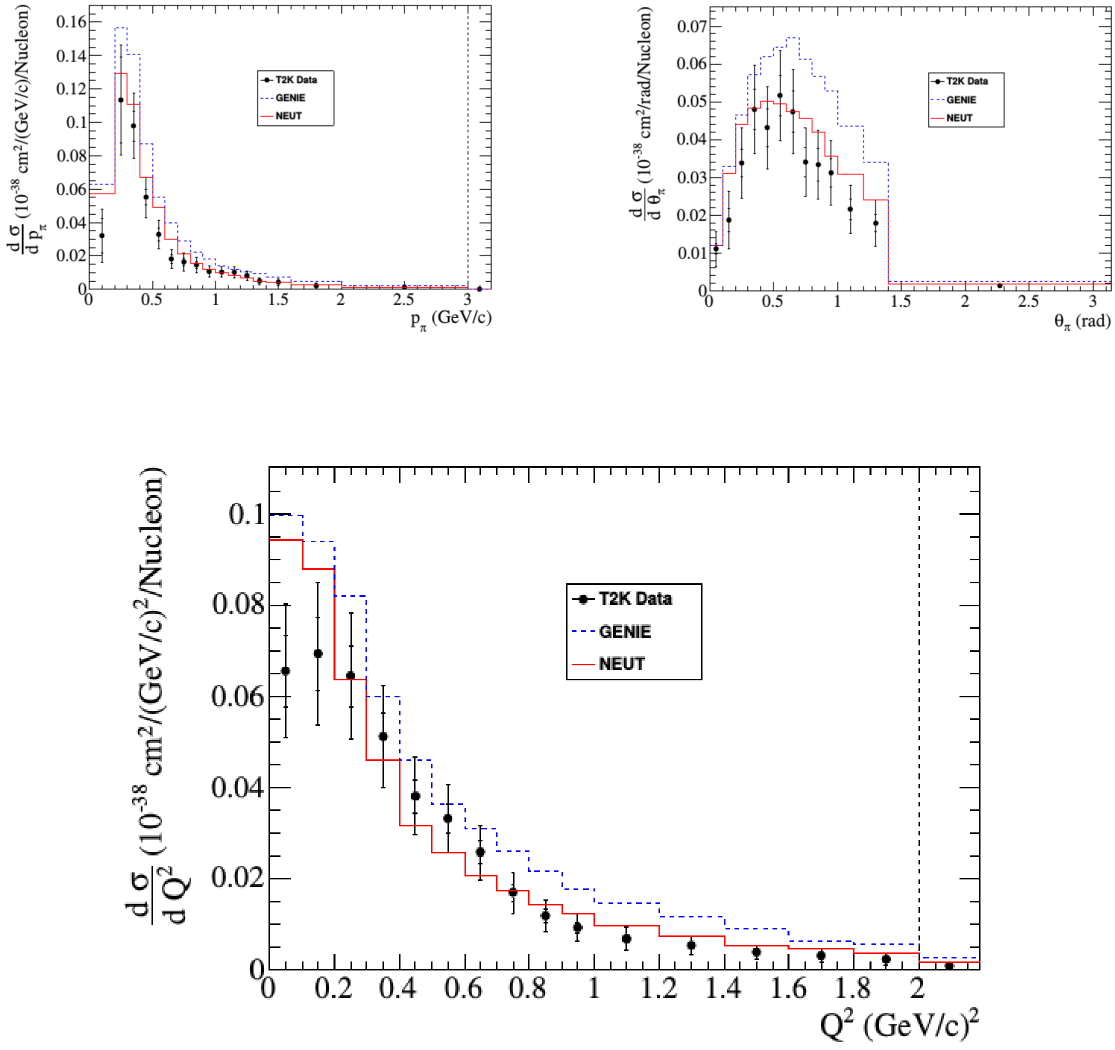

Figure 6.14: $CC1\pi^+$ cross section as a function of pion momentum (top-left), pion angle (top-right) and square of the energy transfer (bottom). The inner (outer) bars show statistical (total) errors. NEUT and GENIE predictions are also shown. Figure from [114].

servables. The discrepancy is more pronounced for low momentum pions and seems independent of the value of the θ_π and $\theta_{\mu\pi}$ angles.

The second measurement of the ν_μ $CC1\pi^+$ cross-section in ND280 uses water as a target for neutrino interactions [119]. The analysis also utilizes data of 5.6×10^{20} protons on target. The signal reaction for the analysis is the ν_μ $CC1\pi^+$ interaction in the water layers of the FGD2 detector. The analysis uses the Bayesian unfolding method with background subtraction and two selected background samples to constrain the main backgrounds. The background samples contain the interactions on carbon and deep inelastic scattering. The cross-section is unfolded in the restricted phase space of $cos\theta_\mu > 0.3$ and $cos\theta_\pi > 0.4$. The single differential cross-section is evaluated for the muon and pion kinematics and for the muon-pion angle. The results are, in general, compatible with the NEUT predictions with a small suppression at $0.3 < p_\pi < 0.8\ GeV$, $cos\theta_\pi > 0.9$ and $E_\nu > 3GeV$ (Fig. 6.15). The

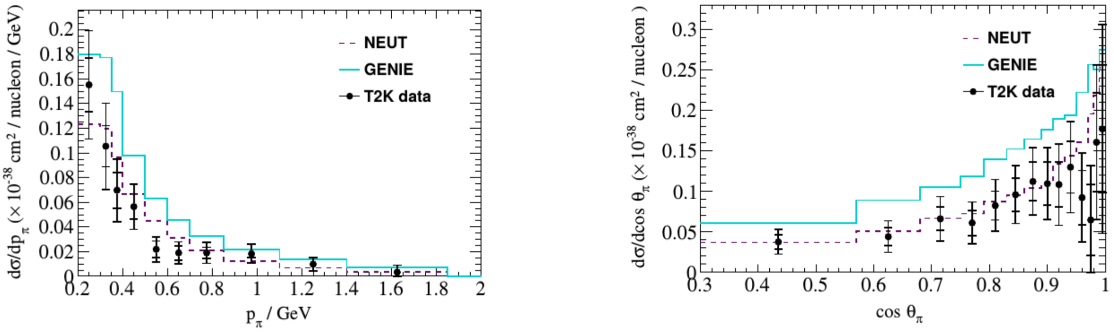

Figure 6.15: ν_μ CC1π^+ cross section on water as a function of pion momentum (left) and pion $\cos\theta$ (right). The cross section is measured in the reduced phase space of $p_{\pi^+} > 200\ MeV/c$, $p_\mu > 200\ MeV/c$, $\cos(\theta_{\pi^+}) > 0.3$ and $\cos(\theta_\mu) > 0.3$. The inner (outer) error bars show the statistical (total) uncertainty of the data. The dashed (solid) line shows the NEUT, version 5.1.4.2, (GENIE, version 2.6.4) prediction. Figure from [119].

observed discrepancy might be related to the model of CC coherent interactions used in NEUT. As it was shown in [113], NEUT greatly overestimates the number of coherent interactions at low pion energies. The GENIE predictions reproduce well the shapes of the distributions but over-estimate the cross-section normalization.

Neutral-current single photon production

The last result presented in this section is a measurement of the neutrino neutral-current induced single photon production (NC1γ) in ND280 [126]. NC1γ is a rare process that is important for accelerator neutrino experiments, including T2K because it is one of the backgrounds for $\nu_e(\bar{\nu}_e)$ appearance studies. The process also has significant theoretical uncertainties. The first search for $NC1\gamma$ below 1 GeV using the T2K ND280 off-axis near detector is performed with 5.738×10^{20} POT. The event selection for this analysis was developed for the ν_e CC measurements in ND280 [100], where photons constitute a major background. A photon sample was made to study this background distribution. In the $NC1\gamma$ analysis the photon sample is used to search for neutrino neutral-current single photon interactions and 95% purity is achieved from the neutrino mode data of 5.738×10^{20} POT. Single photon kinematics from electron-positron pairs is reconstructed in the analysis. No positive evidence of neutral-current induced single photon production in the sample is found. The upper limit on the cross-section for this process is set at $0.114 \times 10^{-38} cm^2 (90\% C.L.)$ per nucleon, using the J-PARC off-axis neutrino beam with an average energy of $< E_\nu > \sim 0.6\ GeV$. This is the first limit on this process below 1 GeV, which is important for current and future oscillation experiments looking for electron neutrino appearance oscillations. It is necessary to stress two drawbacks of this analysis. The study relies on external data to understand $NC\pi^0$ production rate uncertainties. The solution for this issue would be a simultaneous measurement of $NC1\gamma$ and π^0s similarly as it is performed for ν_es and photons in [7] presented in Subsec. 6.1.3. In this way, the systematic uncertainties of π^0 production rate can be better constrained. Second, the analysis relies on the simulation to estimate the external photon background. This model-dependence could be re-

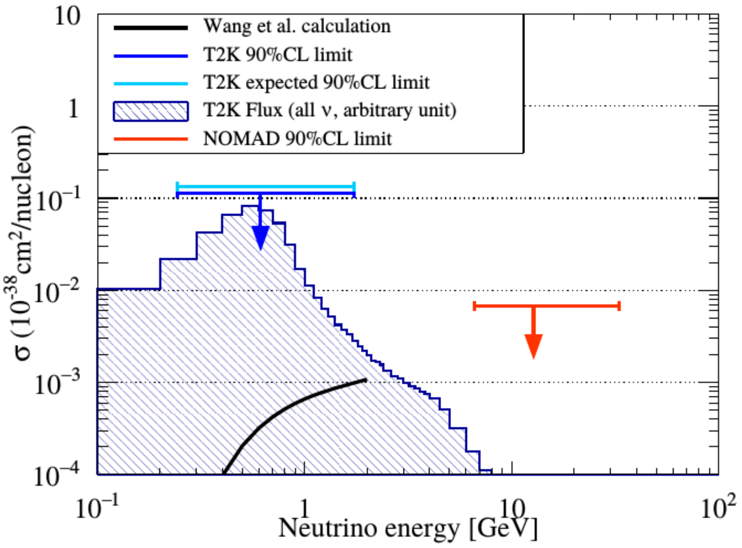

Figure 6.16: Neutral current single photon production cross-section limits. The cyan line shows the 90% C.L. sensitivity from the simulation, and the blue line shows the 90% C.L. limit from the analysis. Both are averaged over off-axis neutrino flux. The blue histogram shows the distribution (arbitrary units) of the neutrino mode muon neutrino flux used by this analysis. The results are compared with one of the recent calculations (black curve) [129]. Note that, the model is terminated at the neutrino energy = 2.0 GeV. The result is also compared with the results from NOMAD (red line) [127, 128]. Figure from [126].

solved by an internal measurement of such a background if the detector had a larger active veto region or reduced and if the detector had less dead material between the veto and the fiducial volume. This improvement can still be made with the current ND280 detector by using the PØD where larger fiducial volume than in FGDs can reduce the external backgrounds.

6.1.3 Comparison of neutrino and antineutrino cross sections

This section describes the analyses that make use of the antineutrino mode data in T2K. The comparisons of neutrino and antineutrino cross sections are very important for the search of CP violation in T2K where the neutrino and antineutrino oscillation probabilities are employed. The measurements of antineutrino cross sections contribute significantly to better understanding and modelling of antineutrino-nucleus interactions.

Charged-current inclusive cross sections

A measurement of the muon neutrino charged current inclusive cross section and the first measurements of the $\bar{\nu}_\mu$ CC inclusive cross section and their ratio $R\frac{\sigma(\bar{\nu}}{\sigma(\nu)})$ at (anti)neutrino energies below 1.5 GeV are reported in [112]. The study uses neutrino mode data with 16.24×10^{19} protons on target and antineutrino mode data with 4.3×10^{19} POT. The total cross sections averaged over the T2K flux in the restricted phase space of $\theta_\mu < 32^\circ$ and $p_\mu > 500\ MeV/c$ are determined in this analysis. The analysis uses event selection based on the $\mu^{-/+}$ tracks starting in the PØD detector fiducial volume and entering TPC, where the charge reconstruction and dE/dx measurement can be utilized. The target for $\nu_\mu/\bar{\nu}_\mu$ CC-inclusive interactions in the PØD is a mixture of carbon, oxygen, hydrogen, and copper. The results are as follows:

$$\sigma(\bar{\nu}) = (0.900 \pm 0.029(stat) \pm 0.088(syst) \times 10^{-39} cm^2/nucleon, \tag{6.11}$$

$$\sigma(\nu) = 2.41 \pm 0.022(stat) \pm 0.231(syst) \times 10^{-39} cm^2/nucleon, \tag{6.12}$$

$$R(\frac{\sigma(\bar{\nu})}{\sigma(\nu)}) = 0.373 \pm 0.012(stat) \pm 0.015(syst). \tag{6.13}$$

The $\bar{\nu}_\mu$ CC inclusive cross section and the ratio $R(\frac{\sigma(\bar{\nu})}{\sigma(\nu)})$ are the first published measurements at ν_μ and $\bar{\nu}_\mu$ flux energies below 1.5 GeV. It can be seen that the large portion of the uncertainties cancels out in the cross-section ratio. These results were compared to predictions of four different 1p1h and 2p2h model combinations. No quantitative conclusions were drawn because of the large uncertainties on the measurement. The extensions of the analysis using a larger amount of experimental data should be valuable for model discrimination in the future.

Charged-current with no pions in the final state

Next, a measurement of the $\bar{\nu}_\mu$ CC double differential cross section on water without pions in the final state averaged over the T2K antineutrino beam flux [131] is presented. The analysis uses a large sample of T2K antineutrino mode data: 6.3×10^{20} POT. The data are divided into two subsets, with the PØD detector being filled with water (water-in) and empty (water-out). The measurement is done in momentum-$\cos\theta$ bins and employs a maximum likelihood fit with unfolding to correct for bin-to-bin smearing related to the detector effects. An interesting feature of the fit is that both the CC0π event rates on water (dominating in the water-in sample) and CC0π event rates on non-water (water-out sample) in 19 muon $\cos\theta$ bins in seven momentum ranges are fitted simultaneously. The fit is also performed without regularization and with regularization to reduce bin to bin fluctuations that are possible when using unfolding methods. The regularized and unregularized results appeared to be nearly identical. The comparisons with the NEUT, GENIE, and NuWro models reveal the lowest χ^2 for NuWro, where nearly all of the measured data bins agreed within a standard deviation of the NuWro predictions (Fig. 6.17). In summary, the first measurement of antineutrino CC0π cross section on water is reported in [131]. The results of the analysis agree with predictions by GENIE, NuWro and NEUT, which is extensively used in modeling of the antineutrino interactions at the Super-Kamiokande far detector.

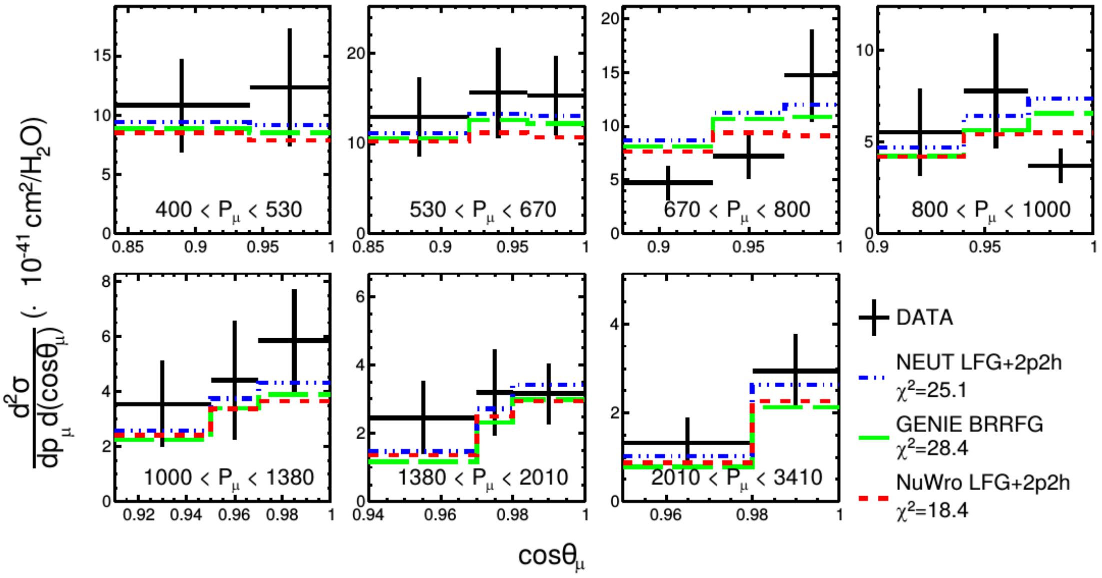

Figure 6.17: Unregularized $\bar{\nu}_\mu$ CC0π cross section on water as a function of 19 $\cos\theta$ bins in seven different momentum ranges with comparisons to the NEUT(ver.5.41), GENIE(ver.2.12.10), and NuWro(ver.18.02.1) predictions. Figure from [131].

Finally, an extensive study of muon neutrino and antineutrino CC0π interactions is performed in [132]. The paper presents the first combined measurement of the double-differential muon neutrino and antineutrino CC0π cross sections on hydrocarbon in ND280. The data analyzed in this work comprise 5.8×10^{20} and 6.3×10^{20} POT in neutrino and antineutrino mode, respectively. In the analysis,

the reconstruction of the particle time of flight was included in the selection of backward-going and high-angle tracks. Thank to this reconstruction the full phase space could be explored with better efficiency than in the previously reported T2K measurements [120]. Moreover, the joint neutrino-antineutrino fit enabled a full treatment of the correlations between the neutrino and antineutrino samples.
Using the measured CC0π neutrino and antineutrino cross sections, the sum, difference, and asymmetry were calculated for a better understanding of the nuclear effects. The analysis contains many comparisons of the result with predictions from various Monte Carlo generators and theoretical models. One of the comparisons related to the presence of multi-nucleon interactions is described below.

To estimate the sensitivity to the two particles-two holes process, the measured cross sections, and their combinations are compared to NEUT with the Local Fermi Gas model (LFG) with and without the addition of 2p2h. The sum of the cross sections is shown in Fig. 6.18. The χ^2 between the analysis result and Monte Carlo predictions and the shape-only χ^2 were calculated, but they showed no sensitivity to discriminate between the models. Some conclusions can be drawn by focusing on specific angular bins. In the high-angle and intermediate bins ($0.2 < \cos\theta_\mu < 0.94$), the presence of 2p2h interactions is preferred both for neutrinos and antineutrinos, similarly to [120] and other analyses. To confirm that, the χ^2 in each angular bin was computed. As an example, in the angular bin $0.6 < \cos\theta_\mu < 0.7$ the χ^2 is 0.8 and 2.4 with and without 2p2h, respectively. On the other hand, one can observe that NEUT with 2p2h overestimates the cross section in the forward region ($\cos\theta_\mu > 0.94$) below 1 GeV. The effect is visible both for neutrinos and antineutrinos. This may suggest incorrect predictions of the initial state models in this region where the energy transfer to the nucleus is small, and the treatment of various nuclear effects is very important.

More detailed studies that include the comparisons of the result with various 2p2h and 1p1h models and their different implementations (i.e., the implementations of the binding energy) and comparisons between the Local Fermi Gas and Spectral Function models are reported in this analysis. This extensive set of comparisons makes the study very useful for the development and precise tuning of the neutrino interaction generators. The important outcome of the analysis is that none of the models can describe the full phase space of the neutrino and antineutrino $CC0\pi$ cross section. Understanding of this mis-modeling may be crucial for the next generation of neutrino oscillation experiments. The sensitivity to solve this problem can be improved with more statistics and reduced systematic uncertainties, and a better understanding of the differences in the approximations built into implementations of the models in different generators.

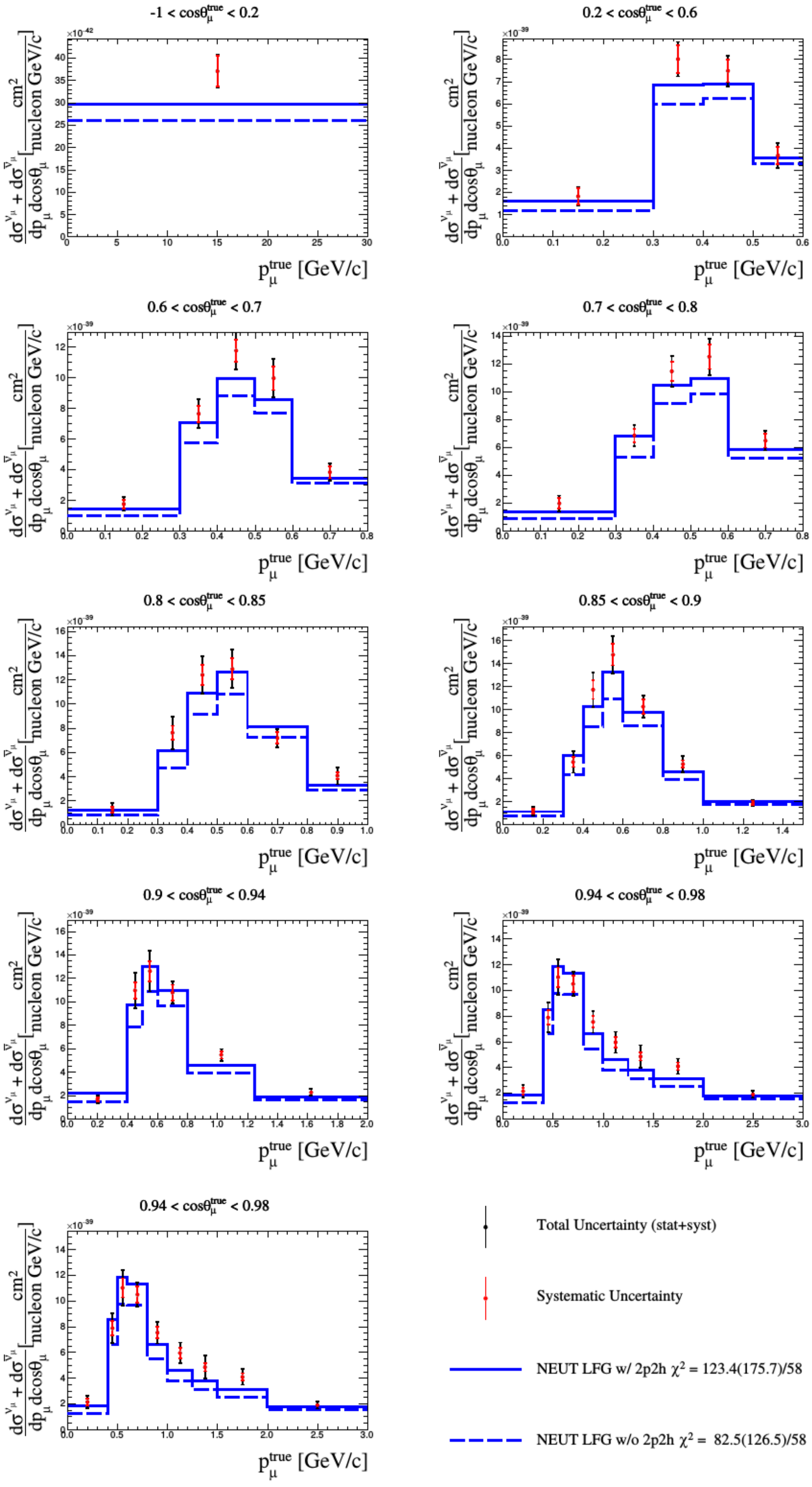

Figure 6.18: CC0π ν_μ-$\bar{\nu}_\mu$ cross-section sum in bins of true muon kinematics with systematic uncertainty (red bars) and total (stat.+syst.) uncertainty (black bars). The results are compared with the NEUT version 5.4.1, which uses an LFG+RPA model, with (solid line) and without (dashed line) 2p2h. The full and shape-only (in parenthesis) χ^2 are reported. Figure from [132].

Electron (anti)neutrino charged current inclusive cross sections

The last analysis described in this chapter is a charged current electron (anti)neutrino cross section measurement at the off-axis near detector of the T2K experiment [7]. This is the extension of the ν_e CC cross-section study [100] reported in Subsec. 6.1.1. Here, electron-like neutrino and antineutrino interactions are selected in the T2K off-axis near detector ND280, using both Forward Horn Current (FHC) and Reversed Horn Current (RHC) modes. For FHC and RHC, 11.92×10^{20} protons-on-target (POT) and 6.29×10^{20} POT are analysed, respectively.
The analysis describes the first charged current ν_e cross-section measurements using FHC and RHC fluxes and the first charged current $\bar{\nu}_e$ cross-section measurement since the Gargamelle measurement [99]. Similar to [100], a significant photon background is present in the low momentum and high angle regions of the phase space. This background is constrained by the photon control sample. There are significant discrepancies between data and MC in the regions dominated by the photon background as a large systematic uncertainty source. The simultaneous fit of the CC inclusive selection (FHC and RHC) and the corresponding selection from the photon control sample are performed in the analysis, which leads to the inclusion of the correlations between the samples and calculation the flux integrated differential cross-section, as a function of momentum. The cross-sections are measured in a limited phase space of $p > 300 MeV/c$ and $\theta \leq 45°$. Two fits: using the NEUT (5.3.2) and GENIE (2.8.0) as an input Monte Carlo are performed and give consistent results. The data results are also compared with NEUT (5.4.0), GENIE (2.12.10), and NuWro (19.02) predictions and agree within the uncertainties (Fig. 6.19).

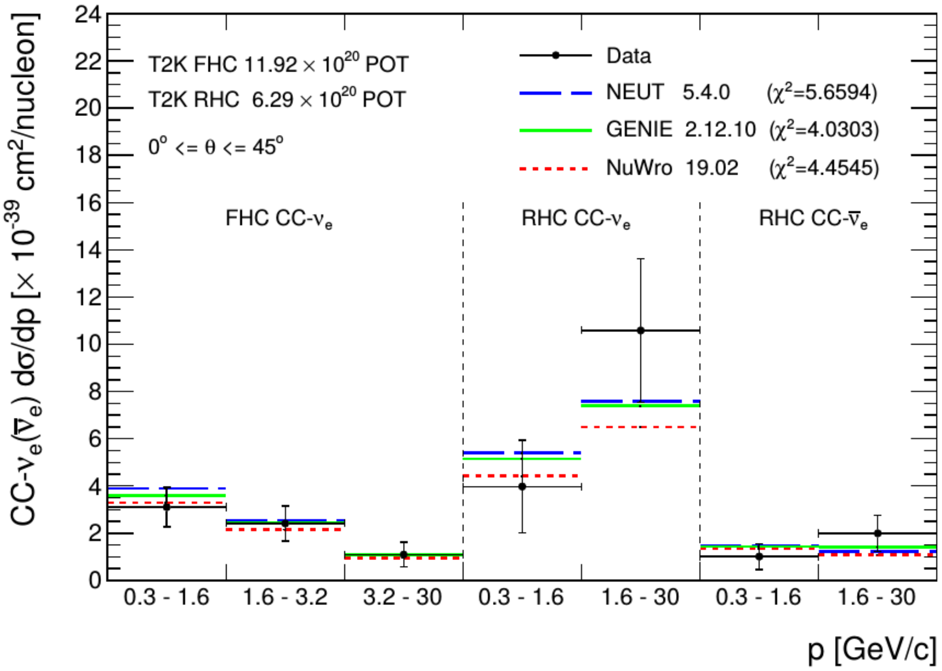

Figure 6.19: ν_e and $\bar{\nu}_e$ CC inclusive cross sections in a limited phase-space ($p > 300MeV/c$ and $\theta \leq 45°$) compared to the neutrino generator models from NEUT 5.4.0, GENIE 2.10.12, and NuWro 19.02. Figure from [7].

6.2 Impact of the T2K measurements on the modeling of (anti)neutrino interactions

In the previous sections, the descriptions of the analyses included only basic comparisons with theoretical models of neutrino-nucleus interactions. This section describes the specific comparisons of the T2K cross-section results with the models available in the Monte Carlo event generators. These comparisons significantly impact the modeling of (anti)neutrino-nucleus interactions because they enable precise tuning of neutrino event generators. The section is focused on charged current interactions with no pions in the final state because T2K has performed the most extensive CC0π cross-section measurements and comparisons with theoretical models so far. Moreover, charged current interactions with no pions have the highest priority for T2K since it is a signal reaction for the measurements of the (anti)neutrino oscillations, especially for the search for CP violation. This reaction is also crucial for the development of future long baseline neutrino experiments.

Particular emphasis in this section is placed on the contribution of multi-nucleon interactions to the quasi-elastic cross section. It is currently the most fascinating topic in neutrino-nucleus interactions in the energy regime below 1 GeV. It might be the key to solving some of the long-standing data-Monte Carlo discrepancies, such as the LSND effect [136].

Although most of the T2K measurements are still limited by the systematic (mostly neutrino flux) and statistical uncertainties and no quantitative conclusions can be drawn, some preferences for specific models in specific regions of phase space are visible. Selected conclusions from data - model comparisons with a significant impact on understanding neutrino - nucleus interactions can be found below.

First, the INGRID CCQE analysis studies the effects of the nuclear model and multi-nucleon interactions in CCQE-like interactions [106]. The dependence of the CCQE cross-section on the existence of multi-nucleon interactions was examined by calculating the cross section using the efficiency correction predicted by the three neutrino-nucleus interaction models: RFG without (Fig. 6.10) and with multi-nucleon interactions (Fig. 6.20), and an SF model without multi-nucleon interactions (Fig. 6.20). Although the results are compatible with the Monte Carlo predictions, the CCQE cross-sections are dependent on the nuclear model and the existence of multi-nucleon interactions at the 10% level. One can also find some indications that the spectral function model better describes the event kinematics.

Further studies of the multi-nucleon contribution to CC0π cross section are done in [9]. The analysis of CC0π interactions on carbon shows that the Relativistic Fermi Gas model (RFG) is able to predict cross section in a limited region of phase space and only when there is no reconstructed proton in the final state (Fig. 6.21). It is disfavoured when the result in δp_T is considered. The Local Fermi Gas (LFG) prediction shows slightly better agreement with data than RFG in interactions with reconstructed protons, especially for the distributions of STV. However, it still overestimates the soft part of the STV spectrum. NEUT 5.4.0 has more consistent LFG implementation and provides better agreement with STV distributions. The agreement is also better in the region without reconstructed protons in the final state and with large muon angle, where other models fail to describe the result. For the events

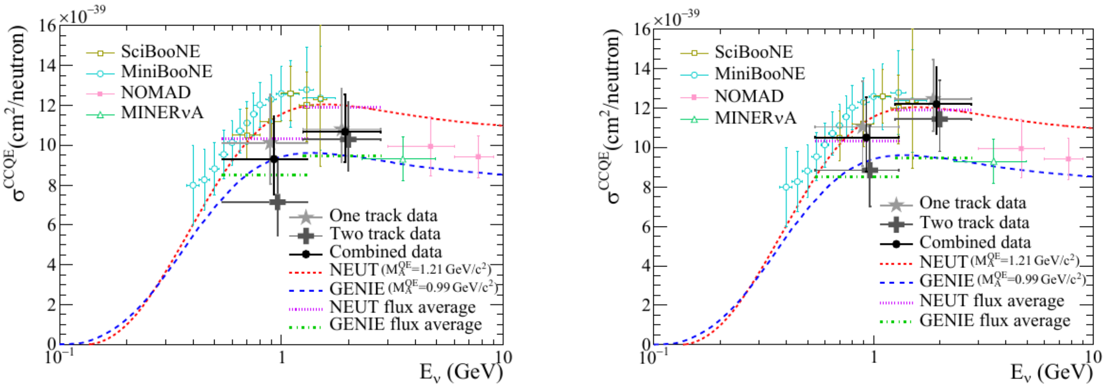

Figure 6.20: INGRID ν_μ CCQE cross section with efficiency correction predicted by the Relativistic Fermi Gas model with multi-nucleon interactions (left). The cross section calculated with the Spectral Function model is shown in the right plot. T2K data point is placed at the flux mean energy. The vertical error bar represents the total (statistical and systematic) uncertainty, and the horizontal bar represents 68% of the flux at each side of the mean energy. Results from SciBooNE [108], MiniBooNE [107], NOMAD [109] and MINERνA [110] are also shown. Figure from [106].

with one or more reconstructed protons in the final state, the best description of the data is given by the Spectral Function (SF) model.

Next, the measurement of CC0π cross section on water reported in [124] was compared to the predictions of the Martini et al. two particles-two holes model for carbon [125]. Fig. 6.22 illustrates this study.
One can observe that the results from the CC0π analysis on water also show a preference for the 2p2h contribution in most regions of phase space. This confirms conclusions from the previous T2K analyses presented in this section and chapter.

Finally, the topic of multi-nucleon interactions is discussed in the framework of joint ν_μ-$\bar{\nu}_\mu$ CC0π analysis [132]. As expected, the neutrino-antineutrino cross section difference shows a preference for the 2p2h contribution, which is related to the change of sign of the axial-vector component in the cross section. The fractional change of the cross-section asymmetry with and without 2p2h is very small, except for the low momentum region where it may reach 50% (forward angle). The statistical uncertainty significantly limits the sensitivity to such an observable. Although most systematic uncertainties cancel out, the detector systematics that are not correlated between neutrino and antineutrino dominate the systematic error.

A more sophisticated test of the 2p2h sensitivity is shown in Fig. 6.23, where the results are compared to different 2p2h models. The 2p2h model in NEUT and the 2p2h model by Martini et al. [125] are both implemented on top of a similar 1p1h LFG model, while the SuSav2 model includes different 1p1h [138] and 2p2h [139] predictions. Predictions from the Martini et al. model are also shown. It appears that none of these models can describe the measured neutrino and antineutrino cross-sections in the entire phase space. Mis-modeling of both the 1p1h and 2p2h contributions might be the source of disagreement with the cross-section measurements. It is currently challenging to discriminate between the models because of the large statistical uncertainty. Looking into the future - with smaller errors, the ν-$\bar{\nu}$ cross-section difference should be the an excellent tool for validating 2p2h models

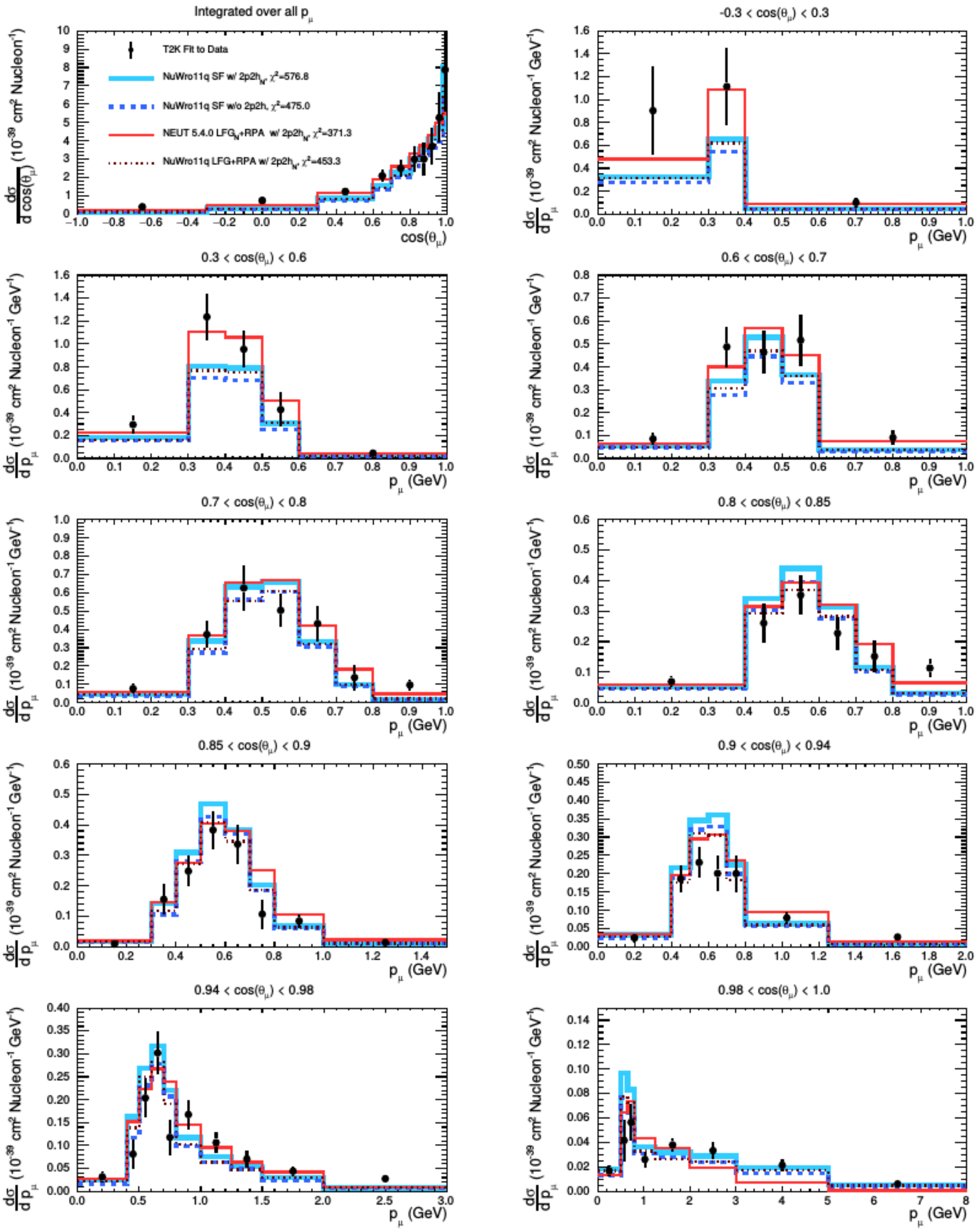

Figure 6.21: ν_μ CC0π cross section as a function of muon kinematics when there are no reconstructed protons (with momenta above 500 MeV). The data are compared to NuWro 11q with the SF nuclear model, both with and without additional 2p2h contribution; NEUT 5.4.0, which uses an LFG+RPA model that includes 2p2h predictions; and NuWro 11q with an LFG+RPA nuclear model and a separate 2p2h prediction. $2p2h_N$ indicates the 2p2h model is an implementation of the Nieves et al. model of Ref. [121]. The 'N' subscript after LFG indicates that the model uses both a 1p1h and 2p2h prediction from the aforementioned model of Nieves et al. More details of these models can be found in [9]. Note that the last momentum bin in each plot is shortened for readability. Figure from [9].

and their implementations because various 2p2h models have different predictions for the axial-vector component of the cross section.

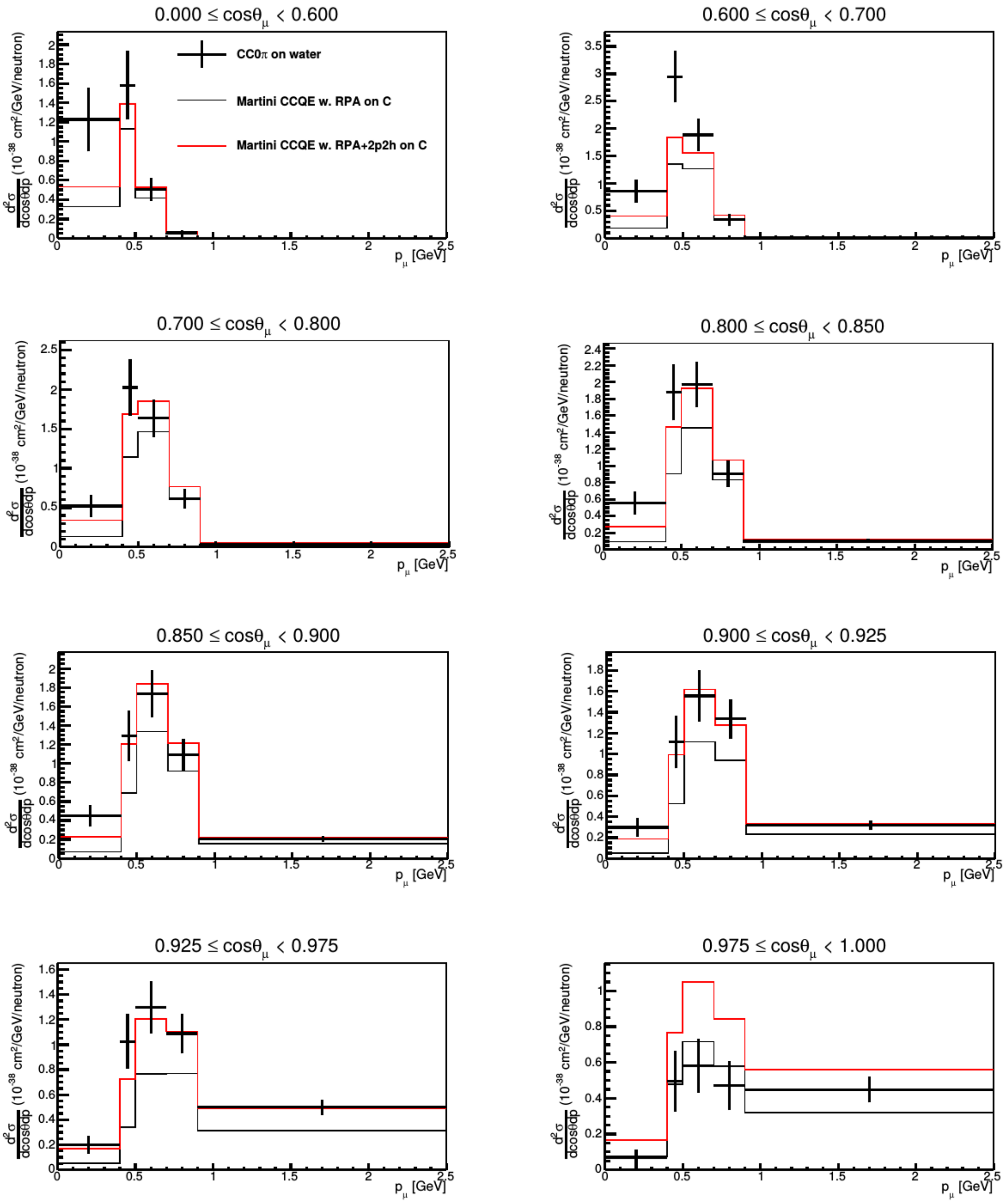

Figure 6.22: ν_μ CC0π cross section on water compared against two Martini model predictions on carbon, one with 2p2h contributions and the other without. Figure from [124].

As mentioned above, the mis-modeling of the CC0π cross section might have its source in the 1p1h model. Further investigation of this problem was conducted, and the results were compared to different LFG implementations as available in the NEUT, NuWro and GENIE neutrino event generators. The difference between these implementations comes down mainly to the treatment of nucleon binding energy. Again, none of the generators is able to predict the measured neutrino and antineutrino cross-sections in the full phase space. The measured CC0π cross-sections are also compared to an SF model. The Spectral Function model, as mentioned above, still suffers from the incomplete implementation of merging with the 2p2h model

(2p2h modeled on top of the RFG is used), resulting in the largest full χ^2 in this study. These problems also manifest themselves in the neutrino-antineutrino cross-section difference and asymmetry distributions where LFG and SF have very similar predictions.

To summarize, comparisons in specific angular regions can lead to some qualitative conclusions, but still, none of the models is able to describe fully the ν_μ and $\bar{\nu}_\mu$ CC0π cross sections in the entire phase space. Among the different combinations, the difference between neutrino and antineutrino cross sections shows interesting sensitivity to different 2p2h models, which is limited by large uncertainties. The poor (anti)neutrino-nucleus interaction modeling revealed in this analysis is a limiting factor for future neutrino oscillation experiments whose primary goal is to measure the CP violation. A deeper understanding of the underlying processes involved in (anti)neutrino-nucleus interactions is needed. New cross-section analyses with larger statistics and improved systematic uncertainties need to be developed.

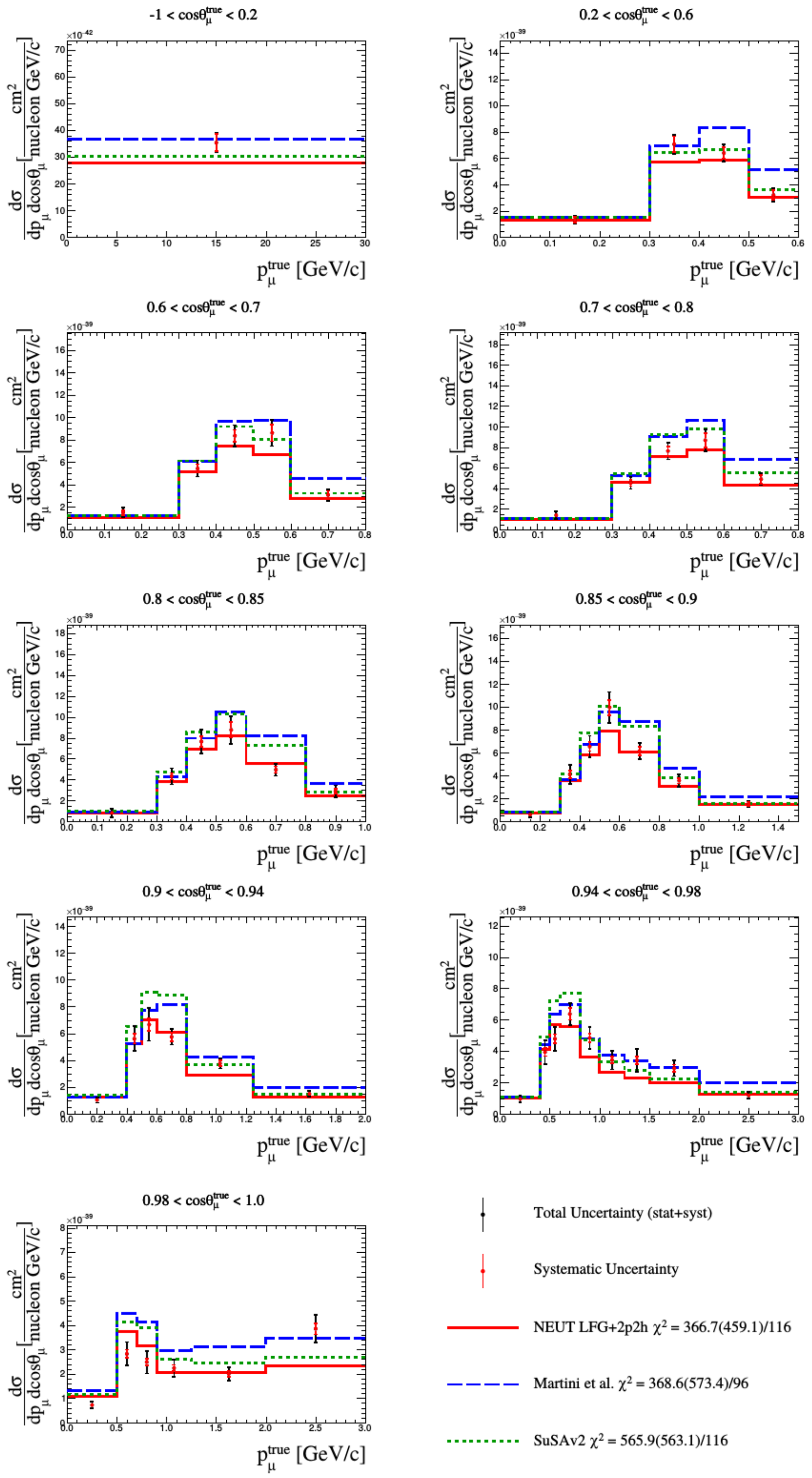

Figure 6.23: Measured ν_μ CC-0π double-differential cross-section per nucleon in bins of true muon kinematics with systematic uncertainty (red bars) and total (stat.+syst.) uncertainty (black bars). The results are compared to NEUT version 5.4.1, which uses an LFG+RPA model with 2p2h (solid red line), Martini et al. (dashed blue line), and SuSAv2 (green dashed line) models. The full and shape-only (in parenthesis) χ^2 are reported. Figure from [132].

6.3 Summary and future measurements

Several conclusions can summarize the analyses described in this chapter:

1. There is a need for developing a universal CC0π/CCQE model, which covers the entire experimental region from 200 MeV to tens of GeV. It is also the case for the contribution from two particles-two holes interactions. This is still an open issue because none of the currently available theoretical models is able to cover this regime. The models that fill the gaps between the generator predictions need to be developed.

2. It is essential to quantify the differences between the muon and electron neutrino cross sections. The electron neutrino cross sections need to be measured more precisely over a broad energy range and compared to muon neutrino cross sections. This is particularly important for the CP violation measurements in future neutrino oscillation experiments.

3. There is a growing interest among experimentalists in the measurements of the hadronic system in neutrino-nucleus interactions (e.g., STV measurements). Therefore, models of outgoing hadrons and final-state interactions in CC0π/CC1π need to be improved and precisely tuned.

4. Generally, T2K's CC1π analyses show that neutrino event generators overpredict the cross section in the low pion momentum range. This kind of model excess has also been observed in other experiments. The discrepancies might result from the incomplete description of the nuclear effects in CC1π interactions. The model of single pion production needs to be improved.

5. Systematic uncertainties are still one of the main factors that limit the sensitivity of the cross-section measurements. Neutrino flux uncertainty remains the dominant systematic error. The effort towards reducing the systematic uncertainties in the cross-section measurements needs to be continued and intensified.

The previous section ends with data - model comparisons in sophisticated joint analyses employing simultaneous maximum likelihood fit to many data samples both for neutrinos and antineutrinos. This approach fully represents the trends and directions in the development of the future T2K cross-section measurements. There are many advantages in the joint fit analysis strategy. The main ones are the complete treatment of the correlations between systematic uncertainties and various data samples and no necessary additional unfolding procedures. The drawbacks seem minor and mainly related to the final graphical representation of the results (regularization).

Several ongoing analyses follow this trend. It is necessary to mention here the first joint INGRID-ND280 analysis of the CC0π interactions, which will simultaneously measure the cross section at these two detectors with two different angles with respect to the beam direction as well as the joint ν_μ CC0π fit of the carbon and oxygen cross sections in ND280.

6.3.1 ND280 upgrade

As it has been pointed out, the differential neutrino-nucleus interaction cross sections are less dependent on Monte Carlo models. Moreover, their uncertainties are usually smaller than those for the total (i.e., integrated over the phase space) neutrino-nucleus interaction cross section. Although a significant improvement in extending the explored phase space in the T2K measurements is observed, there is still some deficit in the selection efficiency for low momentum, high-angle and backward-going muons. It seems that with the current detector setup the efficiency cannot be further improved, so the off-axis near detector will be upgraded in 2022, and new detectors will be installed. The ultimate goal of the ND280 detector upgrade and increase of the J-PARC neutrino beam intensity is to reduce the combined statistical and systematic uncertainties to the level that would allow the sensitivity for leptonic CP violation measurement to be increased significantly. As part of the ND280 upgrade, the PØD detector will be removed, and new Super Fine-Grained Detectors (SuperFGD), High-Angle Time-Projection Chambers (HA-TPCs), and Time of Flight (ToF) detectors will be put instead (Fig. 6.24). The downstream part of the existing ND280 setup, namely three TPCs, two FGDs, ECal and SMRD will remain unchanged. The upgraded ND280 will measure muons from charged current neutrino interactions in a full polar angle and extend the reconstruction and identification capabilities of low energy hadrons in the vicinity of the neutrino interaction vertex.

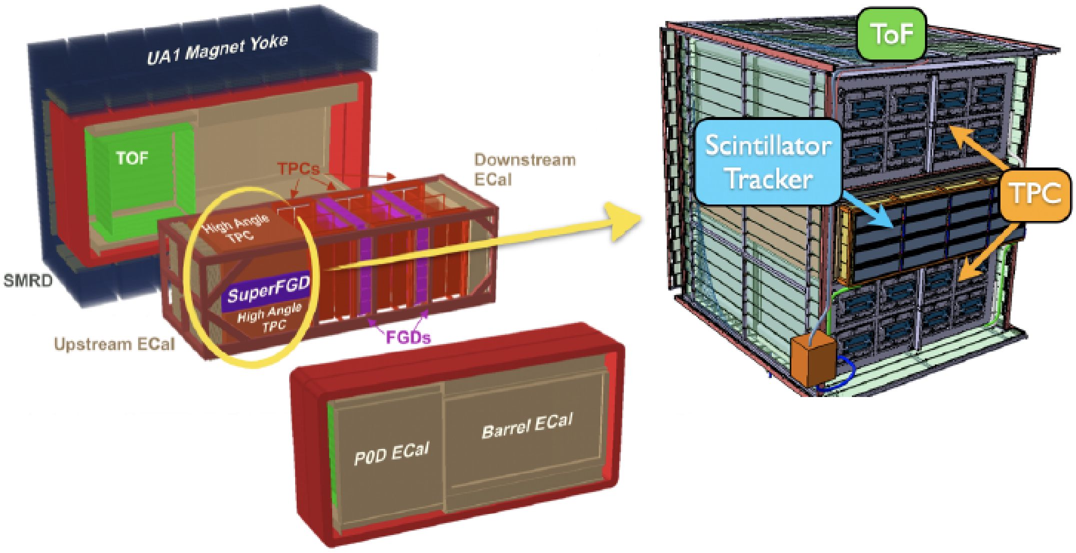

Figure 6.24: Schematic view of the upgraded ND280 detector with new Super FGD and High-Angle TPCs surrounded by the Time of Flight detectors. The picture on the right shows the zoomed area of ND280 where the new sub-detectors are located. Figure from [141].

The SuperFGD is a highly segmented (about 2 millions small, $1cm^3$ optically-isolated, scintillator cubes) active target for neutrino interactions of a total mass of about 2 ton, dimensions of $1.9(width) \times 1.9(length) \times 0.6(height)m^3$, and 192 × 192 × 56 cubes. Three orthogonal wavelength shifting fibers collect scintillation light produced by charged particles. The signal is read out by the Hamamatsu MultiPixel PhotoCounters (MPPC)s placed on the upstream, top, right, and left side and front-end electronics. The light yield, after 1 m attenuation, of about 40 photoelectrons and time resolution of about 0.9. ns for a minimum ionizing particle (MIP), together with high granularity will provide a very good dE/dx resolution. This will result in the reconstruction of charged particles in 4π and protons down to the momentum of about 300 MeV/c.

As the performance of the existing ND280 TPCs has fully met the expectations, the HA-TPCs design follows that of the 'old' ones. The new HA-TPCs will be filled mainly with Argon (95%), with an admixture of CF4 (3%) and iC4H10 (2%). A new resistive Micromegas detector, constructed using the 'resitive bulk' technique, which provides a spread in the charge on the anode plane, will reduce the density of readout pads and eliminate the discharges. A very uniform electric field, parallel to the magnetic field, will be provided by a thin rectangular cage, with a drift length of about 90 cm and wall thickness less than 4% of radiation length. The performance requirements for the HA-TPCs are the same as for the TPCs already in use, i.e. dE/dx resolution of 10% for MIP and 9% momentum resolution at 1 GeV/c, which translates into a space point resolution of about $800\mu m$ for a magnetic field of 0.2 T, and a track length of 64 cm (64 space points).

The TOF detectors will measure precisely (time resolution 100 - 200 ps) the crossing time of charged particles traversing the ND280. This resolution will allow the flight direction of charge particles to be determined unambiguously, i.e., it will distinguish neutrino interactions in the target from those in the areas outside the detector. Moreover, the improvement in particle identification with TOF detectors is expected, mainly in the regions where PID cannot be done using the dE/dx measurement alone. This refers e.g., to electrons and muons in the energy range 100 - 300 MeV, and positrons and protons in the energy range 1 - 2 GeV where the TPCs do not provide satisfactory separation. Six TOF planes are foreseen. They will fully surround the ND280 target and horizontal TPC's. The length of the bars along (perpendicular) the beam direction will be 2.0 m (2.3 m). A bar thickness of 1 cm and a width of 12 cm was chosen. The scintillation light will be propagated without any WLS fiber. The light collection at both bar ends is provided with 6×6 mm MPPC.

The T2K ND280 upgrade technical design report [140] contains a detailed description of the new detectors. It should be noted that extensive tests at CERN, LANL, and DESY of the new detectors confirm the designed performance.

The example of the predicted efficiency for the upgraded off-axis detector is shown in Fig. 6.25. The upgraded ND280 configuration shows a clear improvement in the angular acceptance of the detector both for high-angle muons thanks to the new HA-TPCs and backward-going muons thanks to the ToF detector. SuperFGD detector with finer, three view readout will improve the spatial reconstruction of low momentum particles and the overall track reconstruction efficiency (Fig. 6.26).

Feasibility study shows that the upgraded ND280 detector will introduce an improvement into the measurement of the cross sections as a function of Single Transverse Variables. SuperFGD, with additional statistics and kinematic acceptance, should allow the nuclear effects to be more precisely tested than the current

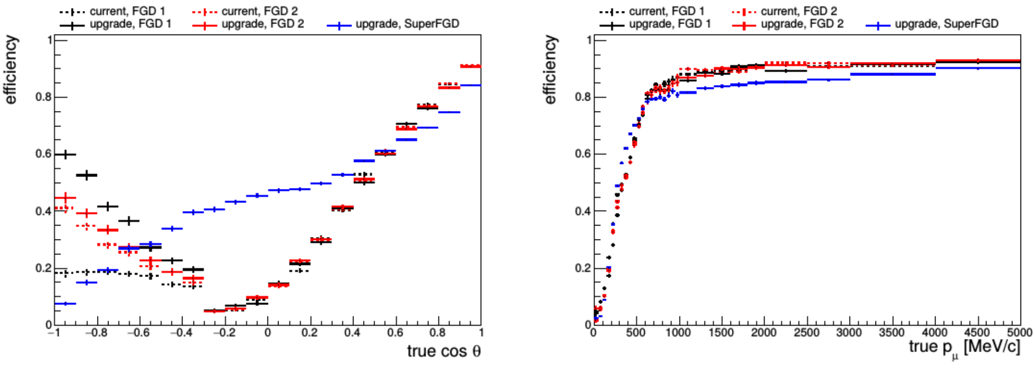

Figure 6.25: ν_μ CC selection efficiency as a function of the true muon polar angle (left) and momentum (right), for both the current ND280 (dashed lines) and the upgrade configuration (solid lines), in neutrino mode. The different curves correspond to neutrino interactions in either FGD1 (black), FGD2 (red), or Super-FGD (blue). Figure from [140].

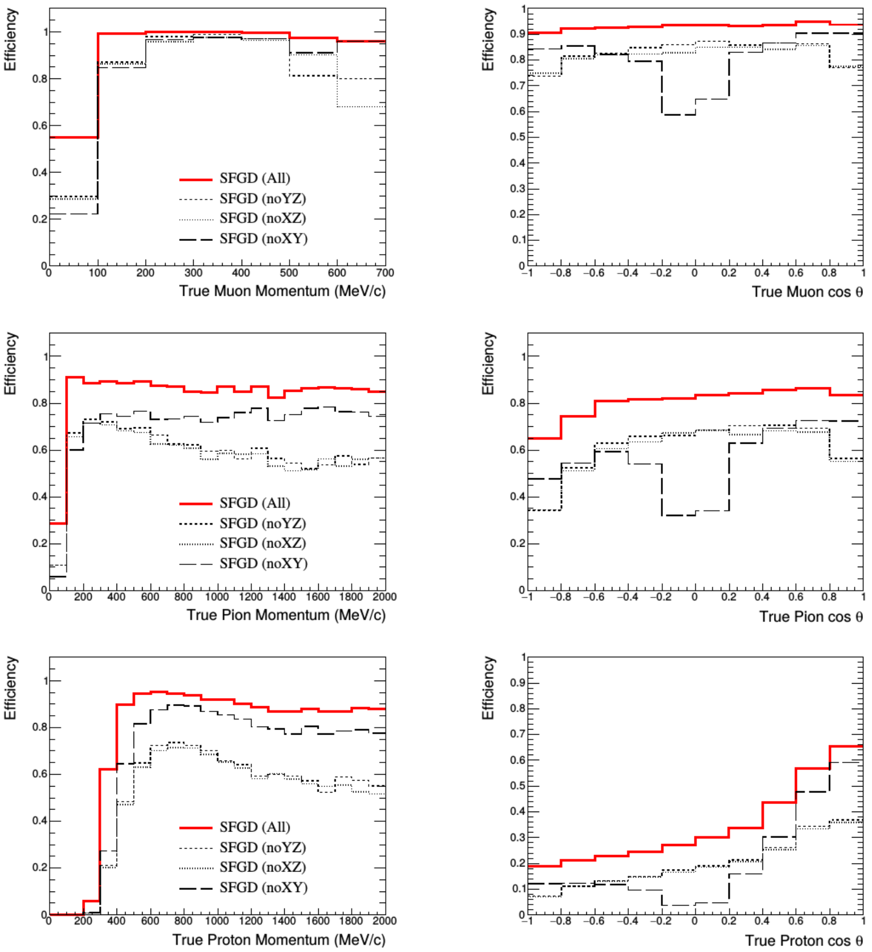

Figure 6.26: Track reconstruction efficiency with the new Super-FGD detector with three readout views compared to the efficiencies with two readout views (as in FGD detector). Figure from [140].

T2K analyses. The almost entire distribution of δp_T can differentiate between the RFG and SF/LFG models. Additionally, the tail of the distribution shows a clear separation of the cases with no FSI and no 2p2h from the others. SuperFGD's improved acceptance has the largest impact on the ND280's ability to measure the $\delta\alpha_T$ parameter. The study shows that SuperFGD is able to measure the relative shape differences between the case with and without FSI. Three characteristic regions of $\delta\alpha_T$: low - (0;$\pi/3$), medium - $(\pi/3, 2\pi/3)$ and high - $(2\pi/3, \pi)$ are distinguishable for SuperFGD, what gives the opportunity to separate FSI and 2p2h effects. In the case of no FSI, the distribution of $\delta\alpha_T$ is expected to be flat [141]. When the FSI is present, the distribution should be shifted towards high values of $\delta\alpha_T$, which is interpreted as the deceleration of the final state protons. SuperFGD can also tag and reconstruct neutrons produced in antineutrino interactions using its large size and high granularity. The measurement of the neutron kinematics can improve the knowledge of the nuclear effects for 2p2h events with neutron-proton or neutron-neutron final states. It has been demonstrated that the upgraded off-axis detector offers many physics advantages by improving the angular acceptance and spatial resolution as well as the measurement of the time of flight. It opens new possibilities for cross-section measurements and gives the opportunity to further reduce systematic uncertainties.

Chapter 7

Muon neutrino induced charged current interactions without pions and with one pion in the final state

This chapter describes two analyses to which the author of this monograph was the main contributor. The first section characterizes single charged pion production in muon neutrino induced charged current interactions. The second section details the muon neutrino-nucleus charge current interactions without pions in the final state on lead and carbon.

7.1 Charged current single charged pion production

The studies of muon neutrino induced charged current single charged pion production ($CC1\pi$) are extremely important both from the point of view of improving our knowledge of the nature of neutrino interactions with the nuclei and from the point of view of the neutrino oscillation physics. ν_μ $CC1\pi$ interactions constitute a substantial background for muon neutrino disappearance measurements in long baseline neutrino experiments. This neutrino interaction channel is characterized by the following particles present in the final state: a muon (μ^-), one positive pion (π^+) and any number of nucleons. If it happens that π^+ from CC1π interaction is not detected and only a muon is observed, the event mimics the ν_μ CCQE interaction, where only a muon and nucleons are present in the final state and contributes to the background. One has to stress that precise determination of the energy spectrum of ν_μ CCQE interactions is crucial for the studies of the ν_μ disappearance channel of neutrino oscillations and the CC1π background make this determination more challenging.

The T2K experiment gives a unique opportunity to study $CC1\pi$ interactions on several targets, in the intermediate energy range, and it provides very useful data for neutrino physics community, e.g., in view of planned designs of the future experiments.

7.1.1 Overview of CC1π analysis strategy

In the analysis presented in this section [161], several event topologies were considered. Event selection cuts were developed and optimized to select two-track events with a single μ^- candidate track and a single π^+ candidate track. Both PØD fully contained (μ^- and π^+ tracks are contained in the PØD) and partially contained (μ^- candidate track is not contained) events were considered for good phase space coverage.

Charged current single pion events could also be reconstructed as one (when all but one particle are below the reconstruction threshold or overlap), three (when μ^-, π^+ and p are all reconstructed) and more (high proton track multiplicity, reconstruction error, or overlap with the second event) track events. These selections are outside the scope of this study, though these additional topologies could be used in future versions of the analysis.

Section (7.1.2) contains of a detailed description of the event selection cuts aiming at selecting CC1π samples for PØD water-in and water-out T2K running periods, which are used further in the analysis.

Section (7.1.3) describes the methodology of the calculation of cross section on water, how exactly the two samples (water-in, water-out) are used, including background subtraction technique, efficiency correction, and the event rate subtraction formulae.

Sections (7.1.4) and (7.1.5) provide full information about statistical and systematic uncertainties associated with this analysis.

Section (7.1.6) outlines the fake data studies that were performed to validate the analysis.

Finally, section (7.1.7) reports the results that were obtained.

7.1.2 Selection of the CC1π neutrino interactions

In this section the procedure for selecting charged current interactions with single charged pion using the PØD detector is described. The pre-selection scheme and all cuts used in the analysis are characterized in detail.

Data and Monte Carlo Sets

The data used in the CC1π analysis comprises the beam runs 1, 2, 3c (hereinafter referred to as run 3), and 4. The modes of the PØD detector running for these runs are as follows: run 1 covers water-in mode; run 2 covers two periods: water-in and water-out; run 3: water-out; run 4 includes two periods: water-in and water-out.

The proper quality of the data is ensured by applying a standard set of cuts, recommended by the ND280 Data Quality group. The data quality cuts are characterized in more detail in Subsec. 7.1.2. Tab. (7.1) summarizes the number of protons on target (POTs) of the data used in the CC1π analysis

The Monte Carlo used in the study is a set of samples produced using as an input the files (*vector* files) consisting of neutrino interactions generated by the NEUT generator. The MC is split into four runs with various PØD detector configurations, in a similar way as the data. Tab. (7.2) presents the details of the Monte Carlo

	PØD water-in mode ($\times 10^{20}$ POT)	PØD water-out mode ($\times 10^{20}$ POT)
Run 1	0.295628	-
Run 2	0.697883	0.359124
Run 3	-	1.35522
Run 4	1.64683	1.77557
Total	2.64034	3.48992

Table 7.1: Data sets used in the CC1π analysis and their POTs (after applying data quality pre-selection).

	PØD water-in ($\times 10^{20}$ POT)	water-out ($\times 10^{20}$ POT)
Run 1	5.51	-
Run 2	7.335	9.745
Run 3	-	16.105
Run 4	48.295	-
Total	61.14	25.85

Table 7.2: Monte Carlo sets used in the CC1π analysis and their POTs.

samples used in the CC1π analysis. The model of the neutrino beam flux which was used in this Monte Carlo set was *v11a*, but the final result was tuned with the flux *11b v3.2*.

Neutrino interactions in the hall and in the sand surrounding the near detector pit are not simulated along with the interactions in ND280. Separate Monte Carlo samples containing neutrino interactions in the sand, outside of the near detector pit, were employed in specific systematic studies, and the parameters of these samples are listed in Tab. (7.3).

PØD water-in ($\times 10^{20}$ POT) mode	PØD water-out ($\times 10^{20}$ POT) mode
11.9925	11.99

Table 7.3: Sets of Monte Carlo samples with neutrino interactions in the sand, outside of the near detector pit used in the systematic error studies for the CC1π analysis.

A collection of data and Monte Carlo utilized in the CC1π analysis is the result of production 5 processing.

Pre-selection Cuts

In this section, the pre-selection conditions that need to be satisfied by ND280 events to be accepted for CC1π selection are described. It includes imposing the data quality criteria and the procedure of grouping events into the bins that reflect the timing structure of the T2K beam (bunches).

Data Quality

In the first step of the event pre-selection, the standard ND280 data quality cuts are applied. The requirements on the data quality in the PØD detector as well as on the proper operation of the ND280 magnet are imposed. The following cuts are applied to the data:

1. require good PØD and magnet flags (all flags equal to zero),
2. require good beam data summary status

The second cut is necessary to get the valid POT information for each event. This information was provided by the T2K beam group and was incorporated into the headers of the analyzed files (*oaAnalysis files*).

Bunching

The second step of the event pre-selection is to divide the events according to the neutrino beam structure. Each ND280 event is equivalent to the T2K beam spill, which consists of eight bunches (six in run 1). ND280 events are split by looking at the timing of the reconstructed objects (tracks, vertices). The reconstructed objects are put in proper time windows corresponding to the bunches. The time window boundaries were selected to be wide enough to cover Monte Carlo and the data from different ND280 running periods. The details of the bunch timing boundaries can be found in Tab. (7.4). The example timing histograms for data and Monte Carlo with the bunch boundaries imposed are shown in Fig. (7.1).

Bunch number	1	2	3	4	5	6	7	8
Min (ns)	2600	3240	3800	4400	5005	5550	6150	6700
Max (ns)	3140	3700	4300	4880	5450	6050	6600	7200

Table 7.4: Bunch timing boundaries in nanoseconds relative to trigger time, used in the CC1π analysis.

Selection Cuts

In this subsection, the core of CC1π selection procedure which is a set of subsequent cuts applied directly after the pre-selection is presented. The plots of the quantities related to each cut before applying the cut are shown. These plots can be treated as sanity checks which indicate whether the cuts work in the same way on data and Monte Carlo.

The actual CC1π selection procedure can be divided into two steps: charged current (CC) two-track selection and pion candidate selection. Furthermore, one can create different selections for different topologies of neutrino interactions in the detector. Two selections are created to pick two major topologies of CC1π interactions in the PØD:

1. A muon exiting through the downstream face of the PØD and entering TPC1 and a pion fully contained within the PØD.
2. Both muon and pion contained in the PØD.

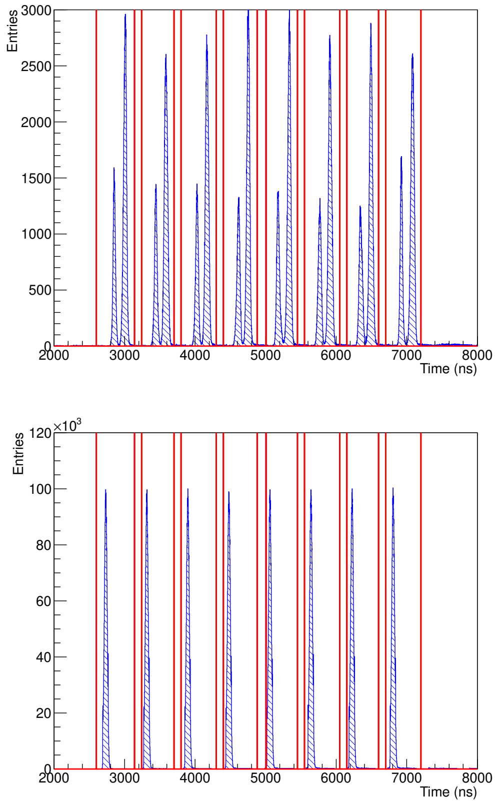

Figure 7.1: Timing of the reconstructed objects and the boundaries of the timing buckets used in the CC1π analysis in data (left) and Monte Carlo (right) for run 2.

This subsection, after presenting the definition of the fiducial volume for the analysis, describes the selection cuts in two parts (selection 1 and selection 2) corresponding to the topologies mentioned above.

Fiducial Volume Definition

Before describing the selection cuts, it is necessary to define the fiducial volume for the analysis. The goal is to select CC1π interactions on water target and to reduce the amount of external background in the sample. Therefore the fiducial volume is defined as a box with the center located in the geometrical center of the PØD water target region with the top, bottom, left, and right edges of the box located at approximately 25 cm from the PØD detector edges, leaving the last 25 cm of the PØD as a veto from the outside activity.

The upstream and downstream borders of the fiducial volume go through the middle of the first upstream and last downstream PØDule [1] of the water target. This definition is adopted from the PØD official water target fiducial volume defined in the $NC\ \pi^0$ analysis [160]. More details of the definition can be found in Tab. (7.5).

---

[1] PØDule has been defined in 3.3.2

Coordinate	Center	Width/2	Min	Max
X	-36	800	-836	764
Y	-1	870	-871	869
Z	-2116	852.5	-2969	-1264

Table 7.5: Fiducial volume definition used in the CC1π analysis [160]. The official ND280 coordinate system as defined in Fig. (3.8) was used.

Selection 1: two tracks - one contained, one TPC-exiting

In this part, the procedure of selecting neutrino interactions with a muon exiting through the downstream face of the PØD and entering TPC1 and a pion fully-contained within the PØD is described. The selection cuts are listed below:

1. Require exactly one PØD reconstructed vertex in the bunch.
2. Reconstructed vertex has to be three dimensional (quality cut). It means that full spatial information about the vertex needs to be reconstructed.
3. Reconstructed vertex has to be located in the PØD water target fiducial volume (as defined in 7.1.2).
4. There are exactly two reconstructed particles associated with the vertex.
5. Both reconstructed particle tracks need to be three-dimensional (quality cut). Again, full spatial information has to be provided by the reconstruction algorithms.
6. One of the particles exits the PØD through its downstream face (muon candidate).
7. Both particles have reconstructed three-dimensional tracks.

The sample resulting from the two-track selection is mostly a mixture of the two charged current interaction channels: CC0π and CC1π, with some fraction of CC-multiπ. In order to pick CC1π^+ reactions from the CC two-track sample with high enough purity, another set of cuts that are applied to the second track (not the muon candidate track) were defined. The second track will be further referred to as *pion candidate*. The cuts applied to the pion candidate are as follows:

1. Pion candidate track has to be fully-contained in the PØD detector.
2. Tracks have to start close to the reconstructed vertex (quality cut).
3. The pull of the energy loss per unit length in the muon/pion hypothesis of the pion candidate track has to be lower than 4.3 and higher than -10 for parametric tracks and lower than 15.3 and higher than -20 for Kalman tracks or the number of Michel clusters is equal to one.

The pion candidate track needs to be fully contained within the PØD detector in order for us to be able to apply the energy loss cut. Only pion candidates with the ending point of their track further than 40 mm (width of two PØDules) from the detector edges are accepted. This requirement means that events with pion candidate tracks ending in the box: $X\epsilon(-796, 724) \cap Y\epsilon(-831, 829) \cap Z\epsilon(-2929, -1304)$ pass the cut.

It is also necessary to require that both the muon and pion candidate start close to the vertex to get rid of some of the cases where the vertexing algorithm is not working correctly (e.g., sand muon overlaying with the true vertex in the same bunch). This cut also removes some of the backgrounds with neutral pions which decay into two photons. Those photons introduce electromagnetic showers at some distance from the vertex. Both the muon and the pion tracks are required to start within 80 mm from the reconstructed vertex, which is roughly equal to the width of the three PØDules.

Finally, the cut on the pull of energy loss of the pion candidate track in the muon/pion hypothesis is applied. The energy loss pull is defined as:

$$Pull_{\mu} = \sum_{i=1}^{N} \frac{\bar{x}_i^{measured} - \bar{x}_i^{expected}}{\sigma_i}, \tag{7.1}$$

where the sum is calculated for six or fewer bins of the distance from the track length starting from the track end until half of the total length of the track is reached. In each bin i, the deviation of the most probable value of the charge $\bar{x}_i^{measured}$ from the expected value of the charge $\bar{x}_i^{expected}$ in the stopping muon hypothesis normalized to the RMS of the charge distribution (σ_i) is calculated. The bins of the distance from the end of the track have a width of 67.8 mm. Expected values of the charge and sigmas were calculated using the sample of data sand muons stopping in the PØD detector. In each bin, the Landau-Gaussian convoluted function was fitted to the charge distribution and $\bar{x}_i^{expected}$ is the most probable value taken from the fit and σ_i is the width also taken from the fit [170].

PØD reconstruction uses two algorithms to fit the track candidates: a Kalman Filter and simple parametric fit. Because the tracks fitted with the Kalman Filter and the parametric fitter have different dE/dx distributions different cuts are applied.

If a pion candidate track does not satisfy the appropriate dE/dx cut, then the cut on the number of reconstructed Michel electron clusters in the event is applied. The event is accepted if the number of clusters is exactly equal to one. By applying this cut, Michel clusters from the $\pi^+ \rightarrow \mu^+ \rightarrow e^+$ decay are counted. The cut on the number of Michel clusters allowed us to recover CC1π^+ events where a high momentum proton is reconstructed as a pion candidate, and a low momentum pion (below reconstruction threshold) decays into Michel electron.

Selection 2: two tracks - both contained

The goal of the second complementary selection is to select CC1π events with both muon and pion candidates contained in the PØD detector. This selection will extend the probed region of the phase space for the measurement.

It is necessary to stress that in selection 1 (One Vertex, Two Tracks, One Contained) 'muon candidate' and 'pion candidate' terminology is used to name the reconstructed tracks in the selected events. In that case, it was well motivated to call 'muon candidate' the track that was exiting the PØD into TPC because of the high muon selection purity (86%). In the case of selection 2, where both tracks are contained in the PØD, this terminology is considered no longer valid. Instead, *longer track* and *shorter track* terms are used.

The cuts for selection 2 are very similar to the previous selection and are listed below:

1. Require exactly one PØD reconstructed vertex in the bunch.
2. Reconstructed vertex has to be three-dimensional (quality cut).
3. Reconstructed vertex has to be located in the PØD water target fiducial volume (as defined above).
4. There are exactly two reconstructed particle tracks associated with the vertex.
5. Both reconstructed particle tracks need to be three-dimensional (quality cut).
6. Both particles are tracks.
7. The first particle is contained in the PØD.
8. The second particle is contained in the PØD.

In the last two cuts, both tracks are required to be contained in the PØD. Tracks that end before outermost 40 mm (the width of two PØDules) at the sides and at the downstream end of the PØD are accepted. Events with tracks ending in the box: $X\epsilon(-796, 724)\ \cap\ Y\epsilon(-831, 829)\ \cap\ Z\epsilon(-2929, -1304)$ are accepted. By applying this cut, one makes sure that dE/dx PID can be applied to both tracks.

After the first set of cuts, the CC two-track sample is selected. To select CC1π^+ events, the second set of cuts is applied to both tracks. The cuts are as follows:

1. Both tracks have to start close to the reconstructed vertex (quality cut).
2. Pull of the energy loss per unit length in the muon/pion hypothesis of both tracks has to be lower than 4.3 and higher than -10 for parametric tracks and lower than 15.3 and higher than -20 for Kalman tracks or the number of Michel clusters is equal to two.

The motivation for the cut on the distance from the reconstructed vertex is the same as in the previous selection. Next, dE/dx cut is applied to both tracks and they are required to be compatible with the stopping muon/pion hypothesis. If dE/dx cut fails, then the cut on the number of reconstructed Michel electron clusters in the event is applied. This time the event is accepted if the number of delayed clusters is exactly equal to two (Michel clusters from muon and pion decays).

Summary and Performance of CC1π Event Selections

To evaluate the performance of the CC1π event selection in the PØD, the efficiency ϵ and the purity p is defined in the following way:

$$\epsilon = \frac{S^{sel(MC)}}{s^{gen}}, \tag{7.2}$$

$$p = \frac{S^{sel(MC)}}{N^{MC}}, \tag{7.3}$$

N^{MC} in Eq. (7.3) is the number of selected events in Monte Carlo, $S^{sel(MC)}$ is the number of selected true CC1π interactions with the true vertex in fiducial volume (in MC) and s^{gen} is the number of all true CC1π interactions (before all cuts) with the true vertex in fiducial volume (MC). The true CC1π interaction definition is based on the multiplicity and content of true particles leaving the target nucleus (after the final state interactions). An event is considered as a true CC1π interaction when there was exactly one negative muon, exactly one charged pion, no other mesons, and any number of nucleons leaving the target nucleus. Tables (7.6) and (7.7) show event reduction and selection progression for data and Monte Carlo (Monte Carlo numbers are scaled to data POT).

	Water-in				Water-out			
Cut	Data	MC	Eff. (%)	Pur. (%)	Data	MC	Eff. (%)	Pur. (%)
1 PØD vtx	1398171	656888	98.95	2.60	1872903	850894	99.68	1.79
3D vtx	1261949	553827	95.33	2.98	1696281	715752	97.56	2.08
PØD fv	151882	137539	86.68	10.90	161637	143970	86.60	9.20
2 part.	35278	32298	36.46	19.52	39892	36129	39.19	16.59
2 3d part.	31828	28997	34.45	20.54	35870	32583	37.32	17.52
1 TPC-exiting part.	9355	8367	12.67	26.17	10160	9025	14.35	24.31
2 tracks	9355	8367	12.67	26.17	10160	9025	14.35	24.31
Pion cand. cont.	7572	6744	10.14	26.01	7887	7134	11.16	23.83
Vtx dist.	4541	3888	7.17	31.87	4768	4130	7.31	27.07
dE/dx & Michel	1543	1413	4.30	52.58	1367	1217	4.36	54.81

Table 7.6: Data reduction and cut progression table for the CC1π analysis for 'One PØD-exiting TPC1-entering track' selection. The numbers in row 6 and 7 are equal because the result of the reconstruction which always returns tracks is used.

	Water-in				Water-out			
Cut	Data	MC	Eff. (%)	Pur. (%)	Data	MC	Eff. (%)	Pur. (%)
1 PØD vtx	1398171	656888	98.95	2.60	1872903	850894	99.68	1.79
3D vtx	1261949	553827	95.33	2.98	1696281	715752	97.55	2.08
PØD fv	151882	137539	86.68	10.90	161637	143970	86.60	9.20
2 part.	35278	32298	36.46	19.52	39892	36129	39.19	16.59
2 3d part.	31828	28997	34.45	20.54	35870	32583	37.32	17.52
2 tracks	31828	28997	34.45	20.54	35870	32583	37.32	17.52
1st trk cont.	19660	17801	20.09	19.52	21013	19046	20.40	16.38
2nd trk cont.	11501	10460	10.64	17.59	11658	10385	10.21	15.04
Vtx dist.	4528	3904	5.99	26.51	4542	3551	4.81	20.70
dE/dx & Michel	1160	1042	2.91	48.37	820	684	1.97	44.15

Table 7.7: Data reduction and cut progression table for the CC1π analysis for 'both tracks contained' selection. The numbers in row 5 and 6 are equal because the result of the reconstruction which always returns tracks is used.

Table (7.8) summarizes the entire event selection (selection 1 and 2 combined) for data and the predictions of the simulation for water-in and water-out modes

N_w $(data)$	2703.00
B_w	1208.03
B_w^{sand}	2.50
ϵ_w	7.21%
p_w	50.79%
N_a $(data)$	2187.00
B_a	931.98
B_a^{sand}	3.85
ϵ_a	6.33%
p_a	50.97%

Table 7.8: Summary of event selection for both sub-selections. Quantities with subscript 'w' correspond water-in sample and 'a' to water-out (air) sample. N_w and N_a are the selected number of events in data. Other quantities are calculated using Monte Carlo simulation.

(scaled to data POT). $N_{w|a}$ is the selected number of events in data, $B_{w|a}$ is the number of background events predicted by MC, $B_{w|a}^{sand}$ is the number of background events resulting from the neutrino interactions in the sand, as predicted by MC, $\epsilon_{w|a}$, and $p_{w|a}$ are the efficiency and purity of the event selection.

The overall value of selection efficiency below 10% results from two main issues.

First, one should stress that only the topology with two particles in the final state is selected. Tables (7.6), (7.7) clearly suggest that 55% (water-out) to 58% (water-in) of CC1π interactions is lost by requiring exactly two particles in the event. The events that are lost end up in 'one particle' and 'more than two particles' topologies. Recovering those interactions would require defining additional selections which would also yield additional systematic errors. It is certainly one of the future improvements which will be made to this analysis. 'One particle' topology pions have low energy and therefore do not leave any tracks or showers in the detector. However, some of the pions decay and produce Michel clusters. The number of Michel clusters can provide some discrimination power against the main background, in this case CCQE-like interactions. This possibility was investigated within the framework of this analysis yielding a low purity CC1π sample, but there might be some reconstruction improvements that can help in this case. The main reason for CC1π interactions ending in more than two particles topology are pion re-interactions in the detector. One can think of methods of selecting those events; however, large $CCMulti\pi$ background is the problem in this topology.

The second issue is that the topologies where the particles exit through the sides of the PØD are missing. Having analyzed Tab. (7.6) and (7.7), one can notice that 10% - 11% CC1π events in selection 1 after 'Pion candidate contained' cut and 10% - 11% in selection 2 after '2nd track contained' cut are selected. This is equivalent to selecting 10% of events in the topology with one track TPC-exiting and the second one contained and another 1̃0% events in the topology with both tracks contained. Summing that up, 20% of CC1π events are selected in general. If this is compared to 34% - 37% efficiency in 2-tracks topology (after 2-tracks cut), it can noted that there are 10% - 17% events to recover. To solve this issue, one should also define and build additional event selections and investigate the properties of "side-exiting particles". These problems are on the list of future improvements of this analysis as well.

After combining both selections, one can check the phase-space that is probed with the sample. The efficiency of the selection as a function of muon candidate true kinematic properties (momentum and angle with respect to the Z axis) and pion candidate true kinematic properties are shown in Fig. (7.2). Plots (7.2) illustrate

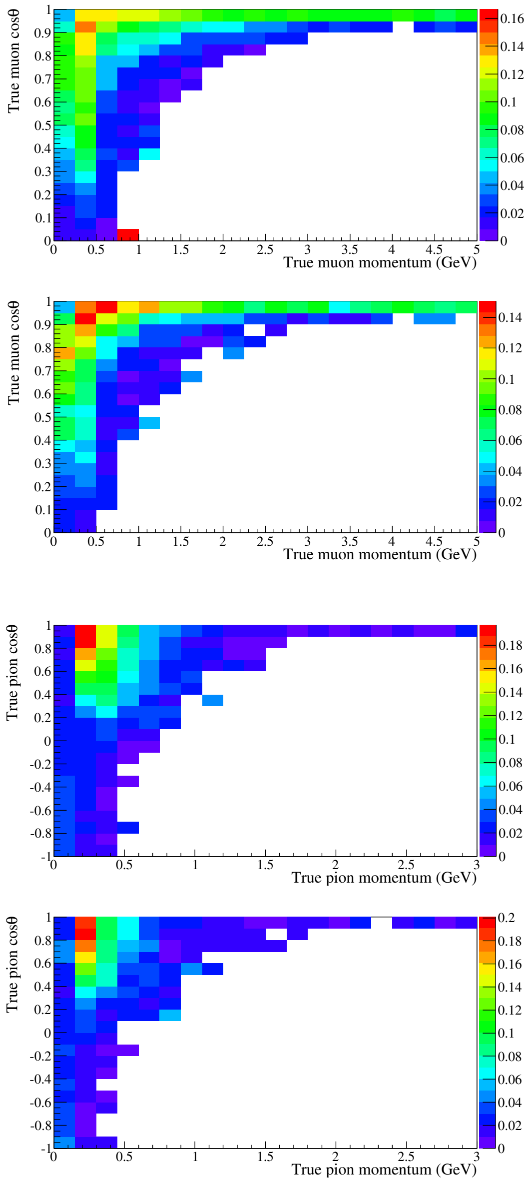

Figure 7.2: Overall efficiency of both selections as a function of muon and pion candidate momentum and cosine theta.

the fact that events with a wide range of muon momentum (even below 100 MeV) and muon angles ($cos\theta$ larger than 0.2) and with pion momentum ranging from 150 MeV to approximately 1 GeV are selected.

It is also essential to check what range of the incoming neutrino energy is probed with this selection. Efficiency as a function of true neutrino energy is shown in Fig.

(7.3). The efficiency of the selection, as one could expect, is low for low neutrino energies and becomes flat above approximately 800 MeV.

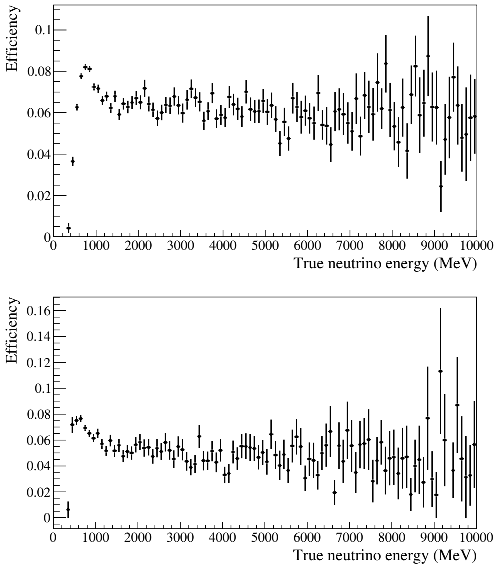

Figure 7.3: Overall efficiency of both selections as a function of true neutrino energy.

MC Corrections

During this analysis several aspects of the Monte Carlo simulation version used in the analysis (MCP5E) were identified as either missing or as wrong, which renders it partially incorrect (by ∼ 1-3%) and requires the implementation of corrections. The MC corrections that are described here are related to the MC fiducial mass, and MC Out-of-Fiducial (OOF) background. The detector fiducial mass is described in more detail in Subsec. (7.1.3). The uncertainty associated with the detector mass is discussed in Subsec. (7.1.4). OOF background is discussed in Section (7.1.3). Systematic uncertainties associated with the OOF background are described in Subsec. (7.1.4).

Fiducial Mass

Due to a bug in the Monte Carlo geometry used in MCP5E, the MC fiducial mass of the PØD was different from the actual detector mass, as shown in Sec. 7.1.3. The small difference was accounted for by correction factors shown in Tab. (7.9). The correction factors (for normalization) were calculated in the T2K technical note dedicated to the PØD geometry and mass [162].

Run	PØD Status	Correction Factor
1	water-in	1.01254
2-4	water-in	1.01615
2-4	water-out	1.03147

Table 7.9: Multiplicative mass correction factors C^{mass} (calculated as data/MC PØD fiducial mass ratios) used to rescale the Monte Carlo predictions [162].

Interference of Sand Muons and Events in ND280

In production 5 sand muons (neutrino interactions in the sand surrounding the near detector pit) and interactions in ND280 were simulated separately. Therefore two separate Monte Carlo samples are used in the analysis: magnet MC (interactions occurring within ND280) and sand MC (interactions outside ND280 but producing particles detected in ND280). One should stress that in this way the effects of the pileup of interactions in ND280 and sand muons are not simulated. To account for that effect, an external study for PØD-TPC CC-inclusive analysis described in [163] is used. Multiplicative correction factors which are used are listed in Tab. 7.10. The correction factors were calculated as the ratios of the number of selected events before sand muon veto cut and after sand muon veto cut in CC-inclusive selection (details in [163]). They are used as weights for selected Monte Carlo events.

Sand Muons Background

To correct the rate of sand muons that enter the selection as a background, external studies done for the tracker CC analysis [164] are used. The tracker CC analysis

Run	PØD Status	Correction Factor
1	water-in	0.9875
2	water-in	0.9802
2	water-out	0.9768
3	water-out	0.9748
4	water-in	0.9721
4	water-out	0.968

Table 7.10: Multiplicative sand muons interference correction factors C^{sp} used to rescale the Monte Carlo predictions [163].

uses a sample of sand muons through-going the PØD selected with a set of simple cuts. The study showed that the data/MC ratio for sand muons is 1.084 ± 0.002 . This ratio is used as a correction (C^{sb}) for the Monte Carlo sand muon background prediction.

Data - Monte Carlo Comparisons

The figures in this section show the comparisons of the kinematic variables for data and NEUT MC for both selections. Monte Carlo is always normalized to corresponding data POT with flux tuning 11b v3.2 (as stated at the beginning of this section), and all corrections are applied unless otherwise stated. Figs. (7.4) and (7.5) show μ^- and π^+ candidates' kinematic distributions for selection 1. Figs. (7.6) and (7.7) show kinematic distributions for selection 2.

One can observe a decent agreement between data and Monte Carlo on the plots. There are some discrepancies in the histograms for selection 1 for events with tracks going in the forward direction ($cos\theta$ close to 1). These differences are most probably related to the poor modeling of charged current coherent pion production in the simulation (confirmed in several other T2K analyses).

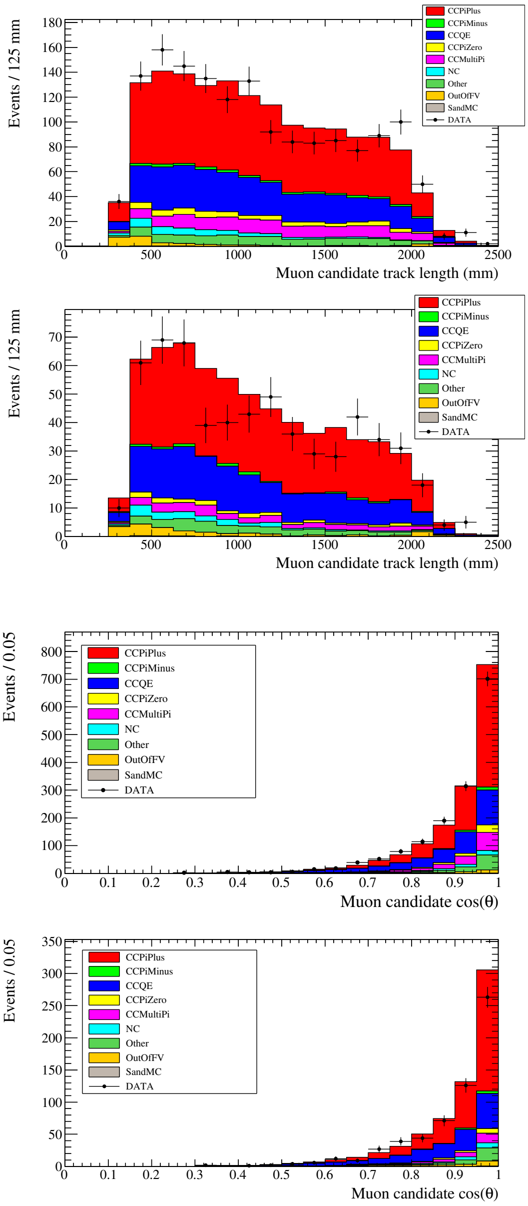

Figure 7.4: Muon candidate track length and $\cos\theta$ for one PØD-exiting TPC1-entering selection. θ is the angle between the muon momentum vector and the z axis.

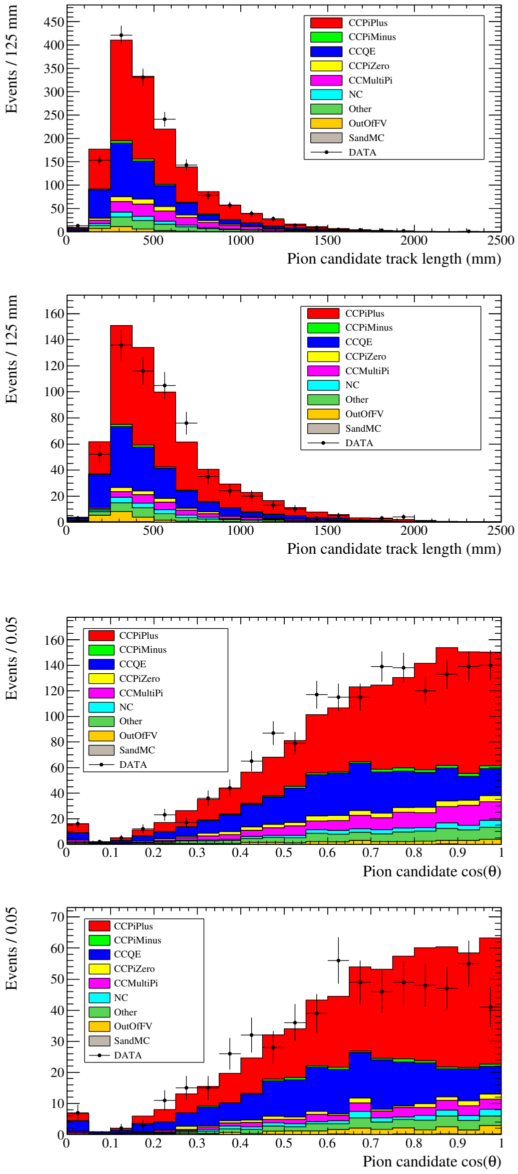

Figure 7.5: Pion candidate length and $\cos\theta$ for one PØD-exiting TPC1-entering selection. θ refers here to the angle between the pion momentum vector and the z axis.

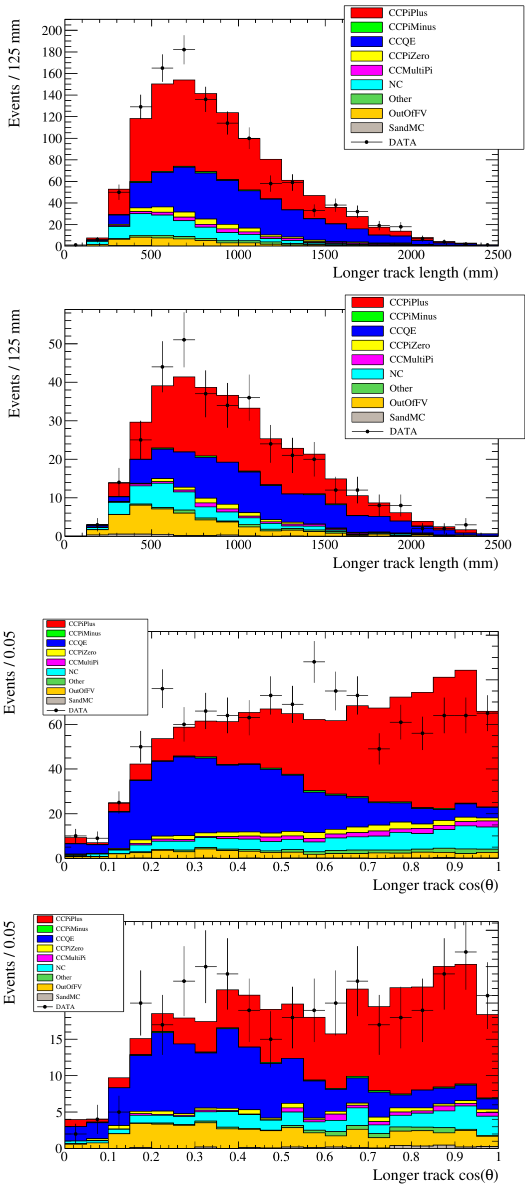

Figure 7.6: Track length and cos θ of the longer track for both-contained selection.

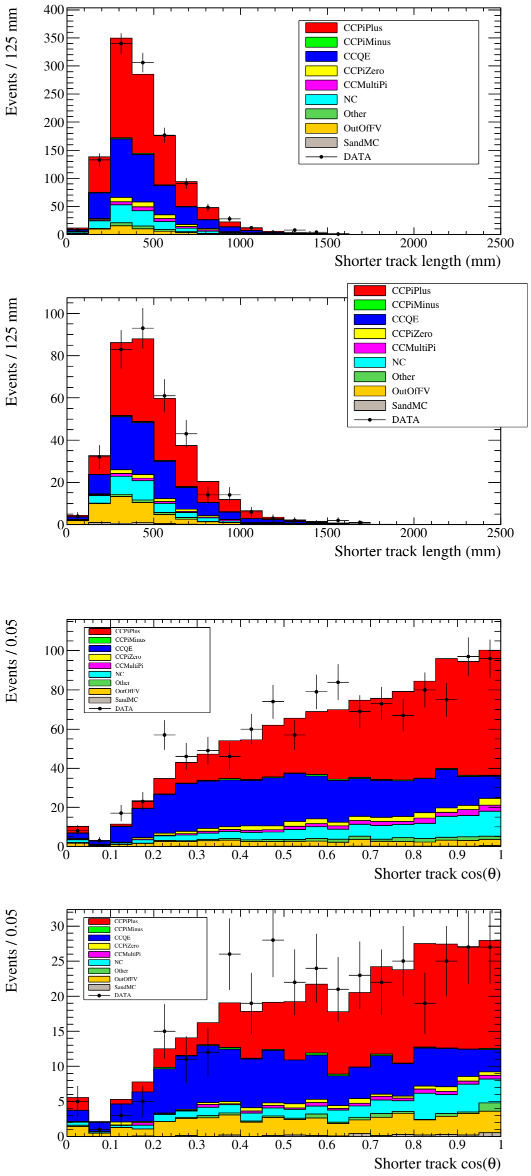

Figure 7.7: Track length and $\cos\theta$ of shorter track for both-contained selection.

7.1.3 Cross-section extraction

For a beam of neutrinos incident on a target, the true number of signal interactions, s, is generally a function of incident neutrino flux, $\Phi(E_\nu)\ \left[\frac{\nu_\mu}{cm^2}\right]$, the signal cross section $\sigma(E_\nu)$, and the number of interacting targets T, and is given by:

$$s = T \int \sigma(E_\nu) \frac{\partial \Phi(E_\nu)}{\partial E_\nu} dE_\nu, \tag{7.4}$$

where flux and cross section in general, are functions of true neutrino energy E_ν. However, for a single-bin measurement, a flux-averaged cross section can be defined as a function of the total integrated flux Φ:

$$\langle \sigma_s \rangle = \frac{s}{T \cdot \Phi} = \frac{1}{\Phi} \cdot \int \sigma(E_\nu) \frac{\partial \Phi(E_\nu)}{\partial E_\nu} dE_\nu, \tag{7.5}$$

so Eq. (7.4) takes a simplified form:

$$s = T \cdot \langle \sigma_s \rangle \cdot \Phi, \tag{7.6}$$

where $\langle \sigma_s \rangle$ is the total flux-averaged signal cross section, T is the number of targets, e.g., molecules or nucleons, Φ is the total integrated neutrino (of a particular flavor corresponding to signal) flux, for the volume containing the targets.

Thus, having measured s and given that T, Φ are also known, the flux-averaged cross section $\langle \sigma_s \rangle$ can be trivially calculated. Here and throughout the monograph, a distinction is made between s and S, where the lower-case denotes the total signal before any cuts, and the upper-case denotes the signal after analysis cuts.

Signal Extraction

Nominal MC Signal and Background Predictions

NEUT mode	Reaction	Fraction (%)
11	$\nu_\mu + p \to \mu^- + p + \pi^+$	53.25
16	$\nu_\mu + N \to \mu^- + N + \pi^+$	32.17
13	$\nu_\mu + n \to \mu^- + n + \pi^+$	9.14
21	$\nu_\mu + (n\|p) \to \mu^- + (n\|p) + \text{multi-}\pi$	2.53
1	$\nu_\mu + n \to \mu^- + p$	1.25
12	$\nu_\mu + n \to \mu^- + p + \pi^0$	1.05
26	$\nu_\mu + (n\|p) \to \mu^- + (n\|p) + \text{mesons}$	0.48
22	$\nu_\mu + n \to \mu^- + p + \eta^0$	0.13

Table 7.11: Fiducial ν_μ-induced post-FSI signal composition (in terms of before-FSI NEUT modes) for PØD water-in NEUT MCP5E sample after cuts for PØD both contained and non-contained selections combined. Percentages are calculated with respect to the total water-in signal in fiducial volume. Rows are sorted in the order of decreasing percentage.

The physics contributing to the signal-after-cuts event category is summarized in Tabs. 7.11 and 7.12 for the water-in and water-out events respectively. It can be seen that for both water-in and water-out samples ∼95% of signal events come from either resonant or coherent single charged pion production, with the remaining ∼5% of the signal coming from either before-FSI multiple or no pion production. Here it must be noted that throughout the monograph *water-out* and *air-in* terms refer to the same PØD configuration and are used interchangeably. Tabs. 7.13 and 7.14 show the background composition for events passing the cuts in terms of different neutrino flux contributions where it can be seen that most of the fiducial background comes from ν_μ-induced events.

NEUT Code	Reaction	Fraction (%)
11	$\nu_\mu + p \to \mu^- + p + \pi^+$	48.23
16	$\nu_\mu + N \to \mu^- + N + \pi^+$	36.87
13	$\nu_\mu + n \to \mu^- + n + \pi^+$	9.93
21	$\nu_\mu + (n\|p) \to \mu^- + (n\|p) + \text{multi-}\pi$	1.87
1	$\nu_\mu + n \to \mu^- + p$	1.32
12	$\nu_\mu + n \to \mu^- + p + \pi^0$	1.25
26	$\nu_\mu + (n\|p) \to \mu^- + (n\|p) + \text{mesons}$	0.50
22	$\nu_\mu + n \to \mu^- + p + \eta^0$	0.02

Table 7.12: Fiducial ν_μ-induced post-FSI signal after cuts composition (in terms of the before-FSI NEUT modes) for PØD water-out NEUT MCP5E sample for both PØD contained and non-contained selections combined. Fractions are calculated with respect to the total water-out signal in fiducial. Rows are sorted in the order of decreasing percetange.

The out-of-fiducial (OOF) background is also dominated by ν_μ which can be seen in Tab. 7.14. All of the backgrounds shown in Tabs. 7.13 and 7.14 are subject to the flux normalization uncertainty, which is described in Sec. 7.1.4 of this monograph. The OOF background percentages are different for water-in and water-out samples. However, a consistent treatment of associated systematic uncertainties accounts for the difference through the OOF volume background systematic uncertainty evaluation. A more detailed ν_μ and $\overline{\nu}_\mu$ fiducial background composition is shown in Tabs. 7.15, 7.16, 7.17 and 7.18. However, the signal and background numbers of events in data and MC are not necessarily the same,

	Water-in	Water-out
Background type	Fraction (%)	Fraction (%)
Fiducial ν_μ	86.51	78.61
Fiducial $\overline{\nu}_\mu$	6.12	6.70
Fiducial ν_e	1.40	1.31
Fiducial $\overline{\nu}_e$	0.1	0.17
Out-of-fiducial	5.87	13.21

Table 7.13: Background composition in terms of neutrino flavors and fiducial/out-of-fiducial categories for Run 4 water-in and Run 3 water-out events after the cuts. The numbers are for both contained and non-contained selections combined.

$$S^{MC} = S^{data} + \delta S, \qquad B^{MC} = B^{data} + \delta B, \tag{7.7}$$

	Water-in	Water-out
OOF Background	Fraction (%)	Fraction (%)
ν_μ	95.44	94.08
non-ν_μ	4.56	5.92

Table 7.14: OOF background composition in terms of neutrino flavors. Fractions are calculated with respect to the total OOF background number of events after the selections cuts, for Run 4 PØD water-in and Run 3 water-out running.

NEUT mode	Reaction	Fraction (%)
1	$\nu_\mu + n \to \mu^- + p$	38.62
11	$\nu_\mu + p \to \mu^- + p + \pi^+$	13.74
12	$\nu_\mu + n \to \mu^- + p + \pi^0$	6.99
13	$\nu_\mu + n \to \mu^- + n + \pi^+$	4.06
17	$\nu_\mu + n \to \mu^- + p + \gamma$	0.05
21	$\nu_\mu + (n\|p) \to \mu^- + (n\|p) + \text{multi-}\pi$	10.85
22	$\nu_\mu + n \to \mu^- + p + \eta^0$	0.90
23	$\nu_\mu + n \to \mu^- + \Lambda + K^+$	0.12
26	$\nu_\mu + (n\|p) \to \mu^- + (n\|p) + \text{mesons}$	1.07
31	$\nu_\mu + n \to \nu_\mu + n + \pi^0$	1.10
32	$\nu_\mu + p \to \nu_\mu + p + \pi^0$	1.67
33	$\nu_\mu + n \to \nu_\mu + p + \pi^-$	1.05
34	$\nu_\mu + p \to \nu_\mu + n + \pi^+$	0.54
36	$\nu_\mu + N \to \nu_\mu + N + \pi^0$	1.72
38	$\nu_\mu + n \to \nu_\mu + n + \gamma$	0.01
39	$\nu_\mu + p \to \nu_\mu + p + \gamma$	0.02
41	$\nu_\mu + (n\|p) \to \nu_\mu + (n\|p) + \text{multi-}\pi$	2.36
42	$\nu_\mu + n \to \nu_\mu + n + \eta^0$	0.17
43	$\nu_\mu + p \to \nu_\mu + p + \eta^0$	0.18
44	$\nu_\mu + n \to \nu_\mu + \Lambda + K^0$	0.05
45	$\nu_\mu + p \to \nu_\mu + \Lambda + K^+$	0.04
46	$\nu_\mu + (n\|p) \to \nu_\mu + (n\|p) + \text{mesons}$	0.80

Table 7.15: Fiducial ν_μ-induced post-FSI background after cuts composition (in terms of before-FSI NEUT modes) for PØD water-in NEUT MCP5E sample for both contained and non-contained selections combined. Fractions are calculated with respect to the total water-in background. Rows are sorted in the order of decreasing percentage.

where δS and δB are the discrepancies between data and MC for signal and background, respectively. This could be due to statistical uncertainties, new physics, or other reasons (e.g systematic bias, a bug in the MC simulation, or systematic uncertainties in the physics models). Statistical and systematic uncertainties relevant to this analysis are discussed in detail in Sec. 7.1.5 and 7.1.4. MC corrections that are utilized in this analysis are discussed in Sec. 7.1.2.

NEUT Code	Reaction	Fraction (%)
-46	$\overline{\nu}_\mu + (n\|p) \rightarrow \overline{\nu}_\mu + (n\|p) + \text{mesons}$	0.05
-43	$\overline{\nu}_\mu + p \rightarrow \overline{\nu}_\mu + p + \eta^0$	0.01
-41	$\overline{\nu}_\mu + (n\|p) \rightarrow \overline{\nu}_\mu + (n\|p) + \text{multi-}\pi$	0.12
-36	$\overline{\nu}_\mu + N \rightarrow \overline{\nu}_\mu + N + \pi^0$	0.11
-34	$\overline{\nu}_\mu + p \rightarrow \overline{\nu}_\mu + n + \pi^+$	0.03
-33	$\overline{\nu}_\mu + n \rightarrow \overline{\nu}_\mu + p + \pi^-$	0.04
-32	$\overline{\nu}_\mu + p \rightarrow \overline{\nu}_\mu + p + \pi^0$	0.04
-31	$\overline{\nu}_\mu + n \rightarrow \overline{\nu}_\mu + n + \pi^0$	0.06
-26	$\overline{\nu}_\mu + (n\|p) \rightarrow \mu^+ + (n\|p) + \text{mesons}$	0.02
-23	$\overline{\nu}_\mu + p \rightarrow \mu^+ + \Lambda + K^0$	0.01
-22	$\overline{\nu}_\mu + p \rightarrow \mu^+ + n + \eta^0$	0.06
-21	$\overline{\nu}_\mu + (n\|p) \rightarrow \mu^+ + (n\|p) + \text{multi-}\pi$	0.54
-16	$\overline{\nu}_\mu + N \rightarrow \mu^+ + N + \pi^-$	2.07
-13	$\overline{\nu}_\mu + p \rightarrow \mu^+ + p + \pi^-$	0.74
-12	$\overline{\nu}_\mu + p \rightarrow \mu^+ + n + \pi^0$	0.35
-11	$\overline{\nu}_\mu + n \rightarrow \mu^+ + n + \pi^-$	1.46
-1	$\overline{\nu}_\mu + p \rightarrow \mu^+ + n$	0.39

Table 7.16: Fiducial $\overline{\nu}_\mu$-induced background composition for PØD water-in MC sample for both contained and non-contained selections combined. Fractions are calculated with respect to the total water-in background.

Background Subtraction

Background prediction from MC, B^{MC}, or simply B, with assigned statistical and systematic uncertainties, can be used to remove the background from the data, i.e., via background subtraction and extract the sought-after signal. The total background comprises nominal MC background and sand muon MC background.

In this analysis, $S^{data}_{w|a,\ i}$, the number of selected signal events per T2K Run data set i can be extracted via background subtraction, where correction factors are applied to the backgrounds:

$$S^{data}_{w|a,\ i} = N^{data}_{w|a,\ i} - C^{mass}_{w|a,\ i} C^{sp}_{w|a,\ i} B_{w|a,\ i} - C^{sb}_{w|a,\ i} B^{sand}_{w|a,\ i}, \tag{7.8}$$

The lower indices w and a stand for water-in and air-in (water-out) samples accordingly, $C^{mass}_{w|a,\ i}$ and $C^{sp}_{w|a,\ i}$ are MC detector fiducial mass correction and MC sand muon pile-up/interference correction correspondingly, $C^{sb}_{w|a,\ i}$ is the sand muon background normalization correction.

The MC background predictions have large uncertainties that are propagated to the result. These uncertainties can be reduced by constraining the MC background predictions with data, but this procedure was not employed in the current version of the analysis. It is on the list of future improvements.

Signal Selection Efficiency

To extract the total number of signal events in the data, the selected number of signal events S^{data} needs to be corrected for the selection efficiency, i.e, signal events

NEUT mode	Reaction	Fraction (%)
1	$\nu_\mu + n \rightarrow \mu^- + p$	40.93
11	$\nu_\mu + p \rightarrow \mu^- + p + \pi^+$	11.59
12	$\nu_\mu + n \rightarrow \mu^- + p + \pi^0$	5.68
13	$\nu_\mu + n \rightarrow \mu^- + n + \pi^+$	3.93
21	$\nu_\mu + (n\|p) \rightarrow \mu^- + (n\|p) + \text{multi-}\pi$	6.42
22	$\nu_\mu + n \rightarrow \mu^- + p + \eta^0$	0.27
23	$\nu_\mu + n \rightarrow \mu^- + \Lambda + K^+$	0.15
26	$\nu_\mu + (n\|p) \rightarrow \mu^- + (n\|p) + \text{mesons}$	0.57
31	$\nu_\mu + n \rightarrow \nu_\mu + n + \pi^0$	1.11
32	$\nu_\mu + p \rightarrow \nu_\mu + p + \pi^0$	1.26
33	$\nu_\mu + n \rightarrow \nu_\mu + p + \pi^-$	1.17
34	$\nu_\mu + p \rightarrow \nu_\mu + n + \pi^+$	0.61
36	$\nu_\mu + N \rightarrow \nu_\mu + N + \pi^0$	1.59
38	$\nu_\mu + n \rightarrow \nu_\mu + n + \gamma$	0.02
41	$\nu_\mu + (n\|p) \rightarrow \nu_\mu + (n\|p) + \text{multi-}\pi$	2.09
42	$\nu_\mu + n \rightarrow \nu_\mu + n + \eta^0$	0.03
43	$\nu_\mu + p \rightarrow \nu_\mu + p + \eta^0$	0.02
44	$\nu_\mu + n \rightarrow \nu_\mu + \Lambda + K^0$	0.09
45	$\nu_\mu + p \rightarrow \nu_\mu + \Lambda + K^+$	0.03
46	$\nu_\mu + (n\|p) \rightarrow \nu_\mu + (n\|p) + \text{mesons}$	0.55

Table 7.17: Fiducial ν_μ-induced post-FSI background after cuts composition (in terms of before-FSI NEUT modes) for PØD water-out MC sample for both contained and non-contained selections combined. Fractions are calculated with respect to the total water-out background.

NEUT mode	Reaction	Fraction (%)
-36	$\overline{\nu}_\mu + N \rightarrow \overline{\nu}_\mu + N + \pi^0$	0.17
-34	$\overline{\nu}_\mu + p \rightarrow \overline{\nu}_\mu + n + \pi^+$	0.02
-33	$\overline{\nu}_\mu + n \rightarrow \overline{\nu}_\mu + p + \pi^-$	0.07
-32	$\overline{\nu}_\mu + p \rightarrow \overline{\nu}_\mu + p + \pi^0$	0.06
-31	$\overline{\nu}_\mu + n \rightarrow \overline{\nu}_\mu + n + \pi^0$	0.02
-26	$\overline{\nu}_\mu + (n\|p) \rightarrow \mu^+ + (n\|p) + \text{mesons}$	0.04
-22	$\overline{\nu}_\mu + p \rightarrow \mu^+ + n + \eta^0$	0.09
-21	$\overline{\nu}_\mu + (n\|p) \rightarrow \mu^+ + (n\|p) + \text{multi-}\pi$	0.35
-16	$\overline{\nu}_\mu + N \rightarrow \mu^+ + N + \pi^-$	2.29
-13	$\overline{\nu}_\mu + p \rightarrow \mu^+ + p + \pi^-$	0.72
-12	$\overline{\nu}_\mu + p \rightarrow \mu^+ + n + \pi^0$	0.38
-11	$\overline{\nu}_\mu + n \rightarrow \mu^+ + n + \pi^-$	2.03
-1	$\overline{\nu}_\mu + p \rightarrow \mu^+ + n$	0.46

Table 7.18: Fiducial $\overline{\nu}_\mu$-induced background composition for PØD water-out MC sample for both contained and non-contained selections combined. Fractions are calculated with respect to the total water-out background.

that did not pass the selection cuts need to be recovered.

The signal selection efficiency $\epsilon_{w|a}$ is predicted by MC and can be defined for water-in and air-in samples similarly:

$$\epsilon \equiv \epsilon^{MC} = \frac{S^{sel}}{s^{gen}}, \tag{7.9}$$

where S^{sel} is the number of selected MC signal events, and s^{gen} is the total number of the generated signal events in the Monte Carlo true PØD fiducial volume.

The efficiency of the selection is, in general, a function of true neutrino energy E_ν, since the number of selected events S^{sel} is a function of E_ν:

$$\epsilon(E_\nu) = \frac{S^{sel}(E_\nu)}{s^{gen}}, \qquad \epsilon_i = \frac{S_i^{sel}}{s^{gen}}, \tag{7.10}$$

where i is the true neutrino energy bin index, S_i^{sel} is the number of the selected signal events in true bin i. This efficiency is a function of the detector's response, particle detection thresholds, and cuts used. In the regions where the efficiency is zero, i.e., bins with no data events, a fully model dependent efficiency correction is utilized.

For the purposes of this one-bin analysis, ϵ, a fully model dependent single bin efficiency correction per T2K run is employed:

$$\epsilon \equiv \langle \epsilon \rangle = \frac{1}{s^{gen}} \cdot \sum_i S_i^{sel}, \tag{7.11}$$

though it is required to be corrected by C^{sand} in order to account for the sand interference effect present in the data but not simulated in the MC. C^{sand} is a function of the T2K beam power, hence a function of T2K run, and the reason why each run must have its' own ϵ correction. Then the efficiency-corrected number of signal events per T2K run, s^{data}, can be obtained via

$$s^{data} = \frac{S^{data}}{C^{sand} \cdot \epsilon}, \tag{7.12}$$

where S^{data} is the signal after cuts, resulting from Eq. (7.8).

MC predictions for water-in and water-out signal selection efficiencies per Run are presented in Tab. 7.35. Statistical and systematic uncertainties on efficiencies are discussed in Sec. 7.1.5 and 7.1.4 of this monograph.

Flux

T2K flux prediction $\Phi(E_\nu)$ is based on a FLUKA [165] and GEANT3 [166] MC simulation, which uses the proton beam monitor data as an input. The simulated flux is tuned or reweighted to pion and kaon production data. The details of flux simulation and subsequent reweighting are discussed in depth in the T2K flux paper [167].

In general, there are 4 types of neutrinos contributing to the T2K flux at ND280, i.e. ν_μ, $\overline{\nu}_\mu$, ν_e and $\overline{\nu}_e$, all of which can contribute to the measurement background, but only ν_μ part of the flux contributes to the signal.

After the background subtraction and efficiency correction, the obtained number of CC1π^+ signal events s^{data}, is a function of incident neutrino flux, $\Phi(E_\nu)$ $\left[\frac{\nu_\mu}{cm^2}\right]$, and the signal cross section $\sigma(E_\nu)$. In case the flux prediction is quantized into discrete bins of true neutrino energy, Φ_i, the following relationships are employed:

$$\Phi = \int \frac{\partial\Phi(E_\nu)}{\partial E_\nu} dE_\nu \equiv \sum_i \frac{\Delta\Phi_i}{\Delta E_i}\Delta E_i,$$

$$\int \sigma(E_\nu)\frac{\partial\Phi(E_\nu)}{\partial E_\nu} dE_\nu \equiv \sum_i \sigma_i\frac{\Delta\Phi_i}{\Delta E_i}\Delta E_i, \tag{7.13}$$

and Eq. (7.5) becomes:

$$\langle\sigma_s\rangle = \frac{s^{data}}{T\cdot\Phi} = \frac{1}{T\cdot\Phi}\cdot\sum_i \sigma_i\Delta\Phi_i, \tag{7.14}$$

where i is the true neutrino energy bin index, σ_i is the signal cross section average value for bin i, $\Delta\Phi_i$ is the incident flux in bin i, ΔE_i is the bin i width. More details about the actual cross section calculation follow in Sec. 7.1.3. Flux tuning 11b v3.2 is used to reweight the nominal ND280 MC. The flux tuning event weights are shown in Fig. 7.8.

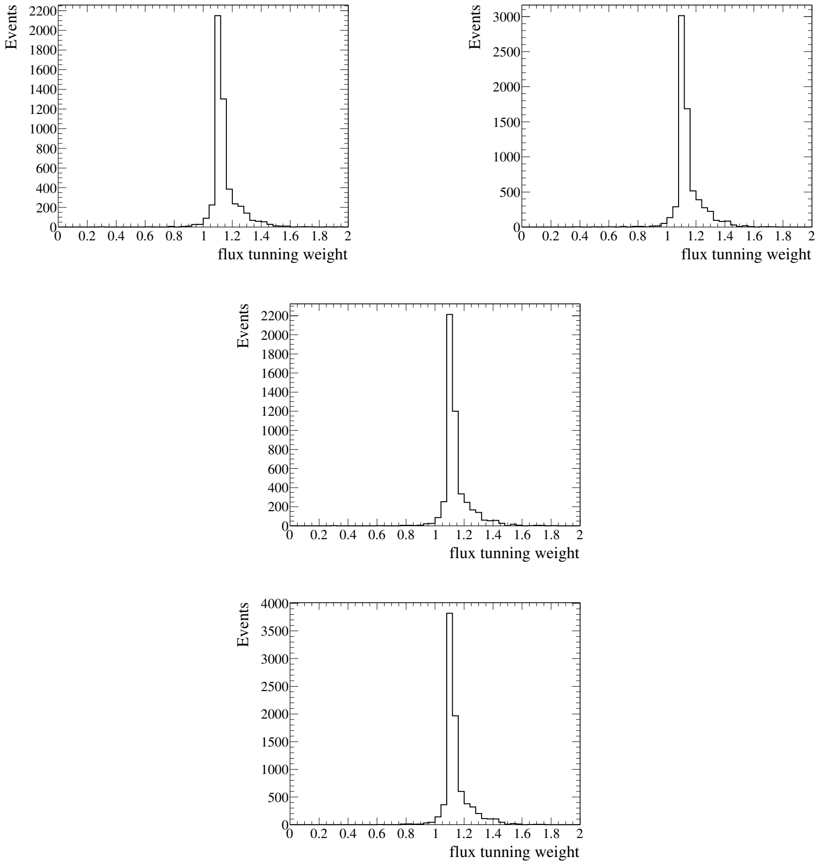

Figure 7.8: Flux tuning weights for events selected after cuts: Run 1 water-in (top-left), Run 2 water-in (top-right), Run 2 water-out (bottom-left), Run 3 water-out (bottom-right). Tuning weights for Run 4 water-in and water-out look similar and are not presented here.

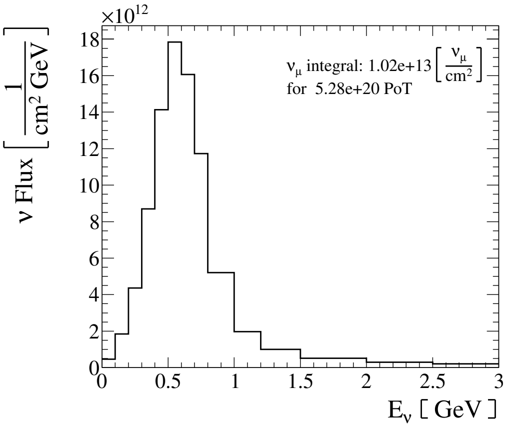

Figure 7.9: Tuned MC ν_μ flux prediction normalized to the combined data POT of Runs 1, 2 and 4 with the PØD detector in the water-in configuration. The PØD water-out configuration POT is not considered since there is no water present in the detector, hence no ν_μ interactions on $\mathrm{H_2O}$ as a target. Flux is normalized to the total PØD water-in data POT after data quality cuts, i.e. good PØD data, and no requirement on the TPC, FGD, or ECALs data quality. The true energy binning scheme is described in Tab. 7.24.

The total tuned ν_μ flux prediction for PØD water-in running periods during T2K Runs 1, 2, and 4 scaled to the corresponding data POT is shown in Fig. 7.9. The flux prediction mentioned above comes with uncertainties that arise from many different sources, including but not limited to hadron production, beam alignment, horn absolute current, etc. These sources and the sizes of corresponding uncertainties are discussed in depth in the T2K flux paper [167]. The propagation of flux uncertainty through this measurement is described in detail in Sec. 7.1.4.

Interacting Targets

The number of interacting targets, $T_{\mathrm{H_2O}}$, is taken to be the number of nucleons in water bags in the fiducial volume of the PØD and can be calculated using the mass of the water in the PØD fiducial volume shown in Tab. 7.19 with

$$T_{\mathrm{H_2O}} = \frac{1}{M_{\mathrm{H_2O}}} \cdot m_{\mathrm{H_2O}} \cdot (n_n + n_p) \cdot N_a = 1.15773^{30} \text{ nucleons}, \tag{7.15}$$

where $M_{\mathrm{H_2O}}$ is the molar mass of water, $m_{\mathrm{H_2O}}$ [162] is the mass of water in the PØD fiducial volume, n_n and n_p are the numbers of neutrons and protons, respectively, per water molecule, and N_a is the Avogadro's constant. The values of constants used can be found in Tab. 7.20.

Systematic uncertainties in the mass of the PØD and their propagation through the measurement are discussed in Sec. 7.1.4.

Water-in/Water-out Subtraction

The PØD detector design offers a unique possibility to add and remove water from its fiducial volume, which provides two detector configurations, i.e., water-in (w) and water-out (a), and consequently enables a cross-section measurement on water, via a water-out statistical event rate subtraction.

Mass [kg]	RDP5D	MCP5E
m_w	5480.30 ± 37.40	5393.22 ± 0.56
m_a	3578.30 ± 33.80	3469.14 ± 0.55
$m_{\mathrm{H_2O}}$	1902.00 ± 16.00	1924.08 ± 0.36

Table 7.19: The fiducial mass of the PØD, m_w and m_a, for water-in and water-out configurations, respectively, and $m_{\mathrm{H_2O}}$. The fiducial water mass is shown for data (RDP5D) versus MC (MCP5E). Uncertainty on $m_{\mathrm{H_2O}}$ for data was obtained via an independent measurement and is explained in T2K-TN-073 [162].

$M_{\mathrm{H_2O}}$	0.01801528	$\left[\frac{kg}{mol}\right]$
N_a	$6.02214129(27) \times 10^{23}$	$[mol^{-1}]$
n_n	8	
n_p	10	

Table 7.20: Constants used in the calculation of $T_{\mathrm{H_2O}}$.

Advantages and Disadvantages

The main advantage of the water-in/water-out subtraction method is the ability to measure the cross sections on a single target material, in this case, water. There is also a significant reduction of systematic uncertainties, e.g., due to the unknown size of the cross section on brass, lead, and other non-water materials. Since the cross sections on these targets are the same for water-in and water-out running the subtraction procedure allows us to subtract such events without worrying about associated systematic uncertainties.

The most significant disadvantage is the increased statistical uncertainty involved in subtracting two large numbers.

Another potential disadvantage of this analysis technique is that it makes it difficult to perform a multiple-bin analysis, since the detector density is different for the two detector configurations, which leads to different detector's responses for the two samples. Thus the events passing the same cuts for the water-in and water-out data sets will occupy different phase space parts.

Water-in Events

In the case of water-in running the signal events in the fiducial volume of the PØD can occur on scintillator, water, brass, etc. The total number of the signal events in the fiducial volume for data can be obtained via:

$$s_w = s_w^{\mathrm{H_2O}} + s_w^{scint}, \tag{7.16}$$

where $s_w^{\mathrm{H_2O}}$ is the total number of signal events on water, s_w^{scint} is the total number of signal events on scintillator, brass, etc. Later in the text s_w^{scint} will be referred to as the number of signal events on scintillator for simplicity.

The purpose of this measurement is to be able to obtain $s_w^{\mathrm{H_2O}}$, which is the total number of signal events on water exclusively in data:

$$s_w^{\mathrm{H_2O}} = s_w - s_w^{scint} = \sum_i \frac{N_{w,i} - C_{w,i}^{mass} C_{w,i}^{sand} B_{w,i}}{C_{w,i}^{sand} \epsilon_{w,i}} - s_w^{scint}, \tag{7.17}$$

where the index i denotes PØD water-in datasets collected during T2K Runs 1, 2 and 4, with $C_{w,i}^{mass}$ and $C_{w,i}^{sand}$ calculated for each dataset. The number of signal events on scintillator s_w^{scint} can be expressed via:

$$s_w^{scint} = \sigma^{scint} \cdot \Phi_w \cdot T^{scint}, \tag{7.18}$$

where σ^{scint} is the signal cross-section on scintillator, Φ_w is the integrated flux for the combined water-in running period, T^{scint} is the number of target nucleons in the scintillator. MC predictions for the signal events after cuts occurring on various target nuclei are shown in Tab. 7.21.

	Water-in Runs		
Element	1	2	4
Carbon	45.0 %	45.7 %	46.3 %
Oxygen	26.5 %	26.2 %	26.5 %
Hydrogen	20.7 %	20.0 %	19.5 %
Copper	6.5 %	7.2 %	6.6 %
Other	1.2 %	0.9 %	1.2 %

Table 7.21: MC predictions of percentages of signal events occurring on specific targets for the PØD water-in configuration.

Water-out Events

In the case of the PØD water-out running the neutrino interactions in the fiducial volume of the PØD occur almost exclusively in the scintillator, with some interactions happening on brass and other materials (Tab. 7.22). The total number of signal events in the fiducial volume for data can be found with

$$s_a = \sum_j \frac{N_{a,j} - C_{a,j}^{mass} C_{a,j}^{sand} B_{a,j}}{C_{a,j}^{sand} \epsilon_{a,j}}, \quad s_a^{scint} = \sigma^{scint} \cdot \Phi_a \cdot T^{scint}, \quad s_a = s_a^{scint}, \tag{7.19}$$

where index j denotes PØD water-out datasets collected during T2K Runs 2, 3, and 4, with each dataset having a different set of corrections, and where σ^{scint} is the signal cross section on scintillator assumed to be the same for water-in and water-out running periods. The flux Φ_a is integrated for the water-out period and T^{scint} is the number of target nucleons in the scintillator, which is the same for both water-in and water-out running periods.

If the ratio of the total number of signal events for water-in and water-out running is taken, σ^{scint} and T^{scint} naturally cancel out, and the equation with

$$\frac{s_w^{scint}}{s_a^{scint}} = \frac{\Phi_w}{\Phi_a}, \tag{7.20}$$

is left which is the ratio of integrated fluxes for water-in and water-out running periods. It can be further reduced to the water-in to water-out ratio of POTs, R_p,

$$\frac{s_w^{scint}}{s_a^{scint}} = \frac{\phi_w \cdot P_w}{\phi_a \cdot P_a} = \frac{P_w}{P_a} = R_p, \tag{7.21}$$

if the flux per POT is the same for both cases $\phi_w = \phi_a$, which is assumed to be the case in this analysis.

MC predictions for the signal events after cuts occurring on various target nuclei are shown in Tab. 7.22.

	Water-out Runs		
Element	2	3	4
Carbon	73.6 %	74.2 %	74.2 %
Oxygen	0.17 %	0.2 %	0.2 %
Hydrogen	13.0 %	13.5 %	13.5 %
Copper	11.4 %	10.1 %	10.1 %
Other	1.8 %	1.9 %	1.9 %

Table 7.22: MC predictions of percentages of signal events occurring on specific targets for the PØD water-out configuration.

Subtracting Events on Non-water

Using Eq. (7.16) through (7.21), one can subtract events that are happening on the non-water target materials resulting in the observed number of events that are on water exclusively:

$$s_w^{\mathrm{H_2O}} = s_w - R_p \cdot s_a = \sum_i \frac{N_{w,i} - C_{w,i}^{mass} C_{w,i}^{sand} B_{w,i}}{C_{w,i}^{sand} \epsilon_{w,i}} - R_p \sum_j \frac{N_{a,j} - C_{a,j}^{mass} C_{a,j}^{sand} B_{a,j}}{C_{a,j}^{sand} \epsilon_{a,j}}. \tag{7.22}$$

Cross section on Water

Finally, using Eq. (7.22), the flux-averaged absolute CC1π^+ cross section on water, $\langle \sigma_{\nu_\mu \mathrm{CC}1\pi^+} \rangle_\Phi$, can be written as

$$\begin{aligned} \langle \sigma_{\nu_\mu \mathrm{CC}1\pi^+} \rangle_\Phi &= \frac{s^{\mathrm{H_2O}}}{\Phi_w \cdot \mathrm{T}^{\mathrm{H_2O}}} \\ &= \frac{1}{\Phi_w \cdot \mathrm{T}^{\mathrm{H_2O}}} \cdot \left(\sum_i \frac{N_{w,i} - C_{w,i}^{mass} C_{w,i}^{sand} B_{w,i}}{C_{w,i}^{sand} \epsilon_{w,i}} - R_p \sum_j \frac{N_{a,j} - C_{a,j}^{mass} C_{a,j}^{sand} B_{a,j}}{C_{a,j}^{sand} \epsilon_{a,j}}. \right), \end{aligned} \tag{7.23}$$

where $\mathrm{T}^{\mathrm{H_2O}}$ is the number of nucleons in the water targets in the fiducial volume of the PØD. Interactions on other materials (e.g., scintillator) are not considered since they are subtracted out in the numerator. Thus the w index was dropped for $s^{\mathrm{H_2O}}$ for convenience.

7.1.4 Systematic error estimation

This section describes the propagation of systematic uncertainties performed in the analyses. All of the uncertainties were propagated using one of the two approaches: analytic or numerical. In certain cases, where it was viable, both methods were employed for cross-checking and validation purposes.

Analytic error propagation

The total uncertainty on the cross section, $\delta\langle\sigma_{\nu_\mu \mathrm{CC}1\pi^+}\rangle_\Phi$ or simply $\delta\langle\sigma\rangle_\Phi$, can be determined analytically, via standard uncertainty propagation valid for a function of uncorrelated variables, i.e., by finding the standard deviation of the cross section function $\langle\sigma_{\nu_\mu \mathrm{CC}1\pi^+}\rangle_\Phi$ described by Eq. (7.23), resulting in:

$$\delta\langle\sigma\rangle_\Phi = \sqrt{\left(\frac{\partial\langle\sigma\rangle_\Phi}{\partial s^{\mathrm{H_2O}}}\right)^2 (\delta s^{\mathrm{H_2O}})^2 + \left(\frac{\partial\langle\sigma\rangle_\Phi}{\partial \Phi_w}\right)^2 (\delta\Phi_w)^2 + \left(\frac{\partial\langle\sigma\rangle_\Phi}{\partial \mathrm{T_{H_2O}}}\right)^2 (\delta\mathrm{T_{H_2O}})^2}, \tag{7.24}$$

where $\delta s^{\mathrm{H_2O}}$, $\delta\Phi_w$, and $\delta\mathrm{T_{H_2O}}$ are the uncertainties on the number of events on water, $s^{\mathrm{H_2O}}$, integrated flux, Φ_w, and the number of interacting nucleons, $\mathrm{T_{H_2O}}$, respectively, all of which are considered to be uncorrelated.

The first term in Eq. (7.24) describes the statistical and systematic uncertainties on the number of events on water, $s^{\mathrm{H_2O}}$, while the last two terms describe uncertainties associated with the flux and the number of interacting targets, correspondingly.

The partial derivatives in Eq. (7.24) are reduced to

$$\frac{\partial\langle\sigma\rangle_\Phi}{\partial s^{\mathrm{H_2O}}} = \frac{1}{\Phi_w \cdot \mathrm{T_{H_2O}}}, \tag{7.25}$$

$$\frac{\partial\langle\sigma\rangle_\Phi}{\partial \Phi_w} = -\frac{s^{\mathrm{H_2O}}}{\Phi_w^2 \cdot \mathrm{T_{H_2O}}}, \tag{7.26}$$

$$\frac{\partial\langle\sigma\rangle_\Phi}{\partial \mathrm{T_{H_2O}}} = -\frac{s^{\mathrm{H_2O}}}{\Phi_w \cdot \mathrm{T_{H_2O}^2}}, \tag{7.27}$$

yielding

$$\delta\langle\sigma\rangle_\Phi = \langle\sigma_{\nu_\mu}\rangle_\Phi \cdot \sqrt{\left(\frac{1}{s}\right)^2 \cdot (\delta s)^2 + \left(\frac{1}{\Phi_w}\right)^2 \cdot (\delta\Phi_w)^2 + \left(\frac{1}{\mathrm{T}}\right)^2 \cdot (\delta\mathrm{T})^2}, \tag{7.28}$$

where the $\mathrm{H_2O}$ index in $s^{\mathrm{H_2O}}$ and $\mathrm{T_{H_2O}}$ was dropped for convenience.

The flux systematic uncertainty was propagated via MC reweighting, which is described later in the current Section, therefore the second term in Eq. (7.28) will be ignored. The last term, which will be shown to be small compared to other sources of uncertainty, is also ignored in this section but revisited in Sec. 7.1.2, resulting in rewriting Eq. (7.28) in a simpler form as

$$\frac{\delta\langle\sigma\rangle_\Phi}{\langle\sigma_{\nu_\mu}\rangle_\Phi} = \frac{\delta s^{\mathrm{H_2O}}}{s^{\mathrm{H_2O}}}. \tag{7.29}$$

The uncertainty on the number of signal events on water, $s^{\mathrm{H_2O}}$, described by Eq. (7.22), can be expressed as

$$\delta s^{\mathrm{H_2O}} = \sqrt{(\delta s_w)^2 + R_p^2 \cdot (\delta s_a)^2 - 2 \cdot R_p \cdot \rho \cdot \delta s_w \delta s_a}, \tag{7.30}$$

where ρ is the water-in to water-out correlation coefficient, which can be ranging from 0, in the case of statistical uncertainties, to 1 (i.e., 100% correlation). For example, ρ is 1 in the case of the flux systematic uncertainty.

Combining Eqs. (7.17) - (7.19), δs_w and δs_a can be obtained via

$$\delta s_w = \sqrt{\sum_i \left(\left(\frac{\partial s_w}{\partial N_{w,i}} \right)^2 (\delta N_{w,i})^2 + \left(\frac{\partial s_w}{\partial B_{w,i}} \right)^2 (\delta B_{w,i})^2 + \left(\frac{\partial s_w}{\partial \epsilon_{w,i}} \right)^2 (\delta \epsilon_{w,i})^2 \right)}, \tag{7.31}$$

$$\delta s_a = \sqrt{\sum_j \left(\left(\frac{\partial s_a}{\partial N_{a,j}} \right)^2 (\delta N_{a,j})^2 + \left(\frac{\partial s_a}{\partial B_{a,j}} \right)^2 (\delta B_{a,j})^2 + \left(\frac{\partial s_a}{\partial \epsilon_{a,j}} \right)^2 (\delta \epsilon_{a,j})^2 \right)}, \tag{7.32}$$

where the partial derivatives are reduced to

$$\frac{\partial s_w}{\partial N_{w,i}} = \frac{1}{C^{sand}_{w,i}\epsilon_{w,i}}, \frac{\partial s_a}{\partial N_{a,j}} = \frac{1}{C^{sand}_{a,j}\epsilon_{a,j}}, \tag{7.33}$$

$$\frac{\partial s_w}{\partial B_{w,i}} = -\frac{C^{mass}_{w,i}}{\epsilon_{w,i}}, \frac{\partial s_a}{\partial B_{a,j}} = -\frac{C^{mass}_{a,j}}{\epsilon_{a,j}}, \tag{7.34}$$

$$\frac{\partial s_w}{\partial \epsilon_{w,i}} = -\frac{N_{w,i} - C^{mass}_{w,i}C^{sand}_{w,i}B_{w,i}}{C^{sand}_{w,i}\epsilon^2_{w,i}}, \frac{\partial s_a}{\partial \epsilon_{a,j}} = -\frac{N_{a,j} - C^{mass}_{a,j}C^{sand}_{a,j}B_{a,j}}{C^{sand}_{a,j}\epsilon^2_{a,j}}, \tag{7.35}$$

giving

$$\begin{aligned}(\delta s_w)^2 = \sum_i \Big(\Big(&\frac{1}{C^{sand}_{w,i}\epsilon_{w,i}} \Big)^2 (\delta N_{w,i})^2 + \Big(\frac{C^{mass}_{w,i}}{\epsilon_{w,i}} \Big)^2 (\delta B_{w,i})^2 \\ &+ \Big(\frac{N_{w,i} - C^{mass}_{w,i}C^{sand}_{w,i}B_{w,i}}{C^{sand}_{w,i}\epsilon^2_{w,i}} \Big)^2 (\delta \epsilon_{w,i})^2 \Big) \end{aligned} \tag{7.36}$$

for the uncertainty on the water-in number of signal events and

$$\begin{aligned}(\delta s_a)^2 = \sum_j \Big(\Big(&\frac{1}{C^{sand}_{a,j}\epsilon_{a,j}} \Big)^2 (\delta N_{a,j})^2 + \Big(\frac{C^{mass}_{a,j}}{\epsilon_{a,j}} \Big)^2 (\delta B_{a,j})^2 \\ &+ \Big(\frac{N_{a,j} - C^{mass}_{a,j}C^{sand}_{a,j}B_{a,j}}{C^{sand}_{a,j}\epsilon^2_{a,j}} \Big)^2 (\delta \epsilon_{a,j})^2 \Big) \end{aligned} \tag{7.37}$$

for water-out, where $\delta N_{w|a}$ denotes the Poisson statistical uncertainties on the number of events $N_{w|a}$ in data

$$\delta N_{w|a} = \sqrt{N_{w|a}},$$

and $\delta B_{w|a}$, $\delta \epsilon_{w|a}$ are uncertainties associated with the predicted backgrounds and selection efficiencies.

All systematic uncertainties on the numbers of water-in and water-out events are correlated to a greater or lesser level. In the case of flux, cross section, and FSI model systematic uncertainties, the correlations are handled in a consistent manner through uncertainty propagation via MC reweighting, and analytic uncertainty calculations were not necessary.

Those systematics that were propagated for water-in and water-out events analytically using Eq. (7.30), e.g., some of the detector systematics, were assumed to be either 100% correlated, or 100% uncorrelated, whichever gave the most conservative uncertainty. Inserting Eq. (7.36), (7.37) into Eq. (7.30), assuming no correlations between water-in and water-out uncertainties, $\rho = 0$, and using Eq. (7.29), the fractional uncertainty on the cross section can be obtained via

$$
\begin{aligned}
\frac{\delta\langle\sigma\rangle_\Phi}{\langle\sigma_{\nu_\mu}\rangle_\Phi} = {} & \frac{1}{\sum_i \frac{N_{w,i}-C^{mass}_{w,i}C^{sand}_{w,i}B_{w,i}}{C^{sand}_{w,i}\epsilon_{w,i}} - R_p\sum_j \frac{N_{a,j}-C^{mass}_{a,j}C^{sand}_{a,j}B_{a,j}}{C^{sand}_{a,j}\epsilon_{a,j}}} \times \\
& \Bigg(\sum_i \bigg(\Big(\frac{1}{C^{sand}_{w,i}\epsilon_{w,i}}\Big)^2 (\delta N_{w,i})^2 + \Big(\frac{C^{mass}_{w,i}}{\epsilon_{w,i}}\Big)^2 (\delta B_{w,i})^2 \\
& + \Big(\frac{N_{w,i}-C^{mass}_{w,i}C^{sand}_{w,i}B_{w,i}}{C^{sand}_{w,i}\epsilon^2_{w,i}}\Big)^2 (\delta\epsilon_{w,i})^2\bigg) + R_p^2 \cdot \sum_j \bigg(\Big(\frac{1}{C^{sand}_{a,j}\epsilon_{a,j}}\Big)^2 (\delta N_{a,j})^2 \\
& + \Big(\frac{C^{mass}_{a,j}}{\epsilon_{a,j}}\Big)^2 (\delta B_{a,j})^2 + \Big(\frac{N_{a,j}-C^{mass}_{a,j}C^{sand}_{a,j}B_{a,j}}{C^{sand}_{a,j}\epsilon^2_{a,j}}\Big)^2 (\delta\epsilon_{a,j})^2\bigg)\Bigg)^{\frac{1}{2}}. \qquad (7.38)
\end{aligned}
$$

Monte Carlo Reweighting

To propagate certain systematic uncertainties, MC reweighting methods can be utilized. There were two reweighting methods used in this analysis: event-by-event reweighting, using T2KReWeight, and bin-by-bin reweighting when dealing with histograms.

The bin-by-bin reweighting method used to propagate the flux model uncertainty is discussed in detail in this section, in part dedicated to the flux systematic uncertainty propagation. Event-by-event MC reweighting was accomplished via the T2KReWeight library and was used to propagate the cross section and FSI model systematic uncertanties, and is discussed in the part dedicated to the cross-section model systematics.

The general idea behind MC reweighting methods in this analysis is that the cross section can be recalculated for each variation i of a given model as follows

$$\langle\sigma_{\nu_\mu}\rangle^{(i)}_\Phi = \frac{s^{(i)}_{\mathrm{H_2O}}}{\Phi^{(i)}_w \cdot \mathrm{T}_{\mathrm{H_2O}}}, \qquad (7.39)$$

where $s^{(i)}_{\mathrm{H_2O}}$ is the number of signal events, $\Phi^{(i)}_w$ neutrino flux and $\mathrm{T}_{\mathrm{H_2O}}$ the number of target neutrinos. In theory, in Eq. (7.39), all three variables can change, but in practice, however, the number of target nucleons would stay the same when varying the flux or FSI models. RMS deviation of the reweighted cross-sections from the nominal central value can be quoted as a systematic uncertainty:

$$\delta\langle\sigma\rangle_\Phi = \sqrt{\frac{1}{k}\cdot\sum_i \left(\langle\sigma_{\nu_\mu}\rangle^{(i)}_\Phi - \langle\sigma_{\nu_\mu}\rangle^{\mathrm{nominal}}_\Phi\right)^2}, \qquad (7.40)$$

where k is the number of necessary model variations, $\langle\sigma_{\nu_\mu}\rangle^{(i)}_\Phi$ is the modified (thrown) cross section in i^th variation, and $\langle\sigma_{\nu_\mu}\rangle^{\mathrm{nominal}}_\Phi$ is the nominal value of the cross section.

Neutrino flux modeling uncertainty

This section describes the propagation of the flux systematic uncertainty through the analysis using the flux covariance matrix.

The flux covariance matrix, described in [167], which contains all of the flux uncertainty information necessary for this analysis, is presented in Fig. 7.10 in the form of a fractional covariance matrix for the T2K flux prediction at ND280, ignoring Super-Kamiokande.

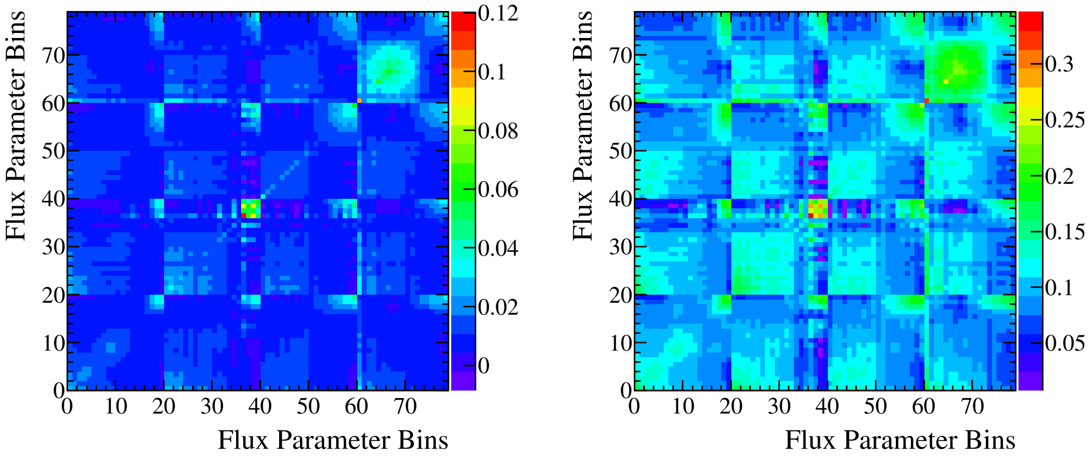

Figure 7.10: Fractional covariance (right) and error (left) matrices for the T2K flux prediction at ND280, version 11b v3.1. Matrices are 80 x 80, corresponding to 80 flux parameter bins of the flux prediction at ND280.

Ordering of the ND280 flux bins, or flux parameter bins, is shown in Tab. 7.23. Twenty neutrino energy bins were used in the variable-size flux binning for each of the contributing neutrino types, with finer binning around the T2K flux peak and coarser at the higher energy tail, are shown in Tab. 7.24.

ν_μ	$\bar{\nu}_\mu$	ν_e	$\bar{\nu}_e$
0 - 19	20 - 39	40 - 59	60 - 79

Table 7.23: Ordering of the flux parameter bins for the contributing neutrino types.

Cross section model systematics

Various neutrino cross section model parameters (knobs) implemented in the NEUT Monte Carlo generator and contributing to the signal and background predictions in this analysis have systematic uncertainties associated with them (Tab. 7.25). The detailed description of these parameters and the implementations of their reweighting procedure in `T2KReWeight` can be obtained from the T2K technical notes [168] and [169]. These uncertainties were propagated through the cross section measurement via MC reweighting, with event weights generated using the `T2KReWeight` library, and the procedure of applying the weights is outlined in this section.

Bin #	Low edge (GeV)	High edge (GeV)
0	0.0	0.1
1	0.1	0.2
2	0.2	0.3
3	0.3	0.4
4	0.4	0.5
5	0.5	0.6
6	0.6	0.7
7	0.7	0.8
8	0.8	1.0
9	1.0	1.2
10	1.2	1.5
11	1.5	2.0
12	2.0	2.5
13	2.5	3.0
14	3.0	3.5
15	3.5	4.0
16	4.0	5.0
17	5.0	7.0
18	7.0	10.0
19	10.0	30.0

Table 7.24: True neutrino energy bins used in the variable-size flux binning, which corresponds to the flux histogram shown in Fig. 7.9.

Parameter Name	Variable	Frac. σ	$\delta\epsilon$	δB
NEUT M_a CCQE shape	NXsec_MaCCQEshape	0.165289	yes	yes
NEUT M_a resonant shape	NXsec_MaRESshape	0.165289	yes	yes
NEUT π-less Δ decay norm.	NSystNucl_PilessDcyRES	0.2	no	yes
NIWG Δ mass mean	NIWGDeltaMass_mean	0.1	yes	yes
NIWG Δ mass width	NIWGDeltaMass_width	0.52	yes	yes
NIWG 2012a CCQE E0 norm.	NIWG2012a_ccqeE0	0.11	yes	yes
NIWG 2012a CCQE E1 norm.	NIWG2012a_ccqeE1	0.3	yes	yes
NIWG 2012a CCQE E2 norm.	NIWG2012a_ccqeE2	0.3	yes	yes
NIWG 2012a CC1π E0 norm.	NIWG2012a_cc1piE0	0.21	yes	yes
NIWG 2012a CC1π E1 norm.	NIWG2012a_cc1piE1	0.4	yes	yes
NIWG 2012a NC1π E0 norm.	NIWG2012a_nc1piE0	0.3	no	yes
NIWG 2012a NC1π^0 E0 norm.	NIWG2012a_nc1pi0E0	0.31	no	yes
NIWG 2012a CC multi-π E0 norm.	NIWG2012a_ccmultipiE0	0.25	yes	yes
NIWG 2012a CCDIS E0 norm.	NIWG2012a_ccdisE0	0.25	yes	yes
NIWG 2012a CC coherent E0 norm.	NIWG2012a_cccohE0	1	yes	yes
NIWG 2012a NC coherent E0 norm.	NIWG2012a_nccohE0	0.3	no	yes
NIWG 2012a NC other E0 norm.	NIWG2012a_ncotherE0	0.3	no	yes
NIWG 2012a ν_e-CC E0 norm.	NIWG2012a_ccnueE0	0.06	no	yes
NIWG 2012a spectral function	NIWG2012a_sf	1	yes	yes
NIWG 2012a binding energy	NIWG2012a_eb	0.36	yes	yes
NIWG 2012a Fermi momentum	NIWG2012a_pf	0.13825	yes	yes

Table 7.25: Cross-section model parameter names and uncertainties, used in the CC1π^+ analysis [168, 169]. $\delta\epsilon$ and δB signify whether reweighting is employed for efficiency and background correspondingly.

MC Model Reweighting

A Monte Carlo reweighting method was used to propagate the cross section model systematic uncertainties, similar to that in [170]. The utilized reweighting method relies on the `T2KReWeight` library, where event-by-event reweighting is performed according to variations in the cross section models. The reweighted cross section for each variation i in the model was obtained using Eq. (7.39). The cross section model parameters are assumed to be uncorrelated, which is largely true (only NC and CC coherent are assumed to be correlated, but their overall contribution is small); therefore, their uncertainty contributions were added in quadrature.

Here, it must be noted that not all knobs are relevant for the signal model, i.e., after-FSI CC1π^+, therefore the signal selection efficiency ϵ was reweighted only for knobs that were relevant for the signal model. For instance, the π-less delta decay model knob is not relevant for the signal model since the signal category by definition cannot contain pion-less delta decay events. Similarly, no NC events are ever considered to be part of the signal. Hence NC model variations are only applied to the background predictions but not to the efficiency.

The effects of positive and negative 1-σ variations in the cross section model parameters on signal and background predictions are shown in Tab. 7.26 and 7.27 respectively. The final cross section model systematic uncertainty obtained via Eq.

Parameter name	s_w	s_a	s_{H_2O}	$100 \cdot (\sigma_i - \sigma)/\sigma$ (%)
NXSec_MaCCQEshape	18561.5	12258.7	6302.77	-1.36
NXSec_MaRESshape	18775.6	12404.3	6371.28	-0.29
NSystNucl_PilessDcyRES	17706.4	11845.7	5860.69	-8.28
NIWG2012a_ccqeE0	18217.7	11986.3	6231.31	-2.48
NIWG2012a_ccqeE1	18371.4	12119.9	6251.46	-2.17
NIWG2012a_ccqeE2	18472.3	12198.3	6274.07	-1.81
NIWG2012a_cc1piE0	18257.6	12170.1	6087.55	-4.7
NIWG2012a_cc1piE1	18065	12102.2	5962.89	-6.68
NIWG2012a_nc1piE0	18659.7	12318.3	6341.44	-0.76
NIWG2012a_nc1pi0E0	18563.3	12281.2	6282.11	-1.69
NIWG2012a_ccmultipiE0	18253.7	12218.3	6035.37	-5.55
NIWG2012a_ccdisE0	18844	12444.9	6399.1	0.145
NIWG2012a_cccohE0	15804.1	9929.51	5874.6	-8.06
NIWG2012a_nccohE0	18662.7	12311.2	6351.54	-0.60
NIWG2012a_ncotherE0	18493.4	12240.1	6253.23	-2.14
NIWG2012a_ccnueE0	18760.5	12394	6366.55	-0.36
NIWG2012a_sf	19404.8	12748.5	6656.28	4.17
NIWG2012a_eb	18863.2	12429.1	6434.07	0.69
NIWG2012a_pf	18602.5	12318.5	6284.09	-1.65
NIWGDeltaMass_mean	18641.8	12337.6	6304.12	-1.34
NIWGDeltaMass_width	18698.1	12355.2	6342.89	-0.73

Table 7.26: The effect of positive 1-σ variations in the cross-section model parameters on signal and background predictions. Water-in and water-out numbers are scaled to corresponding data POT, with flux tuning and a set of corrections applied.

(7.41)

$$\delta \langle \sigma \rangle_\Phi = \sqrt{\sum_i \left(\langle \sigma_{\nu_\mu} \rangle_\Phi^{(i)} - \langle \sigma_{\nu_\mu} \rangle_\Phi^{\text{nominal}} \right)^2}. \tag{7.41}$$

Parameter name	s_w	s_a	$s_{\mathrm{H_2O}}$	$100 \cdot (\sigma_i - \sigma)/\sigma$ (%)
NXSec_MaCCQEshape	18991.2	12551.5	6439.74	0.78
NXSec_MaRESshape	18775.6	12404.3	6371.28	-0.28
NSystNucl_PilessDcyRES	19843.7	12962.5	6881.2	7.69
NIWG2012a_ccqeE0	19331.2	12820.7	6510.55	1.88
NIWG2012a_ccqeE1	19178.3	12687.7	6490.67	1.57
NIWG2012a_ccqeE2	19078.6	12610.2	6468.37	1.22
NIWG2012a_cc1piE0	19177.6	12547.8	6629.84	3.75
NIWG2012a_cc1piE1	19467	12676.3	6790.73	6.27
NIWG2012a_nc1piE0	18890.8	12490	6400.82	0.17
NIWG2012a_nc1pi0E0	18987.2	12527.1	6460.14	1.10
NIWG2012a_ccmultipiE0	19290.8	12586.1	6704.77	4.92
NIWG2012a_ccdisE0	18705.7	12362.2	6343.45	-0.72
NIWG2012a_cccohE0	24317.8	17623.8	6693.99	4.76
NIWG2012a_nccohE0	18887.8	12497.1	6390.73	0.01
NIWG2012a_ncotherE0	19057.2	12568.2	6488.99	1.55
NIWG2012a_ccnueE0	18790.6	12414.6	6376.02	-0.21
NIWG2012a_sf	18111.8	12037.2	6074.65	-4.93
NIWG2012a_eb	18690.1	12380.8	6309.3	-1.26
NIWG2012a_pf	18918.1	12475.2	6442.95	0.83
NIWGDeltaMass_mean	18769	12215.9	6553.12	2.55
NIWGDeltaMass_width	18858.8	12465.7	6393.15	0.05

Table 7.27: The effect of negative 1-σ variations in the cross-section model parameters on signal and background predictions. Water-in and water-out numbers are scaled to corresponding data POT, with flux tuning and a set of corrections applied.

is therefore equal to:

$$100\% \frac{\delta\langle\sigma\rangle}{\langle\sigma\rangle} =^{+15.02\%}_{-16.04\%} \tag{7.42}$$

This uncertainty could be reduced if the efficiency of selecting signal events was increased and/or background was reduced, which is evident in equations in Sec. 7.1.4.

Final State Interactions systematics

FSI systematic errors arise from the uncertainties in the following pion/nucleon re-interaction models, while the pion/nucleon is propagating through the initial target nucleus:

- Pion absorption
- Charge exchange at low energies
- Inelastic scattering at low energies
- Pion production
- Charge exchange at high energies

- Inelastic scattering at high energies

In order to propagate this uncertainty through the analysis, the well-established recipe described in T2K-TN-32 [171] and T2K-TN-131 [170] was used. In short, the `T2KReWeight` library was used to generate event weights corresponding to variations in the FSI model parameters. Using 16 sets of FSI weights, with each set corresponding to a different '1-σ' contour in the FSI parameter space, the systematic uncertainty was calculated using Eq. (7.40) from Sec. 7.1.4, where the number of model variations is equal to the number of FSI parameter sets, $k = 16$. This method assumes that FSI parameters are uncorrelated.

As aforementioned, this analysis utilizes an after-FSI signal definition, i.e., the signal category always has a single π^+ in the final state exiting the nucleus. This implies that events where a single π^+ was created in the initial state but later got either absorbed and/or charge exchanged, will constitute a background interaction. Hence the efficiency ϵ is not reweighted in the course of the FSI parameter variation study. It is only the background, B, that inherits the FSI uncertainty.

Par. Set	$\delta\langle\sigma\rangle$ (cm^2)	$\frac{\delta\langle\sigma\rangle}{\langle\sigma\rangle}$ (%)
1	$-8.17589 \cdot 10^{-42}$	-0.77
2	$-1.36631 \cdot 10^{-41}$	-1.28
3	$2.14468 \cdot 10^{-42}$	0.20
4	$-1.57513 \cdot 10^{-41}$	-1.48
5	$2.37723 \cdot 10^{-41}$	2.23
6	$-1.48963 \cdot 10^{-41}$	-1.40
7	$2.33319 \cdot 10^{-41}$	2.19
8	$-2.26562 \cdot 10^{-41}$	-2.13
9	$-1.75754 \cdot 10^{-41}$	-1.65
10	$-2.7544 \cdot 10^{-41}$	-2.58
11	$-4.68894 \cdot 10^{-42}$	-0.44
12	$-2.69471 \cdot 10^{-41}$	-2.53
13	$2.42747 \cdot 10^{-41}$	2.28
14	$-2.61469 \cdot 10^{-41}$	-2.45
15	$1.10836 \cdot 10^{-41}$	1.04
16	$-3.2231 \cdot 10^{-41}$	-3.02
RMS	$2.0312 \cdot 10^{-41}$	1.91

Table 7.28: The results of 16 FSI parameter variations: absolute and fraction change in the measured cross section. Parameter sets are described in [171].

The results of the reweighting for the 16 parameter sets are shown in Tab. 7.28. The effect of the FSI variations on the signal and background true neutrino energy distributions is shown in Fig. 7.11. FSI systematic uncertainty propagated for this analysis is:

$$100\%\frac{\delta\langle\sigma\rangle}{\langle\sigma\rangle} =^{+1.91\%}_{-1.91\%} \tag{7.43}$$

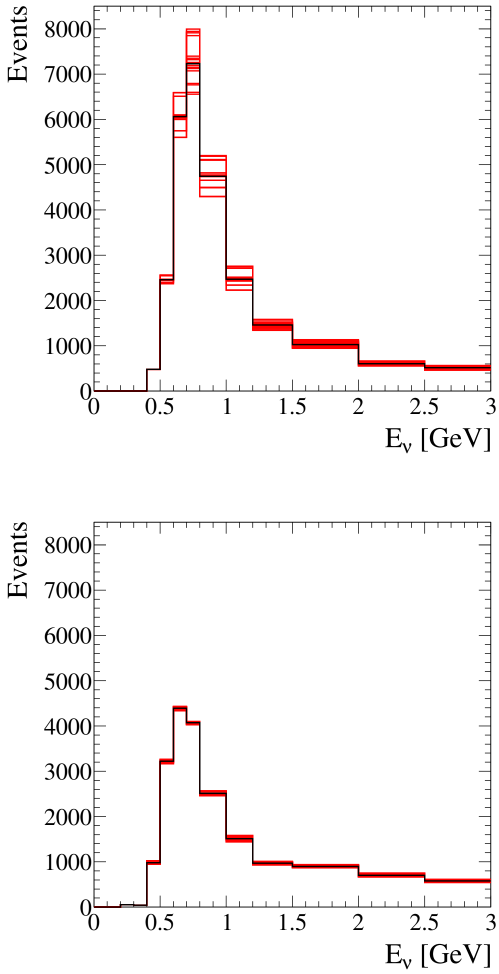

Figure 7.11: Variations in the true neutrino energy distributions for signal (left) and background (right) corresponding to 16 FSI parameter sets. Black (red) histograms are the nominal (varied) distributions.

Pion Secondary Interactions uncertainty

The Secondary Interactions (SI) are similar to FSI in terms of the physics involved, with the only significant difference being the location of re-interactions. SI occur outside the initial target nucleus, not in the primary neutrino vertex. The pions interact in the detector and can be absorbed, can change their charge (charge exchange, double charge exchange) or can be scattered. Those interactions are not necessary well modelled by GEANT4 for the T2K energy range. Tracker analyses already showed some data-MC discrepancies for pion SI. To estimate the effect of pion SI, data-MC differences on the analysis the part of the Monte Carlo with three models of hadronic interactions was re-processed, following the recommendations by the GEANT4 team to use with high energy physics experiments:

1. QGSP_BERT (default) - Bertini cascade model ($E \lesssim 10GeV$), quark-gluon string model ($E \gtrsim 10GeV$)

2. FTFP_BERT - Bertini cascade model ($E \lesssim 5GeV$), FTF (FRITIOF) model

($E \gtrsim 4GeV$),

3. QGSP_BIC - binary cascade model ($E \lesssim 10GeV$), quark-gluon string model ($E \gtrsim 10GeV$)

For each of these models, the number of selected signal events and the number of 'pion background' events (background events accepted by the cuts which contain at least one pion) was calculated. The results of this study are shown in Tab. (7.29).

Model	Water-in		Water-out	
	S (ΔS)	B (ΔB)	S (ΔS)	B (ΔB)
QGSP_BERT	$1013 \pm 3.1\%$	$379 \pm 5.1\%$	$664 \pm 3.9\%$	$209 \pm 6.9\%$
FTFP_BERT	943 (-6.91%)	397 (+4.75%)	631 (-4.97%)	221 (+5.74%)
QGSP_BIC	1027 (+1.38%)	356 (-6.07%)	662 (-0.30%)	224 (+7.18%)

Table 7.29: Number of selected signal (S) and 'pion background' events (B) for three MCs with different models of hadronic interactions. QGSP_BERT is the nominal model for which the statistical errors are shown. ΔS and ΔB (shown in brackets for FTFP_BERT and QGSP_BIC models) are the fractional differences from the nominal model in S and B, respectively.

After applying selection cuts, there is 40.3% of 'pion background' in the backgrounds for water-in and 39% for water-out. These fractions were multiplied by the absolute values of the largest fractional differences ΔB from the Tab. (7.29). This gave us: 2.4% background error for water-in and 2.8% for water-out. Efficiency errors were taken directly as the absolute values of the largest fractional differences ΔS from the Tab. (7.29): 6.9% (water-in) and 5% (water-out). The analytic formula was used to propagate these errors into the final uncertainty on s_{H_2O} and cross section. Assuming the correlated water-in and water-out errors 10.15% uncertainty on the cross section was obtained.

Summary of model uncertainties

The various model systematic uncertainties are summarized in Tab. (7.30). Therefore the total model systematic uncertainty, with all sources added in quadrature is following:

	+1-σ	-1-σ
Flux	25.16 %	20.12 %
Cross-section	15.02 %	16.04 %
FSI	1.91 %	1.91 %
SI	10.15 %	10.15 %

Table 7.30: Summary of the contributions to systematic uncertainty for the CC1π^+ analysis resulting from the uncertainties on physics models, as described in the main text. The contributions are expressed as percentage of the measured central value of the cross section.

$$100\% \frac{\delta\langle\sigma\rangle}{\langle\sigma\rangle} =^{+31.03\%}_{-27.69\%} . \tag{7.44}$$

Detector systematics

PØD Fiducial Water Mass The uncertainty on the water mass in the fiducial volume of the actual PØD detector was obtained via an independent measurement and is described in detail in the PØD geometry technical note [162]. For this measurement, it is less than 0.84% and is simply added in quadrature with the rest of the systematics. The uncertainty of the MC detector mass is less than 0.03% for both water-in (w) and water-out (a) PØD configurations, which is negligible compared to other sources of systematic uncertainty and, therefore it can be ignored.

Out-of-Fiducial Volume Background The main contribution to the out-of-fiducial (OOF) background in the analysis comes from the neutrino interactions inside the PØD but outside of the fiducial volume. These types of events occur mostly in the side buffer of the water target (25 cm in X and Y) and in the Central and Upstream ECAL (Fig. (7.12))

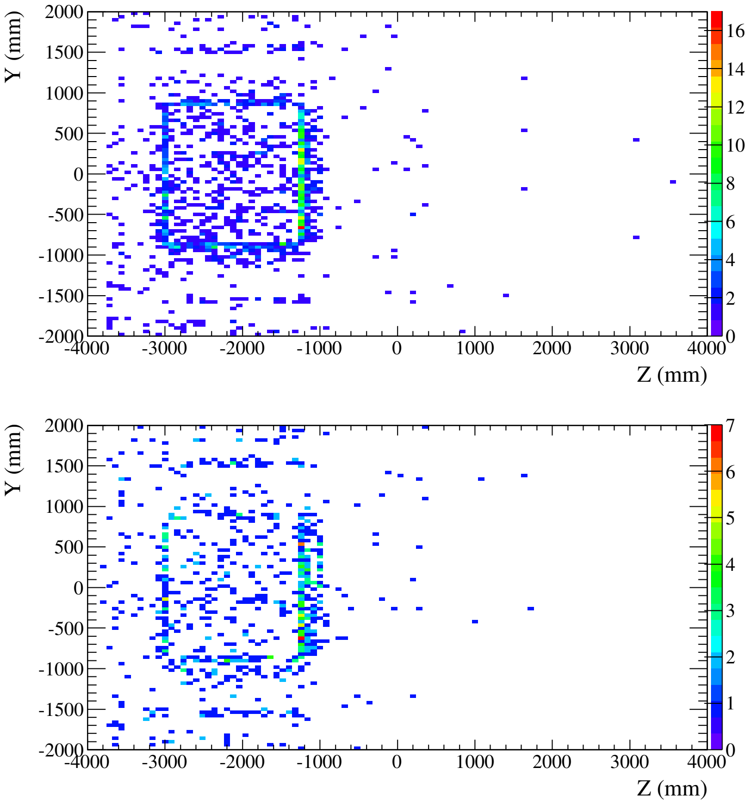

Figure 7.12: YZ view of the true vertices for OOF backgrounds for water-in (top) and water-out (bottom).

If the rate of the interactions in the side buffer and ECALs differs between data and Monte Carlo it will introduce a systematic shift in the calculated cross section.

To evaluate the effect of the potential data-Monte Carlo difference in OOF rates, a dedicated event selection (OOF background enriched side-band sample) was prepared. Two-track sample cuts as described in Sec. 7.1.2, were implemented, but with the 'inverted' definition of the PØD fiducial volume. The starting point of the muon candidate track had to be located in the PØD but outside of the 'standard' fiducial volume. Then the sample was divided into three sub-samples with events originating in Upstream ECal, Water Target buffer, and Central ECal. Data/MC ratios for each of the sub-samples were calculated. The sand muon MC was included in the selection. Flux tuning, mass, and sand muon pileup corrections were applied. The results of this OOF background-enriched side-band selection are shown in Tab. (7.31). It is clear that the absolute scale of the OOF background in MC does not represent well this type of background in the data, and therefore the MC background predictions need to be corrected. One possible explanation for the data vs. MC discrepancy is an incorrect cross-section normalization for the lead present in the ECals. Data/MC ratios from Tab. (7.31) were taken, for the OOF background uncertainty study, as multiplicative correction factors for the predicted OOF backgrounds.

Upstream ECal		Water target		Central ECal	
water-in	water-out	water-in	water-out	water-in	water-out
1.263 ± 0.057	0.964 ± 0.033	0.978 ± 0.066	0.933 ± 0.060	0.858 ± 0.108	0.823 ± 0.090

Table 7.31: Data/MC ratios for two-track OOF background-enriched selection. Errors are statistical. The numbers are used as multiplicative correction factors for different categories of OOF background in the OOF systematic error calculation.

To propagate the data-MC differences in the OOF background into final cross section uncertainty, 10000 toy Monte Carlos (water-in & water-out sets) were generated. For each toy experiment, every OOF background event was classified using MC truth information, whether it happened in Upstream ECal, Water Target buffer, Central ECal or outside PØD. Next, the event was weighted with the appropriate correction factor (data/MC ratio) from Tab. (7.31), which was randomly fluctuated (with Gaussian distribution) within the error (data/MC ratio error also from Tab. (7.31)). If the event appeared to be in the outside PØD category, the factor of 1.0 with 0.2 error (motivated by the external studies of the interactions in SMRD and ECAL) is used. The weights for water-in and water-out events were varied independently, which is equivalent to uncorrelated water-in and water-out errors. Water-in and water-out uncertainties are treated as uncorrelated because of lack of knowledge on the exact correlations for OOF background errors. For each of the toy MCs, the number of selected background events for water-in and water-out was recalculated as well as the final number of signal events on water (after subtraction).

The distributions of the selected background events for water-in and water-out are shown in Fig. (7.13). The fractional differences from the nominal number of selected events on water after subtraction are shown in Fig.(7.14). The RMS of this distribution, which is 2.7% was quoted as a systematic uncertainty on cross section value.

dE/dx Particle ID

The dE/dx cut is the last cut in the selection procedure. Discrepancies between the simulation of the deposited charge and the actual deposited charge in data can lead to bias in the dE/dx PID method.

A standard dE/dx PID algorithm uses constants (means and sigmas) provided by the fits to the stopping sand muons in data. The dE/dx PID cut optimization

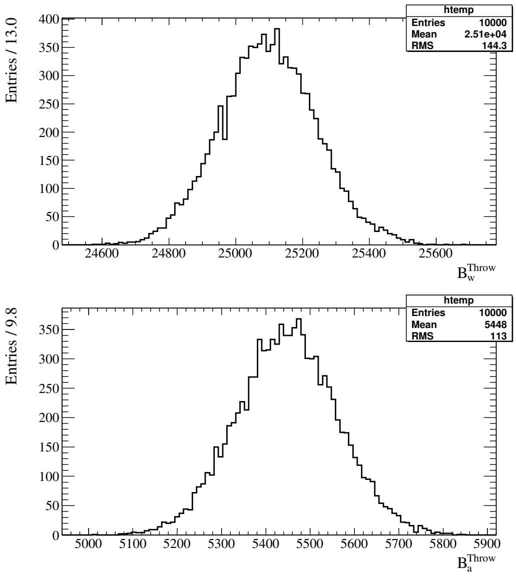

Figure 7.13: Water-in and water-out backgrounds for 10000 toy MCs for out-of-fiducial volume background systematics study.

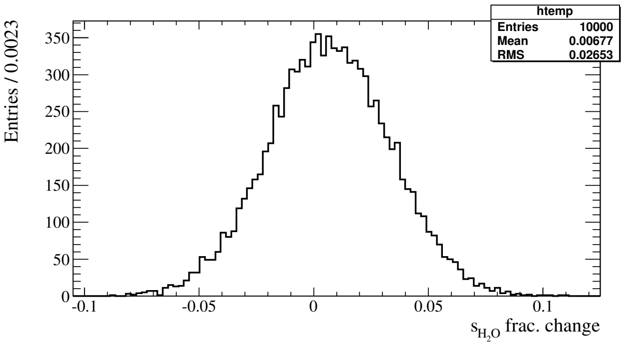

Figure 7.14: Fractional difference between the number of selected events on water for the different number of out-of-fiducial events.

was repeated on the same PID algorithm but with constants taken from the fits to the sand muon MC, instead of data. To evaluate both methods differences, the PID cut between the optimal values for the data-driven (hereinafter referred to as 'nominal') algorithm and the MC-driven algorithm.

The dE/dx cut values were varied between 13.9 and 15.3 for Kalman tracks and 4.3 and 4.7 for parametric tracks. For every water-in cut value, water-out one has been varied independently within the borders mentioned above. This is equivalent to the uncorrelated water-in and water-out uncertainties. For each of the PID cut variations the number of selected events on water after water-subtraction both for nominal and MC-driven PID was recalculated (Fig. (7.15)).

The fractional difference of the number of events on water between nominal and MC-driven PID is shown in Fig. (7.16). The RMS and the mean of the distribution in Fig. (7.16) added in quadrature give 2.1%. This value is quoted as a systematic uncertainty on cross section value.

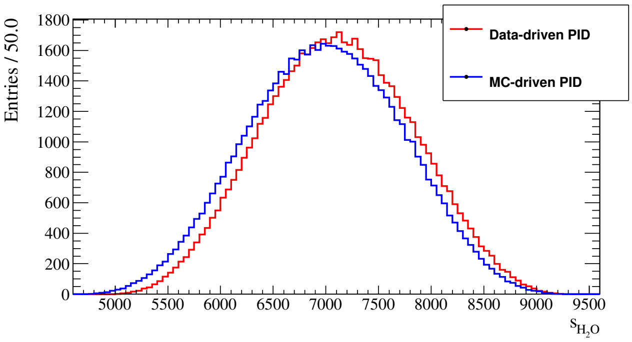

Figure 7.15: Number of selected events on water for nominal and MC-driven dE/dx PID.

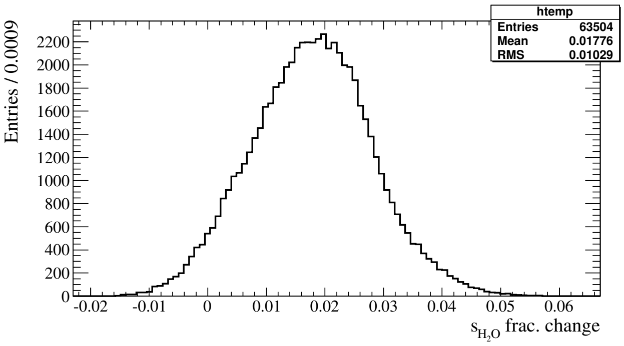

Figure 7.16: Fractional difference between the number of selected events on water between the data-driven and MC-driven dE/dx PID.

Michel Electron Detecting Efficiency

To check for the possible disagreement in the efficiency of finding delayed (Michel) clusters in the PØD between data and MC, the following strategy was adopted.

Side-band samples of data and MC sand muons entering the PØD from the upstream face and stopping in the water target or Central ECAL were used to calculate the Michel electron clustering efficiencies. Every event was required to have exactly one track in the PØD, which starts in its upstream face and stops in the water target or Central ECAL. To get the cleanest possible set of muons, dE/dx PID was also applied to all selected tracks, so every track had to be compatible with the muon/pion dE/dx pull values (*pull* $<$ 13.0 for Kalman tracks and *pull* $<$ 2.0 for parametric tracks). Using this selection of stopping sand muons, the fraction of events where the reconstruction found at least one Michel cluster was calculated . The results of this study are shown in Tab. (7.32).

	water-in	water-out
Data	0.4538 ± 0.0042	0.5201 ± 0.0052
MC	0.4353 ± 0.0017	0.4741 ± 0.0025
(Data-MC)/Data	0.0043 ± 0.0014	0.097 ± 0.017

Table 7.32: Fraction of events with at least one Michel cluster in the PØD for stopping sand muons samples.

To propagate the uncertainty into the final cross-section result, the following strategy was used. For the water-in sample: the number of the signal events accepted by the Michel cut was shifted in the selection procedure by $\pm 1\sigma$. The number of 'pion background' events (background events with pions leaving the target nucleus) accepted by the Michel cut was shifted by $\mp 1\sigma$ simultaneously with the signal shift. The same was done for water-out sample as for water-in one but independently (assuming uncorrelated errors). Finally, the number of selected events on water (after subtraction) and fractional difference from the nominal s_{H_2O} was recalculated. The largest fractional difference value, which appeared to be 2.95%, was taken as the systematic uncertainty on the cross section.

Fiducial Volume

To check the stability of the result for different fiducial volume definitions, the XY, Z upstream, and Z downstream fiducial boundaries were changed from the nominal values in the steps (σ) equal to the vertex resolution: 33 *mm* in XY and 20 *mm* (p0dule size) in Z and investigated the effect of those changes on the data vs. MC relative changes in the water-in and water-out modes. The vertex resolutions along with the ND280 X, Y, and Z axes were obtained using the MC water-in and water-out samples with one reconstructed vertex in the PØD fiducial volume with no restrictions on event multiplicity.The plots illustrating the difference between the true and reconstructed vertex positions, i.e., X and Y vertex resolutions, can be found in Fig. (7.17).

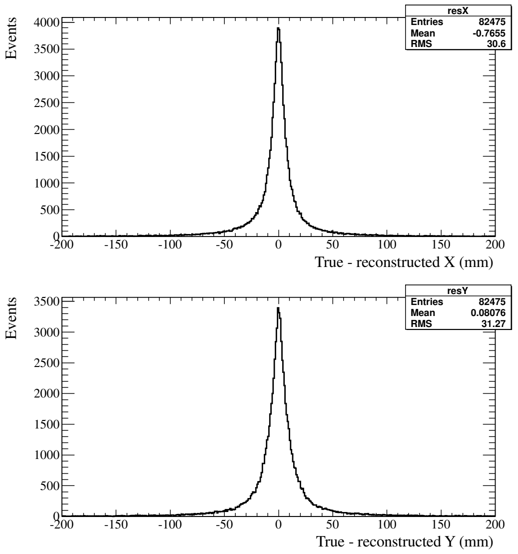

Figure 7.17: Difference between true and reconstructed vertex position in X (top) and Y (bottom) for the water-in MC sample.

The X and Y boundaries were varied simultaneously by $\pm 2\sigma$, $\pm 1\sigma$, 0σ. The upstream Z boundary was varied by -1σ, 0σ, $+1\sigma$, $+2\sigma$ and downstream Z boundary by -2σ, -1σ, 0σ, $+1\sigma$.

In the case of the Z boundaries variations, entering the ECAL regions (-2σ in the upstream Z and $+2\sigma$ in downstream Z case) where there was a material (e.g, lead) with many different properties, than the materials used in the water target section was avoided. All possible combinations of the variations of the boundaries were checked.

For each combination of variations, the difference from the nominal number of events for data and MC was calculated. In the next step, the difference between the data and MC fractional differences was calculated. Fig. (7.18) shows the results for eighty fiducial borders variations for the water-in and water-out samples.

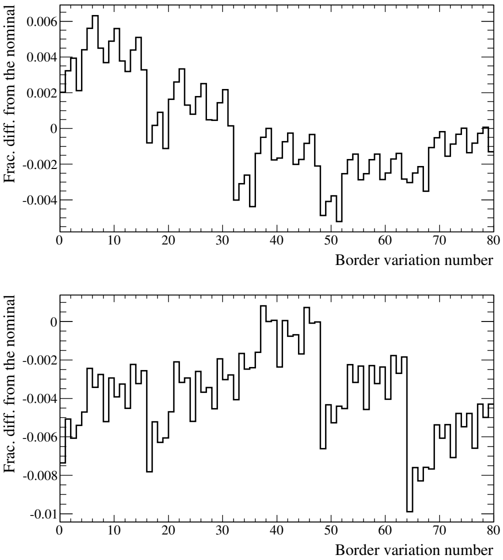

Figure 7.18: Difference of MC and data fractional differences for different fiducial boundaries variations for water-in (top) and water-out (bottom).

The maximal differences between data and MC appeared to be 0.6% for water-in and 1% for water-out. To propagate the differences into the uncertainty on s_{H_2O}, the analytic formula (Eq. 7.30) was used. Data-MC differences induced by the effects on the fiducial volume boundaries affect both background estimation and efficiency. Water-in and water-out maximum differences were used both as the errors on the backgrounds and the efficiencies. The fiducial volume uncertainties between water-in and water-out were assumed to be correlated since the shape of the vertex distributions did not depend on whether water was in the PØD or not. The final uncertainty on the cross section value appeared to be 2.88 %.

PØD Reconstruction Algorithms

To check for the discrepancies between data and MC in PØD event reconstruction a study was performed in which the subsets of data and MC re-processed with different values of the p0dRecon tracking parameters were used. The road-following (tracking) parameters were varied independently with the steps of 1σ within $\pm 2\sigma$ boundaries. The parameters, their nominal values, and the steps are listed below:

1. Width - road width, nominal value $= 80\ mm$, $\sigma = 20\ mm$
2. Layer - acceptable track-hit gap, nominal value $= 2$, $\sigma = 1$

3. Angle - angular road width (in radians), nominal value = 0.55, $\sigma = 0.1375$

Event selection was ran on the re-processed data and MC sets for the same parameter variations and calculated the fractional difference from the nominal number of the selected events in the data and MC. The difference between the fractional differences for the data and MC for each of the parameters' variations was calculated. The maximum value of the latter for water-in is 1.1%, and for water-out: 3.6%.

Fig. (7.19) shows the plots illustrating the difference between the fractional differences between data and MC for all studied parameters variations.

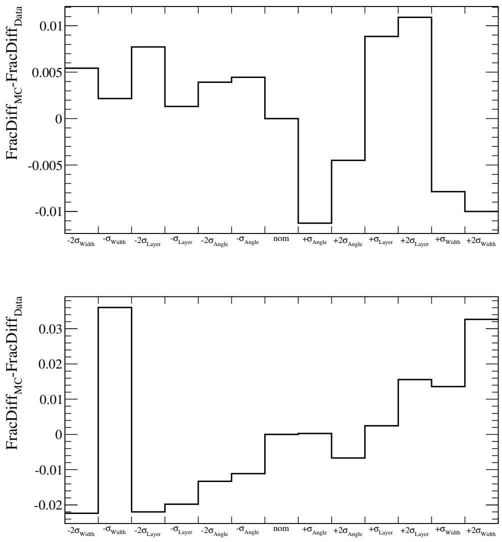

Figure 7.19: Difference between the fractional differences in data and Monte Carlo for water-in (top) and water-out (bottom) for different PØD tracking parameters variations.

The analytic formula (Eq. 7.30) was used to propagate the differences into the uncertainty on the number of selected events on water. The differences in the PØD reconstruction affect both the backgrounds and the efficiency; therefore, water-in and water-out maximum differences were used as the errors both on the backgrounds and on the efficiencies. Tracking in PØD relies on hits in the detector, and there were no additional hits in the water for the water-in mode. Therefore water-in and water-out uncertainties for PØD reconstruction were assumed to be correlated. The final uncertainty appeared to be 0.25%.

Sand Muons

To properly treat sand muon backgrounds, external studies which showed that data/MC ratio for sand muons through-going the PØD was 1.084 ± 0.002 [164] were used. This ratio was was then used as a correction for the Monte Carlo sand muon background prediction. To propagate the error into the final result, 0.2% systematic error was assigned to the efficiency estimation as the fraction of the actual signal events was falsely vetoed due to the sand muons is unknown. For background uncertainty 0.2% (error on data/MC ratio) was assigned and multiplied by the fractions of sand muons for the entire background in the sample (0.00204 (water-in) and 0.00380 (water-out)). To calculate sand muon fractions, Tab. (7.8) was used. The generation of sand muons does not depend on whether the water is in the PØD or not. Therefore the assumption that the water-in and water-out uncertainties related to sand muons were correlated was used. Using the analytic formula for the uncertainty propagation (Eq. 7.30), 3% uncertainty on s_{H_2O} was obtained.

Summary of Detector Systematic Uncertainties

A summary of all the detector-related systematic uncertainty sources is shown in Tab. (7.33). The total uncertainty was calculated by adding all contributions in quadrature and was found to be equal to 6.14%.

	Sys. Uncertainty	Correction
OOF Background	± 2.7%	no
dE/dx PID	± 2.1%	no
Michel electron	± 2.95%	no
Fiducial volume	± 2.88%	no
PØD reconstruction	± 0.25%	no
Sand muons	± 3%	yes

Table 7.33: Summary of detector-related systematic uncertainties for CC1π^+ analysis. The contributions are expressed as percentage of the measured central cross-section value.

7.1.5 Statistical uncertainties

The total statistical uncertainty on the cross section measurement comes from statistical uncertainties in the numbers of data events, N_w for combined T2K Runs 1, 2, and 4, and N_a for combined T2K Runs 2, 3, and 4,

$$\frac{\sqrt{N_w}}{N_w} = 1.92\%, \qquad \frac{\sqrt{N_a}}{N_a} = 2.21\%, \tag{7.45}$$

and statistical uncertainties in the MC predictions for backgrounds, B_w and B_a, and efficiencies, ϵ_w and ϵ_a, due to limited MC statistics. Both the uncertainties were evaluated separately. They were computed via a method of random statistical throws, where the measured numbers of events, N_w and N_a, or B_w, B_a, ϵ_w and ϵ_a, were allowed to vary according to Poisson statistics. The results were cross-checked via a semi-analytic calculation using Eq. (7.38).

Uncertainty due to Limited Data Statistics

Using the statistical throws method, the data cross-section $\langle\sigma_{\nu_\mu \mathrm{CC1}\pi^+}\rangle_\Phi^{(i)}$ was recalculated $k = 10^5$ times for each throw i via equation

$$\sigma_{\mathrm{CC1}\pi^+}^{(i)} = \frac{s_{\mathrm{H_2O}}^{(i)}}{\Phi_w \cdot T_{\mathrm{H_2O}}}, \tag{7.46}$$

where the number of signal interactions on water $s^{(i)}_{\mathrm{H_2O}}$ changes for each throw i according to the following equations

$$s^{(i)}_{\mathrm{H_2O}} = s^{(i)}_{w} - R_p \cdot s^{(i)}_{a}, \tag{7.47}$$

$$s^{(i)}_{w} = \sum_{k} \frac{N^{(i)}_{wk} - C^{mass}_{wk} C^{sand}_{wk} B_{wk}}{C^{sand}_{wk} \epsilon_{wk}}, \tag{7.48}$$

$$s^{(i)}_{a} = \sum_{j} \frac{N^{(i)}_{aj} - C^{mass}_{aj} C^{sand}_{aj} B_{aj}}{C^{sand}_{aj} \epsilon_{aj}}. \tag{7.49}$$

where $s^{(i)}_{w(a)}$ is the number of signal events in the water-in (water-out) samples, $N^{(i)}_{wk}$ and $N^{(i)}_{aj}$ are the number of selected events in the water-in and water-out samples, B_{wk}, B_{aj} are the corresponding number of predicted background events, R_p is the POT ratio for the water-in and water-out data samples, and $C^{mass/sand}_{wk}$, $C^{mass/sand}_{aj}$ are the fiducial mass/sand muons corrections. The probabilities of observing $N^{(i)}_{w|a}$ events, given measured data numbers $\langle N \rangle_{w|a}$, are described by the Poisson distribution

$$P(N^{(i)_{w|a}}) = \frac{e^{-\langle N_{w|a} \rangle} \cdot \langle N_{w|a} \rangle^{N^{(i)}_{w|a}}}{N^{(i)}_{w|a}!}, \tag{7.50}$$

and was implemented using the `TRandom3->Poisson()` method from the ROOT library [172].

The results of random statistical throws for data are shown in Fig. 7.20. The fractional statistical uncertainty on the data cross-section value due to limited data statistics is

$$\frac{\Delta\sigma}{\sigma} \approx \pm 15.0\% \text{ (data stat.)}, \tag{7.51}$$

using the throwing method and

$$\frac{\Delta\sigma}{\sigma} \approx \pm 15.0\% \text{ (data stat.)}, \tag{7.52}$$

for the analytic calculation using Eq. (7.38).

Uncertainty due to Limited MC Statistics

Using the statistical throws method again, the data cross-section $\langle \sigma_{\nu_\mu \mathrm{CC}1\pi^+} \rangle^{(i)}_{\Phi}$ was recalculated $k = 10^5$ times for each throw i via Eq. (7.46) where $s^{(i)}_{\mathrm{H_2O}}$ changes for each throw i according to Eq. (7.47).

$s^{(i)}_{w|a}$ can be found via

$$s^{(i)}_{w} = \sum_{k} \frac{N_{wk} - C^{mass}_{wk} C^{sand}_{wk} B^{(i)}_{wk}}{C^{sand}_{wk} \epsilon^{(i)}_{wk}}, \tag{7.53}$$

$$s^{(i)}_{a} = \sum_{j} \frac{N_{aj} - C^{mass}_{aj} C^{sand}_{aj} B^{(i)}_{aj}}{C^{sand}_{aj} \epsilon^{(i)}_{aj}}, \tag{7.54}$$

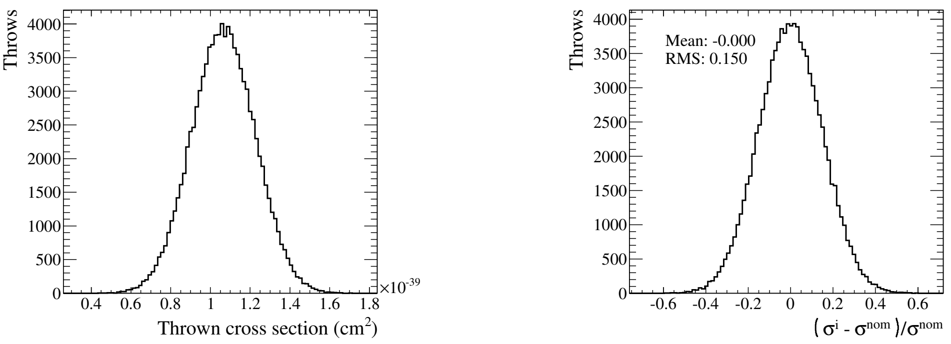

Figure 7.20: A histogram of thrown data cross section values $\langle\sigma_{\nu_\mu \mathrm{CC}1\pi^+}\rangle_\Phi^{(i)}$ (left) and the fractional deviations from the nominal data cross section (right).

$$\epsilon^{(i)} = \frac{S^{(i)}}{s^{gen}}, \tag{7.55}$$

where the number of background events for water-in and water-out $B^{(i)}_{w|a}$ and corresponding efficiencies $\epsilon^{(i)}_{w|a}$ predicted by MC are allowed to fluctuate statistically for MC POT. Efficiency is defined as a ratio of number of selected signal events S and all signal events generated by MC in fiducial volume s^{gen}.

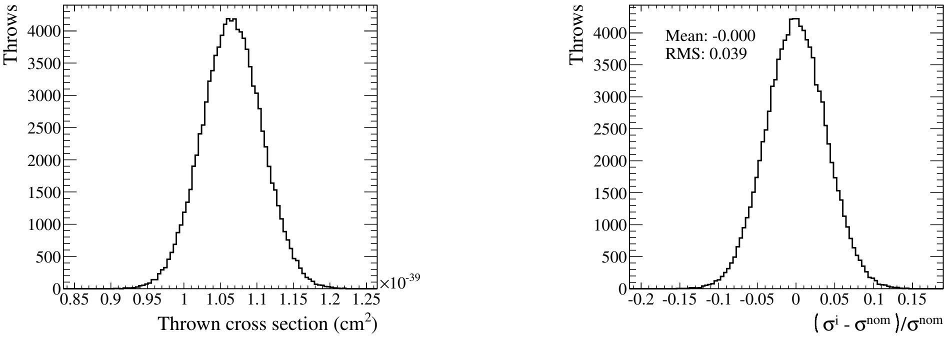

Figure 7.21: A histogram of thrown data cross sections (left) and fractional deviations from the nominal cross sections (right).

The probabilities of observing $B^{(i)}_{w|a}$ background events, given the MC CV numbers $\langle B\rangle_{w|a}$, are described by the Poisson distribution

$$P(B^{(i)_{w|a}}) = \frac{e^{-\langle B_{w|a}\rangle} \cdot \langle B_{w|a}\rangle^{B^{(i)}_{w|a}}}{B^{(i)}_{w|a}!}. \tag{7.56}$$

Similarly, for $\epsilon^{(i)}_{w|a}$ the probability of observing a particular efficiency is

$$P(\epsilon^{(i)_{w|a}}) = P\left(\frac{S^{(i)}}{s^{gen}}\right) = \frac{e^{-\langle \frac{S_{w|a}}{s^{gen}_{w|a}}\rangle} \cdot \langle \frac{S_{w|a}}{s^{gen}_{w|a}}\rangle^{\frac{S^{(i)}_{w|a}}{s^{gen}_{w|a}}}}{\frac{S^{(i)}_{w|a}}{s^{gen}_{w|a}}!}, \tag{7.57}$$

where the statistical uncertainties on $s^{gen}_{w|a}$ are considered negligible.

The MC statistical uncertainty results for data are shown in Fig. 7.21 The fractional statistical uncertainty on the data cross-section value, which was due to limited MC statistics, obtained via the throwing method is

$$\frac{\Delta\sigma}{\sigma} \approx \pm 3.9\% \text{ (MC stat.)}. \tag{7.58}$$

Summary of Statistical Uncertainties

Statistical uncertainties, along with the total statistical uncertainty, are presented in Tab. 7.34. Data and MC contributions were added in the quadrature.

Data	± 15.0%
MC	± 3.9%
Total	± 15.5%

Table 7.34: Summary of data and MC statistical uncertainties for the CC1π^+ analysis.

7.1.6 Fake-data studies

To validate the procedure of calculating CC1π^+ cross section, several fake-data (mock-data) studies were performed, and their results are presented in this Section. The first type of mock-data (MD1) involved Monte Carlo (MCP5E) tuned with the latest (v3.2) flux version and scaled to real data (processing RDP5D) POT (after Data Quality cuts). This mock-data closely represents the statistical uncertainties in the data with Monte Carlo predictions involving all tunings and corrections.Using Eq. (7.23), where N_w and N_a are numbers of events selected in MD1, the following cross section value was obtained:

$$\langle\sigma_{\nu_\mu \mathrm{CC}1\pi^\pm}\rangle_\Phi = 1.26 \cdot 10^{-39} \left[\frac{\mathrm{cm}^2}{\mathrm{nucleon}}\right] \pm 12.9\% \text{ (stat.)}. \tag{7.59}$$

This mock-data cross section is statistically compatible with the 'true' cross section value (calculated using Monte Carlo true values) within the statistical uncertainty. This confirms that the cross section calculation method and the subtraction technique both work and give consistent results. The methods used to obtain the statistical uncertainties and the uncertainties themselves are discussed in Sec. 7.1.5.

The second type of mock-data, i.e., MD2, had the same background, but the signal prediction was scaled by 0.9, therefore changing the number of selected events for water-in and water-out (N_w and N_a). The results for MD2 give:

$$\langle\sigma_{\nu_\mu \mathrm{CC}1\pi^\pm}\rangle_\Phi = 1.13 \cdot 10^{-39} \left[\frac{\mathrm{cm}^2}{\mathrm{nucleon}}\right] \pm 13.9\% \text{ (stat.)}. \tag{7.60}$$

The scaling factor of 0.9 was chosen for the signal, as the same size of the discrepancy between data and MC was observed in several production 4 based ν_μ-induced CC inclusive analyses [173] [163].

MD	Run #	PØD config.	N per 10^{20} POT	ϵ (%)	B per 10^{20} POT
1	1	water-in	1057.09	7.18	520.97
1	2	water-in	1086.94	7.14	531.95
1	4	water-in	1057.46	6.94	523.42
1	2	water-out	593.59	5.95	294.47
1	3	water-out	603.51	6.16	301.48
1	4	water-out	599.36	6.12	299.43
2	1	water-in	1003.48	7.18	520.97
2	2	water-in	1031.44	7.14	531.95
2	4	water-in	1004.06	6.94	523.42
2	2	water-out	563.68	5.95	294.47
2	3	water-out	573.31	6.16	301.48
2	4	water-out	569.36	6.12	299.43

Table 7.35: Mock-data (MD) types 1 and 2: number of selected events N, predicted number of background events B, and efficiency ϵ for PØD water-in and water-out samples.

7.1.7 Results

This analysis utilized data for Runs 1 - 4 with PØD water-in 2.64×10^{20} combined POT and water-out 3.71×10^{20} combined POT. A statistical water-in/water-out event rate subtraction technique was utilized to obtain a cross section on water target material only. A complete set of re-evaluated detector systematic uncertainties was presented as well.

As a result of this analysis, ν_μ-induced charged current single charged pion production cross section on water as a target was calculated to be

$$\langle \sigma_{\nu_\mu \mathrm{CC}1\pi^+} \rangle_\Phi = 1.10 \cdot 10^{-39} \, {}^{+35.27\%}_{-32.38\%} \, \frac{cm^2}{nucleon} \tag{7.61}$$

$$\left(\begin{array}{ccc} {}^{+15.49\%}_{-15.49\%} \, (stat.) & {}^{+25.16\%}_{-20.12\%} \, (flux) & {}^{+15.02\%}_{-16.04\%} \, (xsec) \\ {}^{+1.91\%}_{-1.91\%} \, (FSI) & {}^{+10.15\%}_{-10.15\%} \, (SI) & {}^{+6.14\%}_{-6.14\%} \, (det.) \end{array} \right),$$

where the result is provided in the form of a single neutrino energy bin cross section integrated over the entire T2K flux (0 - 30 GeV). 2703 (2187) data events were selected after analysis cuts with 1387.2 (1046.0) predicted background events for water-in (water-out) PØD detector configurations. The data result uncertainty is dominated by flux and cross section models uncertainties and is consistent with the NEUT-based MC prediction of $1.26 \cdot 10^{-39}$ cm^2. A comparison of the measured cross section with the NEUT and GENIE predictions is shown in Fig. 7.22.

Data results

Using the values from Tab. 7.36, the data cross section on water, $\langle \sigma_{\nu_\mu \mathrm{CC}1\pi^+} \rangle_\Phi$, was obtained with Eq. (7.23):

$$\langle \sigma_{\nu_\mu \mathrm{CC}1\pi^\pm} \rangle_\Phi = 1.10 \cdot 10^{-39} \left[\frac{\mathrm{cm}^2}{\mathrm{nucleon}} \right] . \pm 14.5\% \text{ (stat.)} \tag{7.62}$$

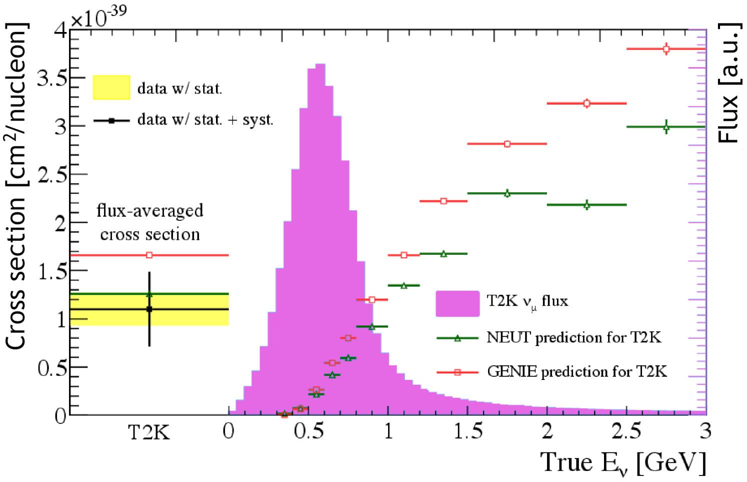

Figure 7.22: Flux-averaged CC1π^+ cross section on water PØD-based measurement compared with NEUT and GENIE predictions.

The statistical and systematic uncertainties associated with this result are discussed in Sec. 7.1.5, 7.1.4. The significance of this result and possible ways to improve the analysis are discussed in Sec. 7.1.7.

Run #	PØD config.	POT	N per 10^{20} POT	ϵ (%)	B per 10^{20} POT
1	water-in	$0.296 \cdot 10^{20}$	960.7	7.18	521.0
2	water-in	$0.698 \cdot 10^{20}$	1001.6	7.14	531.9
4	water-in	$1.647 \cdot 10^{20}$	1044.4	6.94	523.4
2	water-out	$0.359 \cdot 10^{20}$	598.7	5.95	294.5
3	water-out	$1.355 \cdot 10^{20}$	554.2	6.16	301.5
4	water-out	$1.776 \cdot 10^{20}$	608.3	6.12	299.4

Table 7.36: Numbers of data events after cuts, N, normalized to 10^{20} POT. B and ϵ numbers are predicted by the MC.

Discussion and future improvements

The cross section on water result obtained for MD1 type mock-data, i.e., flux-tuned MC scaled to data POT, shown in Eq. (7.59) in Sec. 7.1.6 was compared against the "true" MC flux-averaged cross section on water, and the agreement was shown to be well within the statistical uncertainty, therefore validating the calculation method. The "true" MC cross section method was independently cross-checked using before-FSI cross sections extracted directly from NEUT and good agreement was observed in the case of the oxygen target (no direct benchmark for the cross section on H_2O currently exists).

The data result shown in Eq.(7.62) is consistent with the NEUT MC predicted value, considering the full uncertainty range, statistical and systematic sources added in quadrature. The presented measurement is now dominated by model systematic uncertainties, of which the flux and cross section models are the two largest contributors.

The highest priority item is to increase the selection efficiency by expanding the event selection to include one and more than two track topologies and possibly develop a more efficient signal selection using multi-variate analysis techniques. Another potential possibility is to perform background fits using orthogonal datasets to reduce the uncertainty associated with the background normalizations. Potential sideband samples include one-track events since this topology is dominated by CCQE, primary background mode, and two-track events with inverted dE/dx and Michel cuts. This work has already been started and is in progress.

7.2 Charged current interactions without pions

Muon neutrino induced charged current reactions with no pions in the final state (ν_μ CC0π) play an essential role in neutrino oscillations and are very important for a better understanding of neutrino-nuclei interactions.

ν_μ CC0π interactions are represented by the muon (μ^-) and nucleons solely present in the final state. These reactions are widely used as a signal in neutrino oscillation studies, especially in the sub-GeV region (neutrino energies below 1 GeV), where the CCQE cross section dominates in charge current neutrino interactions. Accelerator neutrino experiments use nuclear targets such as carbon and argon to increase the rate of detected interactions. This fact complicates the signature of $CC0\pi$ reactions because the consequence of having a more complex target nucleus is the appearance of multi-nucleon final states. Multi-nucleon states appear because of the two-particle two-hole interactions and re-interactions inside complex nuclei (final state interactions - FSI). One has to stress that precise determination of the energy spectrum of ν_μ CCQE interactions is crucial for studying the ν_μ disappearance channel of neutrino oscillations. Although nuclei other than carbon and argon (lead, iron) are not directly used as targets for neutrinos in accelerator neutrino experiments, they are widely present in other elements constituting the neutrino detectors such as frames, magnet yokes, radiators, supporting structures etc. Neutrinos interact with these elements, and the particles produced in the final state of such reactions are an important background for the interactions in the designated detector parts.

In the T2K experiment, the studies on $CC0\pi$ interactions on various targets in the intermediate energy range are crucial for determining the CP symmetry violation/conservation in the neutrino sector via the δ_{CP} phase. Better knowledge of the CC0π cross sections will allow the systematic uncertainties in the precise measurements of neutrino oscillations to be reduced.

7.2.1 Analysis overview

The following part of the monograph is dedicated to the analysis of charged current neutrino interactions with no pions in the final state. The ultimate goal of this study is to combine the samples of CC0π reactions on lead in PØD and CC0π interactions on carbon in the FGD1 detector (Fig. 7.23) to calculate muon neutrino-lead and muon neutrino-carbon cross sections and lead-carbon cross-section ratio. The cross sections mentioned above will be calculated in outgoing muon kinematics $p - \cos\theta$ phase space using the maximum likelihood fitting method. At the time of writing this monograph, the CC0π event selection was finalized and is described in the section below. The analysis of the systematic uncertainties and fake data studies needs final validation; therefore, it is not presented here. It is necessary to stress that the selection scheme presented in this section will be used to extract CC0π cross section on lead, lead-carbon cross-section ratio, and can be used in other analyses that would like to utilize the PØD detector as a target for neutrino interactions.

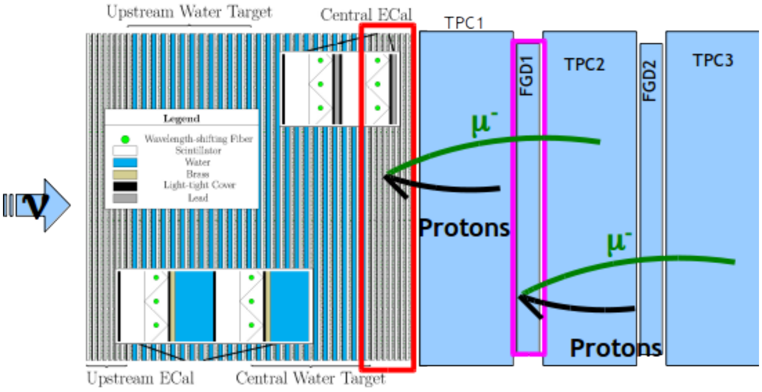

Figure 7.23: Schematic view of CC0π interactions that are of interest in this analysis. Neutrinos from the T2K beam traverse the ND280 detector from the left. Two examples of ν_μ-induced CC0π reactions are shown. The first, is a neutrino interaction with lead radiators in the Central ECal and the second is an interaction with carbon (hydrocarbon) in the FGD1 detector.

This section is divided into two parts: the first, contains a detailed description of CC0π event selection (Subsec. 7.2.2), whereas the second (Subsec. 7.2.3) summarizes the selection study.

7.2.2 Event selection

This part of the monograph is dedicated to the description of the scheme of selecting charged current interactions without pions in the final state using the PØD and TPC detectors. Pre-selection methods and data-quality cuts used in this analysis are the same as for the CC1π analysis and can be found in Subsec. 7.1.2. Monte Carlo samples used in the preparation and evaluation of the selection procedure are also described in Subsec. 7.1.2. The Monte Carlo sample which was used in this study is equivalent to 1.24748×10^{21} protons on target and has the PØD filled with water.

The analysis of CC0π interactions is based on the following set of four Monte Carlo samples selected with a series of dedicated cuts:

1. Sample of PØD CC0π interactions on lead – called *signal sample* or *sample 1* described in detail below.

2. FGD1 CC0π interactions on carbon – using the tracker sector of the ND280 detector to extract CC0π reactions. This is a group of 7 samples, in which

different combinations of FGD and TPC detectors are used to select interactions with a muon track in TPC and no protons detected (muTPC), a muon track in TPC and a proton track in FGD (muTPC+pFGD), both muon and proton tracks detected in TPC (muTPC+pTPC), a muon and one charged pion (CC1π), a muon and more than one pion (CCDIS), a muon track and an electron from a muon decay (CC Michel), a muon track detected in TPC and more than one proton (muTPC+Np). More details on these selections can be found in [26]. This set is called *sample 2*.

3. Sample of CC1π interactions in PØD called *sample 3* - described below
4. CC-Other interactions in PØD called *sample 4* - the selection is also characterized below

The main purpose of using additional samples (apart from the signal sample) is to provide the additional constraints on various background channels as described in Chap. 5. It is necessary to stress that the samples listed above will ultimately be used as the inputs for the simultaneous fit using likelihood fitter.

The signal selection aims at the sample of CC0π interactions on lead in the PØD and is defined using the following cuts:

1. Good event quality requirement. A detailed description of the data-quality cuts can be found in Subsec. 7.1.2.
2. Require at least one reconstructed track with the PØD and TPC segment,
3. Find highest momentum, negative track (HMNT) among PØD-TPC tracks,
4. HMNT is of good quality (long enough) and is starting in Central ECAL fiducial volume,
5. Reject events with activity upstream and on the sides of the PØD,
6. HMNT is compatible with the muon hypothesis (based on dE/dx of the track)
7. There is only one Minimum Ionizing Particle (MIP) track in the event. This is checked by verifying dE/dx of each track.
8. There are no Michel electrons in the event. This cut rejects events with low energy pions that decay into muons decaying into *Michel* electrons.

Sample 2 is the set of CC0π interactions on Carbon in FGD1. It is selected using mainly the tracker part of the ND280 detector. The most important cuts are summarized below.

1. Event quality
2. Find Highest Momentum Negative (HMN) or Positive (HMP) track in event
3. Muon PID - identify muon using TPC or FGD
4. Proton PID - identify proton using TPC or FGD

5. No Michel electron - reject events with Michel electrons
6. ECAL π^0 veto - use ECAL to reject events with energy deposits from π^0 decay photons

Sample 3, focused on CC1π interactions in PØD, was selected by inverting the last cut of the signal selection and requiring at least one Michel electron (from π decay) in the event. Sample 4, directed towards selecting CC-Other interactions in the PØD, had common cuts 1-6 with the signal sample, but instead of one MIP track request, events with more than one MIP track (muon + charged pions in the TPC) are selected. In this sample there is also no cut on the number of Michel electrons.

The fiducial volume used to select interactions in the Central ECal of the PØD detector for samples 1, 3 and 4 is called *Central ECal fiducial volume* and is characterized below. In order to select interactions on lead the fiducial volume is defined as a box containing the vast volume of the PØD Central ECal with the top, bottom, left and right edges of the box located approximately 25 cm from the PØD detector edges. The upstream border of the fiducial volume goes through the middle of the first upstream Central ECal PØDule and the downstream border through the next to the last downstream PØDule. The Central ECal fiducial volume is based on the PØD official water target fiducial volume (X and Y borders), with the Z borders shifted to the Central ECal. More details about the Central ECal fiducial volume can be found in Tab. 7.37. The fiducial volume used to select CC0π interactions on carbon with FGD1 (sample 2) is defined in [26] and Tab. 7.38.

Coordinate	Min	Max
X	-836	764
Y	-871	869
Z	-1233	-970

Table 7.37: Definition of the Central ECal fiducial volume used to select samples 1, 3, and 4. The official ND280 coordinate system as defined in Fig. (3.8) was used.

Coordinate	Min	Max
X	-874.51	874.51
Y	-819.51	929.52
Z	136.875	446.955

Table 7.38: Definition of the FGD1 fiducial volume used in the CC0π analysis. The official ND280 coordinate system as defined in Fig. (3.8) was used.

The purities p_i for each sample were calculated in the following way:

$$p_i = \frac{S_i^{sel(MC)}}{N^{MC}}, \tag{7.63}$$

where N^{MC} is the number of selected events in the sample, $S_i^{sel(MC)}$ is the number of selected true interactions of channel i with the true vertex in the fiducial volume in the sample. The interaction channel i is an element of the following set {CC0piPb, CC0piCarbon, CC0piOther, CC1pi, CCOther, Other, OOFV}, where:

- CC0piPb are true CC0π interactions on lead,
- CC0piCarbon are true CC0π interactions on carbon,
- CC0piOther are true CC0π interactions on other targets,
- CC1pi are true CC1π interactions,
- CCOther are true CC-Other interactions,
- Other are other neutrino interaction channels not listed above with the true vertex in fiducial volume,
- OOFV are interactions with the true vertex outside of the fiducial volume

The purities for all samples and the number of events selected in Monte Carlo were listed in Tabs. 7.39 - 7.42. In addition, Fig. 7.24 illustrates the composition of the selected samples. It can be noted that the most significant backgrounds in the signal sample such as CC0π interactions on carbon, CC1π and CCOther interactions are well represented in samples 2, 3, and 4 respectively.

Interaction channel	Purity [%]	Number of selected events
CC0π Pb	46.143913	17161
CC0π Carbon	28.37289	10552
CC0π Other	7.9971757	2974
CC1π	5.9135807	2199
CCOther	5.5858256	2077
Other	1.1832053	440
OOFV	4.8034093	1786

Table 7.39: The purities of the CC0π signal sample along with the number of selected events in Monte Carlo sample corresponding to 1.24748×10^{21} protons on target.

Interaction channel	Purity [%]	Number of selected events
CC0π Pb	0	0
CC0π Carbon	64.515734	19635
CC0π Other	5.6423599	1717
CC1π	12.475311	3797
CCOther	11.543113	3513
Other	2.4123783	734
OOFV	3.4111036	1038

Table 7.40: The purities of the CC0π Carbon sample along with the number of selected events in Monte Carlo sample corresponding to 1.24748×10^{21} protons on target.

The ultimate goal of the analysis is to calculate the differential cross section in terms of outgoing muon kinematics $(p, \cos\theta)$. Therefore the binning choice had to be

Interaction channel	Purity [%]	Number of selected events
CC0π Pb	16.346608	642
CC0π Carbon	5.3024746	208
CC0π Other	2.4959963	98
CC1π	43.543292	1711
CCOther	17.150297	674
Other	2.8816661	113
OOFV	12.279666	483

Table 7.41: The purities of the CC1π sample along with the number of selected events in Monte Carlo sample corresponding to 1.24748×10^{21} protons on target.

Interaction channel	Purity [%]	Number of selected events
CC0π Pb	8.4506909	103
CC0π Carbon	3.8392704	47
CC0π Other	0.62468837	8
CC1π	13.728283	167
CCOther	54.616784	665
Other	9.2634444	113
OOFV	9.4768393	115

Table 7.42: The purities of the CCOther sample along with the number of selected events in Monte Carlo sample corresponding to 1.24748×10^{21} protons on target.

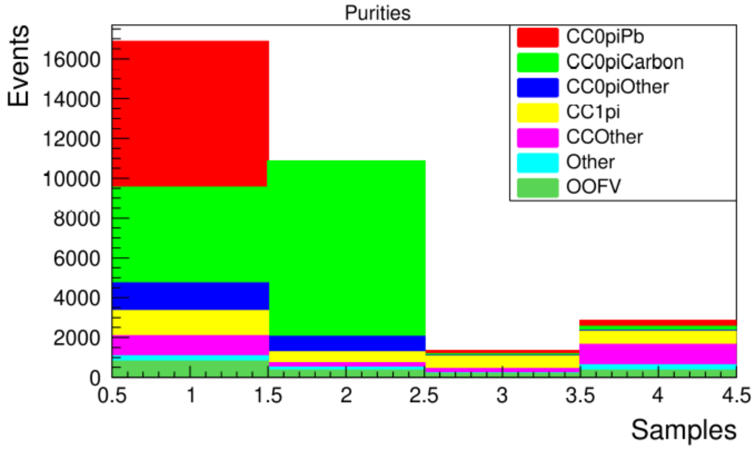

Figure 7.24: Composition of the samples used in CC0π analysis. The horizontal axis is the number of sample: 1 - CC0π interactions on lead in PØD, 2 - CC0π interactions on carbon in FGD1, 3 - CC1π interactions in PØD, 4 - CC-Other interactions in PØD.

made, and the optimal binning borders have to be estimated. The study on binning was performed taking by into account quantities such as the statistical error of the number of selected events per bin, detector resolution, and the selection efficiency. The final binning is shown in Tab. 7.43 and Fig. 7.25.

Another important parameter in the selection procedure is efficiency. It is defined

Bin	$\cos\theta$ slice	Momentum (MeV)
0, 1	0.63, 0.79	200, 450, 600
2, 3, 4	0.79, 0.89	200, 450, 600, 850
5, 6, 7, 8	0.89, 0.96	200, 400, 750, 1150
9, 10, 11, 12	0.96, 1.0	200, 650, 1200, 2250, 3700

Table 7.43: The binning for CC0π analysis. Bin numbers along with the corresponding $\cos\theta$ and momentum limits were listed.

as:

$$\epsilon = \frac{S^{sel(MC)}}{s^{gen}}, \tag{7.64}$$

where N^{MC} in Eq. (7.64) is the number of selected events in MC, $S^{sel(MC)}$ is the number of selected true CC0π interactions with the true vertex in the fiducial volume (in MC), and s^{gen} is the number of all true CC0π interactions (before all cuts) with the true vertex in the fiducial volume (MC). The true CC0π interaction definition is based on the multiplicity and content of a set of true particles leaving the target nucleus (after final state interactions). An event is considered a true CC0π interaction when there was one negative muon, no pions, no other mesons, and any number of nucleons leaving the target nucleus. Efficiency in the signal sample as a function of outgoing muon momentum and $\cos\theta$ with the bin borders overlaid is shown in Fig. 7.25. The figure also shows the projections of the efficiency on the momentum and $\cos\theta$ axes.

The CC0π interactions on carbon, CC1π, and CCOther backgrounds are constrained by the three additional samples: 2, 3, and 4, respectively. The third most significant background in the signal sample comprises ν_μ CC0π interactions with targets other than carbon and lead (defined as CC0π Other category). Further investigations of the target composition in CC0π Other category were performed and are summarized in Tab. 7.44. It appears that CC0π Other interactions are mainly composed of CC0π interactions where muon neutrino scatters on the iron nucleus. This is the most significant background which is not constrained due to the difficulty in finding an appropriate sample. Further investigation shows that CC0π interactions on iron have their vertices in the enclosures of the Central ECAL PØDules that are made of stainless steel.

Target	Contribution to CC0π Other [%]
Iron	81.6
Other	17.5
Oxygen	0.9

Table 7.44: The contributions from the true CC0π interactions on various targets to CC0π Other topology.

An important cut is imposed on the track likelihood function in the muon hypothesis. This likelihood is calculated by comparing the measured energy loss per unit length of the track with the predicted values. The likelihood function distribution before imposing the cut on this quantity in the signal sample is presented in

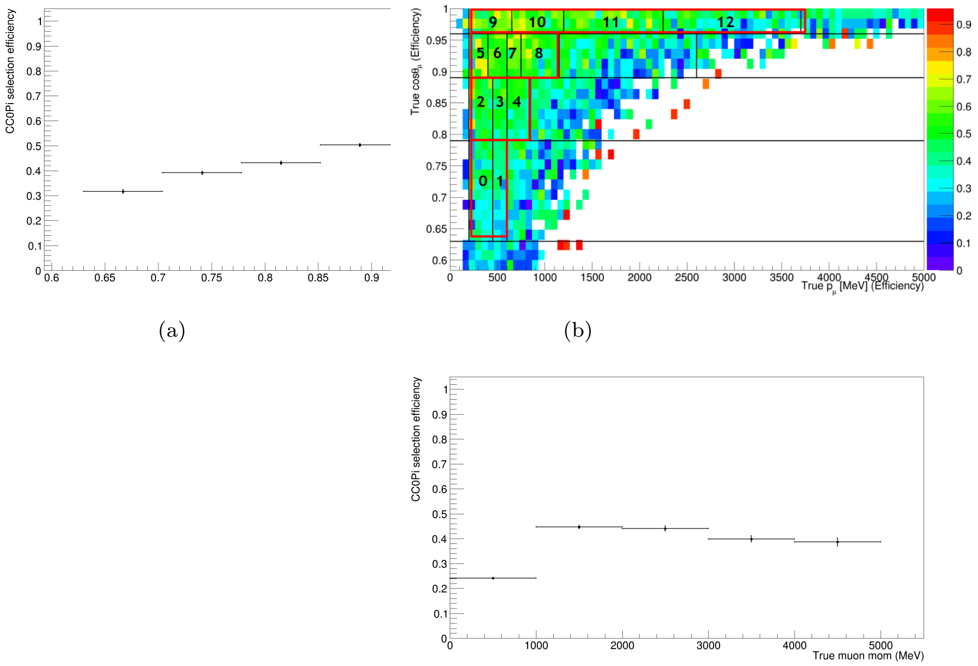

(a) (b)

(c)

Figure 7.25: CC0π selection efficiency for the signal sample as a function of outgoing muon momentum and muon $\cos\theta$ (top-right). The analysis binning was overlaid with red boxes and bin numbers in black. The exact values of the bin borders can also be found in Tab. 7.43. The projections on vertical (top-left) and horizontal (bottom) axes are shown as well.

Fig. 7.26. It can be noted that this cut rejects a large number of electrons while

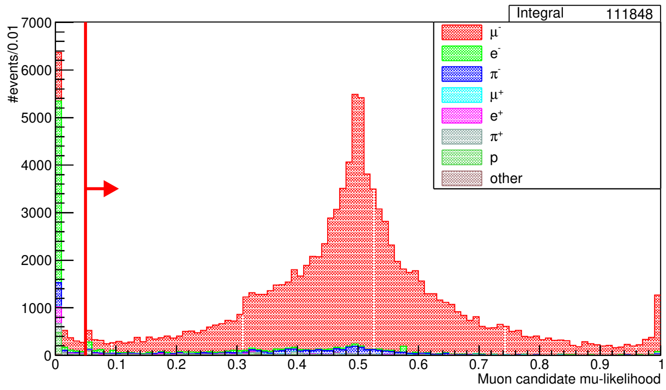

Figure 7.26: Muon likelihood of the selected highest momentum negative track. The red arrow shows the cut which is applied to select muons.

keeping the muon purity at the level of 97.4%. It has a crucial role in enhancing the ν_μ purity of the signal sample.

The distribution of the number of MIP tracks traversing the Time Projection Chamber per selected event in the signal selection is displayed in Fig. 7.27. Requiring exactly one MIP track in TPC per event in the signal sample removes the backgrounds mainly from CC1π and CCOther interactions.

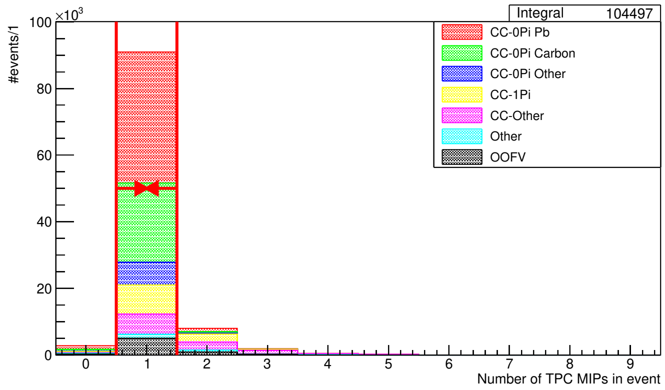

Figure 7.27: Number of MIP tracks in TPC per selected event.

Charged current neutrino interactions with low momentum pions can still be selected with the signal sample cuts if these mesons do not enter TPC (stop in the PØD or in the mechanical structures between the detectors). The cut on the number of Michel electrons rejects pions which decay and, as a result, the delayed electrons are detected (Fig. 7.28).

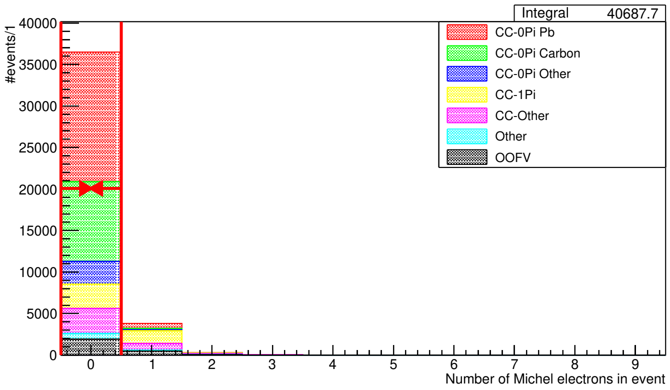

Figure 7.28: Number of Michel electrons in the PØD before the cut on the number of delayed electrons.

The final distributions of momentum and $\cos\theta$ of the muon candidate in the selected signal sample (after all cuts) has been shown in Fig. 7.29.

As it was written before, the purpose of using additional samples is to provide the constraints on background interactions that are present in the signal sample. The aim of sample 2 is to reduce the systematic uncertainty on the predicted number of CC0π interactions on Carbon, while samples 3 and 4 are dedicated to CC1π and CCOther interactions. The main requirement that needs to be imposed on the additional sample is that it should mimic the distributions of the measured variables in the corresponding background in the signal sample or at least occupy the same regions of the phase space as the corresponding background in the signal sample. This condition is tested in Figs. 7.30 - 7.32.

It can be stated that the selected muon candidate momentum and $\cos\theta$ distributions are very similar between the signal and the additional samples and satisfy the

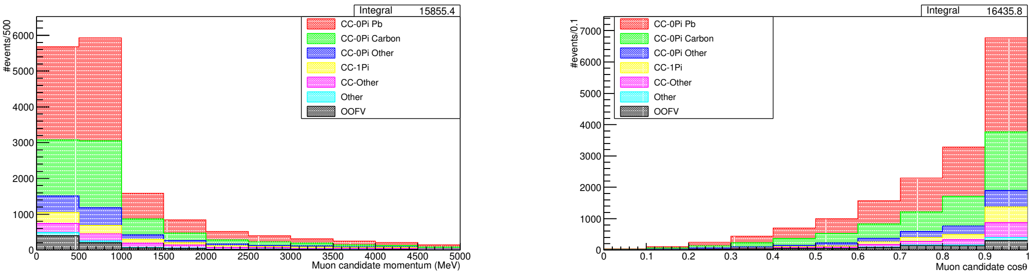

(a) (b)

Figure 7.29: Momentum of the selected muon candidate in the signal sample. Cosine of the angle wrt Z axis for the selected muon candidate in the signal sample.

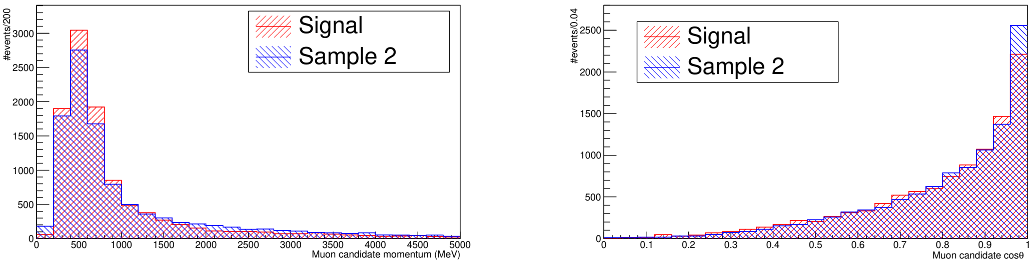

(a) (b)

Figure 7.30: Momentum of the selected muon candidate for the CC0π Carbon interactions in the signal sample (red) vs. all interactions selected with sample 2 (blue) in the left plot. Cosine of the angle wrt Z axis for the selected muon candidate for the CC0π Carbon interactions in the signal sample (red) vs. all interactions selected with sample 2 (blue) in the right plot.

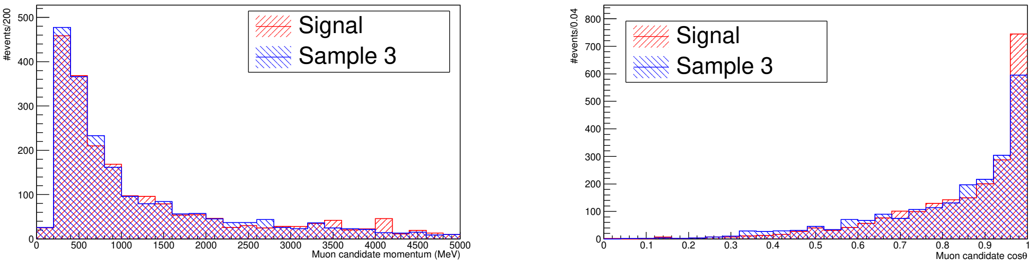

(a) (b)

Figure 7.31: Momentum of the selected muon candidate for the CC1π interactions in the signal sample (red) vs. all interactions selected with sample 3 (blue) in the left plot. Cosine of the angle wrt Z axis for the selected muon candidate for the CC1π interactions in the signal sample (red) vs. all interactions selected with sample 3 (blue) in the right plot.

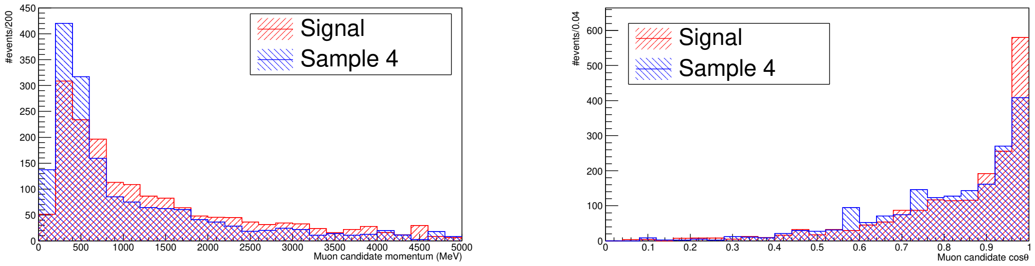

(a)

(b)

Figure 7.32: Momentum of the selected muon candidate for the CCOther interactions in the signal sample (red) vs. all interactions selected with sample 4 (blue) in the left plot. Cosine of the angle wrt Z axis for the selected muon candidate for the CCOther interactions in the signal sample (red) vs. all interactions selected with sample 4 (blue) in the right plot.

requirement. Using these samples as additional inputs for likelihood fitter should allow the uncertainty on the number of background events to be reduced.

7.2.3 Summary

The methods of selecting CC0π interactions on lead and carbon were outlined above. The selection procedures were tested with the Monte Carlo allowing us to evaluate the efficiencies and purities of the set of the four samples. The Monte Carlo that was utilized corresponds to 1.24748×10^{21} protons on target, which is 2.26 times larger than the amount of data collected for runs 1-4 in the T2K near detector. With the techniques described above 37 189 events were selected for the signal sample with the purity of 46.14% for CC0π interactions on lead located in the Central ECal part of the PØD. The overall efficiency for selecting the signal (calculated using the entire phase space) appeared to be 26%.

In this section, the analysis binning was also defined in order to be used in the differential cross section measurement. It was shown that the additional samples that aim at a better estimation of the backgrounds in the signal sample were correctly chosen as the corresponding kinematic distributions were compatible.

Although the parameters that indicate the quality of the signal selection presented in the section above (efficiency, purity) are good, it is necessary to specify the limitations of this analysis. The main limitation is a relatively narrow phase space of the selected CC0π sample, which is related to the fact that mainly events with forward-going muons by requiring that they need to enter TPC are selected. A natural extension of the method would be to include in the selection the neutrino interactions with the outgoing muon that exits the target at high angles (towards the ECALs and SMRD) or is going backwards with respect to the beam direction. This addition would require improving the reconstruction and adding new tools that would support the identification and reconstruction of the kinematics of muons stopping in the PØD and determination of their direction using the time difference between the ending and starting point of the track. These tools have been already developed (with a significant contribution of the author of this monograph), but the validation procedure has yet been finalized and therefore they cannot be used in this analysis. Another interesting enhancement to this analysis would be to incorporate the identification and reconstruction of the proton tracks. This advancement should allow us to investigate the proton multiplicity and two particle-two hole interactions. Some efforts in this direction have already been made, such as using energy loss vs. range relation to discriminate protons and muons and to reconstruct stopping proton's momentum, but their validation is still pending.

It needs to be pointed out again that the selection methods studied in this section are general enough and can be used in other analyses that utilize the PØD detector.

Chapter 8

Summary and outlook

Although we will soon celebrate the centenary of W. Pauli's neutrino postulation, neutrino properties are far from being fully understood despite a number of important discoveries, some of them being awarded Nobel prizes. The list of open questions in neutrino physics in the particle physics sector can be divided into those within the Standard Model three-flavor mixing and those beyond it. The following can be included in the first group of unanswered questions: what is the absolute mass scale of neutrinos?, are neutrinos Majorana or Dirac particles?, what is neutrino mass ordering?, is CP violation in the neutrino sector? are there more than three neutrinos? The latter is the fundamental question beyond the standard paradigm of three massive neutrinos mixing. Apart from particle physics, neutrinos can address other essential questions in geophysics, astrophysics, and cosmology. This monograph is related to T2K, a neutrino oscillation experiment. Both near (ND280) and far (Super-Kamiokande) T2K detectors are massive targets to record a sizable number of neutrino interactions. The lack of precise neutrino-nucleus scattering data for neutrino energies relevant to the T2K experiment (a few hundreds of MeV - few GeV) is one of the significant sources of systematic error in oscillation analyses. Therefore, precise measurements of neutrino-nucleus cross sections are of fundamental importance for developing theoretical models of neutrino interactions and for making progress in neutrino oscillation searches.

This monograph provides a summary of cross-section measurements performed by the T2K experiment using the ND280 near detector. A large number of analyses from the T2K Collaboration were presented against the results of other experiments. Despite the enormous progress in understanding the properties of neutrinos, the uncertainty of the neutrino cross-sections, along with the uncertainty of the neutrino flux, are the main barriers limiting the accuracy of measurements in present and future neutrino oscillation experiments, including those using the accelerator neutrino beams. Moreover, the influence of the knowledge of the neutrino cross sections on the development of neutrino interaction generators, which are necessary for oscillatory measurements, cannot be overestimated.

A large part of the monograph is devoted to the results of the original study, carried out by the author, on the measurement of the cross-section of muon neutrino induced charged current interactions with a charged pion and without pions in the final state. As in other modern experiments studying neutrino-nucleus interactions, the signal reactions were defined using the particles in the final state, after all reinteractions that might have occurred in the nucleus.

The ν_μ-induced charged current single charged pion production cross section on water target was calculated to be

$$\langle \sigma_{\nu_\mu \mathrm{CC}1\pi^+} \rangle_\Phi = 1.10 \cdot 10^{-39} \, {}^{+35.27\%}_{-32.38\%} \, \frac{cm^2}{nucleon},$$

where the result is provided in the form of a single neutrino energy bin cross section integrated over the entire T2K flux (0 - 30 GeV). The obtained cross section uncertainty is dominated by flux and cross section models uncertainties and is consistent with the NEUT-based MC prediction of $1.26 \cdot 10^{-39}$ cm^2.

The analysis of charged current neutrino interactions with no pions in the final state resulted in establishing the event selection that will be a crucial ingredient of future cross-section measurement.

The analysis of the data from the T2K experiment was preceded by the participation of the author of the monograph in developing reconstruction tools for event reconstruction. The proposed novel PØD-tracker incremental matching algorithm significantly improved the efficiency of reconstructing particle trajectories and neutrino interactions in the most downstream part of the PØD. Owing to this improvement, the efficiency of reconstructing muons produced in the most downstream layers of the PØD and entering TPC1 was increased from zero up to 98%. The reconstruction of backward-going FGD1 muons stopping in the PØD was also significantly improved. After successfully passing all the validation tests, the PØD-tracker incremental matching algorithm has been included in the official reconstruction software of the T2K experiment and will be used in future neutrino cross-section measurements.

There is no doubt that neutrino-nucleus scattering is a complex problem, especially in a neutrino energy region of hundreds of MeV to a few GeV. The energy region which is used in current (T2K and NOvA) and will be used in future (Hyper-Kamiokande and DUNE) neutrino oscillation experiments. There is also no doubt that it is necessary to reduce the systematic errors of the neutrino-nucleus scattering cross sections, to make the 5σ coverage of the δ_{CP} parameter (responsible for the leptonic sector CP symmetry breaking/conserving) the largest possible. The summary of the results of the T2K experiment in the study of the neutrino-nucleus interactions presented in this monograph, along with the original results obtained by the author constitute a valuable contribution to the neutrino cross-section and neutrino oscillations physics. It can be assumed that many experiments will soon provide further interesting results pertaining to the mechanism of the neutrino-nucleus interactions.

Bibliography

[1] A.Aguilar et al. (LSND Coll.), Phys. Rev. D64 (2001) 112007
https://doi.org/10.1103/PhysRevD.64.112007

[2] A. A. Aguilar-Arevalo et al. (MiniBooNE Coll.), Phys. Rev. Lett. 110 (2013) 161801, arXiv:1207.4809v1
https://doi.org/10.1103/PhysRevLett.110.161801

[3] A. A. Aguilar-Arevalo et al. (MiniBooNE Coll.), Phys. Rev. Lett. (2018), arXiv:1805.12028v2
https://doi.org/10.1103/PhysRevLett.120.141802

[4] M. Antonello et al., arXiv:1503.01520
https://arxiv.org/abs/1503.01520

[5] K. Abe et al. (T2K Coll.), Nature 580 (2020) 339
https://doi.org/10.1038/s41586-020-2177-0

[6] K. Abe et al., Phys.Rev.D 103 (2021) 11 112009
https://doi.org/10.1103/PhysRevD.103.L011101

[7] K. Abe et al. (T2K collaboration), JHEP 10 (2020) 114, arXiv:2002.11986 [hep-ex]
https://doi.org/10.1007/JHEP10(2020)114

[8] K. Abe et al., Phys.Rev.D 101 (2020) 11 112004
https://doi.org/10.1103/PhysRevD.101.112004

[9] K. Abe et al. (T2K collaboration), Phys. Rev. D98 (2018) 032003
https://doi.org/10.1103/PhysRevD.98.012004

[10] T. Wachala (for the T2K collaboration), Acta Phys. Polon. B 50 (2019) 1757-1764
https://doi.org/10.5506/APhysPolB.50.1757

[11] T. Wachala (for the T2K collaboration), The latest results from the long-baseline neutrino experiment T2K
https://indico.jinr.ru/event/410/contributions/3341/

[12] T. Wachala, Acta Phys.Polon.B 48 (2017) 1969
https://doi.org/10.5506/APhysPolB.48.1969

[13] T. Wachala (for the T2K collaboration), Nuovo Cim.C 38 (2016) 4, 121
https://doi.org/10.1393/ncc/i2015-15121-3

[14] T. Wachala, Acta Phys.Polon.B 46 (2015) 2291-2300
https://doi.org/10.5506/APhysPolB.46.2291

[15] L. Alvarez-Ruso et al. (NuSTEC group), arXiv:1706.03621v2
https://arxiv.org/abs/1706.03621

[16] Y. Hayato, Acta Phys. Pol. B40 (2009) 2477
http://th-www.if.uj.edu.pl/acta/vol40/abs/v40p2477.htm

[17] C. Andreopoulos at al., Nucl. Instr. Meth. A614 (2010) 87, arXiv:0905.2517
https://doi.org/10.1016/j.nima.2009.12.009

[18] C. Juszczak, J. A. Nowak and J. T. Sobczyk, Nucl. Phys. Proc. Suppl. 159 (2006) 211, arXiv:0512365
https://doi.org/10.1016/j.nuclphysbps.2006.08.069

[19] R. Smith and E. Moniz, Nucl. Phys B43 (1972) 605
https://doi.org/10.1016/0550-3213(72)90040-5

[20] S. Kuzmin, V. LYubushkin and V. Naumov, Eur. Phys. J. C54 (2008) 517
https://doi.org/10.1140/epjc/s10052-008-0582-x

[21] O. Benhar, A. Fabrocini, S. Fantoni and I. Sick, Nucl. Phys. A579 (1994) 493
https://doi.org/10.1016/0375-9474(94)90920-2

[22] J. Nieves, I. Ruiz Simo and M. J. Vicente Vacas, Phys. Rev. C83 (2011) 045501
https://doi.org/10.1103/PhysRevC.83.045501

[23] M. Martini, Phys. Rev. C80 (2009) 065501
https://doi.org/10.1103/PhysRevC.80.065501

[24] C. Juszczak, J. T. Sobczyk and J. Zmuda, Phys. Rev. C82 (2010) 045502, doi: https://doi.org/10.1103/PhysRevC.82.045502

[25] R. Gran, J. Nieves, F. Sanchez, and M. J. Vicente Vacas, Phys. Rev. D88 (2013) 113007
https://doi.org/10.1103/PhysRevD.88.113007

[26] S. Dolan Ph.D.thesis, University of Oxford (2017)
https://ora.ox.ac.uk/objects/uuid:16cef4e8-b52b-48c4-a954-81fba0b7536b

[27] H. De Vries, C.W. De Jager and C. De Vries, Atom. Data Nucl. Data Tabl. 36 pp. 495536 (1987)
https://doi.org/10.1016/0092-640X(87)90013-1

[28] P.K.A. de Witt Huberts, J.Phys. G16 (1990) 507544, doi:10.1088/0954-3899/16/4/004
https://iopscience.iop.org/article/10.1088/0954-3899/16/4/004

[29] M. Tanabashi et al. (Particle Data Group), Phys. Rev. D93 (2018) 030001
https://doi.org/10.1103/PhysRevD.98.030001

[30] C. Anderson et al. (ArgoNeuT Coll.), Phys. Rev. Lett. 108 (2012) 161802, arXiv:1111.0103
https://doi.org/10.1103/PhysRevLett.108.161802

[31] P. Adamson et al., Nucl. Instr. Meth A806 (2016)279
https://doi.org/10.1016/j.nima.2015.08.063, arXiv:1507.06690v2

[32] B. G. Tice et al. (MINERvA Coll.), Phys. Rev. Lett. 112 (2014) 231801, arXiv:1403.2103
https://doi.org/10.1103/PhysRevD.93.071101

[33] J. Mousseau et al. (MINERvA Coll.), Phys. Rev. D93 (2016) 071101, arXiv:1601.06313
https://doi.org/10.1103/PhysRevD.93.071101

[34] J. Devan et al. (MINERvA Coll.), Phys. Rev. D94 (2016) 112007, arXiv:1610.04746
https://doi.org/10.1103/PhysRevD.94.112007

[35] P. A. Rodrigues et al. (MINERvA Coll.), Phys. Rev. Lett 116 (2016) 071802, arXiv:1511.05944
https://doi.org/10.1103/PhysRevLett.116.071802

[36] H. Faissner et al., Phys. Lett. B125 (1983) 230
https://doi.org/10.1016/0370-2693(83)91274-1

[37] Y. Kurimoto et al. (SCiBooNE Coll.), Phys. Rev. D81 (2010) 111102(R)
https://doi.org/10.1103/PhysRevD.81.111102

[38] A. A. Aguilar-Arvelo et al. (MiniBooNE Coll.), Phys. Lett. B664 (2008) 41
https://doi.org/10.1016/j.physletb.2008.05.006

[39] M. A. Acero et al. (NOvA Coll.), arXiv:1902.00583v3,
https://journals.aps.org/prd/abstract/10.1103/PhysRevD.102.012004

[40] M. Hasegawa et al. (K2K Coll.), Phys. Rev. Lett. 95 (2005) 252301
https://doi.org/10.1103/PhysRevLett.95.252301

[41] K. Hiraide et al. (SciBooNE Coll.), Phys. Rev. D78 (2008) 112004
https://doi.org/10.1103/PhysRevD.78.112004

[42] A. Higuera et al. (MINERvA Coll.), Phys. Rev. Lett. 113 (2014) 261802
https://doi.org/10.1103/PhysRevLett.113.261802

[43] A. Mislivec et al. (MINERvA Coll.), Phys. Rev. D97 (2018) 032014
https://doi.org/10.1103/PhysRevD.97.032014

[44] K. Abe et al. (T2K Coll.), Phys. Rev. Lett. 117 (2016) 192501
https://doi.org/10.1103/PhysRevLett.117.192501

[45] R. Acciarri et al. (ArgoNET Coll.), Phys. Rev. Lett. 113 (2014) 261801
https://doi.org/10.1103/PhysRevLett.113.261801

[46] K. Hiraide et al., Phys. Lett. B313 (1993) 267
https://doi.org/10.1016/0370-2693(93)91223-A

[47] J. L. Hewett, H. Weerts et al., arXiv:1205.267v1
https://arxiv.org/abs/1205.2671

[48] K. Mahn, Ch. Marshall and C. Wilkinson, Annu. Rev. Nucl. Part. Sci. 68 (2018) 105
https://doi.org/10.1146/annurev-nucl-101917-020930

[49] A. A. Aguilar-Arevalo et al. (MiniBooNE Coll.), Phys. Rev. D81 (2010) 092005, arXiv:1002.2680
https://doi.org/10.1103/PhysRevD.81.092005

[50] A. A. Aguilar-Arevalo et al. (MiniBooNE Coll.), Phys. Rev. D88 (2013) 032001, arXiv:1301.7067
https://doi.org/10.1103/PhysRevD.88.032001

[51] L. Alvarez-Ruso, Y. Hayato and J. Nieves, New Journal of Physics 16 (2014) 075015
https://doi.org/10.1088/1367-2630/16/7/075015

[52] D. Ruterbories et al. (MINERvA Coll), Phys. Rev. D99 (2019) 012004, arXiv:1911.02774
https://doi.org/10.1103/PhysRevD.99.012004

[53] C. E. Patrick et al. (MINERvA Coll), Phys. Rev. D97 (2018) 052002, arXiv:1801.01197
https://doi.org/10.1103/PhysRevD.97.052002

[54] R. Gran et al. (MINERvA Coll.), Phys. Rev. Lett. 120 (2018) 221805, arXiv:1803.09377
https://doi.org/10.1103/PhysRevLett.120.221805

[55] A. A. Aguilar-Arevalo et al. (MiniBooNE), Phys. Rev. D83 (2011) 052007, arXiv:1011.3572
https://doi.org/10.1103/PhysRevD.83.052007

[56] A. A. Aguilar-Arevalo et al. (MiniBooNE), Phys. Rev. Lett. 103 (2009) 081801, arXiv:0904.3159
https://doi.org/10.1103/PhysRevLett.103.081801

[57] A. A. Aguilar-Arevalo et al. (MiniBooNE), Phys. Rev. D83 (2011) 052009, arXiv:1010.3264
https://doi.org/10.1103/PhysRevD.83.052009

[58] D. Rein and L. M. Sehgal, Ann. Phys. 133 (1981) 79
https://doi.org/10.1016/0003-4916(81)90242-6

[59] R.P. Feynman, M. Kislinger, F. Ravndal, Phys. Rev. D3, (1971) 27062732
https://doi.org/10.1103/PhysRevD.3.2706

[60] M. Tzanov et al. (NuTeV Coll.), Phys. Rev. D74 (2006) 012008
https://doi.org/10.1103/PhysRevD.74.012008

[61] G. Onengut et al., Phys. Lett. B632 (2006) 65
https://doi.org/10.1016/j.physletb.2005.10.062

[62] J. Altegoer et al., NIM A404 (1998) 96
https://doi.org/10.1016/j.physletb.2007.12.027

[63] B. G. Tice et al. (MINERvA Coll.), Phys. ReV. Lett. 112 (2014) 231801, arXiv:1403.2103
https://doi.org/10.1103/PhysRevD.93.071101

[64] https://microboone.fnal.gov

[65] https://icarus.fnal.gov

[66] https://sbn-nd.fnal.gov

[67] https://www.dunescience.org

[68] https://www.hyperk.org

[69] K. Abe et al. (T2K collaboration), Nucl. Instrum. Meth. A659 (2011) 106-135
https://doi.org/10.1016/j.nima.2011.06.067

[70] Z. Maki, M. Nakagawa, S. Sakata, Progress of Theoretical Physics. 28 (5) (1962): 870;B. Pontecorvo, Soviet Physics JETP. 7 (1958): 172
https://doi.org/10.1143/PTP.28.870

[71] M. Tanabashi et al. (Particle Data Group), Phys. Rev. D98 (2018) 030001 and 2019 update
https://doi.org/10.1103/PhysRevD.98.030001

[72] Y. Fukuda Y. et al. (Super-Kamiokande collaboration), Phys. Rev. Lett. 81 (1998) 1562
https://doi.org/10.1103/PhysRevLett.81.1562

[73] K. Abe et al. (T2K collaboration), Phys.Rev.Lett. 107 (2011) 041801
https://doi.org/10.1103/PhysRevLett.107.041801

[74] K. Abe et al. (T2K collaboration), Phys.Rev.Lett. 112 (2014) 061802
https://doi.org/10.1103/PhysRevLett.112.061802

[75] K. Abe et al. (T2K collaboration), Phys.Rev. D96 (2017) 092006, Phys.Rev. D98 (2018) 019902
https://doi.org/10.1103/PhysRevD.98.019902

[76] K. Nishikawa et al. (T2K collaboration), *Fundamental Physics Breakthrough Prize Laureates webpage*
https://breakthroughprize.org/Laureates/1/L155

[77] M. Tanabashi et al. (Particle Data Group), Phys. Rev. D98 (2018) 030001
https://doi.org/10.1103/PhysRevD.98.030001

[78] K. Abe et al. (T2K collaboration), Phys. Rev. D 91 051102(R) (2015), Phys. Rev. D 95 111101(R) (2017), Phys Rev D93 012006 (2016)
https://doi.org/10.1103/PhysRevD.93.012006

[79] https://j-parc.jp/researcher/en/about/what/index.html, Accessed on 20 March 2020

[80] K. Abe et al. (T2K collaboration), Phys.Rev. D87 (2013) 012001
https://doi.org/10.1103/PhysRevD.87.012001

[81] T. Ovsiannikova et al., Journal of Physics: Conference Series 675 012030 Feb 2016.14
https://doi.org/10.1134/S1063779617060478

[82] M. Antonova et et al., PoS NuFact2017 (2018) 078
https://doi.org/10.22323/1.295.0078

[83] Internal webpage of the T2K experiment - t2k.org

[84] K. Abe et al. (T2K collaboration), Nucl. Instrum. Meth. A694 (2012) 211-223
https://doi.org/10.1016/j.nima.2012.03.023

[85] S. Assylbekov et al. (T2K collaboration), Nucl. Instrum. Meth. A686 (2012) 48
https://doi.org/10.1016/j.nima.2012.05.028

[86] D. Gonzalez-Diaz et al., Nucl.Instrum.Meth. A878 (2018) 200-255
https://doi.org/10.1016/j.nima.2017.09.024

[87] N. Abgrall et al., Nucl.Instrum.Meth. A637 (2011) 25-46
https://doi.org/10.1016/j.nima.2011.02.036

[88] P.A. Amaudruz et al., Nucl.Instrum.Meth. A696 (2012) 1-31
https://doi.org/10.1016/j.nima.2012.08.020

[89] D. Allan et al., Journal of Instrumentation 8 (2013) P10019
https://doi.org/10.1088/1748-0221/8/10/P10019

[90] S. Aoki et al., Nucl.Instrum.Meth. A698 (2013) 135-146
https://doi.org/10.1016/j.nima.2012.10.001

[91] Y. Fukuda et al. (Super-Kamiokande Coll.), Nucl. Instrum. Meth. A501 (2003) 418
https://doi.org/10.1016/S0168-9002(03)00425-X

[92] M. G. Hogan, PhD dissertation, Colorado State University, https://t2k.org/docs/thesis/103, Accessed on 22 March 2020

[93] T. Wachala, Acta Phys.Polon. B46 (2015) 2291-2300
https://doi.org/10.5506/APhysPolB.46.2291

[94] G. D'Agostini, Nucl. Instrum. Methods 362 (1995) 487
https://doi.org/10.1016/0168-9002(95)00274-X

[95] Y. Nakajima et al. (SciBooNE Collaboration), Phys. Rev. D 83 (2011) 012005
https://doi.org/10.1103/PhysRevD.83.012005

[96] A. I. Mukhin et al., Sov. J. Nucl. Phys. 30 (1979) 528

[97] K. Abe et al. (T2K collaboration), Phys.Rev. D87 (2013) 092003
https://doi.org/10.1103/PhysRevD.87.092003

[98] N. Abgrall et al. (NA61/SHINE Collaboration), Phys. Rev. C 84 034604 (2011), Phys. Rev. C 85 035210 (2012)
https://doi.org/10.1103/PhysRevC.85.035210

[99] J. Blietschau et al. (Gargamelle Collaboration), Nucl. Phys. B133 (1978) 205
https://doi.org/10.1016/0550-3213(78)90299-7

[100] K. Abe et al. (T2K collaboration), Phys.Rev.Lett. 113 (2014) 241803
https://doi.org/10.1103/PhysRevLett.113.241803

[101] K. Abe et al. (T2K collaboration), Phys.Rev.D 90 (2014) 5 052010
https://doi.org/10.1103/PhysRevD.90.052010

[102] Q. Wu et al. (NOMAD Collaboration), Phys. Lett. B 660 19 (2008)
https://doi.org/10.1016/j.physletb.2007.12.027

[103] Y. Nakajima et al. (SciBooNE Collaboration), Phys. Rev. D83 012005 (2011)
https://doi.org/10.1103/PhysRevD.83.012005

[104] K. Abe et al. (T2K collaboration), Phys.Rev.D 93 (2016) 7 072002
https://doi.org/10.1103/PhysRevD.93.072002

[105] P. Adamson et al. (MINOS collaboration), Phys.Rev. D81 072002 2010
http://dx.doi.org/10.1103/PhysRevD.81.072002

[106] K. Abe et al. (T2K collaboration), Phys.Rev.D 91 (2015) 11 112002
https://doi.org/10.1103/PhysRevD.91.112002

[107] A. A. Aguilar-Arevalo et al. (MiniBooNE Collaboration), Phys. Rev. D81 092005 (2010)
https://doi.org/10.1103/PhysRevD.81.092005

[108] J. L. Alcaraz-Aunion and J. Walding (SciBooNE Collaboration), AIP Conf. Proc. 1189 145 (2009)
https://doi.org/10.1063/1.3274145

[109] V. Lyubushkin et al. (NOMAD Collaboration), Eur. Phys. J. C63 355 (2009)
https://doi.org/10.1140/epjc/s10052-009-1113-0

[110] G. A. Fiorentini, D. W. Schmitz, P. A. Rodrigues, et al. (MINERνA Collaboration), Phys. Rev. Lett. 111 022502 (2013)
https://doi.org/10.1103/PhysRevLett.111.022502

[111] K. Abe et al. (T2K collaboration), Prog. Theor. Exp. Phys. 9 (2019) 093C02
https://doi.org/10.1093/ptep/ptz070

[112] K. Abe et al. (T2K collaboration), Phys.Rev. D96 (2017) 052001
https://doi.org/10.1103/PhysRevD.96.052001

[113] K. Abe et al. (T2K collaboration), Phys.Rev.Lett. 117 (2016) 192501
https://doi.org/10.1103/PhysRevLett.117.192501

[114] K. Abe et al. (T2K collaboration), Phys.Rev. D101 (2020) 012007
https://doi.org/10.1103/PhysRevD.101.012007

[115] A.A. Aguilar-Arevalo et al. (MiniBooNE Collaboration), Phys. Rev. D 83 052007 (2011)
https://doi.org/10.1103/PhysRevD.83.052007

[116] B. Eberly et al. (MINERνA Collaboration), Phys.Rev. D 92, 092008 (2015)
https://doi.org/10.1103/PhysRevD.92.092008

[117] C.L. McGivern et al. (MINERνA Collaboration), Phys.Rev. D 94 052005 (2016)
https://doi.org/10.1103/PhysRevD.94.052005

[118] P.Stowell et al., Phys. Rev. D 100, 072005 (2019)
https://doi.org/10.1103/PhysRevD.100.072005

[119] K. Abe et al. (T2K collaboration), Phys.Rev. D95 (2017) 012010
https://doi.org/10.1103/PhysRevD.95.012010

[120] K. Abe et al. (T2K collaboration), Phys.Rev. D93 (2016) 112012
https://doi.org/10.1103/PhysRevD.93.112012

[121] J. Nieves, I. R. Simo, and M. V. Vacas, Phys. Lett. B707 72 (2012)
http://dx.doi.org/10.1016/j.nuclphysbps.2015.09.295

[122] O. Buss et al., Phys. Rept. 512 1 (2012)
https://doi.org/10.1016/j.physrep.2011.12.001

[123] K. Abe et al. (T2K collaboration), Phys. Rev. D 101, 112001 (2020)
https://doi.org/10.1103/PhysRevD.101.112001

[124] K. Abe et al. (T2K collaboration), Phys.Rev. D97 (2018) 012001
https://doi.org/10.1103/PhysRevD.97.012001

[125] M. Martini, M. Ericson, G. Chanfray, and J. Marteau, Phys. Rev. C80, 065501 (2009)
https://doi.org/10.1103/PhysRevC.80.065501

[126] K. Abe et al. (T2K collaboration), J. Phys. G 46 08LT01 (2019)
https://doi.org/10.1088/1361-6471/ab227d

[127] C. Kullenberg et al. (NOMAD collaboration), Phys.Lett. B706 268 (2012)
http://nrs.harvard.edu/urn-3:HUL.InstRepos:11870365

[128] Q. Wu et al. (NOMAD collaboration), Phys. Lett. B660 19 (2008)
https://doi.org/10.1016/j.physletb.2007.12.027

[129] E. Wang, L. Alvarez-Ruso, J. Nieves, Phys.Rev. C89 015503 (2014)
https://doi.org/10.1103/PhysRevC.89.015503

[130] K. Abe et al. (T2K collaboration), Phys.Rev. D98 (2018) 012004
https://doi.org/10.1103/PhysRevD.98.012004

[131] K. Abe et al. (T2K collaboration), Phys. Rev. D 102, 012007 (2020)
https://doi.org/10.1103/PhysRevD.102.012007

[132] K. Abe et al., Phys.Rev.D 101 (2020) 11, 112001
https://doi.org/10.1103/PhysRevD.101.112001

[133] D. Cherdack, M. Hogan, J. Schwehr, *Measurement of the CC1pi+ cross section on water in the P0D*, T2K Technical Note 333 (Internal document)

[134] A. Hillairet et al. *ND280 Reconstruction*, T2K Technical Note 072 (Internal document)

[135] A. Finch, D.R. Hadley, T. Wachala *ND280 Reconstruction for Production 7*, T2K Technical Note 329 (Internal document)

[136] A. Aguilar-Arevalo et al. (LSND collaboration), Phys.Rev.D 64 (2001) 112007
https://doi.org/10.1103/PhysRevD.64.112007

[137] R. Gonzalez-Jimenez et al., Phys. Rev. C90 035501 (2014); G. D. Megias et al., Phys. Rev. D91 073004 (2015); G. D. Megias et al., Phys. Rev. D94 013012; G. D. Megias et al., Phys. Rev. D94, 093004 (2016)
https://doi.org/10.1103/PhysRevC.90.035501

[138] J. A. Caballero et al., Phys. Rev. Lett. 95 252502 (2005)
https://doi.org/10.1103/PhysRevLett.95.252502

[139] I. Ruiz Simo et al., J. Phys. G44 065105 (2017)
https://doi.org/10.1088/1361-6471/aa6a06

[140] K. Abe et al., *T2K ND280 Upgrade Technical Design Report*, arXiv:1901.03750 [physics.ins-det]
https://arxiv.org/abs/1901.03750

[141] D. Sgalaberna, PoS: Proceedings of Science 390, http://doi.org/10.22323/1.390.0175

[142] J. Nieves, I. Ruiz Simo, and M. J. Vicente Vacas, Phys. Rev. C83 045501 (2011)
https://doi.org/10.1103/PhysRevC.83.045501

[143] T. Golan, C. Juszczak, and J. T. Sobczyk, Phys. Rev. C86 015505 (2012)
https://doi.org/10.1103/PhysRevC.86.015505

[144] O. Benhar, A. Fabrocini, S. Fantoni, and I. Sick, Nucl.Phys. A579 493 (1994)
https://doi.org/10.1016/0370-2693(94)91218-1

[145] K. Gallmeister, U. Mosel, and J. Weil, Phys. Rev. C94 035502 (2016)
https://doi.org/10.1103/PhysRevC.94.035502

[146] J. S. O' Connell, T. W. Donnelly, and J. D. Walecka, Phys. Rev. C6 719 (1972)
https://doi.org/10.1016/0370-2693(72)90577-1

[147] S. Dolan, U. Mosel, K. Gallmeister, L. Pickering, and S. Bolognesi, Phys. Rev. C98 045502 (2018)
https://doi.org/10.1103/PhysRevC.98.045502

[148] [54] X. G. Lu et al., Phys. Rev. C94 1 015503 2016
https://doi.org/10.1103/PhysRevC.99.055504

[149] D. Rein and L. Sehgal, Nucl. Phys.B223 29 (1983)
https://doi.org/10.1016/0550-3213(83)90090-1

[150] D. Rein and L. Sehgal, Phys. Lett. B657 207 (2007)
https://doi.org/10.1016/j.physletb.2007.10.025

[151] M. Gluck, E. Reya, and A. Vogt, Eur. Phys. J. C5 461 (1998)
https://doi.org/10.1007/s100529800978

[152] A. Bodek and U. K. Yang, AIP Conf. Proc. 670 110 (2003)
https://doi.org/10.1063/1.1594324

[153] J. Allison et al., Nucl. Instrum. Meth. A 835 (2016) 186-225; J. Allison et al., IEEE Trans. Nucl. Sci. 53 (2006) 270-278; S. Agostinelli et al., Nucl. Instrum. Meth. A 506 (2003) 250-303
https://doi.org/10.1109/TNS.2006.869826

[154] A.Cervera-Villanueva, J.J.Gómez-Cadenas, J.A.Hernando, Nucl. Instr. Meth. A534 1–2 180-183 (2004)
https://indico.cern.ch/event/408139/contributions/979725/attachments/815609/1117558/paper.pdf

[155] R. E. Kalman, Journal of Basic Engineering 82: 35–45 (1960)
https://doi.org/10.1115/1.3662552

[156] Radon J., Parks P.C., IEEE Transactions on Medical Imaging, 5 (4): 170–176 (1986)
https://doi.org/10.1109/TMI.1986.4307775

[157] Cholesky factorization, N.J. Higham (originator), Encyclopedia of Mathematics, Springer, ISBN 978-1-55608-010-4

[158] A. Hoecker et al., Nucl.Instrum.Meth. A372 (1996) 469-481
https://doi.org/10.1016/0168-9002(95)01478-0

[159] S.Schmitt, JINST 7 (2012) T10003
https://doi.org/10.1088/1748-0221/7/10/T10003

[160] K. Abe et al., Phys.Rev.D 97 (2018) 3 032002
https://doi.org/10.1103/PhysRevD.97.032002

[161] S. Assylbekov, T. Wachala, R. J. Wilson, *Measurement of* ν_μ*-induced Charged Current Single Charged Pion Production Flux-averaged Absolute Cross-Section on Water in the P0D Detector*, T2K Technical Note 136 (Internal document)

[162] K. Gilje, *Geometry and mass of the* π^0 *detector in the ND280 basket*, T2K Technical Note 73 v3.1 (Internal document)

[163] T. Campbell et al., *CC inclusive in the P0D*, T2K Technical Note 80 v4 (Internal document)

[164] C. Bojechko et al., *CC-multiple-pion* ν_μ *event selections in the ND280 tracker using Run 1+2+3+4 data*, T2K Technical Note 152 v4.2 (Internal document)

[165] FLUKA version 2008.3c, 2008
http://www.fluka.org/fluka.php

[166] GEANT3, A detector description and simulation tool, 1993. Application Software Group, Computing and Networks Division, CERN, Geneva
https://cds.cern.ch/record/1073159/files/cer-002728534.pdf

[167] K. Abe et al. (T2K Collaboration), Phys. Rev. D 87 012001 (2013)
https://doi.org/10.1103/PhysRevD.87.019902

[168] P. De Perio et al., *Cross section parameters for the 2012a oscillation analysis*, T2K Technical Note 108 (Internal document)

[169] P. De Perio at al., *Implementation of the NIWG Cross Section Parametrization*, T2K Technical Note 113 (Internal document)

[170] D. Ruterbories, *Measurement of NCE with the P0D*, T2K Technical Note 131 (Internal document)

[171] P. de Perio, *NEUT systematic studies for 2010a analysis*, T2K Technical Note 32 v1.0 (Internal document)

[172] ROOT, TRandom3 class documentation
https://root.cern.ch/doc/master/classTRandom3.html

[173] M. Ravonel, *Measurement of the* ν_μ *flux and inclusive charged current cross section at T2K's near detector*, T2K Technical Note 117 (Internal document)

Glossary

PØD Pizero Detector.

ECAL Electromagnetic Calorimeter.

FGD Fine-Grained Detector.

FHC Forward-Horn Current.

IH Inverted Hierarchy.

IO Inverted Ordering.

J-PARC Japan Proton Accelerator Research Complex.

MPPC Multi-Pixel Photon Counter.

MR Main Ring.

MSW Mikheyev–Smirnov–Wolfenstein.

MUMON Muon Monitor.

NH Normal Hierarchy.

NO Normal Ordering.

NOvA NuMI Off-axis ν_e Appearance.

PEU Pixel Equivalent Unit.

PMNS Pontecorvo-Maki-Nakagawa-Sakata.

POT Protons On Target.

RCS Rapid-Cycling-Synchrotron.

RHC Reversed-Horn Current.

SMRD Side Muon Range Detector.

TFB Trip-t Frontend Board.

TPC Time Projection Chamber.

WLS WaveLength-Shifting.